Measurements of Cross Sections and Double Longitudinal Asymmetries of $\pi^{\pm}$ production in $p+p$ collisions to constrain the Gluon Spin contribution to the Proton Spin

A Dissertation Presented

by

SOOK HYUN LEE

to

The Graduate School

in Partial Fulfillment of the Requirements

for the Degree of

Doctor of Philosophy

in

Physics

Stony Brook University

May 2013

Stony Brook University

The Graduate School

SOOK HYUN LEE

We, the dissertation committee for the above candidate for the Doctor of Philosophy degree, hereby recommend acceptance of this dissertation.

Abhay Deshpande – Dissertation Advisor
Professor, Department of Physics and Astronomy

Jianwei Qiu – Chairperson of Defense
Professor, Department of Physics and Astronomy

Thomas Weinacht
Professor, Department of Physics and Astronomy

Alexander Bazilevsky
Physicist
Brookhaven National Lab

This dissertation is accepted by the Graduate School.

Lawrence Martin
Dean of the Graduate School

Abstract of the Dissertation

Measurements of Cross Sections and Double Longitudinal Asymmetries of $\pi^{\pm}$ production in $p+p$ collisions to constrain the Gluon Spin contribution to the Proton Spin

by

SOOK HYUN LEE

Doctor of Philosophy

in

Physics

Stony Brook University

2013

The spin of the proton is known to be $\frac{1}{2}\hbar$. Although its angular momentum sum rule in terms of constituent quark and gluon components has been established, its detailed decomposition is poorly known. What fraction is attributed to the spin (polarization) and orbital angular momentum component is completely unknown, and how much of the spin component is from the quarks and gluons is only partially known. Dedicated experiments in the past few decades have measured the sum of quark and anti-quark spin contribution to account for only $\sim$25% of the proton spin, whereas separating the sea-quark polarizations or constraining the contribution of gluon polarization is still a subject of active experimental research.

The Relativistic Heavy Ion Collider (RHIC) is a unique facility that provides collisions between polarized protons and thereby excellent tools to study the role of gluons in the proton intrinsic angular momentum. The double longitudinal asymmetry A_{LL} of single inclusive production allows access to the polarized gluon distribution Δg. It does so when the asymmetry measurements are incorporated into the so-called global analysis where polarized parton distribution functions and fragmentation functions are simultaneously fitted to best describe various measurements from different experiments. While π^0 at PHENIX and jets at STAR have mainly been putting constrains on ΔG, the first moment of Δg, other channels that provide complementary information on ΔG are critical.

The high p_T charged pion production is expected to be sensitive to the sign of ΔG. The isospin symmetry with other pion species will enables us to visually see the sign via the ordering of A_{LL} of the three pion species even without performing global analysis. The interpretation can also be cross checked with the one drawn from global analysis, where the dominance of $q-g$ scattering in $\pi^{\pm}$ production enhances the sensitivity. For this dissertation, high p_T charged pion production at mid-rapidity in polarized $p+p$ collisions at $\sqrt{s} = 200$ GeV has been analyzed. In this work, I developed a new analysis including the Hadron Blind Detector, a gas-based Cerenkov detector, to overcome the major challenge, a large fraction of electrons misidentified with $\pi^{\pm}$, and achieved >98% purity in $\pi^{\pm}$ sample. Along with A_{LL}, invariant differential cross section has been measured for different charges separately to validate the current perturbative Quantum Chromo-dynamics framework. Through these first successful measurements, we demonstrated $\pi^{\pm}$ is a promising channel to extract crucial information on ΔG in that complete discussions will be available with further constrained charge-separated fragmentation functions and improved statistics.

Dedicated to my parents,
who always have given me unconditional love and support.

Contents

List of Figures

List of Tables

Chapter 1

Introduction

1.1 History of polarized physics

Spin is one of most fundamental properties of elementary particles. It dictates the symmetry behavior under spacetime transformation. This additional degrees of freedom can therefore be used in high energy experiments to study aspects of interactions between elementary particles that we will not be able to learn at experiments with unpolarized beams.

One important aspect physicists have been aiming to unveil is how the intrinsic angular momentum of nucleons is composed of the angular momentum of their constituents, quarks and gluons. To this end, producing polarized sources of elementary particles or nucleons is critical. While the Stern-Gerlach experiment made possible the production of polarized atoms, the advent of polarized lepton beams in 1972 at Yale opened up a whole new field of polarized (spin) physics.

The first generation of polarized experiments were carried out largely at SLAC[1] and CERN[2] in 70s∼80s. Experiment E80 which took place in 1976 at SLAC used longitudinally polarized electron beam with 6∼13 GeV to scatter off a polarized butanol fixed target [1]. Although the average beam and target polarization[3] was rather high at 50∼60%, the spin 0 nuclei in the butanol target, carbon and oxygen, caused a reduction of effective target polarization, a large dilution factor (ratio of the number of hydrogen nucleons over the total number of nucleons) of $\sim \frac{10}{74}$. E80 was able to access the kinematic range of $0.1 < x_{BJ} < 0.5$ and Q^2 ∼2 GeV^2 through the deep inelastic scattering

[1] Stanford Linear Accelerator Center

[2] Conseil Européen pour la Recherche Nucléaire (European Council for Nuclear Research)

[3] See Chapter 3.1 for the definition of polarization for beam or target particles.

(DIS) processes at this experiment[4]. In 1983, E130 experiment upgraded the beam energy to 23 GeV and extended the kinematic coverage in x_{BJ} from 0.2 to 0.65 and in Q^2 range from 3 to 10 GeV^2 [2]. Beam polarization was also enhanced to 80%. One observable measured at these experiments with longitudinally polarized beam and target was the virtual photon-proton cross section asymmetry A_1^p designed to extract information on $\Gamma_1^p(Q^2)$. $\Gamma_1^p(Q^2)$ is the first moment[5] of the polarized proton structure function $g_1^p(x, Q^2)$ which is a linear combination of the polarized parton distribution functions for constituent quark + anti-quark ($\Delta q + \Delta\bar{q}$) in the parton model[6]. The result showed that the measured quantity was in roughly good agreement with the prediction based on the parton model. The combined result of E80 and E130 turned out to be $\Gamma_1^p(\langle Q^2\rangle \approx 4 \text{ GeV}^2) = 0.17 \pm 0.05$, which was consistent with the value $\frac{5}{9}$ of the Ellis-Jaffe sum rule[7] [3] and static SU(6) quark model.

The polarized DIS experiments at CERN [4], on the other hand, started as an addendum to the unpolarized EMC experiments[8]. Muon beam with energies 100∼200 GeV was produced from the semi-leptonic decay of pions which were produced in proton collisions. The V-A nature[9] of the decay made possible to achieve very high muon beam polarization $\sim$ 80%. High energy polarized muon beam hitting a polarized ammonia (NH_3) target allowed for accessing small x_{BJ} range of 0.01 to 0.1 and high $\langle Q^2\rangle$=10.7 GeV^2. Although this suited the original intent of the experiment, extending the kinematic coverage to an unreached small x_{BJ} and high Q^2 range and confirming the Ellis-Jaffe sum rule, the interpretation of the results came as a major surprise. The measured value of $\Gamma_1^p(\langle Q^2\rangle \approx 10.7 \text{ GeV}^2) = 0.123 \pm 0.013 \pm 0.019$ was well below the Ellis-Jaffe expectation of 0.18± 0.01. The low value of Γ_1^p is attributed to the low values of the asymmetries at small x_{BJ} that translate into low values for the polarized proton structure function $g_1^p(x, Q^2)$. This is turn leads to a conclusion that the quark and anti-quark spin components account for surprisingly small fraction of 25% of the proton spin.

This surprise motivated a second CERN experiment with polarization, the

[4] Q^2 is the hard scale of deep inelastic scattering. x_{BJ} is referred to as the Bjorken scaling variable x and used as a proxy for the parton momentum fraction of an incoming proton. See Chapter 1.4.2 for exact definitions.

[5] i.e. $\Gamma_1^p(Q^2) = \int_0^1 g_1^p(x, Q^2)dx$

[6] Formal definitions will be given in Chapter 1.4.2

[7] This sum rule assumes a vanishing total polarization of strange sea quarks in the parton model expression of Γ_1.

[8] European Muon Collaboration

[9] The interaction between vector current and axial vector current in weak decay ensures muons are 100% left-handed in the pion rest frame. In laboratory frame, the muon beam polarization goes as $\frac{E_\mu}{E_\pi}$.

SMC experiment[10], which used polarized butanol target instead of ammonia. SMC [5] was able to measure A_1^d and A_1^p in order to infer information on neutron as the only polarized nucleons in butanol are protons and deutrons that make up 12% and 19%, respectively. Extracted first moment of the polarized neutron structure function and the proton structure function both were inconsistent with the Ellis-Jaffee expectation of -0.002±0.005 and 0.18±0.01 at the measured Q^2:

$\Gamma_1^n(Q^2 \approx 5\ \text{GeV}^2) = 0.08 \pm 0.04 \pm 0.04$

$\Gamma_1^p(Q^2 \approx 10\ \text{GeV}^2) = 0.136 \pm 0.013 \pm 0.011.$

Combining all data from SMC, EMC and SLAC still returns us a measured Γ_1^p significantly below the parton model expectation. Later SLAC experiments such as E142 and E143 adopted high current polarized electron beam with energy 10∼30 GeV and polarized ^{3}He and ND_3 target in order to extend the Γ_1^n and Γ_1^p measurements to lower Q^2 region. Their results showed consistency with the original SMC results.

The interpretation of the disagreement described above led to a conclusion that constituent quarks' contribution to the proton spin accounts for much less than what the parton model prediction tells us. This interpretation naturally turned physicists' attention to other partons, gluons, as a candidate contributor to the proton spin.

In inclusive measurements of lepton-nucleon DIS processes, which were the main tools for the analysis at the first generation of polarized experiments, gluons enter the picture at next-to-leading order in strong coupling constant α_s while quarks enter at leading order[11]. The next generation of polarized experiments like HERMES and COMPASS[12] are therefore mainly dedicated to accessing $\Delta g(x, Q^2)$ at leading order by performing semi-inclusive DIS (SIDIS) measurements rather than inclusive measurements.

The HERMES experiment at HERA[13] had an advantage in that polarized electron beam of 30 GeV polarized H or ^{3}He gas target significantly reduced dilution factor coming from unpolarized material. The accessed x_{BJ} range was from 0.02 to 0.8 and Q^2 from 1 to 10 GeV^2. The COMPASS experiment at CERN, consisting partly of the former SMC, measured semi-inclusive deep inelastic $\mu p(d)$ (both beam and target polarized) scattering at the muon beam energy of 100∼200 GeV. At these experiments, the open heavy flavor production via the fusion process like $\gamma^* g \to c\bar{c}$ (for charm) allowed to directly probe gluons and thereby Δg at LO. Also, the thin target providing very good statistics enabled to even measure g_2 structure function that emerge only at

[10] Spin Muon Collaboration

[11] See Chapter 1.4.2 for more details.

[12] Common Muon and Proton Apparatus for Structure and Spectroscopy

[13] Hadron Elektron Ring Anlage (Hadron Electron Ring Facility)

next-to-leading twist[14]. Furthermore, SIDIS asymmetry measurements like $A^{\pi}_{p,n}$ from polarized $ep(n)$ scatterings allowed to extract separately the polarized valance quark distributions[15] Δu_v and Δd_v.

RHIC[16] is an unique, relatively new, experiment where both proton beams with energy of 100 or 250 GeV are polarized. The PHENIX[17] and STAR [18] experiment at RHIC were proposed to measure the double longitudinal asymmetry A_{LL} to decisively determine the polarized gluon distribution. PHENIX π^0 and STAR jet single inclusive measurements using data taken in 2005/6 at beam energy 100 GeV had already started to have statistically significant impact on constraining the distribution. Various measurements using other channels are expected to reveal different and complementary aspects of the gluon distribution. η, $\pi^{\pm}$, direct γ and open heavy quark measurements are among those channels. In addition, RHIC has measured the single longitudinal asymmetry A_L in parity violating W boson production to decompose the sea quark polarization contributions to the proton spin. With transversely polarized beam running, RHIC also measured the single transverse asymmetry A_N to study the transversity distribution and higher twist effects[19].

The outline of the rest of this chapter is as follows. In 1.2, the proton angular momentum sum rule is introduced with a focus on the role of the gluon polarization at the end. 1.3 will describe the theoretical foundation in which the observable is defined in terms of extractable distribution functions and how the desired information can be extracted. Then the scope will be narrowed down to the $\pi^{\pm}$ measurements, which is the subject of this dissertation, and their physical implications. The rest will be dedicated to a few key theoretical concepts. Definitions will be given in 1.4.1 and 1.4.2 of fragmentation functions and parton distribution functions, respectively. These functions come naturally in curing divergences of the theory and integrate into the center of the theoretical framework. Lastly in 1.4.3, the asymptotic freedom in QCD and running behavior of strong coupling constant α_s will be reviewed. It is crucial to understand these two tightly related phenomena for reasons that follow. The former not only reveals the compatibility of the parton model as a limiting case of QCD but also explains its limitations. Also, the latter is one of the main theoretical uncertainty sources in the analysis.

[14] power in Q^{-1}

[15] $\Delta q_v = \Delta q - \Delta \bar{q}$.

[16] Relativistic Heavy Ion Collider

[17] Pioneering High Energy Nuclear Interaction eXperiment

[18] Solenoid Tracker At Rhic

[19] All nonvanishing asymmetries measured with longitudinally polarized beam discussed here can be explained at leading twist (twist 2) of perturbative Quantum Chromo Dynamics.

1.2 The proton angular momentum sum rule

Quantum Chromo Dynamics (QCD) is a theory of strong force that governs interactions between (anti-)quarks and gluons (gauge bosons that mediate the force). It is formally defined as a field theory by its Lagrangian density. General properties that can be deduced from the form of QCD Lagrangian density are summarized in Appendix A. Here we only concentrate on the symmetry properties which are relevant to the proton angular momentum sum rule.

Spacetime symmetries in QCD form a symmetry group called the Poincare group. The Lorentz (rotation+boost) symmetry and translation symmetry are generators of the Poincare symmetry. Also, the generators of each symmetry form its own Poincare subgroup. According to the Nother's theorem, any differentiable symmetry of the action of a physical system has a corresponding conservation law. The energy-stress tensor $T_{\mu\nu}$ is the conserved current associated the translation invariance. Integrating $T^{0\mu}$ over 3-space, one can obtain the conserved charges $P^\mu \equiv \int d^3x T^{0\mu}$ which are also the generators of translation. They are symmetric and gauge invariant. The current associated with the Lorentz transformation is constructed from $T_{\mu\nu}$:

$$M^{\mu\nu\lambda} \equiv x^\nu T^{\mu\lambda} - x^\lambda T^{\mu\nu} \tag{1.1}$$

This rank-3 tensor is gauge invariant and has no totally antisymmetric part. The conserved charges (or generators) for the Lorentz transformation are obtained in a similar way:

$$J^{\nu\lambda} \equiv \int d^3 M^{0\nu\lambda} \tag{1.2}$$

Based on this result, there are two widely accepted approaches to constructing the angular momentum sum rule for nucleons. The main difference between Ji's and Jaffe's approaches is in the decomposition of spin and orbital angular momentum contribution from gluons. Ji's sum rule divides the nucleon intrinsic angular momentum into three gauge invariant parts without breaking the gluon component, whereas Jaffi's sum rule decompose the gluon contribution into two gauge noninvariant components. See Eq. 1.3.

$$
\begin{aligned}
J_{Ji} &= \frac{1}{2} = \sum_q \frac{1}{2}(\Delta q + \Delta\bar{q}) + \mathrm{L}_q + \mathrm{J}_g \\
J_{Jaffe} &= \frac{1}{2} = \sum_q \frac{1}{2}(\Delta q + \Delta\bar{q}) + L_q + \Delta G + L_g
\end{aligned} \tag{1.3}
$$

The quark spin term is straightforward and gauge invariant in both approaches, so it has been indeed measured at experiments with good precision [4] and the result that (anti-)quarks account for only $\sim 25\%$ of the total proton intrinsic angular momentum came as a surprise as the understanding at the time was based on simple parton model that did not take gluon's role into consideration.

We will follow the derivation by Jaffe since the role of gluon spin becomes more explicit in the gauge chosen in his approach. In the process, we will also learn that the quark angular orbital term in Jaffe's approach is defined in a non-gauge-invariant way in contrast to Ji's approach. In Ref. [8], the authors lay the groundwork by deriving a general expression for constructing the angular momentum sum rule independent of the frame and the contents of the tensor $M^{\mu\nu\lambda}$ in a model field theory. They consider a form factor, as shown in Eq. 1.4, for an insertion of $T^{\mu\nu}$ (and $M^{\mu\nu\lambda}$) with momentum k on a single nucleon line in which initial and final spin states are equal ($s' = s$).

$$
\begin{aligned}
\mathfrak{T}^{\mu\nu}(p,k,s) &\equiv \int d^4x < p',s|T^{\mu\nu}(x)|p,s > e^{ik\cdot x} \\
\mathfrak{M}^{\mu\nu\lambda}(p,k,s) &\equiv \int d^4x < p',s|M^{\mu\nu\lambda}(x)|p,s > e^{ik\cdot x}
\end{aligned} \tag{1.4}
$$

$|p,s>$ represents the plane wave nucleon state with momentum p^μ and spin s^μ, and the states are normalized to $< p,s|p',s' >= 2E(2\pi)^3\delta^3(\mathbf{p} - \mathbf{p'})$. Comparing the two expressions for $\mathfrak{T}^{00}$ in the limit $k^{\mu\nu} \to 0$, the one obtained by translating $T^{\mu\nu}(x)$ to $x = 0$ and integrating over x and the one resulted from directly substituting the relation $H \equiv \int d^3x T^{00}(x)$, one can find $< p,s|T^{\mu\nu}(0)|p,s >= 2p_\mu p_\nu$. To get to the angular momentum sum rule, we go through similar steps. Translate $M^{\mu\nu\lambda}$ to $x = 0$, integrate it over x and insert the expression for $< p,s|T^{\mu\nu}(0)|p,s >$. Using the relation $J^k \equiv \frac{1}{2}\epsilon^{kij}\int d^3x M^{0ij}$ together with the spin $\frac{1}{2}$ properties, one obtains the wanted expression for the angular momentum sum rule.

$$\frac{\mathfrak{M}^{012}(p_0,0,s_0)}{(2\pi)^4\delta^4(0)2E}=\frac{1}{2} \tag{1.5}$$

The arbitrariness of $\mathfrak{M}^{\mu\nu\lambda}$ is what results in differences in sum rules. By arbitrariness, it means that in the newly defined tensor in Eq. 1.6 the second term on the right hand side does not contribute to the Lorentz generators: $J'^{\mu\nu}=J^{\mu\nu}$. That is, the super-potential $B^{[\mu\beta][\nu\lambda]}$ represents the arbitrariness of $M^{\mu\nu\lambda}$.

$$M'^{\mu\nu\lambda}=M^{\mu\nu\lambda}+\partial_\beta B^{[\mu\beta][\nu\lambda]} \tag{1.6}$$

While there is little ambiguity in the quark angular momentum when it comes to decomposing it into the spin and orbital angular momentum contribution, there is no proven way of decomposing the gluon angular momentum into gauge invariant counterparts.

To see this, first take the case of spin $\frac{1}{2}$ particles. From the energy-strength tensor for spin $\frac{1}{2}$ Dirac fields $T^{\mu\nu}_{\frac{1}{2}}=\frac{1}{4}i\bar{\psi}(\gamma^\mu\partial^\nu+\gamma^\nu\partial^\mu)\psi+h.c.$, we can determine $M'^{\mu\nu\lambda}_{\frac{1}{2}}$. This can be rewritten in terms of gauge invariant terms and a super-potential term as shown in Eq. 1.7.

$$\begin{aligned} M'^{\mu\nu\lambda}_{\frac{1}{2}} &= \frac{1}{2}i\bar{\psi}\gamma^\mu(x^\nu\partial^\lambda-x^\lambda\partial^\nu)\psi+h.c.+\frac{1}{2}\epsilon^{\mu\nu\lambda\sigma}\bar{\psi}\gamma_\sigma\gamma_5\psi \\ &\quad -\frac{1}{8}\partial_\beta[\bar{\psi}x^\nu\{\gamma^\lambda,\sigma^{\mu\beta}\}\psi-(\nu\leftrightarrow\lambda)] \end{aligned} \tag{1.7}$$

Dropping the super-potential term, we obtain an expression for $M^{\mu\nu\lambda}$ and the resulting angular momentum generators for the Dirac fermions as shown in Eq. 1.8. The first term is the orbital angular momentum and the second term is the spin. As mentioned before, the orbital angular momentum term is apparently not gauge invariant. The reason for this is because Jaffe chose to cancel out the fermion-gauge boson interaction term, leaving gluon and fermion terms completely separated. In Ji's approach, on the other hand, he keeps the quark-gluon interaction term and obtain a term for the quark orbital angular momentum, in which a covariant derivative replaces the spatial derivative. As a result, his sum rule does not allow further decomposition of the gluon angular momentum.

$$J^k_{\frac{1}{2}} = \int d^3x i\psi^\dagger(\mathbf{x}\times\bigtriangledown)^k\psi + \frac{1}{2}\int d^3x\psi^\dagger\sigma^k\psi \tag{1.8}$$

In the controversial case of spin 1 gauge field, the angular momentum is analogously obtained from the energy-strength tensor $T^{\mu\nu}_g = Tr\{F^{\mu\alpha}F^\nu_\alpha\} - \frac{1}{4}g^{\mu\nu}TrF^2$. After a bit of algebra one can then separate the tensor $M'^{\mu\nu\lambda}$ into three terms and a super-potential term. Dropping the super-potential term, the 3 remaining terms are shown in Eq. 1.9.

$$\begin{aligned} M^{\mu\nu\lambda}_g &= -2Tr\{F^{\mu\alpha}(x^\nu\partial^\lambda - x^\lambda\partial^\nu)A_\alpha\} + 2Tr\{F^{\mu\lambda}A^\nu + F^{\nu\mu}A^\lambda\} \\ &\quad -\frac{1}{2}Tr\{F^2(x^\nu g^{\mu\lambda} - x^\lambda g^{\mu\nu})\} \end{aligned} \tag{1.9}$$

The first term is the orbital angular momentum and the second term is the gluon spin and the third term contributes to boosts. Only the first two terms contribute to the angular momentum generators. Putting together the fermion and gluon contributions in the generic form Eq. 1.5, Jaffe's angular momentum sum rule becomes:

$$\begin{aligned} \frac{1}{2} &= <PS|\int d^3x[i\psi^\dagger(x\times\bigtriangledown)^3\psi + \frac{1}{2}\psi^\dagger\sigma^3\psi \\ &\quad +2TrE^k(x\times\bigtriangledown)^3A^k + (A\times E)^3]|PS> \frac{1}{2E(2\pi)^3\delta^3(0)} \end{aligned} \tag{1.10}$$

Except for the quark spin term, which is the second term, the rest terms are not measurable as they are not gauge invariant. Nonetheless, we can define a gauge invariant object which carries pure gluon's spin information under a certain condition: $\Delta G^{g.i.}$ in Eq. 1.11 is the newly defined gauge invariant observable. It indeed reduces to the gluon spin term in the "light cone" gauge as only good spin components in the Dirac field remain in this gauge and spurious terms drop out [7]. ΔG in this gauge then becomes the first moment of the polarized gluon distribution function. As can be seen in Eq. 1.11, the polarized gluon distribution is denoted as Δg and defined in terms of the distribution of gluons with helicity parallel and anti-parallel to the nucleon's.

$$\Delta G(\mu^2) = \frac{1}{4P^+}\int_{-\infty}^{+\infty} dy^- \epsilon(y^-) < PS|F_a^{+\mu}(0) e^{(-ig\int_{y^-}^{0} A^+(y')dy'^-)_{ab}} \epsilon^{+-}{}_{\mu\nu} F_b^{+\nu}(y^-)|PS >$$
$$= \int_0^1 dx\,(g_\uparrow(x,\mu^2) - g_\downarrow(x,\mu^2)) \equiv \int_0^1 dx\,\Delta g(x,\mu^2) \tag{1.11}$$

Similarly, the quark spin terms can be expressed as the first moment of polarized quark distribution functions independent of gauge choice. Defining the first term as L_q and the second term as L_g, we obtain the concise form that agrees with Jaffe's decomposition in Eq. 1.3.

The next section will present the theoretical framework in which the proton-proton collision processes are described. It will become clear how one can extract information on the polarized gluon distribution and thereby ΔG through measurements in proton-proton collisions.

1.3 Perturbative QCD framework for proton-proton collisions and Global Analysis

A major advantage of using proton-proton ($p+p$) collisions in studying gluon distributions is they allow to access gluon distributions at the same order in α_s as quark distributions. The two are treated on the equal footing in this collision system. This becomes clear when one considers partonic hard scattering processes of the $p+p$ collision. There are four different generic types of partonic reactions at leading order (LO) $O(\alpha_s^2)$ [21]. The generic types depend on the kinds of two incoming and outgoing partons: $qq' \to qq', qq \to qq, q\bar{q} \to gg$ and $gg \to gg$ (q: quark, g: gluon). A pair of incoming partons originate from the constituents of both the two incoming protons, and gluons can break from parent protons as quarks do. There is no discrimination between quarks and gluons.

The distribution of parton momentum fraction of an incoming proton reflects the structure of the proton. This distribution is called the parton distribution function (PDF) of protons if protons are unpolarized and the polarized PDF if protons are polarized. They are formally defined as a function of x_{BJ} and Q^2 and enter into the hadronic cross section in lepton-nucleon DIS processes where there is only one proton involved in the collision[20]. Although the situation is a bit more complicated in $p+p$ collisions where both sides of

[20] See Chapter **??**.

incoming particles are structured, the PDFs defined in DIS processes apply to the hadron-hadron collision as well. The structure of two incoming protons is reflected in the cross section as a sum of contributions from different types of constituent partons involved in the scattering process. Each contribution is expressed as a convolution of the two PDFs associated with the two partons.

The two (at leading order) outgoing partons go through hadronization in a manner similar to what we will see in the e^+e^- annihilation process. Their behavior is formally described by the fragmentation function (FF) which is a function of hadronic momentum fraction of outgoing parton z and Q^2 [21]. Up to three outgoing partons, all of which hadronize, are considered at next to leading order (NLO) [22]. The number of final state particles one observes determines the class of measurement and corresponding theoretical formalism. At PHENIX at RHIC, single inclusive production has been the main focus of "the spin program" rather than two particle correlation measurements due to unfavorable statistics caused by limited detector coverage and particle reconstruction efficiencies. Six additional partonic subprocesses are added at NLO to the 10 existing ones from LO. The description of single inclusive production requires a fragmentation associated with the final state particle hadronizing from a parton. In the case of unpolarized initial protons, factorization theorem allows us to write the differential cross section of single inclusive particle production in the following form.

$$d\sigma^h = \sum_{ab(=qg,gg,q\bar{q})\to cX} f_{p\to a}(x_a,\mu_F) * f_{p\to b}(x_b,\mu_F) \\ *d\hat{\sigma}^c_{ab}(\mu_R,\mu_F,\mu_F^{'},\cdots) * D^h_c(z_c,\mu_F^{'}) \tag{1.12}$$

In the equation above, $f_{p\to a}$ denotes the PDF for the type a parton inside the proton and D^h_c denotes the FF for the hadron created from the type c parton. $d\hat{\sigma}^c_{ab}$ is the partonic cross section for incoming partons a and b, and outgoing parton c. μ_R is the renormalization scale introduced to remedy the ultra-violet (UV) divergence[22]. The infra-red (IR) divergence in single inclusive partonic cross section shows up in the form of collinear singularity. As this is long distance sensitive, it can be absorbed into PDFs and FF in exchange of introducing a factorization scale. The resulting short distance hard scattering cross section shown above is therefore finite.

An expression for spin dependent differential cross section is obtained by replacing hard scattering processes and PDFs in Eq. 1.12 with polarized ones.

[21] See Chapter 1.4.1.
[22] See Chapter 1.4.3.

$$d\Delta\sigma^h = \sum_{ab(=qg,gg,q\bar{q})\to cX} \Delta f_{p\to a} * \Delta f_{p\to b} * d\hat{\sigma}^c_{ab} * D^h_c. \tag{1.13}$$

It is not straightforward how to deconvolute the experimental information of PDFs and FFs from the cross section measurements. Information is smeared over the light-cone momentum fraction x^+, mixed in the sum of many different partonic subprocesses. A global QCD analysis is an endeavor to effectively extract the set of universal PDFs that simultaneously and optimally describe the combined data taken through different scattering processes at different hard scale Q. It assumes a certain form of phenomenological distributions with unknown parameters, which parameterize the cross sections, and finds the best fit to data. There are a number of independent groups pursuing this analysis with available data sets, revealing different aspects of distribution functions.

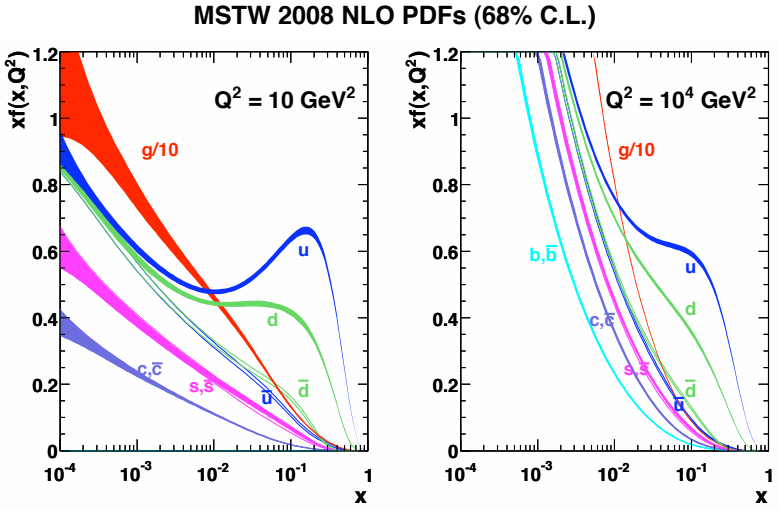

Figure 1.1: Unpolarized PDFs of the proton at $Q^2 = 10$ and 10^4 GeV^2 in the $\bar{M}S$ scheme. Taken from [23].

For unpolarized PDFs, MRST group has been providing continuous updates in theoretical technique as well as improvement of analysis at LO, NLO and NNLO using extensive data sets available since the very first global analysis at NLO by MRS. The most recent update was made by MSTW [23] and the analysis used data sets from fixed target experiments, HERA and Tevatron. CTEQ group also provides precise unpolarized PDFs from their independent

analysis.

For polarized PDFs, polarized DIS and semi-inclusive DIS (SIDIS) at HERMES and COMPASS were among the experiments providing essential data sets for the global analysis before $p+p$ data at RHIC were available. Each data set is suitable for extracting different information on polarized PDFs. Fully inclusive DIS data [24] allow us to determine the sum of quark and anti-quark distribution with an excellent precision. SIDIS data [25] help us tell different quark flavors as well as quark and anti-quark apart. Global analyses have been done by many groups such as GRSV, BB, and LSS using DIS [28] and DIS+SIDIS [29] to constrain these distributions. The observable for inclusive DIS data is the ratio of polarized (g_1) and unpolarized (F_1) structure function and analogous observable can be obtained for SIDIS data.

Determining FFs of the class described in the paragraph before Eq. 1.12 is pivotal for successfully extracting (not only unpolarized but also) polarized PDFs from polarized SIDIS and pp data where single identified hadron in the final states is observed. The reason for this is because present theoretical formalism adopts unpolarized fragmentation functions instead of differentiating the final spin state. The set of FFs for identified hadrons has been obtained by KKP [30] and DSS [31] group at NLO.

As was stressed at the beginning of this section, polarized $p+p$ data [27] are ideal for directly constraining polarized gluon distribution. A global analysis that includes all available polarized DIS and SIDIS data, and polarized $p+p$ data from RHIC for the first time, has been carried out at NLO by DSSV group [32]. This analysis adopted MSTW unpolarized PDFs (See Fig. 1.1) and DSS fragmentation functions. The PHENIX neutral pion measurements in $p+p$ data were also used for this analysis. The DSSV best fit results for polaized PDFs are shown in Fig. 1.2. This dissertation is dedicated to independent and complementary measurements of charged pions with high transverse momentum p_T. It is expected that high p_T $\pi^{\pm}$ channel is sensitive to the sign of polarized gluon distribution. In addition, the SU(2) quark flavor isospin symmetry provides a cross check with neutral pions. We will return to this point later.

The observable in this analysis is the double helicity asymmetry A_{LL} defined by Eq. 1.14.

$$A_{LL} = \frac{d\sigma^{\uparrow\uparrow} - d\sigma^{\uparrow\downarrow}}{d\sigma^{\uparrow\uparrow} + d\sigma^{\uparrow\downarrow}} = \frac{d\Delta\sigma}{2d\sigma}. \tag{1.14}$$

The two up arrows represent two up polarization or equivalently like sign

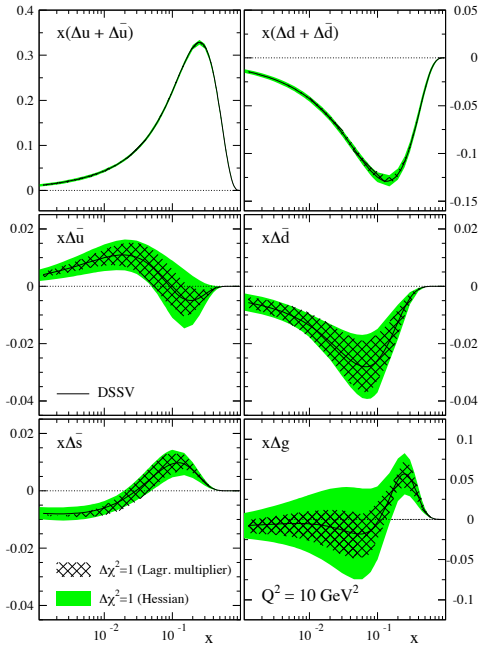

Figure 1.2: Polarized PDFs of the proton at $Q^2 = 10$ GeV^2 in the $\bar{M}S$ scheme. Taken from [32].

polarization as the pion production is parity conserving process. By measuring the ratio one can remove many sources of systematic uncertainty.

The perturbative QCD prediction of A_{LL} is made based on Eq. 1.12 and Eq. 1.13. The best fit is determined by χ^2 minimization, where χ^2 is defined in terms of both experimentally measured observable and theoretical estimation. The theoretical estimation is computed using the calculated hard scattering cross section and the nonperturbative distribution functions which are not to be fitted. FFs determined from other experiments are used as an input when fitting data to determine the gluon polarized PDF. Also, the universality of PDFs is assumed so that the particles of same species share common distribution functions regardless of scattering processes that they go through. Best fit PDFs determined at an initial scale μ_0 are evolved to a higher scale relevant in experiment through the evolution equations[23]. In the case of DIS and SIDIS, the DGLAP equations[24] that govern evolutions can be analytically solved by performing Mellin transform of PDFs and FFs and thereby decoupling them. Taking Mellin moments of the cross section,

[23] See Chapter **??** for details.

[24] DokshitzerGribovLipatovAltarelliParisi

however, does not result in a simple product of Mellin moments of PDFs and partonic cross sections in the hadron-hadron scattering case as multiple kinematic variables involved cause complications. For this reason, a method of storing a look-up table (or a grid) that contains numerically time consuming calculations was adopted.

Charged pions and ΔG

Simple considerations allow us to infer what aspects of distributions we will be able to learn from particular measurements before going through full global analysis. As we saw in Eq. 1.13, hadronic cross section can be broken into three parts. It is easy to see that the charge asymmetry of high p_T charged pion production is determined by three components, partonic double helicity asymmetries $\hat{a}_{LL}$, polarized PDFs and pion fragmentation functions. One should first note that high p_T pion production is dominated by $qg \to qg$ partonic process at LO, while $gg \to gg$ process crosses over at lower p_T. In other words, polarized quark PDFs relevant to pion production play an important role in this analysis. The sign of polarized u quark distribution Δu is measured to be positive whereas the one of Δd is negative. The partonic helicity asymmetry $\hat{a}_{LL}$ for all processes but $q\bar{q}$ annihilation, which does not have significant contribution, is positive. Lastly, u and d quark is favored for positive and negative pion production, respectively.

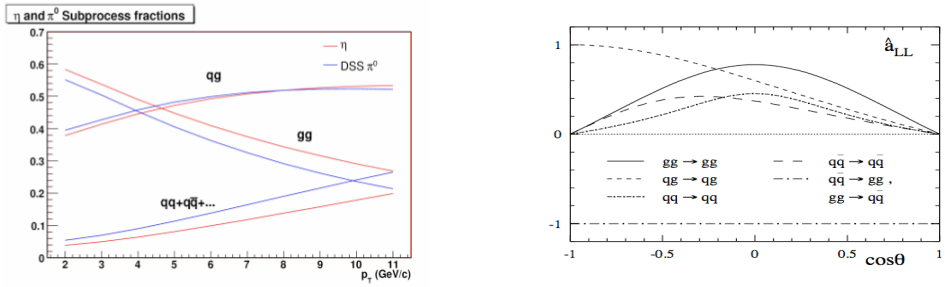

(a) Fractional partonic subprocesses for scalar meson production.

(b) Various partonic $\hat{a}_{LL}$ vs. $\cos\theta$ (θ: the scattering angle in center of mass frame)

Figure 1.3: Composition of partonic processes for scalar meson production and partonic double helicity asymmetries.

Consequently, one should expect $A_{LL}^{\pi^+} > A_{LL}^{\pi^0} > A_{LL}^{\pi^-}$ for positive polarized gluon PDF and vice versa. The inequality among charged and neutral pions is understood from the quark flavor isospin symmetry between the three pion species. This makes the charged pion production an indispensable channel that provides us with qualitative cross check and complementary information with neutral pions on the polarized gluon distribution. For these reasons, this dissertation will be dedicated to the measurement of differential cross section, to first validate the inputs used in the framework, and the double helicity asymmetries of high p_T charged pion production.

1.4 Parton Distribution Functions, Fragmentation Functions and running coupling constant α_s

Along with the physics behind the running coupling constant α_s, the concepts and behavior of parton distribution functions and fragmentation functions play the most essential roles in consistently describing the proton-proton collision system in the framework of QCD. The concepts of distribution functions are introduced in analyzing rather simple scattering processes : e^+e^- annihilation and lepton-proton deep inelastic scattering processes. They then can be applied to describe much more complex hadron-hadron collision processes. How to extract the desired information via global analysis was discussed in Section 1.3. In this section, we will review in moderate detail how these concepts come about in describing rather simple collision systems in QCD framework.

1.4.1 e^+e^- scattering and Fragmentation Functions (FFs)

e^+e^- annihilation is the most basic scattering process that is easy to analyze experimentally as well as theoretically. This is due to the structurelessness nature of its incoming particles in the process. Studying this process is crucial as it provides essential concepts and tools to analyze more complex cases. One can define an experimentally measurable "fragmentation function" in a rigorous manner through the analysis of singlely inclusive hadron production. The fragmentation functions for various charged hadrons have been indeed measured with good precision at BELLE in Japan [13].

Total inclusive e^+e^- annihilation cross section is known to be finite. First, note that there are two mechanisms of virtual photon (γ^*) decay at next-to-leading order $O(\alpha_{em}\alpha_s)$. We only consider the γ^* decay process diagrams at order α_s and leave purely electromagnetic subdiagram factored out. Real gluon emissions from outgoing (anti-)quarks and virtual gluon corrections to the interaction vertex are the two mechanisms for higher order contribution to the Born level $\gamma^* \to q\bar{q}$ decay process. Diagrams for the two mechanisms are summed and squared independently of each other and the result is separately divergent. More explicitly, the double differential cross section for gluon emission process $\frac{d\sigma}{dx_q dx_{\bar{q}}}$, which is inversely proportional to s ($=2\ p_{\bar{q}} \cdot p_g$) and t ($=2\ p_q \cdot p_g$), is divergent as s (or t) $\to 0$. The origin of the divergence is either when gluons are emitted with very small energy fraction with respect to the γ^* energy or when the momentum of radiated gluons is in parallel with the (anti-)quark from which they radiated. The former is referred to as the "soft or infrared (IR) divergence" and the latter the "collinear divergence". When the differential cross section is integrated over the entire phase space in order to get the inclusive cross section, or equivalently over x_q and $x_{\bar{q}}$, the divergence from the virtual gluon correction has an opposite sign with respect to one from the real gluon emission. This leaves the total cross section finite: $\sigma^{e^+e^-}_{Born}(1+\frac{\alpha_s}{\pi})$.

Cancellation such as the one above does not happen when we consider less inclusive processes. From the relations $s = Q^2(1-x_q)$ and $t = Q^2(1-x_{\bar{q}})$ in the massless quark limit, we know that the divergence in the differential cross section $\frac{d\sigma}{dx_q dx_{\bar{q}}}$ occurs only when x_q or $x_{\bar{q}} \to 1$. One can exploit this fact and define an object called the "+ function" in order to include the virtual gluon correction into the differential cross section. The "+ function" is defined as

$$(F(x))_+ \equiv \lim_{\beta\to 0}\{F(x)\theta(1-x-\beta) - \delta(1-x-\beta)\int_0^{1-\beta} F(y)dy\}, \quad (1.15)$$

meaning $(F(x))_+ = F(x)$ for $x < 1-\beta$, but the integral over x of $(F(x))_+$ vanishes. The parton differential cross section then can be expressed as

$$\begin{aligned} \frac{d\sigma}{dx_q} &= (\frac{d\sigma}{dx_q})_+ + \frac{\alpha_s}{\pi}\sigma^{e^+e^-}_{Born}\delta(1-x_q) \qquad \text{,where} \\ \frac{1}{\sigma^{e^+e^-}_{Born}}(\frac{d\sigma}{dx_q})_+ &= \frac{\alpha_s}{2\pi}P_{q\to qg}(x_q)log(Q^2/m_g^2) + \alpha_s f^{e^+e^-}_{MG,q}(x_q) \qquad (1.16) \end{aligned}$$

for quarks and analogously for anti-quark, and

$$\begin{aligned} \frac{d\sigma}{dx_g} &= (\frac{d\sigma}{dx_g})_+ + \frac{\alpha_s}{\pi}\sigma^{e^+e^-}_{Born}\delta(x_g) \qquad \text{,where} \\ \frac{1}{\sigma^{e^+e^-}_{Born}}(\frac{d\sigma}{dx_g})_+ &= 2\frac{\alpha_s}{2\pi}P_{q\to gq}(x_g)log(Q^2/m_g^2) + 2\alpha_s f^{e^+e^-}_{MG,g}(x_g) \end{aligned} \tag{1.17}$$

for gluons. The + function of parton differential cross section is written in terms of new objects which are also + functions. These plus functions are called the splitting function $P_{q\to qg}(1-x_q)$ and $P_{q\to gq}(x_g)$ and they are regularization scheme independent. $P_{j\to j_1 j_2}(z)$ has a physical meaning of the probability of a parton j splitting into j_1 and j_2 with the momentum fraction of z and $1-z$, respectively. The subscript MG in little f function indicates the regularization is performed in the massive gluon scheme and m_g denotes the fictitious gluon mass. It is important to note that these differential cross sections are therefore regularization scheme dependent.

In order to get the single hadron cross section, these parton differential cross sections have to be embedded into the hadronic description of the process. Partonic variables also need to be replaced with observable hadronic variables. The basic structure for embedding partonic differential cross section is

$$d\sigma(z_h, Q^2) = \sum_{i=q,\bar{q},g} (\frac{d\sigma}{dy_i})dy_i D^h_{0,i}(x_i)dx_i, \tag{1.18}$$

where $z_h = \frac{2E_h}{Q}$ is an observable energy fraction, $\frac{d\sigma}{dy_i}dy_i$ is the probability of finding a parton i with energy $E_i = \frac{1}{2}y_i Q$, $D^h_{0,i}dx_i$ is the probability that a parton i of energy E_i fragments into a hadron carrying fractional energy $x_i = \frac{E_h}{E_i}$, and there exists a relation $x_i = \frac{z_h}{y_i}$ with $0 \le x_i \le 1$ and $z_h \le y_i \le 1$. We have now come to a point where the observable fragmentation functions (FFs) are defined in terms of bare FFs and nonobservable parameters. Comparing the full expression for the single hadron cross section, which is obtained by substituting the partonic differential cross sections into Eq. 1.18,

$$\frac{d\sigma}{dz_h}(Q^2) = 3\sigma(\gamma^* \to \mu^+\mu^-)\int_{z_h}^1 \frac{dy}{y}\{\sum_{i=1}^{n_f} e_{q_i}^2[D_{0,q_i}^h(\frac{z_h}{y}) + D_{0,\bar{q}_i}^h(\frac{z_h}{y})]$$
$$\cdot[(1+\frac{\alpha_s}{\pi})\delta(1-y) + \frac{\alpha_s}{2\pi}P_{q\to qg}(y)log(Q^2/m^2) + \alpha_s f_q^{e^+e^-}(y)]$$
$$+2\sum_{i=1}^{n_f} e_{q_i}^2 D_{0,g}^h(\frac{z_h}{y})[\frac{\alpha_s}{2\pi}P_{q\to gq}(y)log(Q^2/m^2) + \alpha_s f_g^{e^+e^-}(y)]\}(y_i = y) \quad (1.19)$$

with the simple parton model,

$$\frac{d\sigma}{dz_h}(e^+e^- \to h + X) = 3\sigma(\gamma^* \to \mu^+\mu^-)\sum_{i=1}^{n_f} e_{q_i}^2[D_{q_i}^h(z_h, Q^2) + D_{\bar{q}_i}^h(z_h, Q^2)] \quad (1.20)$$

one can "define" an experimentally observable FF for quarks as

$$D_q^h(z_h, Q^2) = D_{0,q}^h * (1 + \frac{\alpha_s}{2\pi}P_{q\to qg}log(Q^2/m_g^2) + \alpha_s f_{MG,q}^{e^+e^-})$$
$$+D_{0,g}^h * (\frac{\alpha_s}{2\pi}P_{q\to gq}log(Q^2/m_g^2) + \alpha_s f_{MG,g}^{e^+e^-}), \quad (1.21)$$

where we used the convolution notation: $C(z) = A * B = \int_z^1 \frac{y}{dy}A(z/y)B(y)$. The anti-quark fragmentation function is similarly defined with q replaced by $\bar{q}$. For computational convenience, a set of two new functions are introduced here. A nonsinglet function is defined as the difference of quark and anti-quark FFs and the singlet function is defined as the sum of the two. The nonsinglet function $D_{NS}^h(z_h, Q^2) \equiv D_q^h(z_h, Q^2) - D_{\bar{q}}^h(z_h, Q^2)$ has the gluon contribution eliminated so it is expressed in a very simple form: $D_{NS}^h(z_h, Q^2) = D_{0,NS}^h * (1 + \frac{\alpha_s}{2\pi}P_{q\to qg}log(Q^2/m_g^2))$.

At this point, it is important to realize that the bare FF is expressed as a product of a pertubative expansion and an unknown finite parameter. An explanation for this is that the experimentally observable FF cannot have any dependence on nonphysical parameters and so the m_g dependence in the logarithm and its divergence has to be absorbed into the bare FF and cancel the m_g dependence. This will leave a finite unknown parameter $\bar{D}_{0,NS}^h$ and a mass scale Λ_{FF}, which is related to the size of hadrons, in the expression for the observable FF. This mechanism resembles the one for effective strong coupling

constant $\alpha_s^{\rm eff}(Q^2)$ in that defining an effective finite quantity in order to regularize the divergence have us pay the price of introducing a new arbitrary mass scale[25].

$$\begin{aligned} D^h_{NS}(z_h,Q^2) &= D^h_{0,NS} * (1+\frac{\alpha_s}{2\pi}P_{q\to qg}(log(Q^2/\Lambda^2_{FF}) + log(\Lambda^2_{FF}/m_g^2) + \cdots) \\ &= D^h_{0,NS} * (1+\frac{\alpha_s}{2\pi}P_{q\to qg}log(\Lambda^2_{FF}/m_g^2)) * (1+\frac{\alpha_s}{2\pi}log(Q^2/\Lambda^2_{FF}) + \cdots) \\ &= \bar{D}^h_{0,NS} * (1+\frac{\alpha_s}{2\pi}P_{q\to qg}log(Q^2/\Lambda^2_{FF})) + O(\alpha_s^2) \end{aligned} \tag{1.22}$$

Similarly, the gluon fragmentation function can be consistently defined as

$$\begin{aligned} D^h_g(z_h,Q^2) = \bar{D}^h_{0,g} * (1+\frac{\alpha_s}{2\pi}P_{g\to gg}log(Q^2/\Lambda^2_{FF})) \\ + \sum_{j=1}^{2n_f} \bar{D}^h_{0,q_j} * (\frac{\alpha_s}{2\pi}P_{g\to q\bar{q}}log(Q^2/\Lambda^2_{FF})), \end{aligned} \tag{1.23}$$

where the singularity is also absorbed into a unknown function.

Getting an explicit Q dependence of the FFs can be accomplished by setting up a set of integro-differential equations (renormalization equations) making use of the scale invariance of the physical observables or summing up the parton shower process. The latter is referred to as the "resummation" and the result is essentially equivalent to the solution of the former.

The nonsinglet function can be easily resummed by hand as it does not involve the gluon FF that complicates the picture. Performing resummation for the nonsinglet function is equivalent to so-called the "leading pole approximation". What is meant by that is one assumes the quark radiates a gluon with a very small transverse momentum relative to the initial quark direction so the double differential cross section $\frac{1}{\sigma^{e^+e^-}_{Born}}\frac{d\sigma}{dx_q^+ d\hat{t}}$ is approximated to a simple form $\frac{\alpha_s(t)}{2\pi\hat{t}}P_{q\to qg}(x_q^+)$, which contains only leading pole contribution. In this approximation, the probability of emitting n gluons become a product of the contribution from each emission. If we set the minimum cutoff invariant mass t to t_c, the nonsinglet function $D^h_{NS}(z_h,Q^2)$ can be written as the sum of $D^h_{NS}(z_h,t_c)$ which corresponds to no gluon emission and all possible n-gluon emission terms. This pertubative expansion can be simplified into the

[25]See the next section. In fact, the arbitrary renormalization scale μ can be set equal to this mass scale Λ_{FF}, which then allow us to compute the Q^2 dependence via the renormalization equations.

exponential form with some change of variables:

$$D^h_{NS}(z_h, Q^2) = e^{(\kappa P_{q\to qg}*)}\, D^h_{NS}(z_h, t_c), \text{ where } \kappa = \frac{2}{\beta_0}\, log[\alpha_s(t_c)/\alpha_s(t)] \quad (1.24)$$

This is the partial solution of Altarelli-Parisi evolution equations [14], which can be obtained by differentiating Eq. 1.24 with respect to κ. The leading order change of singlet function and gluon FF with respect to κ can be deduced from Eq. 1.21 and Eq. 1.23. The quark and gluon FFs mix together, therefore the differential equations are written in a nondiagonal matrix form:

$$\frac{d\mathbf{D}^h(z_h, Q^2)}{d\kappa} = \mathbf{P} * \mathbf{D}^h(z_h, Q^2), \text{ where}$$
$$\mathbf{D}^h(z_h, Q^2) = \begin{pmatrix} D^h_s(z_h, Q^2) \\ D^h_g(z_h, Q^2) \end{pmatrix} \text{ and } \mathbf{P}(y) = \begin{pmatrix} P_{q\to qg}(y) & 2n_f\, P_{q\to gq}(y) \\ P_{q\to q\bar{q}}(y) & P_{g\to gg}(y) \end{pmatrix} \quad (1.25)$$

And the solution is again expressed in an exponential form:

$$\mathbf{D}^h(z_h, Q^2) = e^{\kappa \mathbf{P}*}\, \mathbf{D}^h(t_c) \quad (1.26)$$

Evolution of fragmentation functions is one of the most important physics phenomena. It is a result of broken scale invariance caused by mass singularities and their regularization. It can be experimentally measured [13] by repeating the fragmentation measurements at different Q^2 and thus an excellent test of QCD.

1.4.2 Deep Inelastic Scattering (DIS) and Parton Distribution Functions (PDFs)

Studies of deep inelastic $l^{\pm}$ (lepton)-N (nucleon) scattering provides us with various observables that give us much insights into the structure of nucleons. Above all, parton distribution functions and their evolution equations can be derived through the analysis of γ^* (virtual photon)/$W^{\pm}/Z$ - q (quark) scattering cross sections. In this section, we consider the case of virtuality $Q^2 < M_W, M_Z$, so only γ^*-q scattering cross sections will be dealt with. To see how parton distributions come about from this analysis, one can start with the cross section for inclusive process e^- (electron)-P (proton)$\to e^- + X$. See Fig. 1.4. The 4-momentum of an initial proton, a parton and a virtual photon will be denoted as P^μ, p_i^μ and q^μ, respectively. The cross section of this process

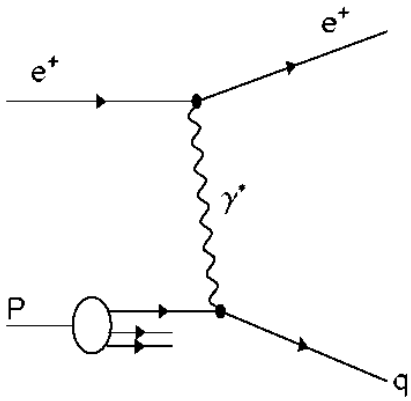

Figure 1.4: A schematic diagram of the γ^*-proton Deep Inelastic Scattering (DIS) process.

can be decomposed into a leptonic tensor and a hadronic tensor as given in Eq. B.1 in Appendix B.

In perturbative QCD, the γ^*-q cross section and initial asymptotic hadron states can be factorized as the former accounts for short distance interactions while the latter is a long distance phenomenon. Indeed, the γ^*-N cross section can be written as a convolution of the γ^*-q hard scattering cross section and the probability distribution of finding an incoming quark with 4-momentum $p = yP$ (Eq. 1.27). Similarly, the partonic structure functions $\hat{F}$ can be factored out of the nucleon structure functions (Eq. 1.28). They are then written as a function of a partonic variable $z \equiv \frac{Q^2}{2p\cdot q}$ instead of $x = x_{BJ} \equiv \frac{Q^2}{2P\cdot q}$. Virtual photon polarization dependent partonic structure functions are defined in the same way as the nucleon structure functions are, the only difference being the γ^*-N scattering cross sections replaced by the γ^*-q cross sections.

$$d\sigma = f^{(0)}_{p\to q}(y)dy\,(\frac{d\hat{\sigma}}{dz})dz. \tag{1.27}$$

$$F(x,Q^2)dx = f^{(0)}_{p\to q}(y)dy\,\hat{F}(z,Q^2)dz. \tag{1.28}$$

At Born level where only simple process $\gamma^* q \to q$ is considered, the structure function for unpolarized γ^* is obtained by plugging the partonic cross section $\hat{\sigma}_\Sigma = \frac{8\pi^2\alpha_{EM}e_q^2 z}{Q^2}\delta(1-z)$ into Eq. 1.28 and performing integration

over y: $F_\Sigma = \int_x^1 \frac{dy}{y} f^{(0)}_{p\to q}(y)(\frac{Q^2}{8\pi^2\alpha_{EM}z})\hat{\sigma}_\Sigma(\gamma^* q)$. The resulting structure function is simply written as $F_\Sigma = e_q^2 f^{(0)}_{p\to q}(x)$. Using the spin projection operator, the structure function for longitudinally polarized γ^* is proved to be zero. The physical picture of this result is in agreement with Feynman's parton model. For instance, the Collan-Gross relation [16] holds at this level: $2F_1 = \frac{F_2}{x} = e_q^2 f^{(0)}_{p\to q}(x)$. There is indeed experimental evidence [17] that this relation holds at x>0.2, supporting the spin $\frac{1}{2}$ nature of constituent quarks that was proposed in parton model.

At order α_s, richer information can be drawn about the parton distribution functions. The processes considered at this level include initial gluon-γ^* annihilation into $q\bar{q}$ pairs, gluon loop vertex interactions and real gluon emissions via Compton scattering. As it did in the e^+e^- case, divergence coming from the collinear (to incoming or outgoing quarks) and soft gluons are canceled against the vertex corrections in totally inclusive cross sections when properly regulated. The inclusive cross section at this order is computed to be $\sigma^{DIS}_{Born}(1 - \frac{\alpha_s}{\pi})$. In less inclusive cases, defining a + function for the partonic differential cross section in order to include the virtual gluon corrections is convenient. Introducing splitting functions relevant to the partonic processes then allows again for more explicit physical interpretation. Eq. 1.29 shows the differential cross section regulated by giving a gluon nonzero fictitious mass.

$$\begin{aligned}
\frac{1}{\sigma_0}\frac{d\sigma^{\text{Compton}}}{dx} &= \frac{\alpha_s}{2\pi}P_{g\to qg}(z)log(\frac{Q^2}{m_g^2}) + \alpha_s f(z) - \frac{\alpha_s}{\pi}\delta(1-z), \\
\frac{1}{\sigma_0}\frac{d\sigma^{\gamma^* g\to q\bar{q}}}{dx} &= 2\frac{\alpha_s}{2\pi}P_{g\to q\bar{q}}(z)log(\frac{Q^2}{m_g^2}) + 2\alpha_s f(z).
\end{aligned} \tag{1.29}$$

Now, the structure functions can be written in terms of the splitting functions as well because these differential cross sections are related to the total cross sections via Eq. 1.27 and Eq. 1.28.

(Born+Compton)

$$F_\Sigma^q = e_q^2 \int_x^1 \frac{dy}{y} f^{(0)}_{p\to q}(y)\{(1-\frac{\alpha_s}{\pi})\delta(1-z) + \frac{\alpha_s}{2\pi}P_{g\to qg}(z)\ \log(\frac{Q^2}{m_g^2}) + \alpha_s f(z)\},$$

$(\gamma^* g \to q\bar{q})$

$$F_\Sigma^g = 2\, e_q^2 \int_x^1 \frac{dy}{y} f^{(0)}_{p\to q}(y)\{\frac{\alpha_s}{2\pi}P_{g\to q\bar{q}}(z)\ \log(\frac{Q^2}{m_g^2}) + \alpha_s f(z)\}. \tag{1.30}$$

While the structure functions obtained above are for unpolarized γ^*, the parton distribution functions in the naive parton model is defined through F_2 structure function:

$$\frac{F_2}{x}(x,Q^2) = \sum_{i=1}^{n_f} e_{q_i}^2 (f_{p\to q_i}^{(2)} + f_{p\to \bar{q}_i}^{(2)}). \tag{1.31}$$

Therefore, one needs to get an expression for $\frac{F_2}{x}$ at order α_s in order to define the parton distribution functions in a way consistent with the parton model. One can readily get the desired expression using the relation $\frac{F_2}{x} = F_\Sigma + \frac{3}{2}F_L$. The results follow next:

$$\begin{aligned}\frac{F_2}{x}(x,Q^2) &= e_{q_i}^2 \int_x^1 \frac{dy}{y}(f_{p\to q}^{(0)} + f_{p\to\bar{q}}^{(0)})\{\delta(1-z) + \frac{\alpha_s}{2\pi}P_{q\to qg}(z)log(Q^2/m_g^2) + \alpha_s f_{MG,2}^{q,DIS}(z)\} \\ &\quad +2e_q^2 \int_0^1 \frac{dy}{y} f_{p\to g}^{(0)}(y)\{\frac{\alpha_s}{2\pi}P_{g\to q\bar{q}}(z)log(Q^2/m_g^2) + \alpha_s f_{MG,2}^{g,DIS}(z)\}. \end{aligned} \tag{1.32}$$

The subscript MG indicates the function f is regularization scheme dependent and the superscript (2) refers to the F_2 structure function. Comparing Eq. 1.31 and Eq. 1.32, we can define the parton distribution functions consistently at the next leading order:

$$\begin{aligned} f_{p\to q}^{(2)}(x,Q^2) &= f_{p\to q}^{(0)} * (1 + \frac{\alpha_s}{2\pi}P_{q\to qg}\, log(Q^2/m_g^2) + \alpha_s f_{MG,2}^{q,DIS}) \\ &\quad + f_{p\to g}^{(0)} * (\frac{\alpha_s}{2\pi}P_{q\to q\bar{q}}\, log(Q^2/m_g^2) + \alpha_s f_{MG,2}^{g,DIS}). \end{aligned} \tag{1.33}$$

Note that the convolution notation introduced in the previous section is used here. In much the same manner as in e^+e^- scattering process, the unphysical divergence in log $\frac{Q^2}{m_g^2}$ terms is absorbed into unknown distributions, paying the price of introducing an arbitrary scale Λ_{PDF}. We will again have the parton distribution function written in terms of a product of a finite unknown parameter $\bar{f}^{(0)}$ and a logarithmic term log $\frac{Q^2}{\Lambda_{PDF}^2}$ instead of $f^{(0)}$ and log $\frac{Q^2}{m_g^2}$. All leading log terms of the form $[\alpha_s(Q^2)log(Q^2)]^n$ are order α_s^0, and thus are to be summed up. Using the same trick as in e^+e^- scattering, a nonsinglet distribution is defined as $f_{NS}(x,Q^2) = f_{p\to q}^{(2)}(x,Q^2) - f_{p\to\bar{q}}^{(2)}(x,Q^2)$. One can easily recognize this distribution function is in exactly the same form as the nonsinglet parton distribution function. The solution is, therefore, straightforward:

$$f_{NS}(x,Q^2) = e^{(\kappa P_{q\to qg}*)} f_{NS}(t_c).$$

Taking derivative with respect to τ will give us the evolution equation for the nonsinglet parton distribution function, $\frac{df_{NS}(x,Q^2)}{d\kappa} = f_{NS}(Q^2) * P_{q\to qg}$. Furthermore, the evolution of the quark (similarly for the anti-quark) and the gluon distributions can be obtained separately from simple enumeration of partonic processes. The results are shown in Eq. 1.34.

$$\begin{aligned}
\frac{df_{p\to q}(x,Q^2)}{\kappa} &= f_{p\to q}(Q^2) * P_{q\to qg} + f_{p\to g}(Q^2) * P_{g\to q\bar{q}} \\
\frac{df_{p\to g}(x,Q^2)}{\kappa} &= \sum_{j=1}^{n_f} f_{p\to q_j}(Q^2) * P_{q\to gq} + f_{p\to g}(Q^2) * P_{g\to gg} \qquad (1.34)
\end{aligned}$$

Here, the superscript (2) is dropped as the reference function for PDFs becomes irrelevant in the evolution equations ; the dependence disappears. These coupled equations are solved in a manner similar to the fragmentation functions, i.e., by introducing a singlet distribution function and put it in a matrix along with the gluon distribution. The above equations are then written in a linear matrix form.

$$\begin{aligned}
\frac{d\mathbf{f}(x,Q^2)}{d\kappa} &= \mathbf{P} * \mathbf{f}(x,Q^2), \text{ where} \\
\mathbf{f}(x,Q^2) = \begin{pmatrix} f_s(x,Q^2) \\ f_{p\to g}(x,Q^2) \end{pmatrix} &\text{ and } \mathbf{P}(z) = \begin{pmatrix} P_{q\to qg}(z) & 2n_f\, P_{q\to q\bar{q}}(z) \\ P_{q\to gq}(z) & P_{g\to gg}(z) \end{pmatrix}. \qquad (1.35)
\end{aligned}$$

Since the contents of the $\mathbf{P}$ matrix is different from the one for fragmentation functions, the singlet and the gluon parton distribution functions evolve differently from the fragmentation functions. The Q^2 dependence of the structure functions F_1 and F_2 have been measured at various experiments [18].

Using the solutions of evolution equations and properties of splitting functions, one can easily see that the net number of quarks N_q does not depend on Q^2:

$$\frac{dN_q}{d(logQ^2)} = \frac{d}{d(logQ^2)}(\int_0^1 [f_{p\to q}(x,Q^2) - f_{p\to\bar{q}}(x,Q^2)]) = 0.$$

This feature is referred to as "the net quark number conservation". Furthermore, the second moment of the sum of the singlet and the gluon PDFs

also proves to be independent of Q^2. Since the second moment of a PDF is interpreted as the momentum fraction of a parton, the sum corresponds to the total momentum of all the partons. For this reason, we normalize the sum of second moment of all the partons to 1 and refer it to as "the momentum sum rule":

$$\frac{d}{d(logQ^2)}(\int_0^1 x[f_s(x,Q^2)+f_{p\to g}(x,Q^2)]dx)=0,\ Q+\bar{Q}+G=1.$$

The antisymmetric counterpart in Eq. B.1 carries additional independent information. In this case, the structure functions in the parton model can be written in terms of polarized (or longitudinal helicity) quark distributions as shown in Eq. 1.36.

$$g_1(x,Q^2)=\frac{1}{2}\sum_{i=1}^{n_f}e_{q_i}^2(\Delta f_{p\to q_i}+\Delta f_{p\to\bar{q}_i}), \tag{1.36}$$

where $\Delta f_{p\to q}=f_{p\to q^+}-f_{p\to q^-}$ and $+(-)$ is the helicity of a quark. This naive parton model proved to be incorrect when it comes to the measurement of the proton angular momentum. The failure is attributed to neglecting gluons' contribution. A full QCD calculation adds a gluon contribution into g_1 via the γ_5 triangle anomaly as first pointed out in Ref. [14]. g_1 function then becomes:

$$\begin{aligned} g_1(x,Q^2) &= \frac{1}{2}\sum_{i=1}^{n_f}e_{q_i}^2\int_x^1\frac{dy}{y}(\Delta f_{p\to q_i}+\Delta f_{p\to\bar{q}_i})\{\delta(1-z)+\frac{\alpha_s}{2\pi}\Delta P_{q\to qg}+f_q\} \\ &+\frac{1}{9}\int_x^1\frac{dy}{y}\Delta f_{p\to g}\{n_f\frac{\alpha_s}{2\pi}\Delta P_{g\to gg}+f_g\}, \end{aligned} \tag{1.37}$$

where $\Delta f_{p\to g}=\Delta g=f_{p\to g^+}-f_{p\to g^-}$ and $\Delta P_{AB}=P_{A^+B^+}-P_{A^-B^+}$. The solution to the evolution equation for the nonsinglet polarized distribution function is the same as the one for the nonsinglet FF and the unpolarized PDF. Solving the Q^2 evolution equations of the singlet (Δf_s) and the gluon (Δg) polarized PDFs returns the results given in Eq. 1.38.

$$\frac{d}{d(logQ^2)}\Delta f_s = 0 + O(\alpha_s^2)$$
$$\frac{d}{d(logQ^2)}\alpha_s\Delta g = 0 + O(\alpha_s^2) \tag{1.38}$$

The above equation emphasizes that inclusive g_1 function measurements do not allow for direct access to the polarized gluon distribution function Δg at the same order as the polarized quark PDFs. Less inclusive measurements such as semi-inclusive processes are needed in order to access Δg as mentioned at the end of Chapter 1.1. Open charm and high p_T di-hadron production via photon-gluon fusion (PGF), $\gamma^* \rightarrow q\bar{q}$, have been indeed measured at HERMES, COMPASS and SMC [19],[20].

In p+p collisions, on the other hand, the gluon distributions can be accessed at the same order as the quark distributions in single inclusive measurements already. Also, $p + p$ collisions are more sensitive to the gluons in a sense that partonic scattering processes include gluon-gluon interactions as well as quark-gluon interactions. These are the main reasons why the experiments at RHIC have been dedicated in ΔG program. Although the theoretical formalism of hadron-hadron collisions is more complex than the DIS case, underlying logic is quite similar and they share the common concepts of initial and final state distributions, i.e., PDFs and FFs, for long distance interactions. In particular, in both formalisms the polarization of initial beam particles are sensitive to the polarization of constituent partons in the proton and not to the polarization of final hadrons observed.

1.4.3 Asymtotic freedom and running coupling constant α_s

The behavior of asymptotic freedom in QCD states that the bonds between particles become asymptotically weaker as energy increases and distance decreases. The discovery of this phenomenon was made in analyzing ultraviolet (UV) divergence of the theory or properly renormalizing QCD theory. The UV divergence is one type of divergence that occurs in quantum field theory. This divergence comes from radiative corrections which appear as loops in Feynman diagrams where associated momentum integrals involve large values of momenta. Divergences in general can be regulated by introducing a cutoff momentum or by dimensional regularization. Renormalization procedure then has to follow in order to obtain a finite result for an amplitude involving diver-

gent diagrams. This procedure reveals one of the most crucial characteristics of the theory, the "asymptotic freedom". It was one of the greatest achievements in high energy physics in the sense that the theory agreed well at the "Born level" with the simple parton model that was conjectured without rigorous theoretical foundation but described prominent features such as scaling at high Q^2. The factorization between the short and long distance phenomenon [10] was based on the finding of this agreement. The former is described by partonic hard cross sections and the latter is described by the PDFs and FFs.

Renormalization procedures are described in Appendix C. Procedures are developed with an example case of Quantum Electro Dynamics (QED) and applied to the QCD case. The result of computing all relevant diagrams presented in Appendix C.2 is shown in Eq. 1.39. β_0 denotes the lowest order contribution and plugging in $C_2(G) = 3$ and $C(r) = \frac{1}{2}$ returns $\beta_0 = 11 - \frac{2}{3}n_f$, where n_f is the number of flavors. The solution of the β function equation can be written in terms of the effective coupling constant at an energy scale Q^2 and the experimental coupling constant "defined" at μ^2, i.e., $\alpha_s^{\text{eff}}(Q^2)$ and $\alpha_s \equiv \alpha_s(\mu^2)$, as shown in Eq. 1.40. The implication of this is significant. It led to an understanding of the behavior of the running strong coupling constant α_s [9]. It is also worth noting that the sign of β function determines the behavior of coupling constants. In QED, the β function is positive and the coupling constant becomes larger as the scale becomes larger. In contrast, the β function in QCD is negative and g_s decreases with increasing energy scale. This phenomenon is called the asymptotic freedom and is the fundamental underlying physics in the field of QCD.

$$\beta(g_s) = -\frac{g_s^3}{(4\pi)^2}[\frac{11}{3}C_2(G) - \frac{4}{3}n_f C(r)] = -\frac{g_s^3}{(4\pi)^2}\beta_0 \tag{1.39}$$

$$\alpha_s^{\text{eff}}(Q^2) = \alpha_s(Q^2) = \frac{\alpha_s(\mu^2)}{1 + \alpha_s(\mu^2)\frac{\beta_0}{4\pi}log(\frac{Q^2}{\mu^2})} \tag{1.40}$$

Another consequent feature of QCD is the "dimensional transmutation" which is attributed to the broken scale invariance caused by the renormalization process. Dimensional transmutation is a process that exploits the necessity of effective coupling constant, which is a result of renormalization, to introduce dimensionful parameters into the predictions of theory. More explicitly, the effective coupling constant $\alpha_s(Q^2)$ is not a function of two separate parameters $\alpha_s(\mu^2)$ and μ^2. Instead, it can be written as a function of single parameter Λ, where $log(\Lambda^2) = -\frac{4\pi}{\beta_0\alpha_s(\mu^2)} + log(\mu^2)$. And thus,

$$\alpha_s(Q^2) = \frac{4\pi}{\beta_0 log(\frac{Q^2}{\Lambda^2})}$$

When $\alpha_s(Q^2)$ equals one, we call this parameter Λ_{QCD} or the QCD scale. The QCD scale Λ_{QCD} has to be determined from experiments and through fitting procedure in the global analysis. And it is renormalization scheme dependent. Current experimental value has been determined to be 213^{+38}_{-35} in Minimum Subtraction (MS) scheme. The logarithmic decrease of coupling constant has been measured at SLAC, DESY, LEP and Tevatron [11]. Especially with LEP, the strong coupling constant has been measured rather precisely at the scale of Z boson mass [12].

The apparent Q^2 dependence of α_s is clearly a source of theoretical uncertainties in global analysis. The partonic hard scattering cross section will depend on the choice of scale as it is expressed as a power series expansion in α_s in perturbative QCD. A proper scale will be chosen in order to incorporate this measurement in the global analysis and the uncertainties stemming from the choice of this scale will be estimated by varying this scale.

In the following chapters, experimental methods and data analysis for single inclusive $\pi^{\pm}$ measurements in p-p will be discussed. The main observables are the differential cross sections and A_{LL} for different charge separately. Additional observables derived from the original ones such as the ratio of cross sections with different charge and A_{LL} of $\pi^+ + \pi^-$ will also be presented to conclude the dissertation.

Chapter 2

Experiment setup at PHENIX at RHIC

2.1 Polarized Protons at RHIC

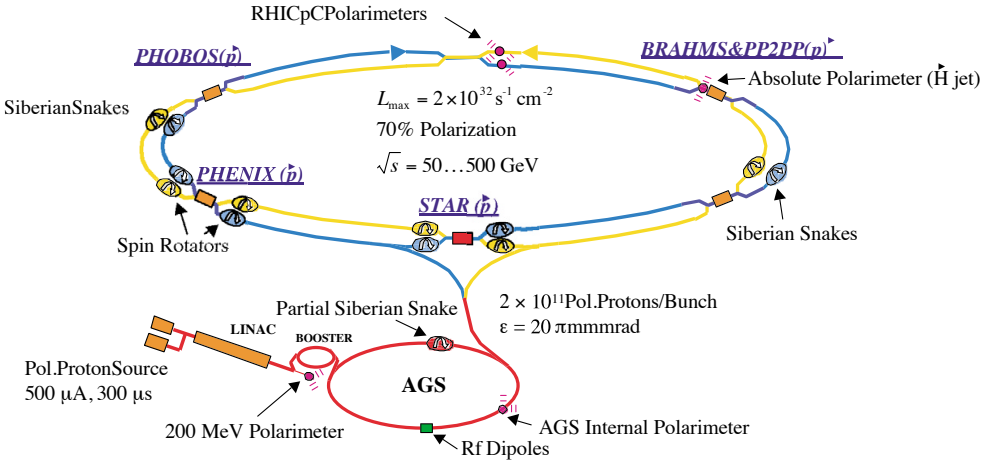

Figure 2.1: The Relativistic Heavy Ion Collider.

The Relativistic Heavy Ion Collider (RHIC) is an accelerator facility at Brookhaven National Laboratory (BNL) on Long Island, New York. Not only does it have capabilities of creating symmetric as well as asymmetric collisions with heavy ions such as deuteron, gold, copper and lead, it is the only facility colliding polarized protons. In the former case, the center of mass energy ranges from 7.7 to 200 GeV, whereas it ranges from 62.4 to 500 GeV in the latter case. At RHIC, polarized protons are produced, accelerated and

brought to collisions at interaction points (experiments) in multiple stages. The essential components pertinent to measurements involving polarized proton collisions at RHIC accelerator complex are drawn in Fig. 2.1. The acceleration chain begins at left bottom where polarized H^- proton source is generated.

Polarized proton source

The RHIC Optically Pumped Polarized Ion Source (OPPIS) produces reliably 0.5∼1.0 mA (maximum 1.6 mA) polarized H^- current with 85∼90% nuclear polarization during a single pulse of 400 μs. The Electron Cyclotron Resonance (ECR) method was adopted to produce an initial stage primary proton source (H^+) during construction at TRIUMF. High current production at RHIC was required in order to meet the beam intensity requirement and was made available after upgrade of primary ECR proton source [34]. 0.5 mA H^- ion current corresponds to a beam intensity of $12{\cdot}10^{11}$/pulse which is sufficient to allow for some losses during the transfer to RHIC for acceleration.

The ECR makes use of the electron cyclotron resonance to ionize a plasma. Microwaves are injected into a volume, at a frequency corresponding to the electron cyclotron resonance defined by a magnetic field applied to a region inside the volume. The volume contains a low pressure H_2 gas. The alternating electric field of the microwaves being synchronous with the gyration period of the free electron of the gas, it increases their perpendicular kinetic energy. When the kinetic energy of the energized free electrons becomes greater than the molecule or atom ionization energy, it causes ionization when electrons collide with the atoms or molecules of the gas in the volume. The ECR primary proton source realized at RHIC and its schematic view is shown as a first stage in the RHIC OPPIS system in Fig. 2.2. The OPPIS ECR at RHIC uses high frequency (29 kH) microwave generator in the magnetic field of 25 kG in order to extract protons (H^+) with 3 keV.

These protons pass through optically pumped Rb gas cell producing a beam of electron-spin polarized H^0. A pulsed laser with a wavelength of 795 nm is used to optically pump rubidium vapor and the laser beam is a primary source of polarization. That is, when rubidiums and protons collide with a cross section of 10^{-14} cm^{-2}, a charge-exchange occurs and the rubidium transfers its electron with spin polarization to the proton leaving electron-spin polarized H^0.

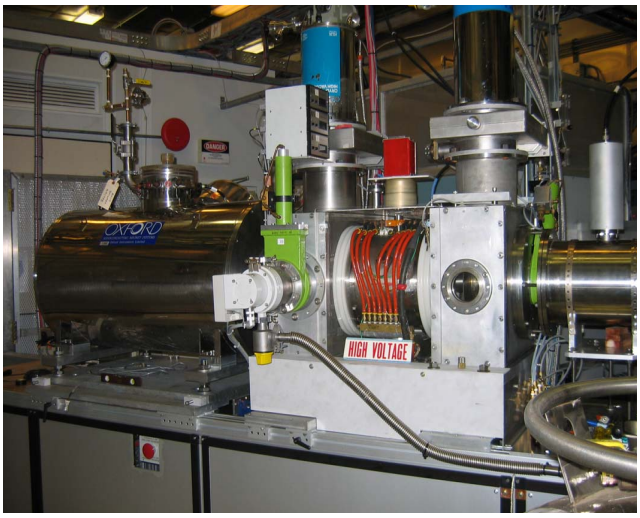

(a) OPPIS Experiment setup at RHIC

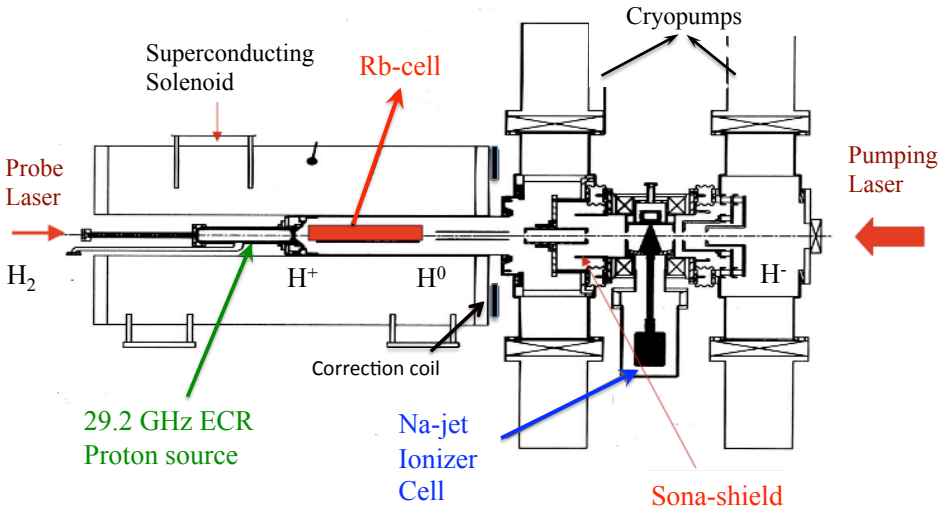

(b) Schemetic view

Figure 2.2: The RHIC OPPIS system.

The electron spin is transferred to the proton through a Sona transition. The Sona transition adiabatically brings the magnetic field from large positive to large negative values with a rapid jump between $\pm$ 1 gauss. During the adiabatic ramps, the atoms follow energy levels according to the usual Zeeman effect and hyperfine structure, but the rapid jump causes the atoms to jump from electron-spin polarized atoms to nuclearly polarized atoms. Nuclearly

polarized atoms are ionized when passing through an isolated Na-jet vapor cell with a bias voltage of -32 keV to facilitate acceleration. At the final state of OPPIS system H^- ions are accelerated in a two-stage acceleration system which consists of 2 extraction plates with applied voltages of -28 keV and -15 keV. This results in nuclearly polarized H^- ions with kinetic energy of 35 keV.

LINAC[1]

H^- ions are accelerated to 200 MeV in a spin transparent LINAC in 200 MHz with an efficiency of about 50%. At the end of LINAC the hydrogen ions are stripped of their electrons in the H^- injector line and a pulse of protons are captured into a single bunch in the Booster. A bunch contains about $5 \cdot 10^{11}$ at this stage.

Booster

The Booster is a fast cycling synchrotron and accelerates protons to 2.3 GeV kinetic energy. The bunch in the Booster will contain about $2 \cdot 10^{11}$. The potentially lost polarization caused by the coinciding spin precession frequency (ν_{sp}) with the depolarizing resonance can be easily corrected by a harmonic correction of closed orbit, at the Booster, since there are only 2 weak depolarzing resonances, $\nu_{sp} = 3$ and 4 (imperfection resonance resulting from vertical closed orbit errors) [33].

AGS[2]

Proton bunches injected from the Booster are accelerated upto 25GeV in AGS. A 5% (rotation of 9° around the beam direction) partial Siberian Snake was installed to one of straight sections in the upper circle of AGS. A full Snake could not be added due to spacial limit. Depolarizing effects caused by imperfection resonance ($\nu_{sp} = n$, where n is an integer) can be mostly avoided with the Snake as it is designed to overcome this particular type of depolarization by producing a full spin flip at every integer ν_{sp}. Intrinsic resonance resulting from vertical betatron motion ($\nu_{sp} = kP \pm \nu_y$, where k is an integer, P is the superperiodicity and ν_y is the vertical betatron tune) is among the remaining depolarizing effects. While weak intrinsic resonance can be additionally reduced with the use of a fast tune jump method, strong intrinsic resonance requires a different method be adopted.

[1] LINear ACcelerator

[2] Alternating Gradient Synchrotron

The RF dipoles located at the lower circle of the AGS shown in Fig. 2.1 was added to accomplish full spin flip to eliminate the depolarization effects caused by strong intrinsic resonance. The idea is to tune the modulation frequency ν_m near the intrinsic resonance and let the spin motion dominated by the RF frequency. By doing so, one can control the spin near the intrinsic resonance to adiabatically follow the closed orbit of the artificial RF spin resonance. Such a controlled coherent betatron oscillation can produce full spin flip and thus cancels depolarization effects.

RHIC

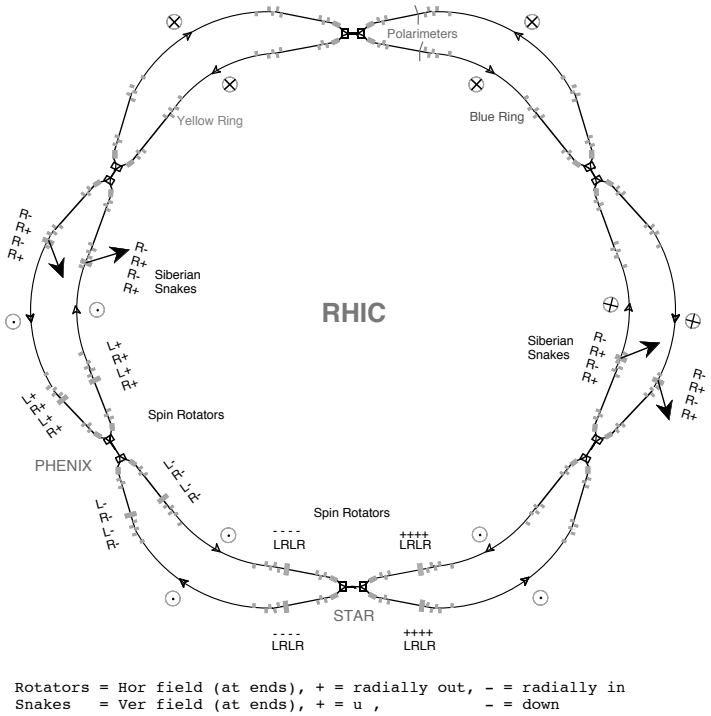

Figure 2.3: The configuration of Siberian Snakes and rotators. Arrows indicate axes of rotation for Snakes.

PHENIX and STAR are the only two experiments actively taking data at RHIC since decommission of the two other experiments, PHOBOS and BRAHMS. Accelerated proton beams are transported into the two RHIC rings (Yellow rotating counterclockwise and Blue rotating clockwise) through the AGS to RHIC transfer line (AtR) to allow collisions at experiments. At this stage, each injected bunch contains roughly $1.4{\cdot}10^{12}$ protons. There is a total

of 120 crossings of bunches as result of filling every third bucket out of 360 buckets available. These crossings are separated from one another by 106 ns. This separation can change depending on the number of filled bunches. There are also 10 empty crossings designed to study systematic effects of background, the bulk of which is called the "abort gap". Injected proton beams are set to be polarized in vertical direction for operational stability with Siberian Snakes.

Two full Siberian Snakes are located on opposite sides of RHIC at 3 and 9 o'clock for each of the counter-rotating rings. Each Siberian Snake consists of a set of four superconducting helical dipole magnets, powered in pairs. Each Snake rotates the spin by 180° around a horizontal axis and the two axes, say x-axis and z-axis, of the two Snakes for each ring are perpendicular to each other. The axis configuration is shown in Fig. 2.3. The two rotations through the two full Snakes effectively result in 180° spin precession around the stable vertical direction, y-axis. Consequently, the spin tune becomes $\frac{1}{2}$, independent of the beam energy and the depolarizing resonance conditions cannot be met anymore as long as the fractional betatron tune $\Delta\nu_y \neq \frac{1}{2}$.

Two pairs of spin rotators are added to each experiment for the purpose of preparing a longitudinal polarization direction at each interaction point. This is required for the measurements in this dissertation. On either side of an interaction region, there is a set of 4 helical dipole magnets, which composes a rotator, for each ring. These magnets are the same ones as used in Snakes, but the currents in each helical dipole are set differently. Each experiment has their own control over the spin polarization direction and in 2009, PHENIX was operated only in longitudinal polarization mode at $\sqrt{s}$ =200 and 500 GeV.

Polarimeters

Polarimeters are one of the most crucial instrumentation in RHIC for polarized proton collisions. There are three types of polarimeters at RHIC. Two of them are designed to measure the magnitude of the proton polarization and one is dedicated to monitor the direction of the polarization. The Hydrogen-Jet (H-Jet) polarimeter [36] and proton-Carbon (p-C) polarimeters [37] belong to the former and they are located at 12 o'clock region. On the other hand, local polarimeters are located at local experiments as the name indicates.

H-jet and p-C polarimeters are complementary to each other and both use elastic scattering events in the Coulomb Nuclear Interaction (CNI)

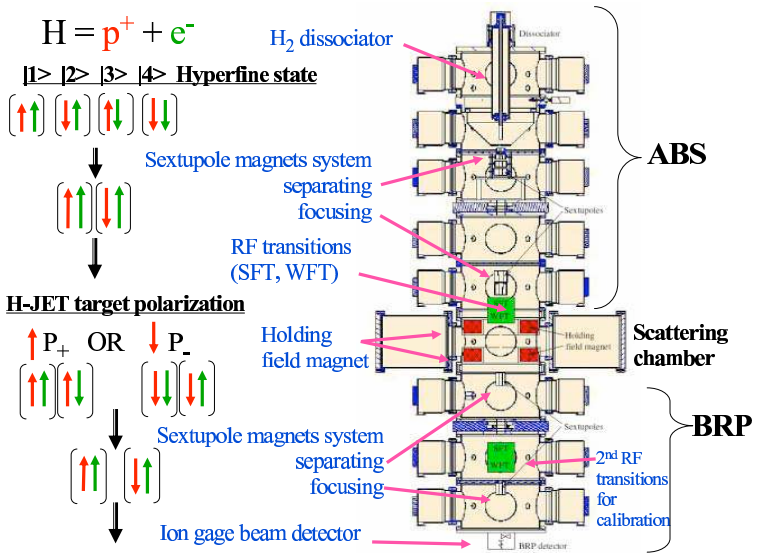

Figure 2.4: The schematic view of the RHIC H-Jet polarimeter at 12'oclock. The three main components Atomic Beam Source (ABS), scattering chamber and Breit-Rabi Polarimeter (BRP) are presented. Taken from Ref. [35].

region. The symmetry between the projectile beam and the target (both polarized protons) in H-jet measurements enables us to measure the absolute polarization of the beam by comparing the target analyzing power[3] and the beam single transverse spin asymmetries, but it does with much statistical significance. The p-C measurements that have as high an event rate as 2 million events per second allow us to keep track of variations of polarization over the course of each fill, which is on average 2∼3 hours, not to mention the fill by fill polarization. It is, however, not capable of directly measuring the analyzing power and it is only a relative measurement with a large uncertainty of 31%. In order to achieve a total of 5% polarization uncertainty, it is necessary to combine a few fills to determine the absolute polarization to within 1∼2% accuracy.

The schematic view of the RHIC H-Jet polarimeter is displayed in Fig. 2.4. Hydrogen gas is ionized, polarized and brought in to collisions with one of the RHIC beams. The polarized beam protons deflect from the original path by a very small angle, making it virtually impossible to place a detector to measure the angle. Polarized protons from H-jet, on the other hand, are

[3]analyzing power is defined as single transverse spin asymmetry scaled down by polarization. More details in Chapter 3.

scattered and fly out with nonrelativistic speed to the detectors in either left or right direction carrying the polarization information with them. Details of analysis for data taken in 2009 can be found in Chapter 3.

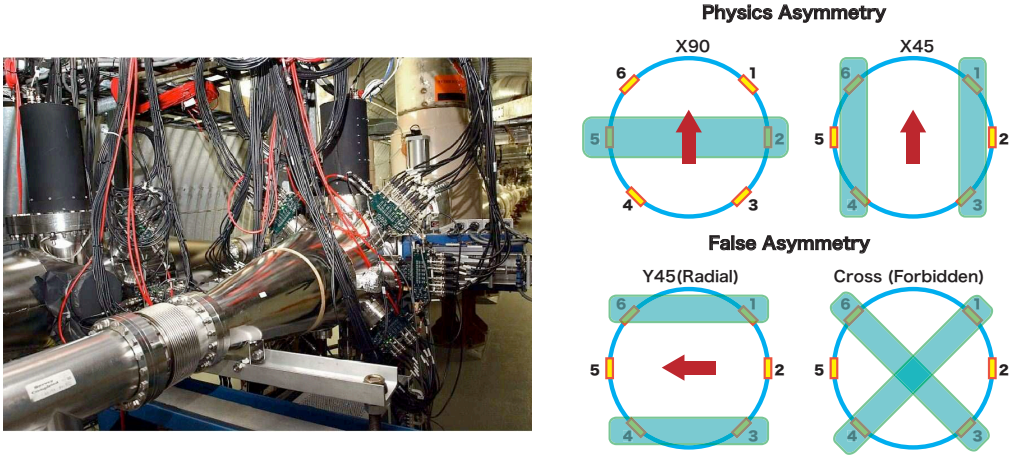

(a) p-C polarimeters at RHIC 12'clock interaction point

(b) Various asymmetries from different combination of detectors

Figure 2.5: The RHIC p-C polarimeters.

The p-C polarimeters consist of a carbon target and six silicon strip detectors. The scattering chambers of the blue and yellow polarimeters are mounted on the blue and yellow beam pipes separately which can be seen in Fig. 2.5(a). The six detectors are placed at 18.5 cm from the thin (a width of 4∼10 μm) carbon ribbon target and aligned 45, 90, 135 degrees azimuthally in both left and right sides with respect to the beam. Fig. 2.5(b) shows that certain combinations of detectors (X90 or X45) provide physics asymmetries coming from vertical spin state protons, while other combinations can reveal the existence of radial spin direction (Y45) or forbidden asymmetries, rendering them good means for a cross check.

The local polarimeters at PHENIX was devised to monitor the spin direction of polarized protons at the experiment as a cross check with the other two polarimeters. The PHENIX local polarimeter consists of the Shower Maximum Detector (SMD) and Zero Degree Calorimeter (ZDC) located at very forward region. See more details in Section 2.2.2. As will be described in that section, the magnets steer away the charged particles and only neutral particles hit the local polarimeter detectors. Neutrons produced from singly transversely

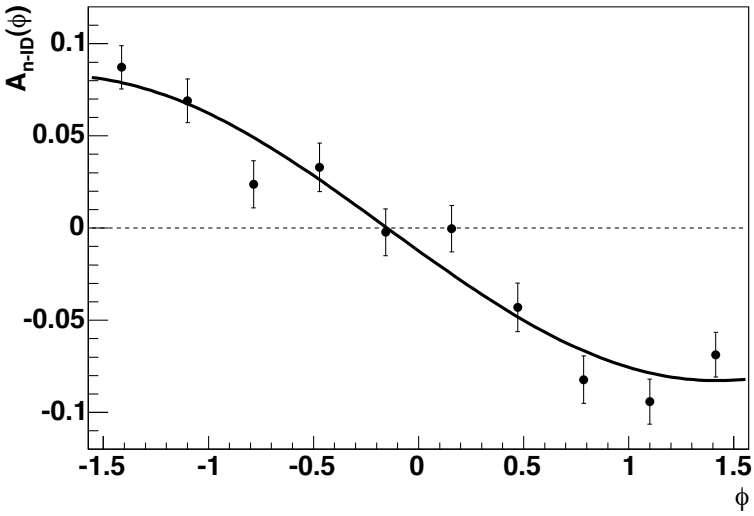

Figure 2.6: A typical measurement of neutron A_N. Taken from Ref. [38].

polarized proton-proton collisions were discovered to have an azimuthal dependence of the left-right asymmetry [38]. The segmentation of the hadronic calorimeter ZDC with independent readout gives discriminating power against photons. The position of neutrons is determined by SMD, a hodoscope array of scintillators, which is composed of 8 (7) scintillator strips of width 2 (1.5) cm in the vertical (horizontal) direction. The azimuthal modulation is parameterized as in Eq. 2.1.

$$A_N(\phi) = \mathrm{A_N} \sin(\phi - \phi_0) \tag{2.1}$$

, where ϕ is the defined counterclockwise from the vertical spin direction ϕ_0 and $\mathrm{A_N}$ is the amplitude. A typical result is shown in Fig. 2.6.

2.2 Global Detectors at PHENIX

Global detectors measure the global characteristics of collisions such as event vertex location, $\mathrm{t_0}$ for the Time of Flight (ToF), centrality and, most importantly, event recognition by issuing an on-line trigger decision to read out information (so-called "minimum bias triggering"). They are sometimes called the luminosity counters to emphasize their role as an event trigger. In PHENIX, there are two such detectors, the Beam Beam Counter (BBC) and

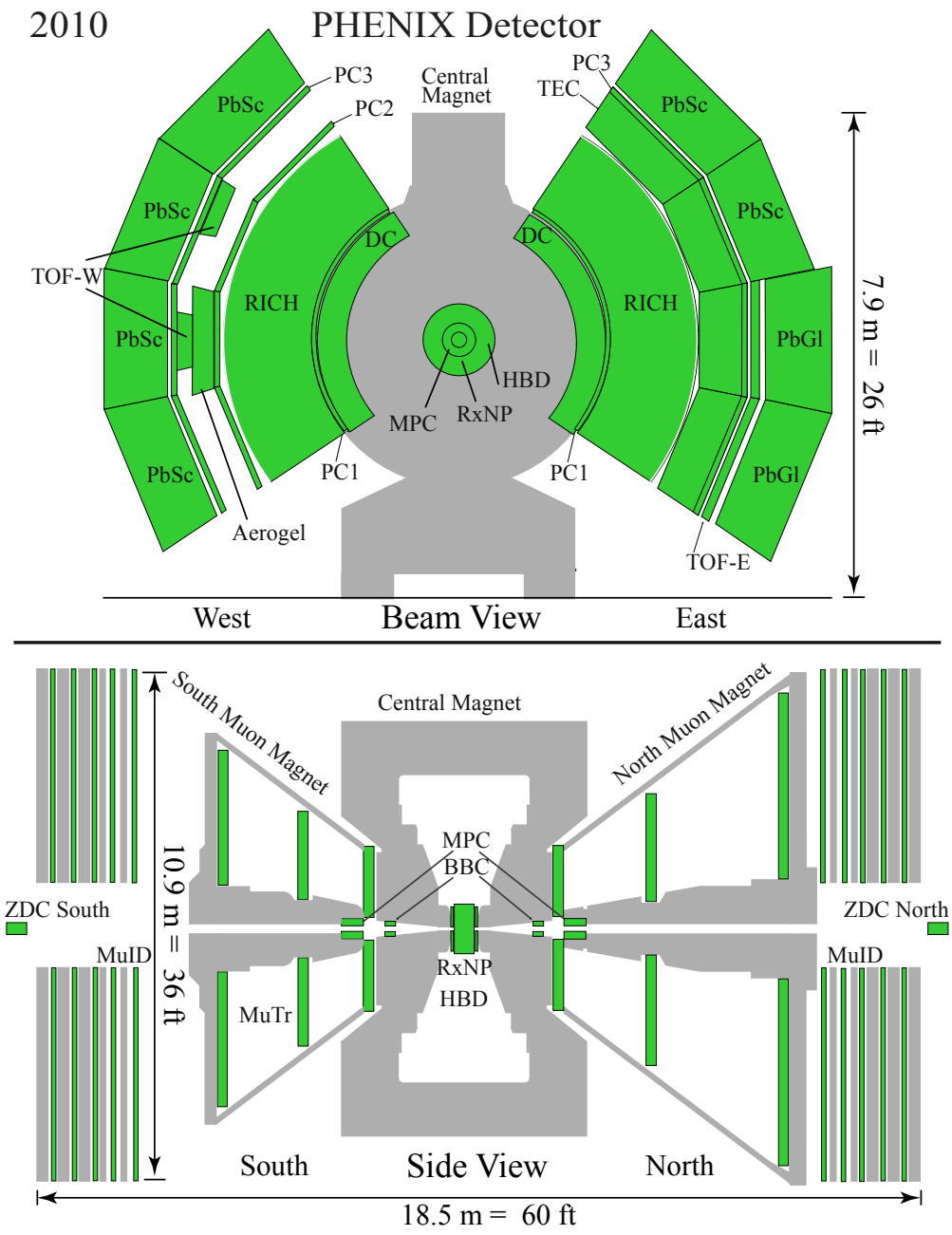

Figure 2.7: Configuration of PHENIX Detectors in 2009 (Same as in 2010).

the Zero Degree Calorimeter (ZDC). They both are located at very forward region in the north and south, covering full azimuth.

2.2.1 Beam-Beam Counter (BBC)

BBC consists of two sets of quartz tube Cerenkov arrays, which measure relativistic charged particles produced in a narrow cone defined by $3.0 \leq \eta \leq 3.9$ and full azimuth around each beam axis. They are positioned $\pm$ 1.4 m in the z-direction from the nominal PHENIX center point.

Each BBC consists of 64 photomultiplier tube (PMT) arrays which are arranged between the inner radius of 5 cm and the outer radius of 30 cm. The front of each PMT is equipped with a quartz Cerenkov radiator. The dynamic range of this radiator, which allows to register 1$\sim$30 minimum ionizing particles (See Sec. 2.3.4 for relevant discussions), makes it possible to take the role as a main Minimum Bias trigger detector in PHENIX for any collision species.

Each BBC PMT has an intrinsic timing resolution of $\sigma_t = 52 \pm 4$ ps and provides high precision measurements of collision time. For each collision, BBC measures the time of a collision with respect to the RHIC clock which is synchronized with the beam bunches. This time is usually referred to as $t_0^{\rm BBC}$ (calculated via Eq. 2.2) and is one critical information about a collision.

$$t_0^{\rm BBC} = \frac{1}{2}(t_{\rm N}^{\rm BBC} + t_{\rm S}^{\rm BBC}); \qquad z_{\rm vtx}^{\rm BBC} = \frac{c}{2} \cdot (t_{\rm N}^{\rm BBC} - t_{\rm S}^{\rm BBC}), \tag{2.2}$$

where c is the velocity of particles, and $t_{\rm N}^{\rm BBC}$ ($t_{\rm S}^{\rm BBC}$) is the average time-of-flight of prompt particles seen by BBC South (North).

On one hand, it sets the start time for all the subsystems performing timing measurements. For instance, determining the time-of-flight as accurately as possible is pivotal for particle identification for low p_T (<4) hadrons. It can also be useful for identifying π^0 particles. On the other hand, it allows to calculate the event vertex position $z_{\rm vtx}^{\rm BBC}$. The vertex resolution in $p+p$ collisions can be evaluated under an assumption that the multiplicity in BBC is small and we have one hit in each BBC. Using Eq. 2.2, we can estimate $\sigma_z = \frac{\sigma_t}{\sqrt{2}} c \approx 1.2$ cm.

The timing information combined with the event vertex information is used as an input for the minimum bias trigger. Level-1 trigger electronics generate a trigger-accept signal if a vertex lies within $\pm$50 cm from the PHENIX center point. It will reduce contributions from the beam gas interactions or any interactions inside the magnet poles. This enables the

experiment to obtain a clean sample of events for a variety of interesting physics processes, which is why this triggering scheme is referred to as the "minimum bias".

One has to keep in mind that locating an event vertex can fail when there are multiple collisions as they can mix the$t_{\mathrm{N}}^{\mathrm{BBC}}$ and $t_{\mathrm{S}}^{\mathrm{BBC}}$ pairs from different collisions, causing a falsely reconstructed vertex position. This is expected to be not an issue in data taken since 2011, the year in which the Silicon Vertex Detector (VTX) was installed and commissioned.

2.2.2 Zero Degree Counters (ZDC)

ZDCs are hadronic calorimeters, designed to measure the rate of very forward neutrons. Protons and other charged particles produced in collisions bend in the magnetic field of the RHIC D_x dipole magnets as shown in Fig. 2.8 and miss the ZDC acceptance. They are located ±18 m from the PHENIX center point and cover a cone of radius 2 mrad about the beam axis corresponding to $|\eta| > 6$.

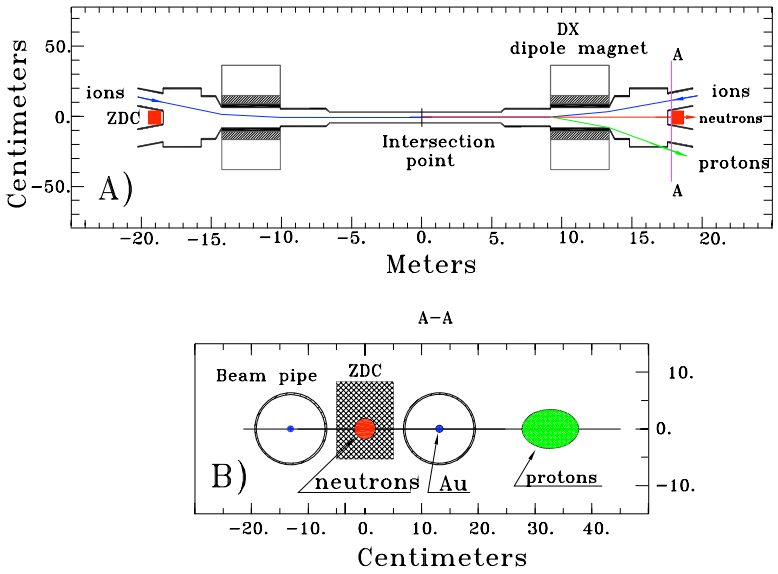

Figure 2.8: Schematic view of ZDC. Illustrates different particle species' A) path near the ZDC in side view and B) the projected proton and neutron deflection area at ZDC placement.

Each ZDC consists of 3 modules with optical fiber sandwiched between Tungsten layers, which correspond to 1.7 nuclear interaction length (λ_I) per module. A single ZDC is read out by a single PMT. A Shower Maximum Detector (SMD) sits between the first and the second module of each ZDC and is used to determine the position of a hadronic shower. Photon showers are primarily contained in the first module, and so showers detected in SMD are expected to be largely neutrons. The detector consists of 7 strips of vertical scintillator and 8 strips of horizontal scintillator, from which the x and y coordinates of the shower position can be determined.

ZDC provides timing and amplitude information similar to BBC, but with a decidedly lower resolution. The timing resolution of ZDC is $\sim$ 150 ps and the energy resolution at one neutron peak is 21%. Similarly to BBCs, the ZDC information is taken as an input to the minimum bias trigger. The Collider Accelerator Department (CAD) uses ZDC pairs installed at each experiment at RHIC for luminosity determination. For spin analyses at PHENIX, ZDCs are used in conjunction with BBCs for determination of systematic uncertainties on the spin dependent luminosity. For heavy ion collisions, by measuring the flux of neutrons in ZDC in correlation with the charged particles multiplicity in BBC one can determine the centrality[4] of a collision [39].

2.3 Central Arm Detectors at PHENIX

For the measurement of mid-rapidity charged π mesons, we used the Central Arm detectors at PHENIX which covers the pseudo-rapidity range of $|\eta| < 0.35$ (a bit wider for the Hadron Blind Detector). A beam view and a side view of the Central Arm Detectors are shown in Fig. 2.7.

2.3.1 Hadron Blind Detector (HBD)

The Hadron Blind Detector (HBD) is a Cherenkov detector operated with pure CF_4 gas. The detector is made of two identical arms, placed just outside the beam pipe with an entrance window starting at $\sim$5 cm in the radial direction and a radiator extending to $\sim$60 cm. The radiator in each arm is directly coupled without an window to a triple Gas Electron Multiplier (GEM) photon detector which is subdivided into 12 modules, 6 along the ϕ-axis $\times$ 2 along the z-axis. (See the schematics on the left in Fig. 2.9) In 2009, 10 modules were installed for each arm, resulting in the kinematic

[4]It hold the information on the impact parameter of a collision.

coverage of an azimuthal range of 112.5° for each arm and ±0.45 units in η [40]).

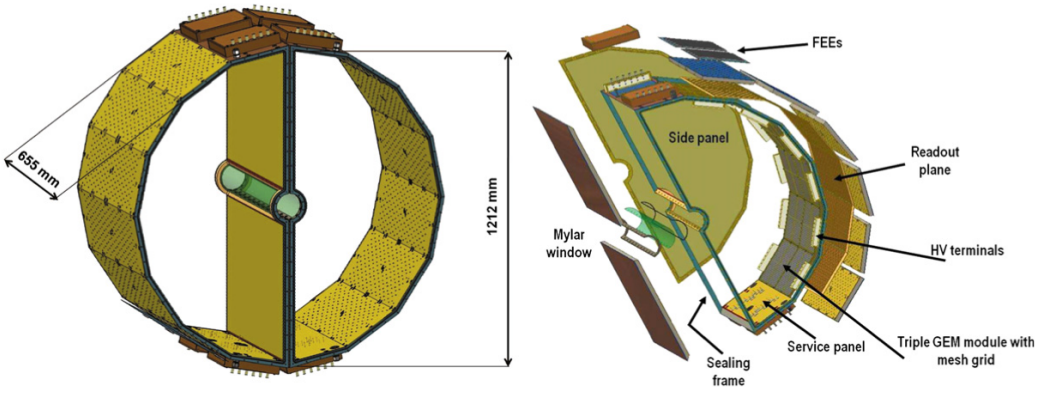

Figure 2.9: Left: 3D configuration of the Hadron Blind Detector. Right: exploded view of one HBD arm. Taken from [40].

Both the radiator and the GEM detectors are operated in a common windowless gas volume in order to have a signal strong enough to differentiate a single and merged photon(s). One HBD panel (two detector modules) consists of a core honeycomb sandwiched between two supporting FR4 sheets, readout boards on the bottom and finally a mesh and GEM stacks on the top. See Fig. 2.10. The three GEMs and the mesh are pinned down on a vessel to keep the tension on the GEM foils and the mesh and to minimize deformation of the frames. Each GEM is made of 50 μm thick kapton foil and is chemically etched in order to produce a highly dense pattern of 60∼80 μm holes with 140 μm pitch. A triple GEM detector is made photosensitive by evaporating a thin layer of CsI on the top surface of the first GEM foil. In this reflective photo-cathode scheme, photoelectrons are pulled into the holes in GEMs by strong electric field inside the holes and the photo-cathode is totally screened from the photons produced in the avalanche process. The 2-sided Printed Circuit Board (PCB) works as detector anode and has a hexagonal pad (with a side length of 15.5 mm) pattern on the inner side and short signal traces on the other side. A hexagonal pad plane is connected by wires to the readout board. The detector gain was set to give an output of ±100 mV to an input signal of 16 fC (100,000 e), which corresponds to an average primary charge of 20 photoelectrons at a gas gain of 5×10^3.

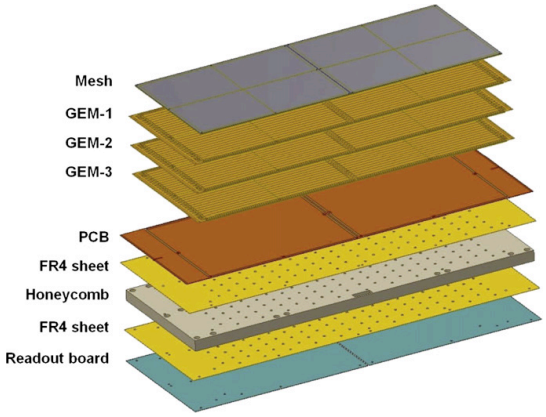

Figure 2.10: Exploded view of one pannel of the HBD vessel and readout board. Taken from [40].

The naming of the detector comes from the fact that the original motivation of developing this detector was to improve the signal to background ratio for di-electron pair measurements at low mass range of 0.3 GeV/c^2 $<$ 0.5 GeV/c^2. This is the region where precision spectroscopy measurements of the light vetor mesons ρ, ω and ϕ can be done with great electron identification capabilities at PHENIX. Due to detector configuration, however, di-electron measurements suffer from huge combinatorial background with a signal to background ratio of 1/200 without HBD. Main sources of combinatorial background are from π^0 Dalitz decays and γ conversions. With HBD, a strategy towards distinguishing the main background sources from the light vector meson decays is to exploit a feature that the opening angle of di-electron pairs from the background is very small. These pair electrons will consequently deposit double the photo-electron charge of a single electron on HBD pads as the angular resolution of the detector, which can be estimated by the size of a hexagon pad (hexagon side length a is 1.55 cm), does not permit separation of such an angle. Furthermore, the detector was built to be "blind" to all the other hadrons including the lightest ones, pions in the interested p_T range. For this reason, utilizing HBD for charged pion measurements in a systematic and an effective manner had not been considered as a viable approach initially. What is meant by blindness and how to overcome challenges will be discussed in detail in Chapter 4.

2.3.2 Drift Chamber (DC) and Pad Chamber (PC)

The Drift Chamber (DC) and the Pad chambers (PC1, PC2 and PC3) are the main PHENIX tracking detectors. They both have an azimuthal coverage of 90° in each arm and are located at 2.02∼2.46 m (DC), 2.50 m (PC1), 4 m (PC2) and 5 m (PC3) from the interaction point. Before the installation of HBD, DC and PC1 were the first detectors with which a charged track interacted after a collision. The central arm tracking system is based on the bending angle of a track, caused by magnetic field generated by the PHENIX central magnet. There are 2 magnetic field configurations (++) and (+−) due to the 2 (inner + outer) coil operation scheme. Each sign represents each coil's polarization. Magnetic field lines in each mode are shown in Fig. 2.11. The same polarization mode (++) provides the strongest magnetic fields in the central arm acceptance and thereby enhance the momentum resolution of high p_T charged tracks. The opposite polarization mode (+−) enables the creation of zero field at R≈0 region. This field configuration was chosen for the operation at $\sqrt{s} = 200$ GeV in 2009 in order to maximize the differentiability between "photonic" and "non-photonic" electrons by preserving the opening angle inside the HBD.

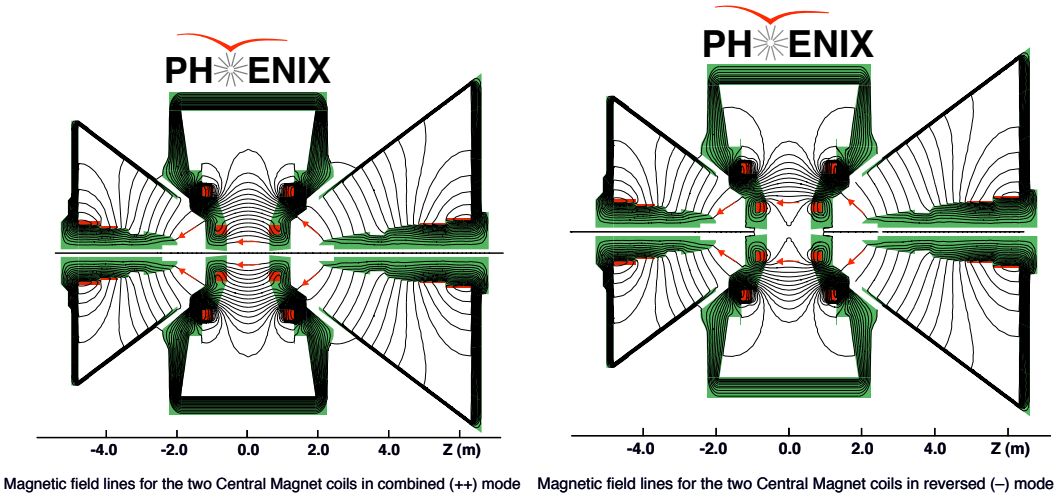

(a) In (++) mode (b) In (+−) mode

Figure 2.11: The central magnet magnetic field configurations in (++) and (+−) modes.

More specifically, DC can accurately measure charged particle tracks in the $r - \phi$ plane to determine their transverse momentum p_T. PC1 has high precision z measurement capabilities, and DC and PC1 together with BBC

can measure the θ of a charged particle track. DC can also provide input for correctly determining global coordinate system.

The Drift chamber is a multi-wire gas detector filled with Argon (50%) and Ethane (50%) gas mixture at STP. Charged particles ionize the gas particles in DC, creating charge clusters. The drift time ($t_{\rm dr}$) of these clusters to the nearest anode wire is used to measure the position of the track. The drift velocity ($v_{\rm dr}$) has a very weak dependence on the electric field in the drift region of a wire cell. The average drift velocity is on the order of $< v_{\rm dr} > \sim 50$ μm/ns. The position of a hit within the cell is then calculated by the $x - t$ relation shown in Eq. 2.3. t_0 is a reference constant corresponding to the creation of charge in the vicinity of anode wire.

$$x = v_{\rm dr} \cdot (t_{\rm dr} - t_0) \tag{2.3}$$

There is a total of 80 identical wire structure called nets around the azimuthal angle. Each net covers 1.125° and is subdivided into 6 separate sections along the radius. The sections are named X1, U1, V1, X2, U2 and V2, ordered from inside to outside radius. X wires measure the track trajectory in the $r - \phi$ plane, while U and V wires are used to reconstruct z information for a track. One cell consist of an anode wire net, surrounded by a pair of cathode wire nets. The wire and voltage configuration is designed so as to create a desired electric field in the drift region that is confined to a region of ∼2 cm between the cathode and the anode net. The configuration of X1 cell is displayed in Fig. 2.12(a). A group of four wire cells called a keystone shares common electronics set and high voltage supply. The wire configuration within a keystone is presented in Fig. 2.12(b).

Finding a track is an iterative procedure performed with hits on the wires. The algorithm involves several sophisticated steps: first find initial guess parameters utilizing the Combinatorial Hough Transformation algorithm [42] which defines a line by a pair of angles, next remove randomly associated tracks by iterative linear fitting, and finally associate a hit to a track with one-to-one correspondence. With this algorithm, the tracking efficiency achieved in low multiplicity environment, i.e., $p + p$ collisions, exceeds 98%.

PCs are multi-wire proportional chambers using a pixelation scheme. Each detector contains a single plane of wires inside a gas volume bounded by two cathode planes. One cathode is segmented into an array of interlaced pixel-pads and each track fires three pixel-pads. The coincidence reduces the false hit rate to be entirely negligible and localizes the track three times

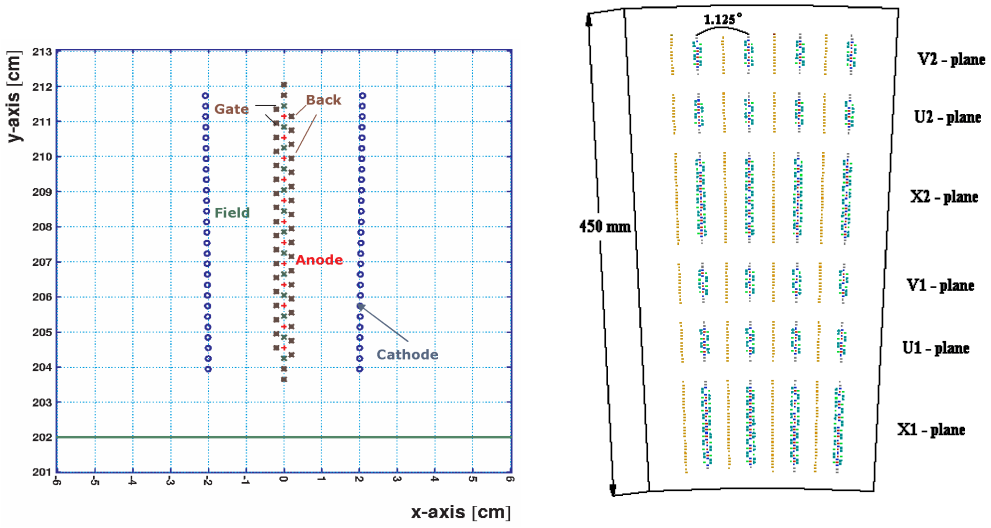

(a) X1 cell (b) A set of 6 Keystones

Figure 2.12: The wire structure of the Drift chamber.

better than a standard pixel chamber with the same number of channels. The position resolution of PC1 is 1.7 mm along z and 2.5 mm in $r - \phi$. The pad size for PC2 and PC3 are chosen such that they have comparable angular resolution with PC1. The efficiency for all three PCs is very high, $> 99\%$.

The quality of reconstructed tracks is determined based on the hit information on DC and PC1. Six binary bits are used to define a variable called 'track quality'. Each bit has the following information.

- 0 (1) X1 used
- 1 (2) X2 used
- 2 (4) UV found
- 2&3 (12) UV unique
- 4 (16) PC1 found
- 4&5 (48) PC1 unique

Valid 'track quality' values include:

49, 50, 51 1 1 0 0 x x PC1 found/unique, no UV
61, 62, 63 1 1 1 1 x x PC1 found/unique, UV found/unique

17, 18, 19	0 1 0 0 x x	PC1 found/ambiguous, no UV
21, 22, 23	0 1 0 1 x x	PC1 found/ambiguous, UV found but tied
29, 30, 31	0 1 1 1 x x	PC1 found/ambiguous, UV found/unique

A variable called $|zed|$ is the z coordinate at which the track projected track crosses PC1. Applying cuts on this variable effectively remove background tracks coming from magnetic pole tips.

Central arm tracking is also provides the projected z and ϕ coordinates of PC3. Requiring matching between the projected and real tracks coordinates enables us to eliminate tracks with falsely reconstructed momentum. The difference in the two independent coordinates are taken first and then normalized by the standard deviation of its distribution for convenience. These 'sigmalized variables are denoted as $pc3sdz$ and $pc3sd\phi$.

2.3.3 Ring Imaging Cerenkov detector (RICH)

The PHENIX Ring Imaging Cerenkov (RICH) detector is composed of two detectors, one in either arm, and is placed after the tracking detectors in each arm. Each detector has a volume of 40 cm^3 with an entrance and exit window of area 8.9 cm^2 and 21.6 cm^2, respectively, and thickness 125 μm. As shown in the schematic view in Fig. 2.13, composite mirror panels are installed near the exit window forming two intersecting spherical surfaces for the purpose of reflecting and focusing Cerenkov lights onto the 2 dimensional arrays of PMTs located on either side of the entrance window.

Cerenkov photons emitted at an angle of $\theta = \cos^{-1}\frac{1}{\beta n}$ are focused in the shape of a ring onto the PMT array. The total number of photo-electrons for a charged particle above the Cerenkov threshold is proportional to the length of the radiator and $\sin^2\theta$ as written in Eq. 2.4.

$$N_{npe} = L\frac{\alpha^2 z^2}{r_e m_e c^2}\int \epsilon_c\,\epsilon_d\,\sin^2\theta\,dE \tag{2.4}$$

where $\frac{\alpha^2 z^2}{r_e m_e c^2} = 370\ \mathrm{cm}^{-1}\mathrm{eV}^{-1}$, L is the path length of particles in the gas volume, ϵ_c is the PMT Cerenkov-light-collecting efficiency and ϵ_d is the quantum efficiency of PMT.

The detector was designed primarily for detecting electrons with a very high rejection power against hadrons. Reflecting this fact, the pion threshold

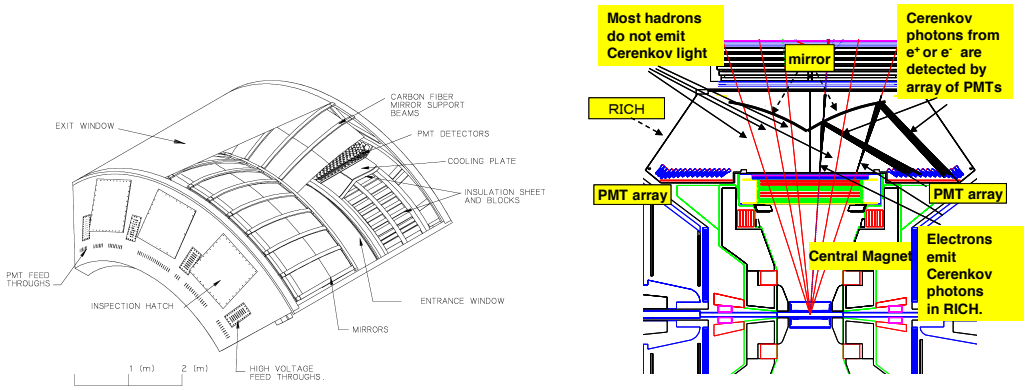

(a) A cutaway view of one arm

(b) A schemetic view and illustration of electron detection

Figure 2.13: The PHENIX RICH detector.

of Cerenkov radiation when using CO_2 is 4.65 GeV/c. The other concern was the background $e^{\pm}/\gamma$ coming from π^0 decay and photon conversion into di-electron pairs especially due to presence of detectors behind RICH. Minimizing the thickness of the detector was crucial for this reason. (See Eq. 2.4) The choice of radiator gas was made based on this line of considerations, although the total thickness of 2.14% is not the best that can be achieved. Opting for Ethane gas will provide the best total thickness of 2% of a radiation length. But the π threshold for Cerenkov radiation is lower at 3.71 GeV/c, limiting the p_T range for electron measurements. Another compromise was the photon yield which is important for $e^{\pm}/\pi^{\pm}$ separation. Ethane gas radiates more Cerenkov photons, 20 photons per ring, for a $\beta = 1$ particle, for a path length of 1.2 m. CO_2 produces, on the other hand, an average of 12 photons per ring.

The ring of photons reflected onto the PMT array has a radius of 11.8 cm, while the diameter of each PMT is 2.5 cm. For electron identification a variable called n_0 is used in PHENIX. It is defined as the number of PMTs fired in the region between the radii 3.4 cm and 12.8 cm from the track projection point. For hadrons this is inappropriate since the ring diameter can be smaller than the lower end when the momentum of tracks is only immediately above the threshold. For this reason, a slightly differently defined variable n_1 is used for hadrons. The searching window for this variable n_1 is a disk instead of a ring.

2.3.4 Electro Magnetic Calorimeter (EMCal)

The PHENIX Electro Magnetic Calorimeters (EMCal) are composed of 8 sectors (4 sectors in each arm) providing azimuthal coverage. Six of them are the Lead Scintillator (PbSc) calorimeter and the remaining two are the Lead Glass (PbGl) calorimeter. The primary role of EMCal in PHENIX is to provide a measurement of the energy and the spatial position of photons and electrons produced in collision: for hadrons, the measurement is rather ambiguous for reasons that will be explained later. In addition, the EMCal system can trigger on rare events with high transverse momentum photons, electrons and less efficiently hadrons. The two types of calorimeters employ very different method of extracting the energy released in the electromagnetic shower.

Electromagnetic showers are produced largely by the two fundamental processes, namely electromagnetic Bremsstrahlung radiation and e^+e^- pair production from photon-photon collisions. A highly energetic photon can emit a photon through Bremsstrahlung radiation and the created photon will decay into a electron-positron pair. Each charged particle generated can Bremsstrahlung immediately and this whole process can continue until the nth generation particles have an energy called the critical energy, E_C where the $\frac{dE}{dx}$ from Bremsstrahlung (described by Bethe-Heitler formula [44]) equals that of ionization. The EM showering refers to the exponential division of the initial particle's energy into more and more particles.

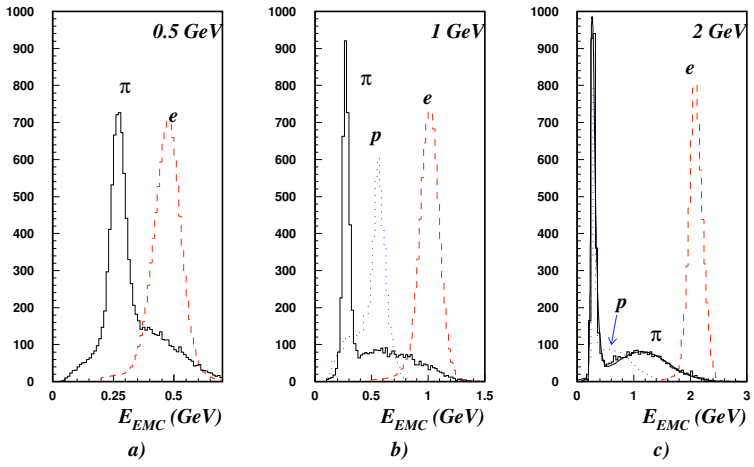

Figure 2.14: The energy spectra measured in the PHENIX EMCal.

In hadronic showering, on the other hand, high energy hadronic fragments are exponentially created from the initial hadron striking a nucleus. As these created hadrons are mostly pions and half of them are neutral ones which decay into a photon pair, EM showering occurs simultaneously. While nearly all of the released energy is in principle detectable for an original electron or photon, the total EM energy released is generally a small fraction of the energy of the original particle as a large portion of energy is lost in the undetectable hadronic processes in the collision. The long tail structure in the energy spectra of hadrons in Fig. 2.14, shown at 3 different p_T, is attributed to the hadronic interactions with materials in the detector.

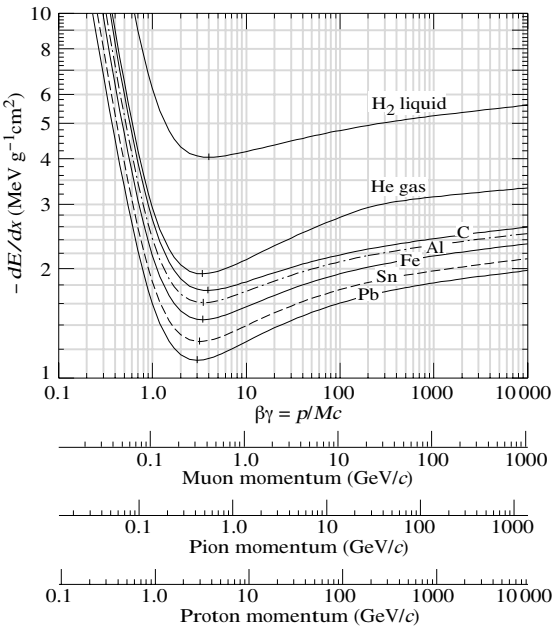

Figure 2.15: Mean energy loss rate in liquid hydrogen, gaseous helium, carbon, aluminum, iron, tin and lead. Radiative effects not included. Taken from Ref. [49].

Another primary mechanism for relativistic charged particles, other than electrons losing energy in matter, is by ionization and atomic excitation. The mean rate of energy loss is given by the Bethe-Bloch equation. Relativistic hadrons with the relativistic parameter $\beta\gamma$ greater than $\sim$3 have the mean energy loss rate close to the minimum and they are called minimum ionizing particles (MIPs). Fig. 2.15 shows the mean energy loss as a function of $\beta\gamma$ and its minimum for several particle species in different detector material. Pions

with energy greater than 200 MeV, and 2 GeV for protons, are expected to be mostly MIPs in EMCal. This is indeed seen in Fig. 2.14 where one can also see the actual measured energy for these MIPs to peak at ∼280 MeV. There is very weak p_T dependence in the position as anticipated. The energy spectra for photons and electrons shown for comparison confirms the explanation given for EM shower as well. It is noteworthy that the PHENIX EMCal was built for specifically achieving EM showering optimization. This is distinct from ZDC that was designed primarily for hadron detection which requires thicker calorimeter and compensation.

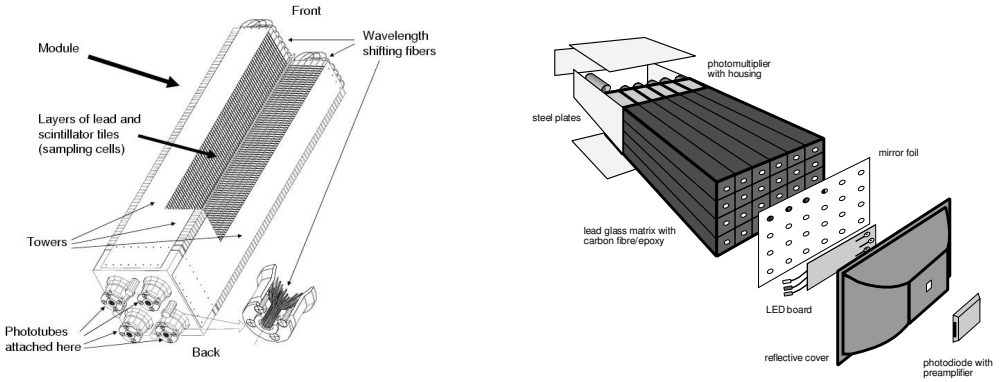

(a) Interior view of a PbSc module (b) Exploded view of a PbGl supermodule

Figure 2.16: Mechanical design of PbSc and PbGl calorimetor module.

The Lead Scintillator is called a sampling calorimeter because of its shower energy detecting scheme. The basic unit of PbSc is a stack of alternating Pb and plastic scintillator blocks. A block is called a "tower" and each PbSc tower is 5.25 cm × 5.25 cm × 37.5 cm deep. The 2×2 units of towers are grouped into a "module". 36 modules are constructed into a rigid structure to form a "super-module". And 18 super-modules make a "sector". The scintillator detects radiation by a photomultiplier tube (PMT). PMTs output a current (photo-electrons) that is proportional to the light detected under very high voltage. The light is guided with other translucent materials from the scintillators to the PMTs. As a result, a roughly constant fraction of total shower or scintillation energy is detected. For this reason, PbSc is called a sampling calorimeter.

The Lead Glass calorimeter is a Cerenkov calorimeter. The energy collection relies on solid blocks called towers of translucent mixture of Pb, glass and Pb Oxide. The PbGl towers are laterally smaller and slightly deeper than

PbSc towers: 2 cm $\times$ 2 cm $\times$ 40 cm. 6$\times$4 arrays of towers are glued together to form a super-module (SM), the self-supporting unit with shared calibration system. An exploded view of a SM is displayed in Fig. 2.16(b). 16$\times$12 units of SM make a sector. There is no need for light guiding as Cerenkov radiation caused by fast moving charged particles is confined in the light transmitting portion of the calorimeter. Visible light output is again collected by PMTs.

The variable called 'prob' is defined to help the electron or photon identification. It refers to the probability that the particle shower is electro-magnetic, which is quantified by fitting the shower shape of a cluster in EMCal to the known shape.

Matching variables are also available as in the case of PC3 and they are denoted as *emcdz* and *emcd*ϕ.

Chapter 3

Measurement of Polarization with Hydrogen-Jet Polarimeter

3.1 Hydrogen-Jet (H-Jet) target and Single transverse asymmetry (A_N)

H-jet target is a part of polarimetry in RHIC that provides absolute polarization measurements for transversely polarized proton beam. A stable polarization of 0.96 is maintained in the H-jet target throughout the data taking period.

The physical quantity we measure in order to extract beam polarization is the single transverse spin asymmetry of cross section. In this measurement, two incoming protons are transversely polarized and there can be two kinds of single spin asymmetries. Beam (target) asymmetry is defined in such a way that the opposite spin states of target (beam) particles are summed up or unpolarized.

In elastic $p + p$ collision, theory predicts the maximum single transverse asymmetry of 4∼5% at a small collision angle, in the so-called Eikonal limit. This is attributed to the increased magnetic effect at high energy. This effect results in large interference between the spin-flipping electromagnetic amplitude and the spin-nonflipping hadronic amplitude (Coulomb Nuclear Interaction) [47],[48].

The invariant cross section is written in Lorentz noninvariant form as in Eq. 3.1 when the polarization of beam and target protons ($|P_b|, |P_t| \neq 1$) are taken into account.

$$\frac{d^2\sigma^{bt}}{dtd\phi} = \frac{1}{2\pi}\frac{d\sigma}{dt}[1 + A_N \cos\phi(P_b + P_t) + A_{SS}\sin^2\phi P_b P_t + A_{NN}\cos^2\phi P_b P_t] \quad (3.1)$$

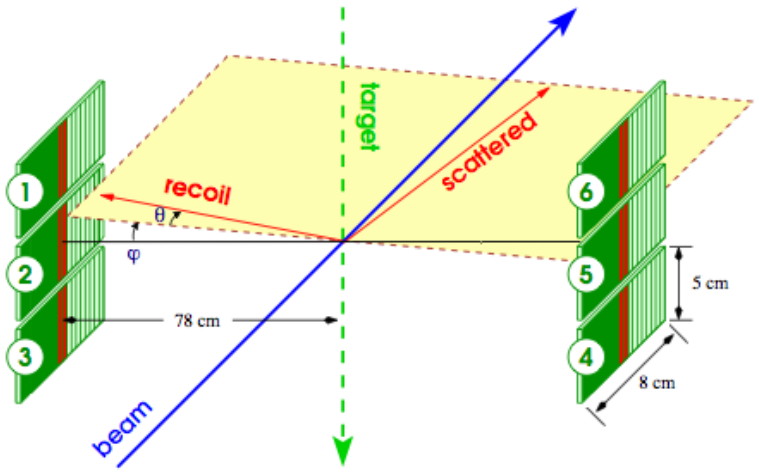

Figure 3.1: Experimental setup. ϕ and θ denotes the angle of collision plane rotated from the $x-z$ plane and the recoil angle of target particle from the $x-y$ plane along collision plane, respectively.

where A_N is the single transverse asymmetry and A_{SS} and A_{NN} are the double spin asymmetries with respect to the x and y axis, respectively, and $\frac{d\sigma^{bt}}{dt}$ is the total differential cross section with a beam (target) spin state b (t). See Fig. 3.1 for geometry. The "polarization" of a bunch with a spin state s is defined as

$$P^s = \frac{N^s - N^{-s}}{N^s + N^{-s}} = \frac{N^{\text{total}} - 2 \cdot N^{-s}}{N^{\text{total}}},$$

where N is the number of protons with the associated spin state. As an example, if 0.7×10^{11} protons are positively polarized and 0.3×10^{11} protons are negatively polarized, the polarization of this bunch is 0.4.

Substituting $P_b = 0$ into Eq. 3.1 and taking the equation with $\phi = 0$ (Left reaction) and π (Right reaction), we get the following relation for polarized target particles.

$$A_N = \frac{1}{|P_t|}\frac{d\sigma^{0+,L} - d\sigma^{0+,R}}{d\sigma^{0+,L} + d\sigma^{0+,R}} = \frac{1}{|P_t|}\frac{d\sigma^{0-,L} - d\sigma^{0-,R}}{d\sigma^{0-,L} + d\sigma^{0-,R}} \equiv \frac{\epsilon_t}{|P_t|},$$

where $P_t = t \cdot |P_t|$. Since hydrogen jet target polarization is measured to be ~ 0.924 with a good precision, about 0.018 even after taking into account the background and the recombination effect, A_N is also well measured. If we substitute $P_t = 0$ into Eq. 3.1, we get analogous expressions for polarized beam

particles due to the symmetry between beam and target particles. The beam polarization then can be measured by equating the two relations obtained.

The H-jet data have been analyzed as part of the dissertation to get the absolute polarization values for data taken in 2009. Discussions regarding a few key parts of this analysis will be presented shortly. Note that the results of this analysis were combined with the results of $p - C$ polarimeter analysis to get final beam polarization values used for the A_{LL} measurements.

3.2 Data collection in 2009 (Run 9)

Experimental setup for Run 9 did not change from previous $p+p$ run years. Experiment was run at the beam energy of 250 GeV followed by 100 GeV. Blue-beam-only mode was chosen at the begining of 250 GeV run and switched to both-beam mode during the 250 GeV running and kept the same for the rest of Run 9. To reduce background coming from irrelevant beam side, collision points for the two beams were vertically separated. And 111/120 bunch mode was selected throughout the run. Note that detector 1 was not used due to burn-out during test period and all detectors used were Hamamatsu type silicon detector. In summary, we have 3 sets of data periods as displayed in Table 3.1.

data set	date	fill number	beam energy	beam mode
0	Mar. 20 - Mar. 24	10402 - 10415	250 GeV	blue
1	Mar. 26 - Apr. 13	10439 - 10536	250 GeV	blue/yellow
2	Apr. 18 - Jul. 4	10616 - 11032	100 GeV	blue/yellow

Table 3.1: Data set summary for year 2009

3.3 Beam polarization extraction

Extraction of beam polarization is done on a fill-by-fill basis. For each fill, one can calculate the asymmetries and beam polarization in two ways. First, one can take an weighted average over beam polarization values at 6 different recoiled proton kinetic energy[1]. Using this method when there is not enough statistics can underestimate the polarization if one takes the central

[1]The kinetic energy of a recoiled proton is equivalent to $-t$ where t is the Mandelstam variable. See Ref. [35] for details.

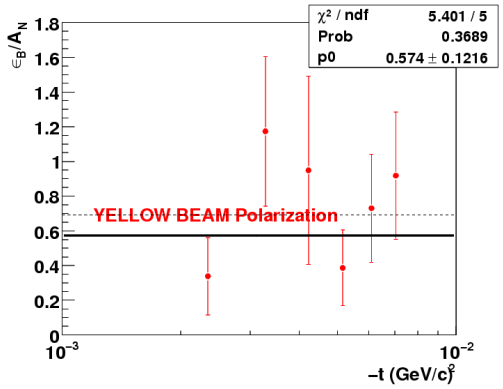

(a) Polarization extracted by taking an weighted average over all bins (solid line) and by combining all kinetic energy bins (dashed line).

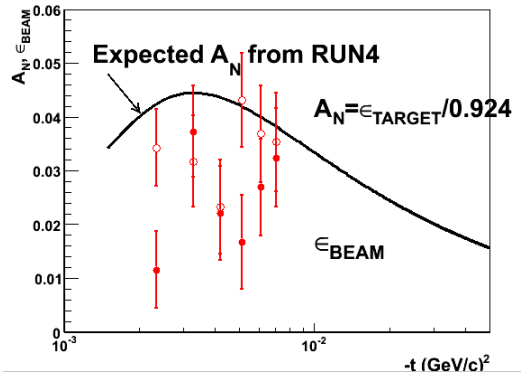

(b) Target asymmetry A_N^{target} (open circle), beam asymmetry A_N^{beam} (closed circle). Legend shows fit result of beam asymmetries.

Figure 3.2: Comparison of beam polarization between combined kinetic energy bin approach and weighted average approach in case of poor statistics. For Yellow beam from fill 10682.

value because large uncertainty at each data point causes asymmetric averaged uncertainty. See an example in Fig. 3.2. Fit results represent the central value of weighted average.

When there is enough statistics, which is true for a fill in most cases, the gap between true and the central value obtained from the method above tends to line up well within uncertainties as shown in Fig. 3.3. However, there is an alternative and more preferable way of extracting beam polarization. That is, one can compute the asymmetries from all kinetic energy bins combined and determine the beam polarization from it. Note that there is a caveat that this can only be justified when the following assumption is satisfied. "The beam polarization does not depend on the recoiled proton kinetic energy." That is because the following relation Eq. 3.2 holds true only if this assumption is proved true.

$$\frac{\sum_i \epsilon_B(i)}{\sum_i \epsilon_T(i)} = \frac{\epsilon_B(1)}{\epsilon_T(1)} = \cdots = \frac{\epsilon_B(n)}{\epsilon_T(n)} \; (i = 1, ..., n : \text{energy bin}) \qquad (3.2)$$

In this analysis, we use combined energy bin approach to extract beam polarization and prove the independence of kinetic energy as a consistency check in the following section.

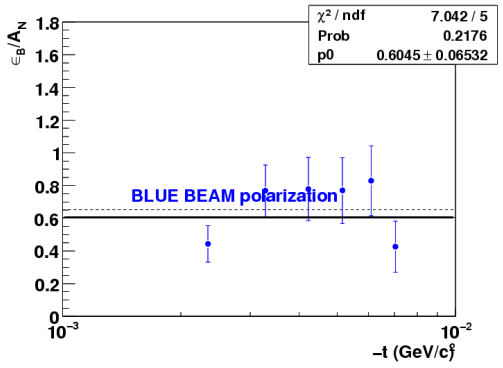

(a) Same as Fig. 3.2(a) with abundant statistics.

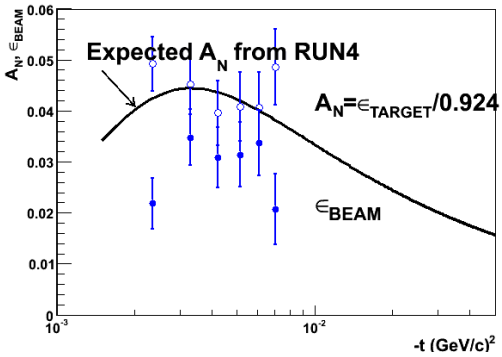

(b) Same as Fig. 3.2(b) with abundant statistics.

Figure 3.3: Comparison between combined kinetic energy bin approach and weighted average approach in case of rich statistics. For Blue beam from Fill 10646.

3.4 Systematic uncertainties

In this section, we discuss potential systematic effects that can affect the beam polarization. To this end, we review a few key steps in beam polarization measurement. The $p + p$ elastic scattering events are collected by detecting scattered target protons. Highly energetic beam particles only get slightly deflected after a collision, while recoiled target protons nonrelativistically drift towards the detector. Strips in the Silicon detector enable us to measure the scattering angle θ and thus the kinetic energy of the recoiled proton[2]. The Time Of Flight (TOF) information of recoiled proton is then used to identify elastic collision events. TOF is the time a recoiled proton flies from the collision point to the detector and the relation between TOF and the kinetic energy (KE) of recoiled proton is dictated by nonrelativistic kinematics. This relation presents itself as a band structure in the TOF-KE plot of the recoiled proton. See Fig. 3.4. And applying cuts on TOF greatly reduce the background level.

Given the procedure, we can think of three different potential systematic uncertainty sources. First, one has to examine if choosing a certain TOF cut over others has any effect on beam polarization. This will prove to be insignificant compared to other sources shortly. Second potential source comes from the acceptance difference between detectors on the right and the left side. This effect will show up indirectly in asymmetry calculations and will be

[2]The kinetic energy of a recoiled proton is proportional to the angle θ and so it is sensitive to detector geometry.

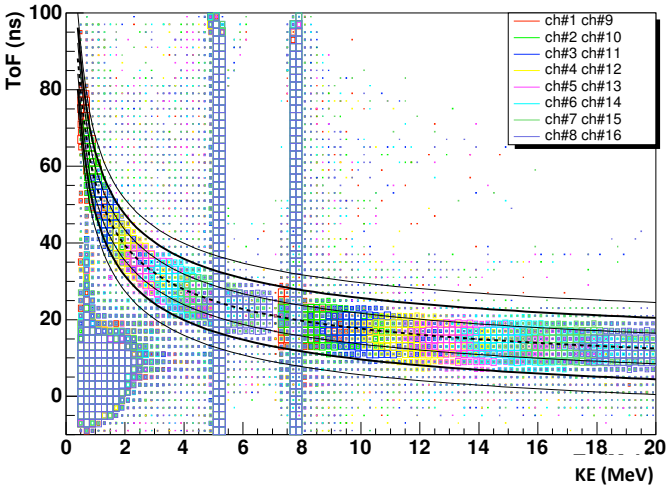

Figure 3.4: TOF [ns] vs. KE [KeV] of detected particles. Bands in the banana shape represent the nonrelativistic kinematics of elastic scattering events. Two lines in the middle are from radioactive sources used for calibration and the blob on the bottom left corner is attributed to the prompt particles from inelastic scatterings.

examined in various tests. At last, background effects on the beam polarization measurements has to be thoroughly studied. This will be discussed later in the section.

There are two classes of systematic uncertainties that can potentially be attributed to the sources mentioned above. Uncorrelated uncertainties, which are the first kind, are studied by a fill-by-fill analysis. Fit probabilities in the beam asymmetry and the TOF cut dependence of the beam polarization are discussed. Correlated uncertainties, the second kind, are also studied on the all-fills-combined data. Recoiled proton's kinetic energy dependence of the beam polarization and the background asymmetries are analyzed in the latter category.

3.4.1 Uncorrelated uncertainties

Fit probability

While H-jet target polarization is maintained stable and under good control, beam polarization is hard to control because of numerous parameters determining beam dynamics. For this reason, a test using fit probability is performed on the beam asymmetries. Spin dependent effects coming from the target side are washed out when summing over target yields to calculate the

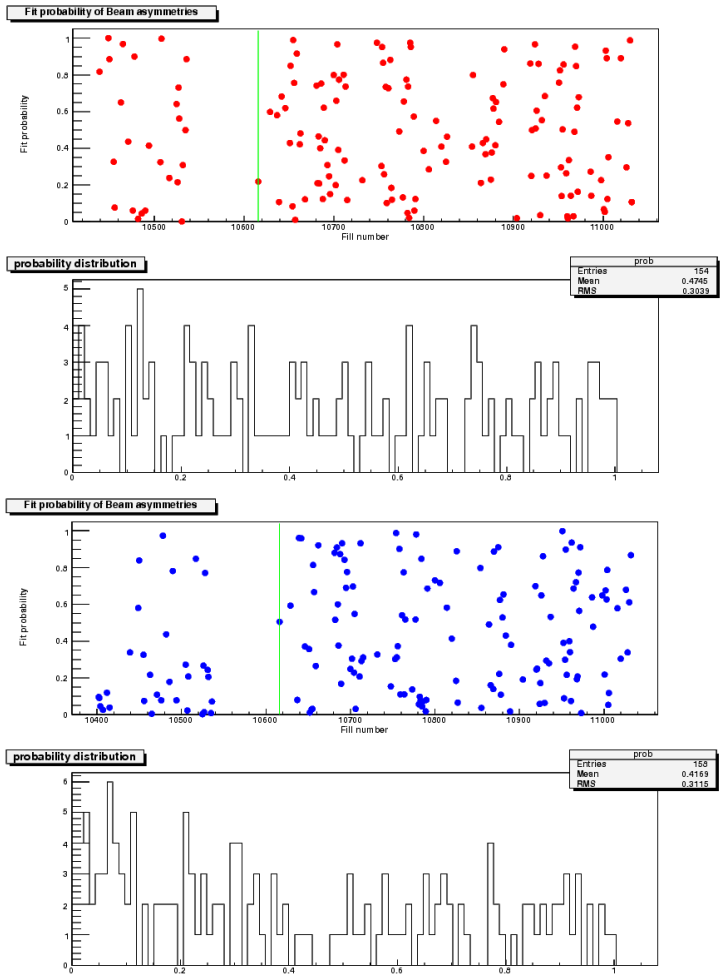

Figure 3.5: Fit probability test for the beam asymmetries. Top: Yellow, Bottom: Blue

beam asymmetries. The fit probability is the probability of having certain value of χ^2 for a given number of degrees of freedom. If the χ^2 distribution is normal, one should expect that the fit probability is evenly distributed in the range between 0 and 1. The fill-by-fill fit probability and its distribution are shown in Fig. 3.5. This confirms that there is no unknown systematic effects coming from sources on the beam side.

Recoiled proton's TOF cut and beam polarization

We choose a narrow TOF cut of 8 ns for this analysis to ensure the minimal background level. To examine potential systematic effects, we examine if

a wider TOF cut of 10 ns gives us consistent results on the beam polarization. Since the beam polarization gets additional relative uncertainties associated with the beam asymmetries, the relative uncertainties on P_B is larger than the one on A_N^{target}. And the same goes for the relative uncertainties on the difference in the variables between the two TOF cuts. The uncertainties on A_N^{target} from choosing a certain TOF cut has been known to be small from analyses in past years. Uncertainties on the jet target polarization, which is negligible, is ignored in this test. Instead of directly calculating uncertainties on the beam polarization measured with the narrow and wide cuts, we rearrange the equation so that the computation of correlated uncertainties is easier. The new observable defined in Eq. 3.3 is measured fill by fill and fit to a constant. The fit parameter is expected to be zero within uncertainties if the beam polarization obtained from the wide cut is consistent with the one obtained with the narrow cut. The fill-by-fill measurement of this observable is shown in Fig. 3.6 and the fit results are summarized in Table 3.2.

$$\frac{\epsilon_B(\text{wide})}{\epsilon_B(\text{narrow})} - \frac{\epsilon_T(\text{wide})}{\epsilon_T(\text{narrow})} = 0 \Leftrightarrow P_B(\text{wide}) = P_B(\text{narrow}) \tag{3.3}$$

Asymmetries are calculated fill by fill and the difference is fit to a constant. See Fig. 3.6 for the results. All asymmetries at both beam energies are consistently zero within uncertainties. Also, see Table 3.2 for the effects on the beam polarization. We can conclude that there is no systematic effect caused by applying a TOF cut.

$\frac{\epsilon_B(\text{wide})}{\epsilon_B(\text{narrow})} - \frac{\epsilon_T(\text{wide})}{\epsilon_T(\text{narrow})}$	Blue beam	Yellow beam
250 GeV	-0.00027±0.00324	-0.00497±0.00356
100 GeV	0.00174±0.00148	0.00078±0.00155

Table 3.2: Fit results of difference in beam polarization between two different recoiled proton's TOF cuts.

3.4.2 Correlated uncertainties

Recoiled proton's Kinetic energy and beam polarization

In order to identify potential correlated uncertainties across the fill, we combine all the fills to calculate asymmetries for each kinetic energy bin. The beam and target asymmetries are shown in Fig. 3.7. The beam polarization

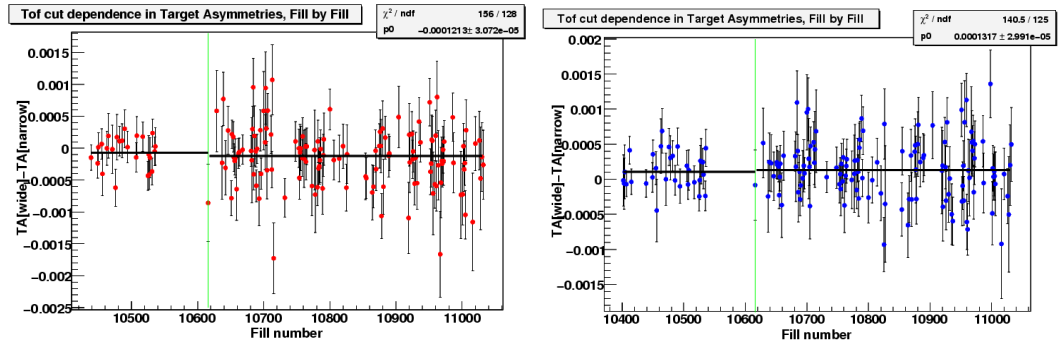

(a) Yellow beam.

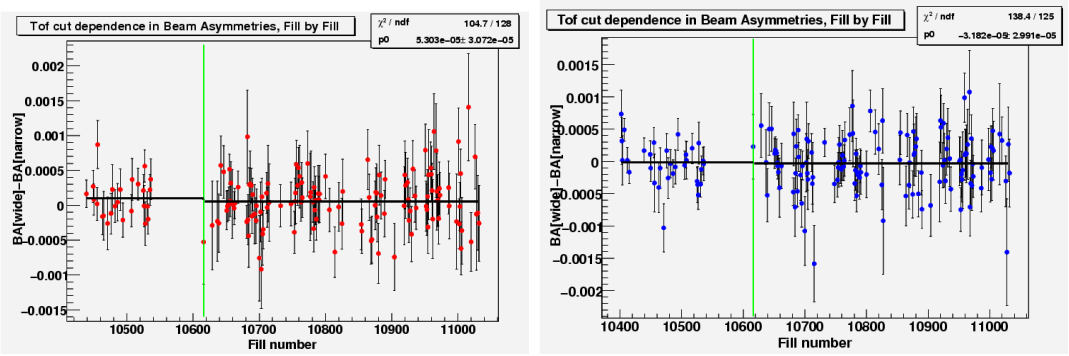

(b) Blue beam.

Figure 3.6: Recoiled proton's TOF cut dependence of asymmetries. Left: Yellow, Right: Blue

value is then extracted by taking the ratio of the two asymmetries scaled by the target polarization for each bin. Then the polarization is fit through the kinetic energy bins to a constant. The result is presented in Fig. 3.8. Good χ^2s indicate that no systematic effects are found.

Recoiled proton's TOF cut and beam polarization

Systematic effects associated with the recoiled proton's TOF cut was previously studied in the fill-by-fill analysis. In order to investigate its correlated effects, we calculate the beam polarization for each fill and fit through all the fills. The results obtained with the narrow and wide cuts are compared at the end.

In one of the data quality assurance performed for this analysis, we dis-

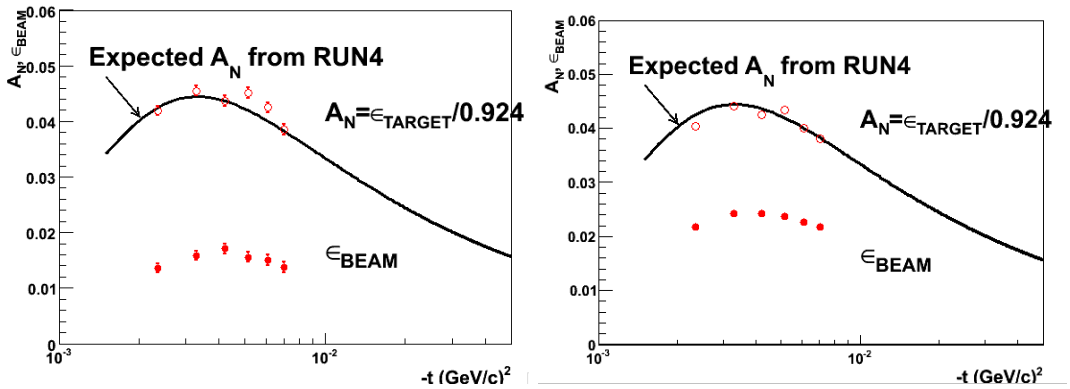

(a) Yellow beam. Left : 250 GeV Right : 100 GeV

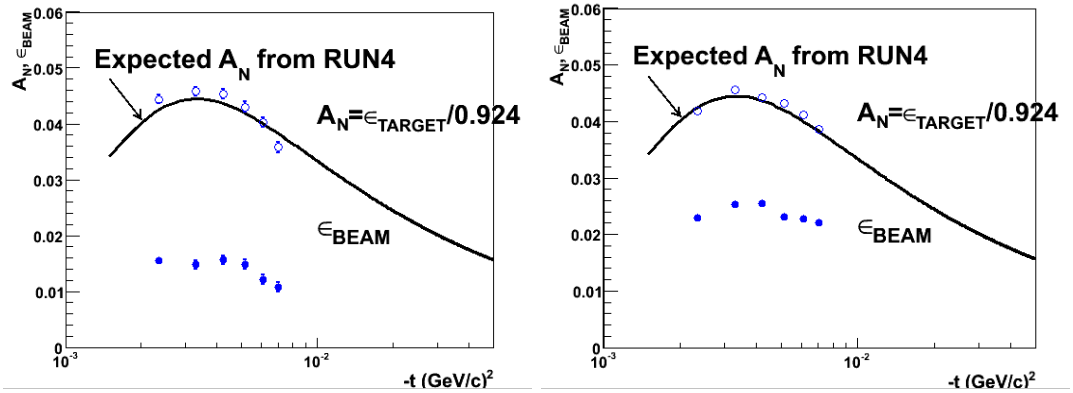

(b) Blue beam. Left : 250 GeV Right : 100 GeV

Figure 3.7: Asymmetries calculated from all fills combined. Fit parameters are the beam asymmetries fitted to a constant.

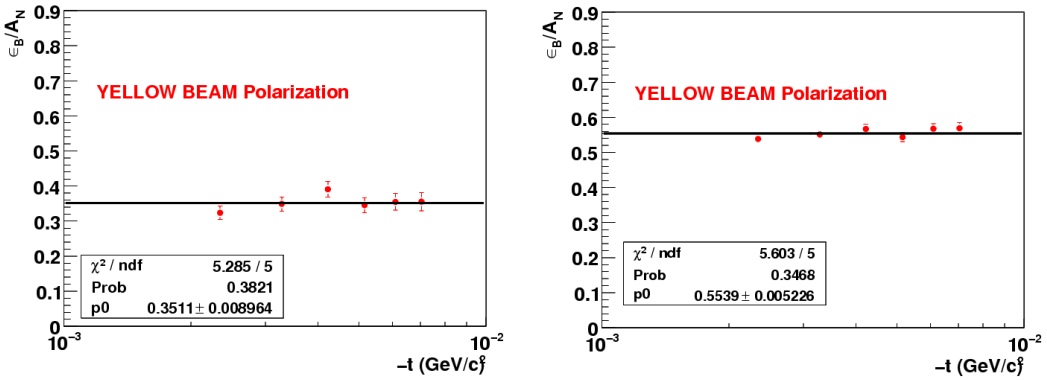

(a) Yellow beam. Left : 250 GeV Right : 100 GeV

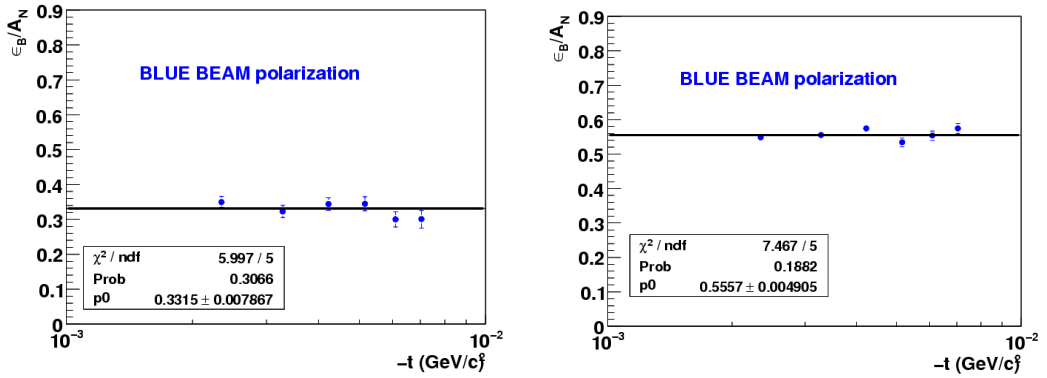

(b) Blue beam. Left : 250 GeV Right : 100 GeV

Figure 3.8: Kinetic energy dependence for beam polarization.

carded runs with abnormal elastic event counts ratio between wide and narrow TOF cut. Its stability is a necessary, and not sufficient, condition for minimizing the difference in polarization coming from different TOF cuts. The ideal situation is the difference in polarization coming from using two different cuts is purely statistical, in which case the difference should be consistent zero within uncertainties. Indeed, the result exhibits good comparisons between the two. The fill-to-fill beam polarization is plotted in Fig. 3.9 and the fit results are summarized in Table 3.3.

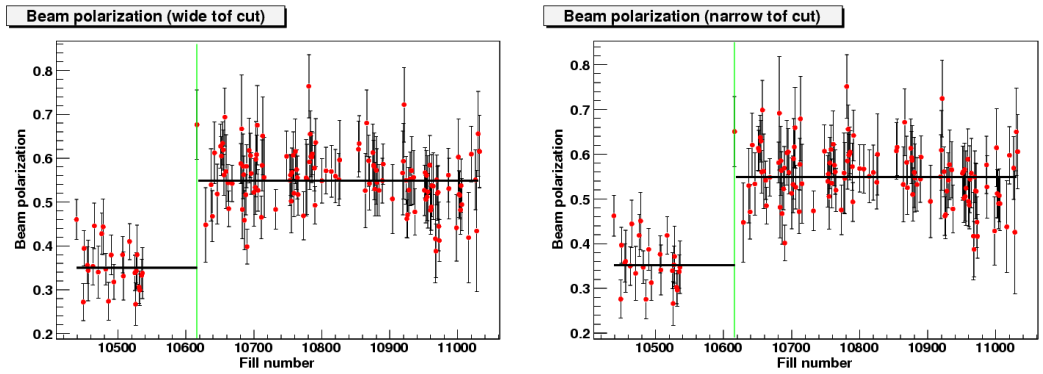

(a) Yellow beam.

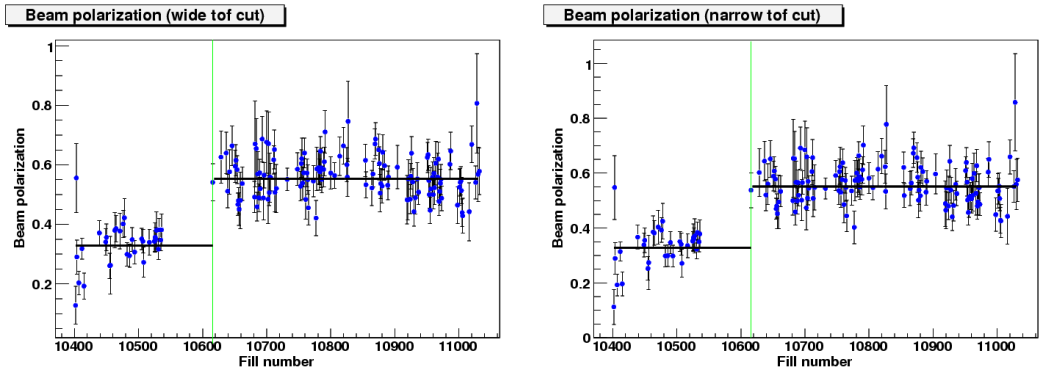

(b) Blue beam.

Figure 3.9: Beam polarization extracted from the wide and narrow TOF cut.

Background asymmetries

The ratio of number of events with the wide and narrow TOF cuts was measured to monitor the background level and the result indicated that the background level was stable throughout the data taking period. Since we confirmed that the background level is stable, the next step is to consider

Beam Energy - TOF cut	Blue	Yellow
250 GeV - wide	0.328± 0.008	0.350± 0.009
250 GeV - narrow	0.328± 0.008	0.351±0.009
100 GeV - wide	0.553± 0.005	0.549± 0.005
100 GeV - narrow	0.551± 0.005	0.549± 0.005

Table 3.3: Fit results of beam polarization obtained with different TOF cuts.

what are sources of background and how background would affect asymmetries. Background asymmetries can be measured by collecting events recorded in the 'background strips'. Three 'Signal strips' are selected for each kinetic energy bin based on the kinematics and the strips that are more than one strip away from the signal strips are defined as background strips. Asymmetries are measured on the background strips and they are referred to as background asymmetries.

Among the known sources of background is the elastic scattering between proton beam particles and molecular hydrogen in H-jet target system. While its effects on the target asymmetries are taken into account by adjusting jet polarization from 0.96 to 0.924, its effects on the beam asymmetries are measured to be very small.

The small beam asymmetries seen in the background tells us that the background source that affects the beam asymmetries is from nonelastic collisions. The background asymmetries are calculated based on the elastic event kinematics. If hydrogen molecules are the main background sources that affect the beam asymmetries, we should expect sizable beam asymmetries. Small beam asymmetry means background particles are mainly from inelastic scattering collisions between the beam and target protons, where we don't expect sizable asymmetries. The background beam asymmetries ϵ_B and the target analyzing power A_N^{target} are shown in Fig. 3.10.

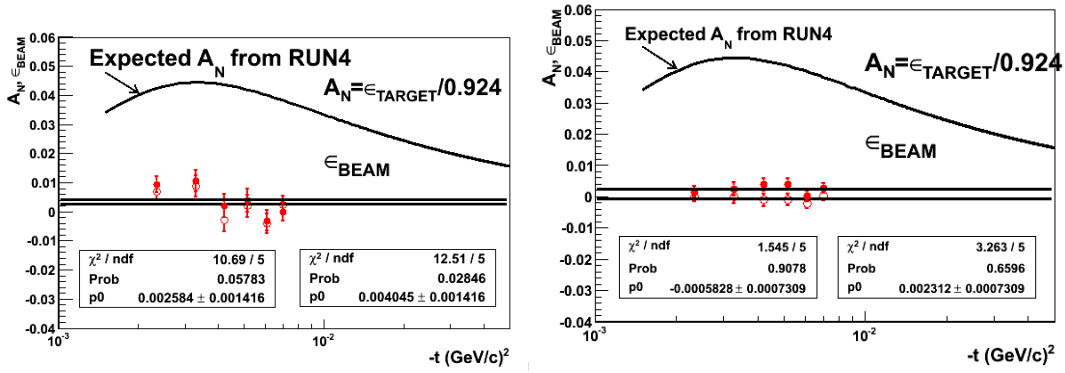

(a) Yellow beam. Left : 250 GeV Right : 100 GeV

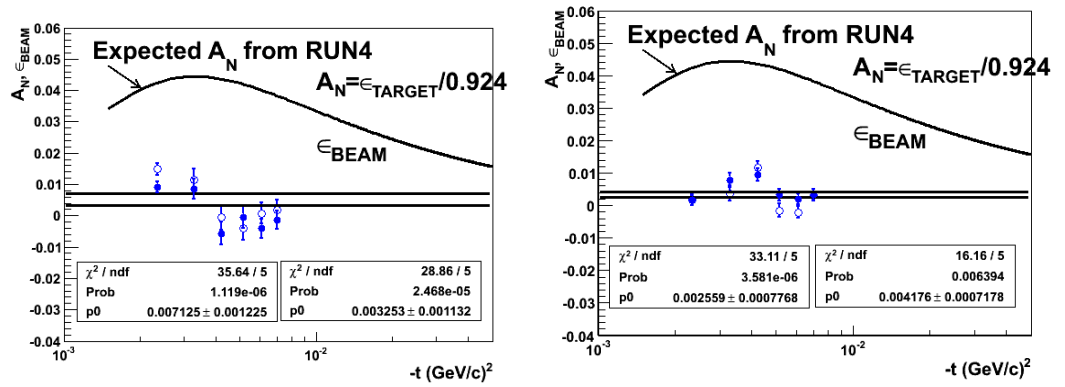

(b) Blue beam. Left : 250 GeV Right : 100 GeV

Figure 3.10: Background A_N^{target} and background ϵ_B. Statistics on left are for A_N^{target} and on right for ϵ_B.

Chapter 4

Charged pions and Hadron Blind Detector

4.1 Particle Identification with HBD

As mentioned previously, HBD was not intended to measure charged pions. More careful analysis was inevitable to successfully utilize this detector. One of the main concerns was that the interested p_T range, or the momentum range since we are interested in $\pi^{\pm}$'s at mid rapidity where p_T is very close to momentum, of $\pi^{\pm}$'s begins in a region very close to the threshold momentum for $\pi^{\pm}$'s to radiate Cerenkov lights. Since the efficiency is steeply rising from zero in this region, it was believed that the description of the HBD charge distribution will not be well understood. To illustrate this point, the p_T range of this analysis is shown in Fig. 4.1 along with the p_T dependent radiation intensity (modulo proportionality factor). Radiation intensity is defined as the number of photons created by Cerenkov radiation per unit length and is expressed in units of 1/length. The plot was made using the knowledge that radiation intensity is proportional to $\sin^2\theta$, where θ is the Cerenkov angle, and the relation $\cos\theta = \frac{1}{n\beta}$ which can be understood from geometrical considerations. Note also that n is the refractive index of the gas in the detector and β is the relativistic Lorentz invariant. The broadness of the curves in p_T direction is attributed to the fact that the momenta of particles can be different between particles with the same p_T, depending on their θ angle.

As will be discussed in great detail in the following sections, it turns out that charged pions can be treated in the same fashion as electrons as long as additional care is taken concerning different thresholds. Especially at p_T region where the momentum is near to the threshold, the charge distribution

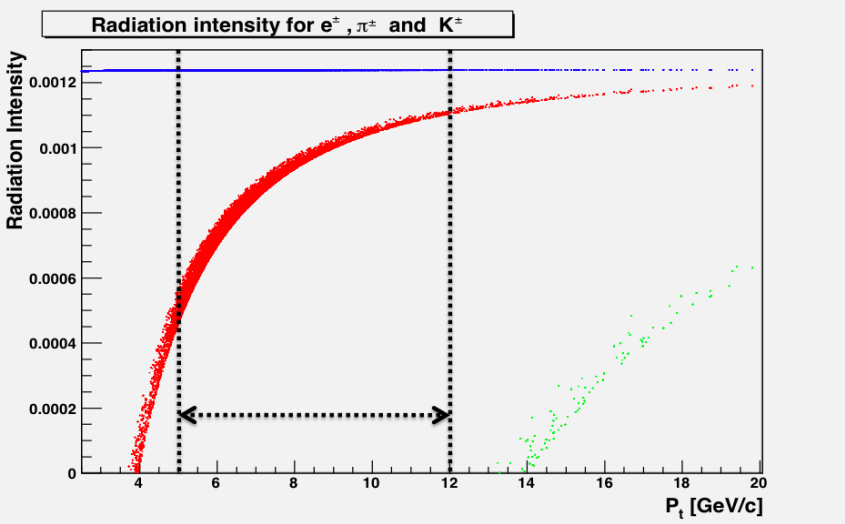

Figure 4.1: Radiation intensity for 3 particle species. Blue : electrons, Red : charged pions and Green : Charged Kaons. Arrow and dashed lines indicate the p_T range of this analysis.

will be proven to closely follow the theoretical description, allowing us to take advantage of it for $\pi^{\pm}$ identification. In next section, a list of background sources for this analysis will follow.

4.2 Background sources for $\pi^{\pm}$ measurement

It is a crucial step to thoroughly comprehend what the background sources of the analysis are and what can be eliminated by using this detector instead of jumping ahead without having a complete picture. Below is the classification of background sources that there are in the $\pi^{\pm}$ candidate sample.

- **Electronic background**
  - Photonic electrons
    - π^0 Dalitz decays
    - γ conversions in material
  - Non-photonic electrons
    - Light meson decays
      - $K^{\pm} \to \pi^0 \nu e^{\pm}$ (long-lived, $c\tau = 3.712$ m [50])

        - ◇ ω, ρ, ϕ $\rightarrow e^+e^-$(short-lived, very near vertex)
      - ▷ Heavy meson decays (short lifetime)
        - ◇ $D^{\pm}, D^0, B^{\pm}, B^0 \rightarrow$ single $e + X$ and $J/\psi, \Upsilon \rightarrow e^+e^-$

- **Hadronic background**
  - ○ Charged pions from other hadronic decays
    - ▷ Light meson decays
      - ◇ η, ω, ϕ $\rightarrow \pi^+\pi^-\pi^0$ and K^0_s, $\rho^0 \rightarrow \pi^+\pi^-$, $\rho^{\pm} \rightarrow \pi^{\pm}\pi^0$ (short-lived)
    - ▷ Heavy meson decays
  - ○ Hadronic showers from the magnet pole tips

To go over item by item, electron background sources written in black are believed to be insignificant. Channels shown in the list are the predominant ones of which end products contain electrons. The π^0 Dalitz decays occur at the event vertex within the spatial resolution ($c\tau$= 25.1 nm) with a branching ratio of 1.173±0.035. Not only the cross section is two orders of magnitude smaller than the one of $\pi^{\pm}$'s, this is also one of the main background sources to di-electron analyses, specifically for which HBD detector is developed. Vector mesons have very short life time and decay into electron pairs very near the vertex with very small branching ratios ((7.7±0.7) $\times 10^{-4}$, (4.72±0.04)$\times 10^{-5}$ and (2.954±0.030)$\times 10^{-4}$ for ω's, ρ's and ϕ's, respectively) as well. Their cross sections are 3∼4 orders of magnitude smaller than the one of $\pi^{\pm}$'s as a result [51]. Heavy mesons are again short-lived and their cross section at high $p_T > 5$ GeV/c is three orders of magnitude smaller [52]. What is common to the sources that have been discussed so far is that they all occur in the vicinity of the beam pipe. That means the momentun of electrons from these sources is most likely correctly reconstructed. Following are the cases where this is no longer true.

When particles decay far off the event vertex as do long-lived light mesons, the momentum of an electron is falsely reconstructed as the bending angle at DC (which determines the momentum) is incorrectly measured. When this is the case, even the electrons with p_T less than the interested p_T range of $\pi^{\pm}$'s cannot be ignored. EMCal and PC3 matching cuts, to a certain extent, remove this type of background as long as there aren't any accidental matching. Nonetheless, with the lack of tracking before DC there is significant percentage of remaining background that cannot be accurately estimated. The same story goes with γ conversion electrons. The only difference is that

γ conversions can happen anywhere in or out of the acceptance. Especially the γ conversion electrons from just before DC that record small bending angle and fake high p_T are believed to be a major contribution to the electron background.

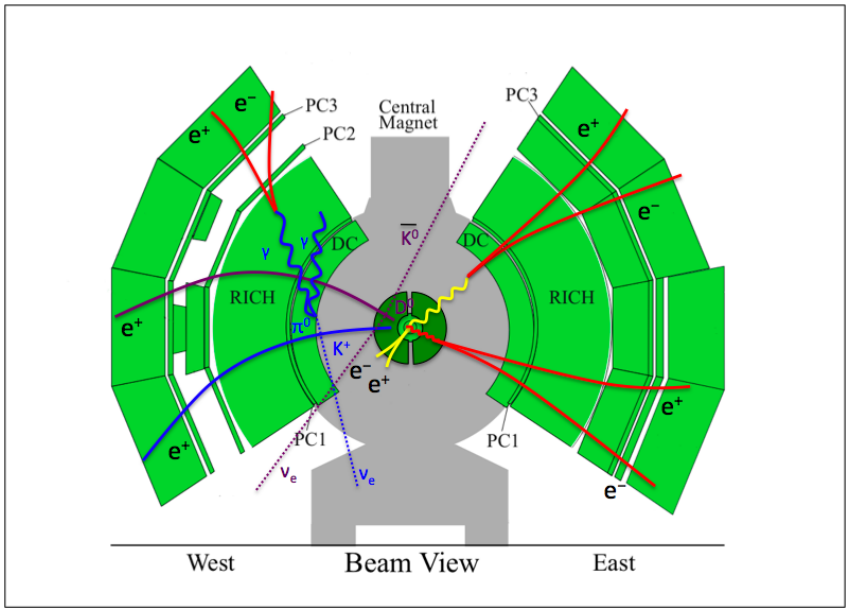

Figure 4.2: Illustration of background

All of these background sources described above are illustrated in the cartoon in Fig. 4.2. Each line overlaid on top of the PHENIX central arm side view corresponds to the track passage of particles. And all the sources are color coded. The bottom line is there are 2 type of remaining electron background sources: long-lived light meson decays and γ conversions.

There are also hadronic background sources that need to be considered. The $\pi^{\pm}$'s decayed from other hadrons belong to this category. In a similar way to the electron background case, one should look into all dominant channels of which end products contain $\pi^{\pm}$('s). The light mesons decay into $\pi^{\pm}$'s with somewhat large branching ratios ((22.74±0.28)%, (89.2±0.7)%, (15.32±0.32)%, (69.20±0.05)%, ∼100% and ∼100% for η's, ω's, ϕ's, K^0_S's, ρ^0's and $\rho^{\pm}$'s, respectively). However, in order for $\pi^{\pm}$'s to fire RICH, the parent particle p_T has to be much larger than the threshold $p_T \sim 4.7$ GeV/c. The cross section for the parent particles with much higher p_T is much smaller by several orders of magnitude, which becomes negligible. This works, of course, because the decays in this category occur nearly at the beam pipe and there

is no need for worrying about incorrectly reconstructed momentum. The K_L^0 decay channel is omitted in the list because it has 5 orders of magnitude smaller branching ratio than the others.

Following the same reasoning as the heavy mesons decaying into electrons, the heavy mesons decaying into $\pi^{\pm}$'s are insignificant source of background.

The last on the list of hadronic background sources is the $\pi^{\pm}$'s generated from hadronic showers in the magnetic pole tips. They are mostly removed by cuts on the acceptance.

4.3 Background reduction using HBD

In the previous section, we discussed all possible background sources and concluded that the remaining background sources after applying matching and various cuts are mainly long-lived meson decays and γ conversions.

This section will describe strategies towards eliminating the background tracks utilizing HBD. Considering background sources in terms of where they are created will be illuminating, so we partition the area into a few as below.

- Beam pipe - Before HBD backplane
- HBD backplane - Before DC
- DC - outer detectors

In the first region, Dalitz decays and γ conversions can occur very near the vertex. The probability of γ conversions happening near the beam pipe is very small (due to small radiation length of the material in the region). So is the probability of Dalitz decays, and the electron pairs from this channel have a small angle at HBD photon detector, causing the two photo-electrons to be inseparable. This merged charge will be removed by applying a maximum HBD charge cut. γ conversions far off the vertex can also be caught by a HBD matching cut as their momentum and track path will be incorrectly reconstructed.

The second region is where we expect the remaining background sources mostly are. The γ conversion electrons from this regions can be removed by HBD matching cuts as they do not leave any charge on HBD. In the case of an accidental matching with scintillation lights on HBD, further removal

is possible by applying minimum HBD charge cuts. The electrons from long-lived meson decays can be eliminated by the same cuts as the decay products, including the main contributor $K^{\pm}$'s, do not radiate Cerenkov lights in the interested p_T range. See Fig. 4.1

The γ conversion electrons and the electrons from long-lived meson decays originating from the third region can mostly be removed DC quality, PC3 matching and EMCal matching cuts.

4.4 HBD charge clustering algorithm

4.4.1 Cluster searching scheme and Definitions

In this section, we will discuss how to associate charge clusters collected on HBD with the $\pi^{\pm}$ candidates. Some definitions will be clarified of the terms that will be used later on for the sake of consistencies within the analysis.

In order to build a highly efficient HBD charge clustering algorithm, we need to have sufficient knowledge on the operational configuration. First, magnetic field configuration with HBD is different from the one without HBD. Fig. 4.3(a) shows the magnetic field along the radial axis in 2009. It is characterized by very weak magnetic field (only ∼10%) inside HBD. There are also two operational modes regarding electric field configuration, so called "forward bias $(-+)$ mode" and "reverse bias $(+-)$ mode". What defines forward or reverse bias mode is the polarity of the mesh voltage in the triple GEM photon detector. See Fig. 2 of Ref. [40] for detailed information. The idea behind operating in reverse bias mode is to reduce ionization electron signal caused by charged hadrons as much as possible. It is believed that in reverse bias mode the mean amplitude of ionization electron signal from charged particles after the entire amplification process drops to ∼10% of its value in forward bias mode. Operating in reverse bias mode has another advantage in gain calibration. This will be discussed later in Sec. 4.5.

Since we know the magnetic field configuration, central arm tracking is available as before. An effective way to find candidate charge clusters is to take advantage of the tracking capabilities. In the "***charged track projection scheme***", the first step is to **project** the tracks that pass other $\pi^{\pm}$ PID cuts.

The second step is to determine the "**searching radius**" within which to look for any charge collected on HBD pads. At an initial stage, one needs to define large enough a radius so that the coordinate shift correction for this

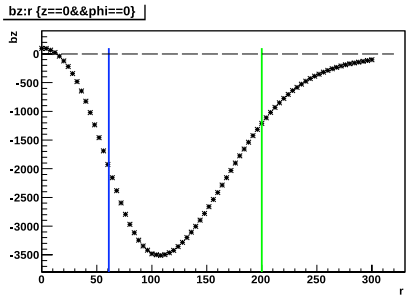

(a) Magnetic field configuration along radial direction in 2009 (Blue: backplane of HBD, Green: beginning of DC)

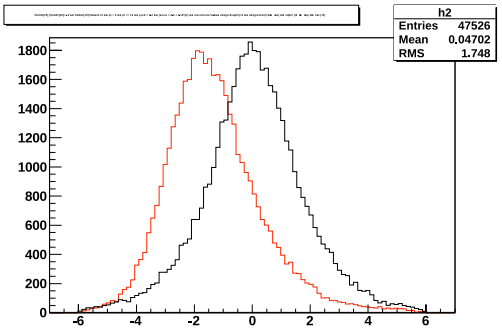

(b) Distribution of hbddz variable before and after coordinate shift corrections.

Figure 4.3: The central arm tracking based on (a) the magnetic field configuration and (b) the detector coordinate shift correction.

detector can be carried out. The logic behind the coordinate shift correction for HBD is the same as the one for any other central arm detectors. Once this is done, an optimal radius can be determined, taking into account reconstruction efficiencies. Fig. 4.3(b) shows the distribution of hbddz variable before and after the correction is done.

With the searching radius determined, the next step is to define basic units to form a cluster - a practical unit for the HBD charge of a track. The amount of pedestal charge in each pad are subtracted to begin with. The amount of remaining charge in each pad is called "**pad charge**". The 3 neighboring pads will form a "**triplet**" - the smallest unit to form a "**cluster**", and the sum of collected charge in a triplet will be called "**triplet charge**". Each coordinate component of a triplet is determined by taking a charge weighted average over the center coordinate of all pads in the triplet. There are two independent coordinates y and z to describe the position of a cluster on HBD.

There are several ways to form a cluster out of triplets. Two methods will be examined in the following section to decide which can serve as the most efficient clustering algorithm for this analysis.

4.4.2 Cluster forming algorithm

Merged Triplets Method

We start with the less desirable method of the two and explain why it is the case. This method is called the "*merged triplets method*". The idea is

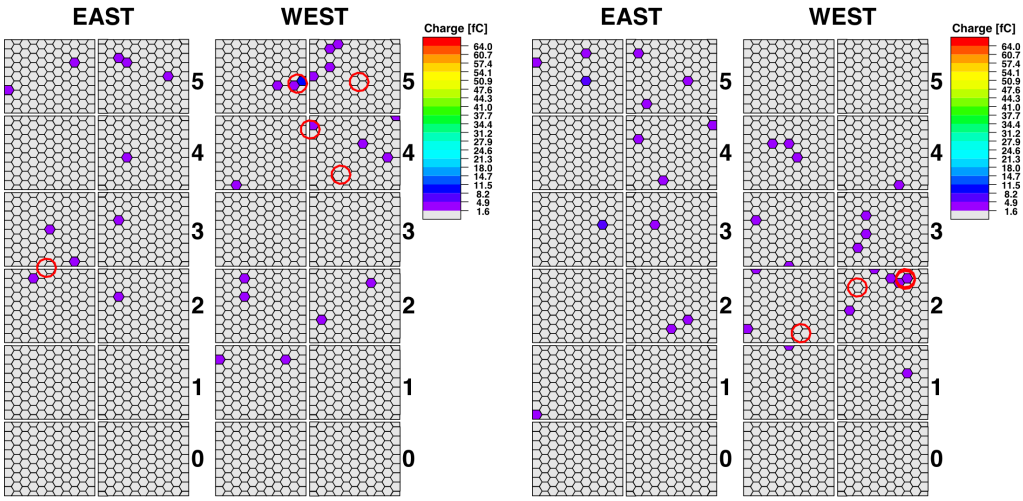

(a) single pad and double pad triplets (b) triple pad triplet

Figure 4.4: Some examples of event display.

that a cluster is formed by adding all triplets within the searching radius and the cluster charge of a track is determined such that charges in all triplets are summed. Each coordinate of a cluster is determined by taking a charge weighted average of the coordinate of all triplets. A case of 3 pads forming a cluster is also shown in Fig. 4.4(b).

To illustrate, let us first look at the examples of event display in Fig. 4.4. Each hexagon corresponds to a single pad and the circles in red represent the searching window (∼2.5 cm in these examples). In (a) are shown some cases where there is only one pad (in section 4) or a couple pads (in section5) within the searching radius that the pad charge is above the threshold (pedestal charge).

If we double the searching radius, the situation will be very different. The circle enclosing the double-pad triplet will additionally enclose a single-pad triplet that is to its left. Also, the double-pad triplet will become a triple-pad triplet. In short, we can have multiple triplets in a cluster in this clustering scheme.

Now let us turn to the HBD cluster charge distribution. To understand better, distributions are made from Monte Carlo (MC) simulation, embedded Monte Carlo (in data) and real data. Embedded MC is a good place to start

as it will allow us to evaluate the effectiveness of charged pion identification in the presence of realistic background. For background studies, we define an object 'swapped cluster' as a cluster found within the searching radius with respect to the 'swapped projection' point. The swapped projection is determined by reversing the sign of x coordinate of the normal projection that is associated with charged tracks. The charge and size distributions are shown in Fig. 4.5 for both $\pi^{\pm}$ candidate clusters and swapped clusters.

There is an apparent trend that the the mean charge, total number and size of HBD clusters associated with the $\pi^{\pm}$ candidates become larger with increasing searching radius. The increase in the total number of swapped HBD clusters with increasing searching radius (by ~600% as distinct from a ~10% increase in the number of $\pi^{\pm}$ clusters) is more dramatic, while it is notable that the size of swapped cluster is relatively stable regardless of

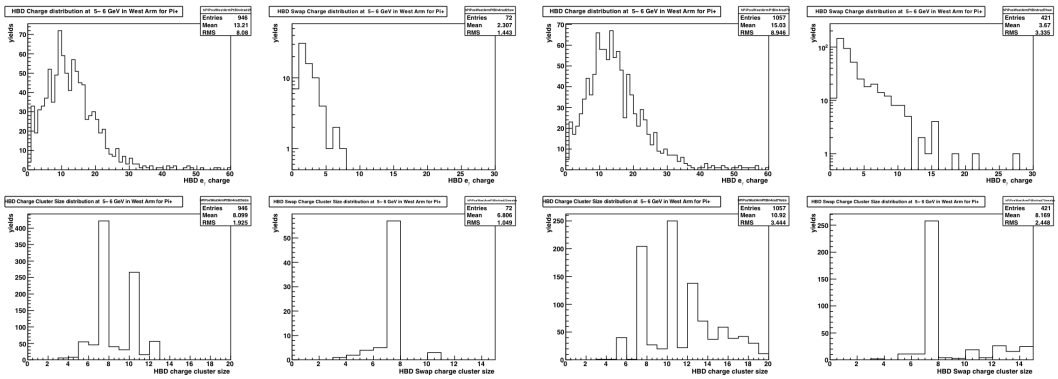

(a) π^{+} in west arm with $5.0 < p_T < 6.0$ GeV/c (Left: 2.5 cm, Right: 7.0 cm)

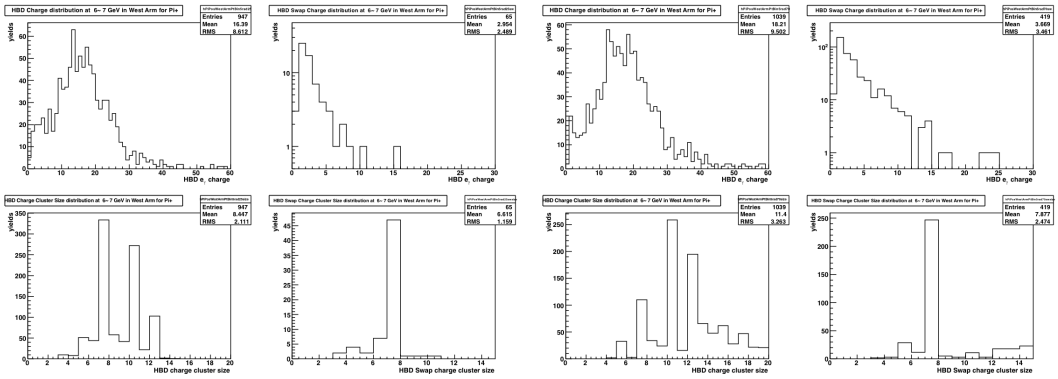

(b) π^{+} in west arm with $6.0 < p_T < 7.0$ GeV/c (Left: 2.5cm, Right: 7.0 cm)

Figure 4.5: Merged triplets method - continued on the next page with description.

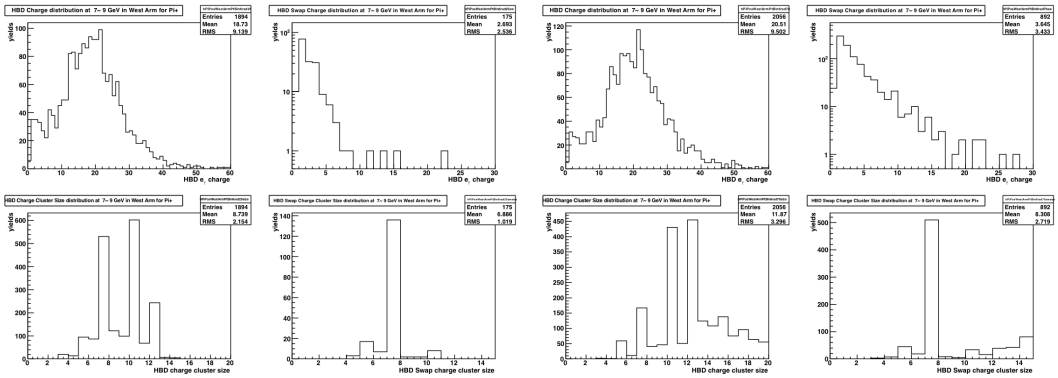

(c) π^+ in west arm with $7.0 < p_T < 9.0$ GeV/c (Left: 2.5 cm, Right: 7.0 cm)

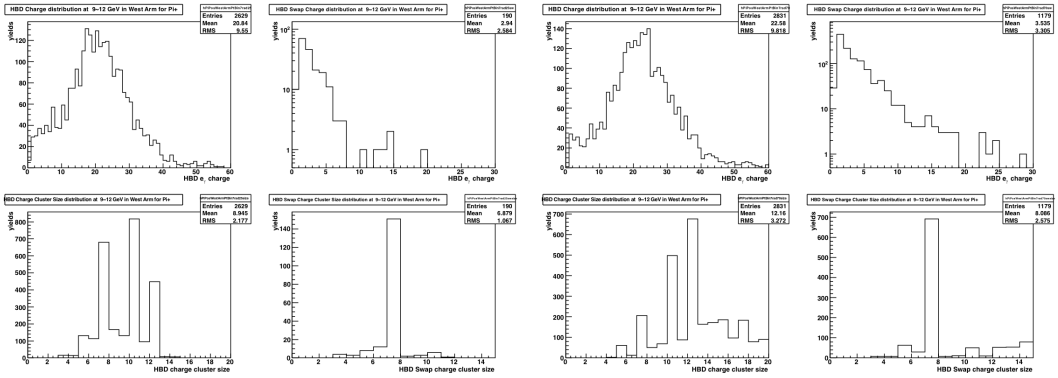

(d) π^+ in west arm with $9.0 < p_T < 12.0$ GeV/c (Left: 2.5 cm, Right: 7.0 cm)

Figure 4.5: Merged triplets method - The comparison between the two different searching radii; R = 2.5 and 7.0 cm. Repeating in a set of 2 by 2 panels are the HBD cluster charge distribution (top left), the HBD cluster size distribution (bottom left), the HBD swap cluster charge distribution (top right) and the HBD swap cluster size distribution (bottom right).

searching radius. As it will become clear as we go along, increasing mean charge is indicative of conflicts between different factors to be optimized. For the moment, we will ignore this and carry on with our current method to explore what we can learn from it. So the next thing in order is to find the minimum searching radius that is large enough to keep most of clusters associated with $\pi^{\pm}$'s. To this end, clustering efficiencies are plotted in Fig. 4.6.

It looks as if the radius greater than 7.0 cm is about right to have high and saturated efficiency for all p_T bins. At this radius, clustering efficiencies do not depend on p_T. This might be counterintuitive at first, considering their very different radiation intensities, but it is a feature that makes HBD a

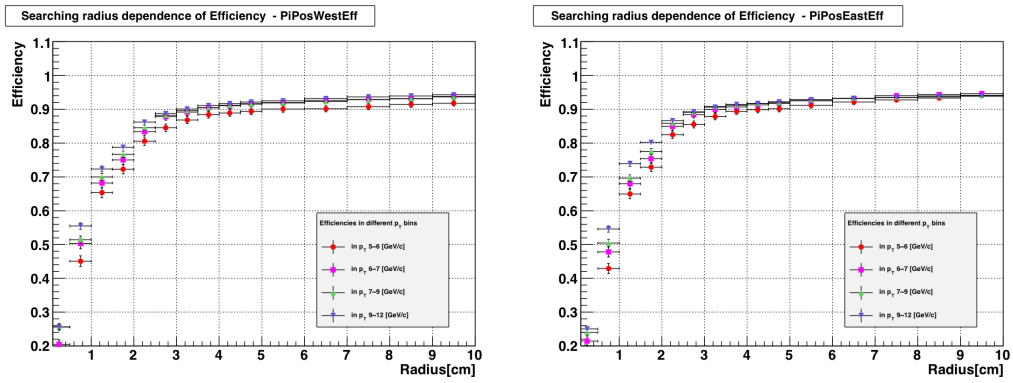

(a) π^+ in west arm

(b) π^+ in east arm

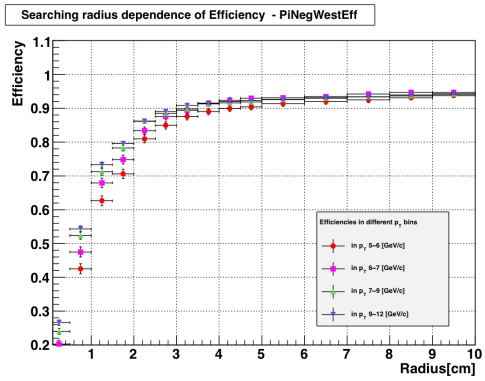

(c) π^- in west arm

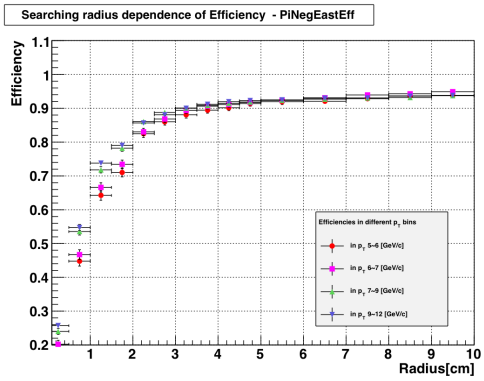

(d) π^- in east arm

Figure 4.6: Merged Triplets Method - The searching radius dependence of clustering efficiency for charged pions with $5.0 < p_T < 6.0$ (red), $6.0 < p_T < 7.0$ (magenta), $7.0 < p_T < 9.0$ (green) and $9.0 < p_T < 12.0$ (blue) GeV/c.

great candidate to be used for a rigorous analysis. The next question to ask is how much fraction of these clusters are from actual $\pi^{\pm}$ clusters and how much from accidental matching with the scintillation background. Knowing the answer to this question is very crucial because in real data there is no way of telling if a track is from real $\pi^{\pm}$ unlike in embedded MC. To be able to estimate the level of scintillation background contamination in the $\pi^{\pm}$ candidate clusters, there needs to be further studies on how normal HBD clusters compare with swapped clusters.

The cluster density as a function of radial distance is a good variable to look at. Calculated cluster density for normal clusters as well as swapped clusters are shown in Fig. 4.7. A searching radius of 10.0 cm was used for this

study. The cluster density for normal ($\pi^{\pm}$ candidate) clusters falls smoothly from the center outward in radius as expected[1]. The information from which we can learn about background is in the radial dependence of the ratio between the normal cluster and swapped cluster distribution.

At this point, the best possible scenario would have been to be able to find a searching radius with which the density level of $\pi^{\pm}$ clusters is comparable to the one for swapped cluster so that we can determine the maximum radius that allows the least amount of background level possible and the saturated high efficiency. This logic seems sound as what compose swapped clusters, which are mostly scintillation lights, also compose the background in the neighborhood of normal clusters. An immediate problem one can see,

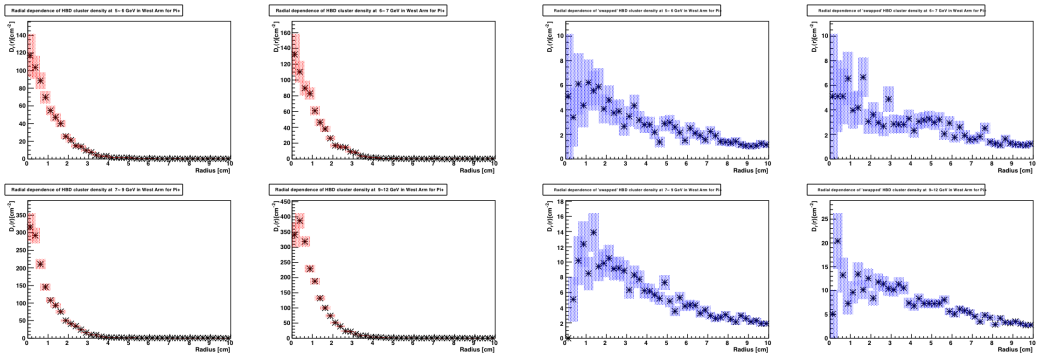

(a) π^{+} clusters in west arm (Left) and associated 'swapped clusters' (Right)

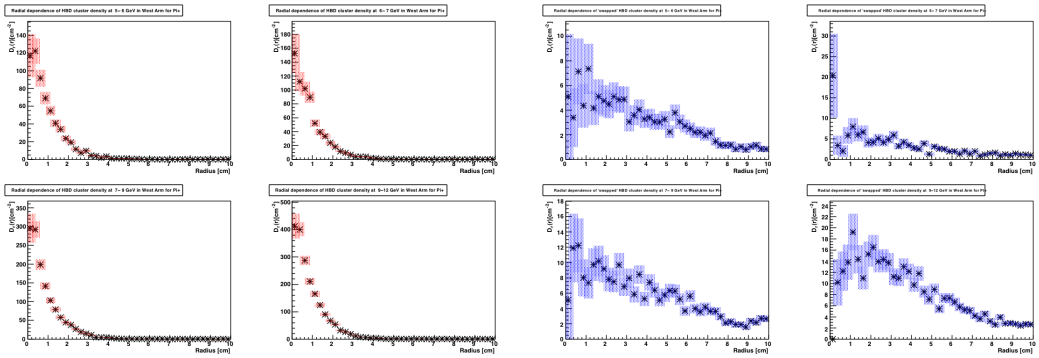

(b) π^{+} clusters in east arm (Left) and associated 'swapped clusters' (Right)

Figure 4.7: Merged Triplets Method - continued on the next page with description.

[1]The absolute scale of the densities is not important as it depends on the number of tracks generated.

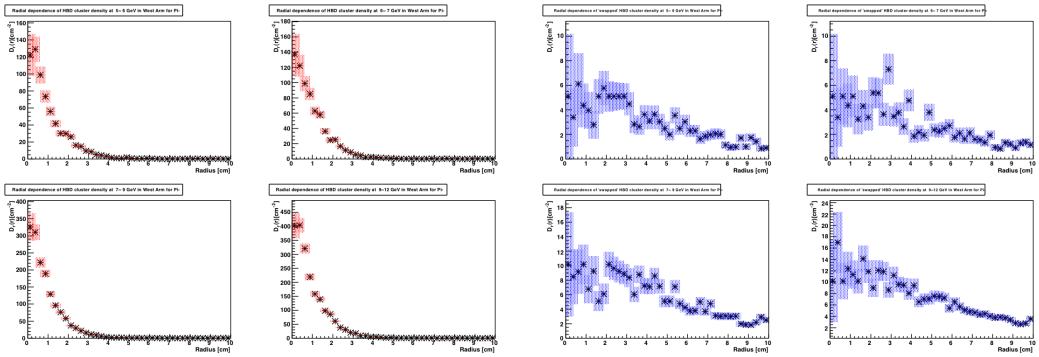

(c) π^- clusters in west arm (Left) and associated 'swapped clusters' (Right)

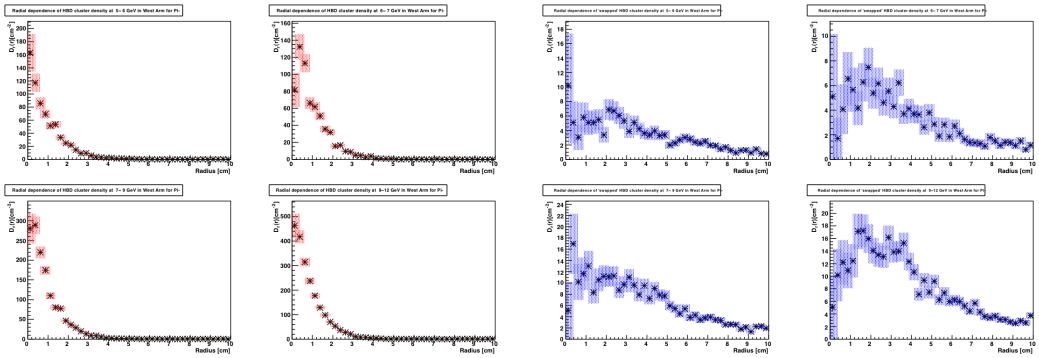

(d) π^- clusters in east arm (Left) and associated 'swapped' clusters (Right)

Figure 4.7: Merged Triplets Method - The radial dependence of cluster densities. Repeating in a set of 2 by 2 panels are for charged pions with $5.0 < p_T < 6.0$ (top left), $6.0 < p_T < 7.0$ (top right), $7.0 < p_T < 9.0$ (bottom left) and $9.0 < p_T < 12.0$ (bottom right) GeV/c. X-axis: the radial distance from the track projection point ranging from 0 to 10 cm, Y-axis: cluster density $D_r(r)$ cm^{-2}.

unfortunately, is that the density level is not flat over the range examined, making it difficult to estimate the true background level. This is attributed to the fact that when multiple triplets are merged in the clustering process, the coordinates of merged clusters gravitate towards the center. Even if we take a wide range of density level for an estimation of background, the second issue that is more fundamental rises. That is, the maximum searching radius allowed based on that background level is roughly $3.5 < r < 4.0$ cm, and this is smaller than the minimum radius required to have a high efficiency.

If we decided to compromise background rejection level in favor of high efficiency, we have to be able to estimate not only how much fraction of cluster charge come from scintillation lights but also how often the charge

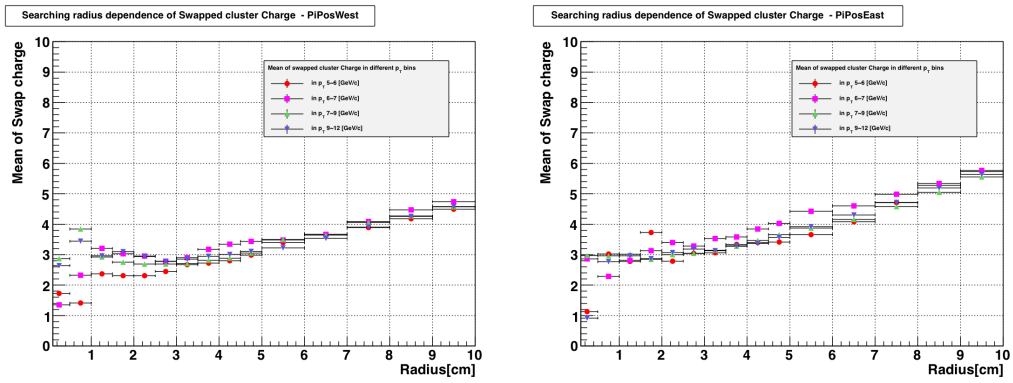

(a) π^+ in west arm

(b) π^+ in east arm

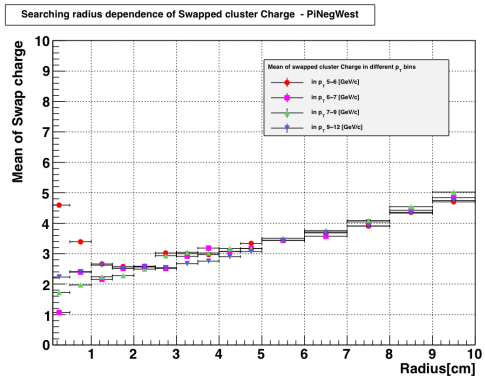

(c) π^- in west arm

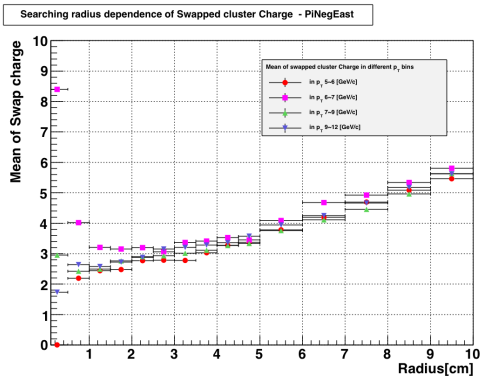

(d) π^- in east arm

Figure 4.8: Merged Triplets Method - The searching radius dependence of the mean charge of 'swapped clusters'. These swapped clusters are associated with charged pions with $5.0 < p_T < 6.0$ (red), $6.0 < p_T < 7.0$ (magenta), $7.0 < p_T < 9.0$ (green) and $9.0 < p_T < 12.0$ (blue) GeV/c.

from scintillation lights are present within the searching window of $\pi^{\pm}$ candidate tracks. As for the former, swapped clusters can be used to study the charge contribution. The mean charge of swapped clusters are presented in Fig. 4.8. The cluster charge distribution of scintillation lights is expected to be dominated by an exponential function with the mean of 1[2]. The background in real data, which is embedded into MC, contains ionization electrons as well though much suppressed in reverse bias mode. This will add exponentials with exponents of up to ∼3, as a result of which the mean swapped cluster charge starts from about 2∼3. As searching radius becomes larger, the mean charge of background clusters almost doubles and calls for

[2]See Sec. 4.5.

systematic subtraction or estimation.

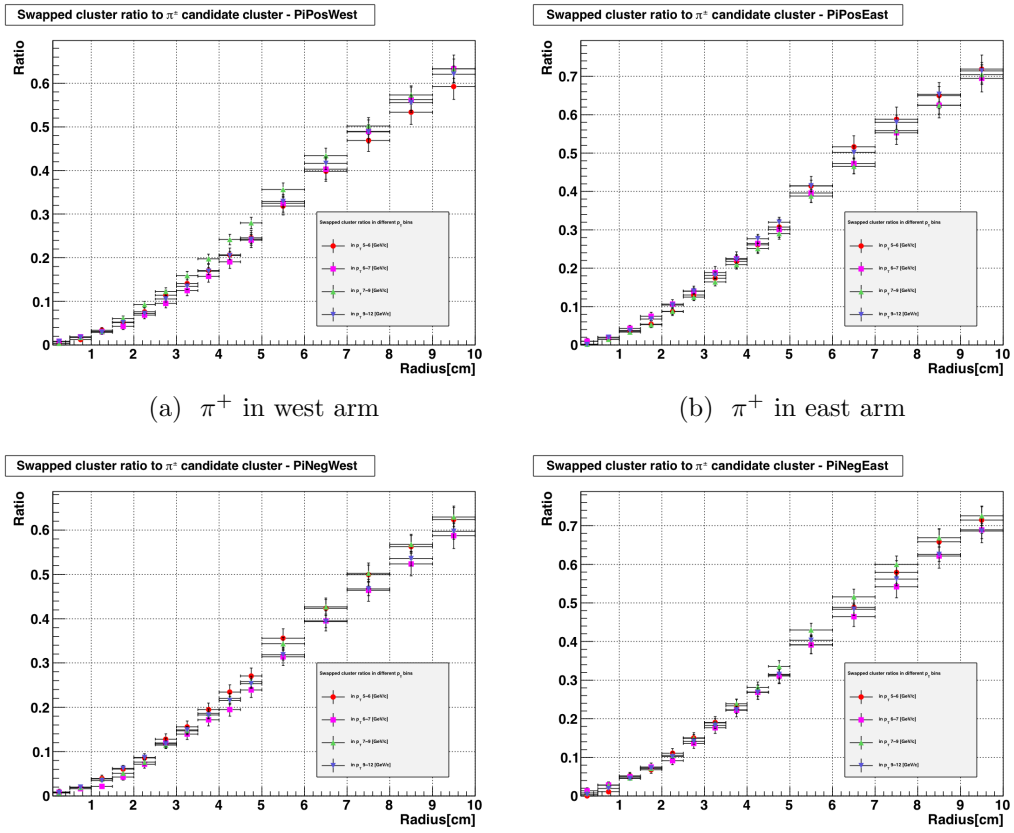

(a) π^+ in west arm

(b) π^+ in east arm

(c) π^- in west arm

(d) π^- in east arm

Figure 4.9: Merged Triplets Method - The searching radius dependence of the swapped to $\pi^{\pm}$ candidate cluster ratio. Color coding is the same as in Fig. 4.6 or Fig. 4.8.

It is in order to ask at this point how often background clusters are present in the $\pi^{\pm}$ clusters. A good way to estimate this is to see what fraction of time the swapped clusters are seen in an event where a $\pi^{\pm}$ cluster is present. The ratios are displayed in Fig. 4.9. With a searching radius of 7.0 cm, there is a 50% chance of background clusters being present. This is a trickier situation than having a chance of less than 10% or more than 90%. Not knowing what happens on an event by event basis, this will lead to very large systematic uncertainties.

Pushing a bit further despite the weaknesses of this method, the charge

distribution of $\pi^{\pm}$ candidate clusters from pure MC and real data are plotted as well in Fig. 4.10. The searching radius used for this is 7.0 cm for comparisons that will be made later with embedded MC (Fig. 4.5). The shape of the distributions is deformed by background tracks pulling the mean charge down to lower values. The separation between the $\pi^{\pm}$ candidate clusters and background clusters, however, is not so obvious except for the highest p_T bin.

The mean cluster charge is compared between MC, embedded MC and 2009 data in Fig. 4.11. What is noteworthy in this plot is that the embedded MC shows the highest mean charge throughout the p_T, and the opposite shows real data. A reasonable explanation for this is, in embedded MC all the clusters are true charged pions and background clusters are more likely to be added to those pion clusters than to form an independent cluster, whereas in data a good fraction of pure background clusters form independent clusters and become falsely identified with charged pions. The mean cluster charge of pure Monte Carlo sits in the middle.

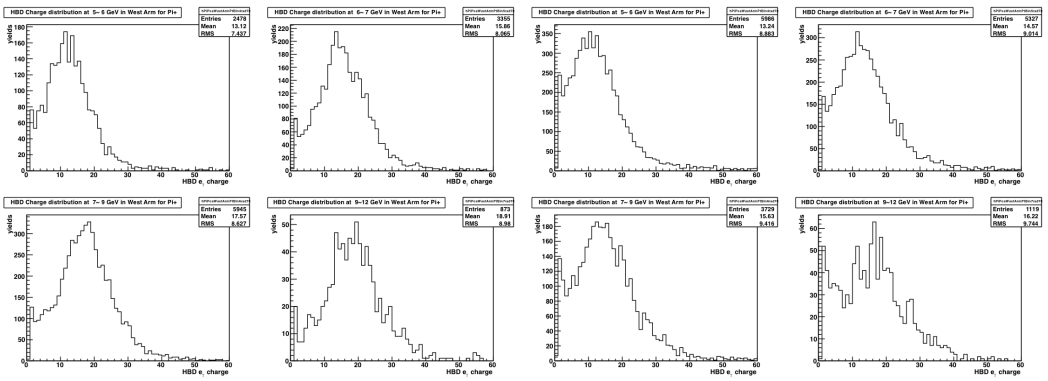

(a) Monte Carlo (b) Data

Figure 4.10: Merged Triplets Method - The HBD cluster charge distribution from Monte Carlo and data. (2009)

To summarize issues discussed so far regarding the merged triplets method, first of all, the cluster charge distribution cannot be described from first principles since the distribution changes depending on searching radius. If we were to optimize searching radius, there are competing factors that are in conflict with each other; background rejection and pion identification (clustering) efficiency. If we went in the direction of keeping high efficiencies and attempting to estimate the background level, it would fail for the following reasons. There are as many $\pi^{\pm}$ candidate clusters whose charge is the sum of

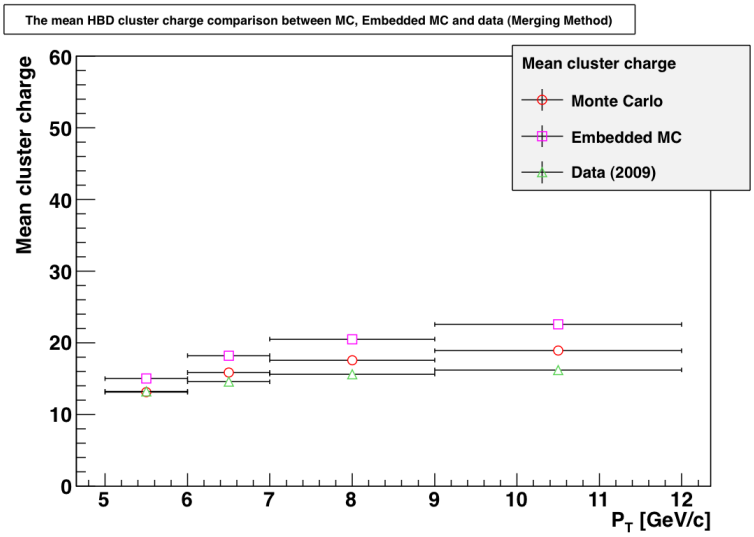

Figure 4.11: Merged Triplets Method. The comparison of the p_T dependent mean HBD cluster charge for $\pi^{\pm}$ candidates.

pure pion and background contributions as there are clusters whose charge is solely from pion contribution. And there is no way of separating them in the distribution. There is no sweet spot we could find with this method.

Maximum Triplet Method

Turning to the second clustering method that we will use for this analysis, it is called the "*maximum triplet method*". The idea is as simple as it can get; choose a triplet within the searching radius that has the highest amount of charge, and this triplet alone forms a cluster. This will resolve a lot of issues that we faced in the previous method. To begin, the HBD cluster charge distributions are shown in Fig. 4.12 with two different searching radii as was in Fig. 4.5.

The mean cluster charge, in general, is lower than it was in merged triplets method since a cluster is always made of a single triplet in this method. There are a few features that are similar to the ones obtained from previous method. It is anticipated that the searching radius dependence of PID efficiencies

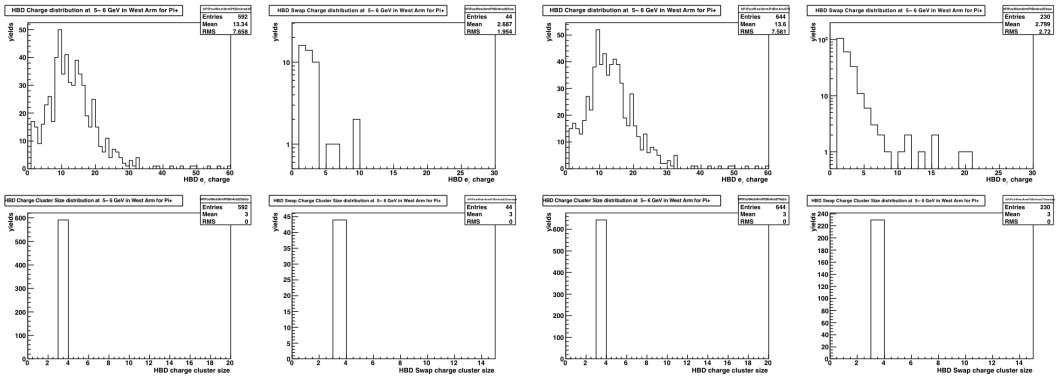

(a) π^+ in west arm with $5.0 < p_T < 6.0$ GeV/c (Left: 2.5 cm, Right: 7.0 cm)

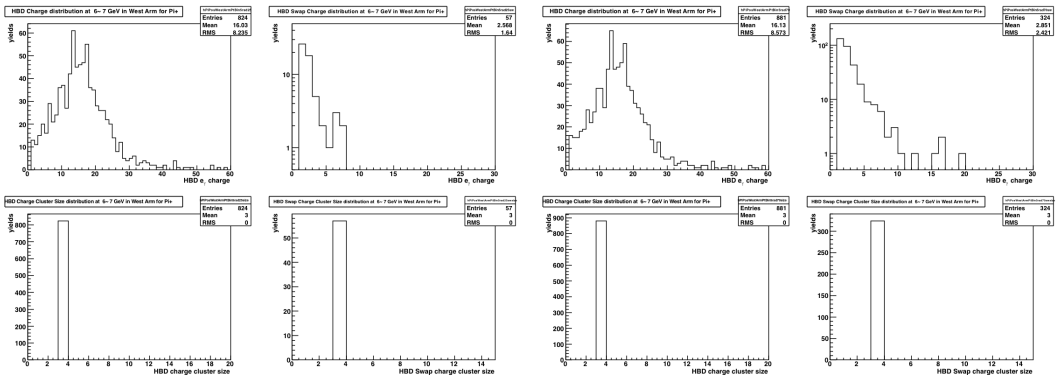

(b) π^+ in west arm with $6.0 < p_T < 7.0$ GeV/c (Left: 2.5 cm, Right: 7.0 cm)

Figure 4.12: Maximum Triplet method - continued on the next page with description.

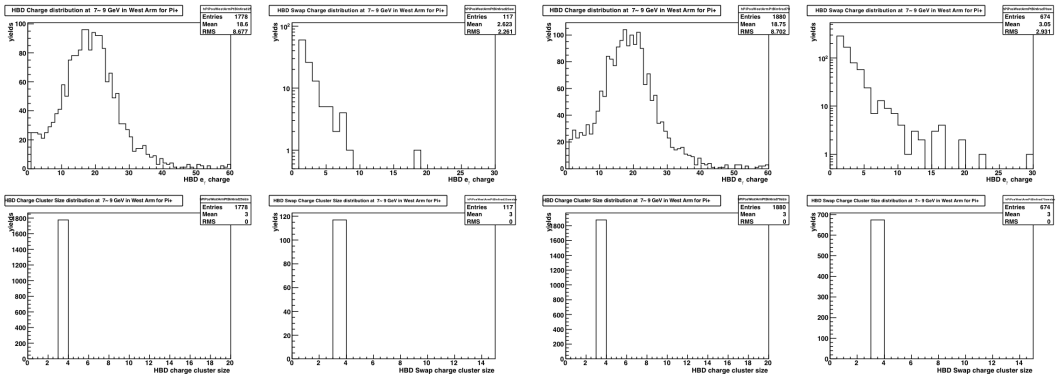

(c) π^+ in west arm with $7.0 < p_T < 9.0$ GeV/c (Left: 2.5 cm, Right: 7.0 cm)

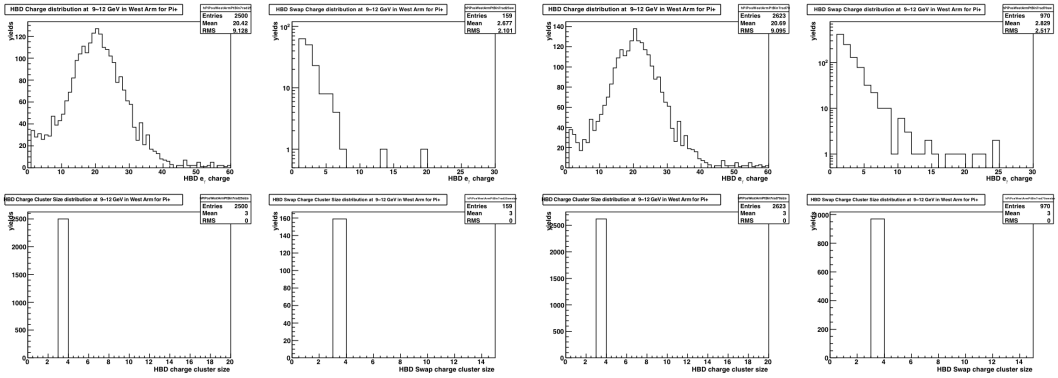

(d) π^+ in west arm with $9.0 < p_T < 12.0$ GeV/c (Left: 2.5 cm, Right: 7.0 cm)

Figure 4.12: Maximum Triplet Tethod - The comparison between the two different searching radii; R = 2.5 and 7.0 cm. Repeating in a set of 4 panels are the HBD cluster charge distribution (top left), the HBD cluster size distribution (bottom left), the HBD swap cluster charge distribution (top right) and the HBD swap cluster size distribution (bottom right).

are comparable to the ones in merged triplets method as the existence of a cluster does not rely on how we define the charge of a cluster. The clustering efficiencies from this method shown in Fig. 4.13 confirm this assertion. By the same token, how often we see a swapped cluster in a candidate cluster is not any different than it was in merged triplets method. However, one should note that the mean candidate cluster charge depends little on searching radius, allowing for the probabilistic principles to reasonably describe the charge distribution[3].

[3]See Sec. 4.5.

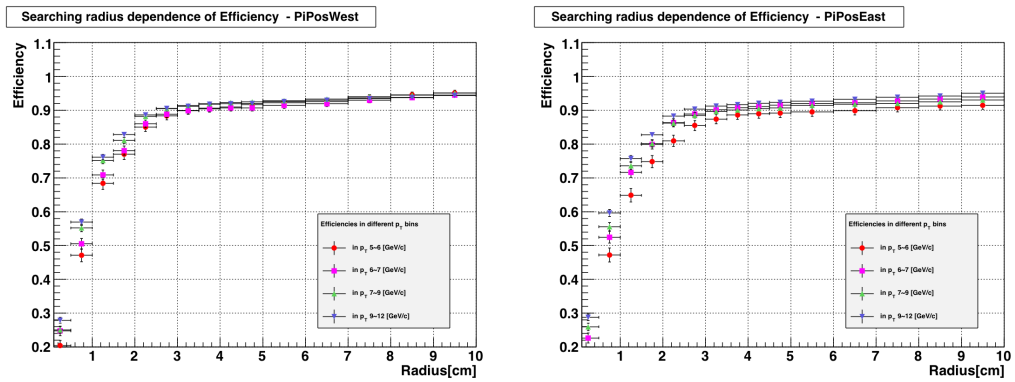

(a) π^+ in west arm (b) π^+ in east arm

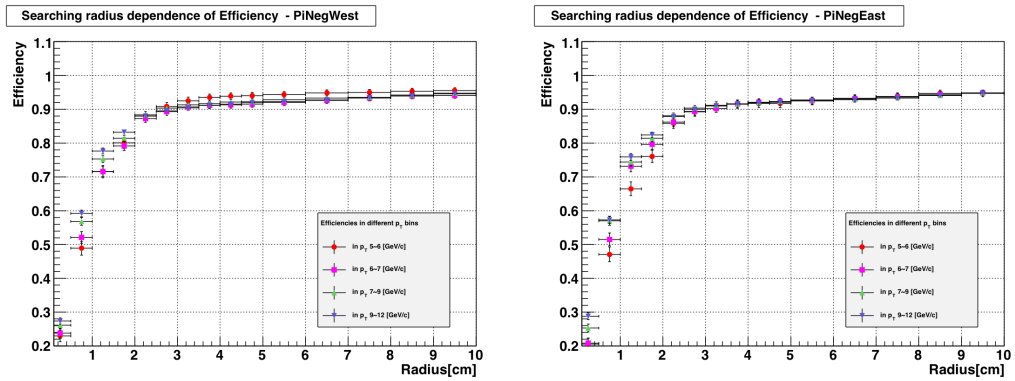

(c) π^- in west arm (d) π^- in east arm

Figure 4.13: Maximum Triplet Method - The searching radius dependence of clustering efficiency for charged pions with $5.0 < p_T < 6.0$ (red), $6.0 < p_T < 7.0$ (magenta), $7.0 < p_T < 9.0$ (green) and $9.0 < p_T < 12.0$ (blue) GeV/c.

Looking into the radial distribution of cluster density in Fig. 4.14, it is flat a distribution in swapped clusters. It indicates that background clusters are evenly distributed over the HBD acceptance. What is worth stressing at this point is that in this method, in contrast to the merged triplets method, the

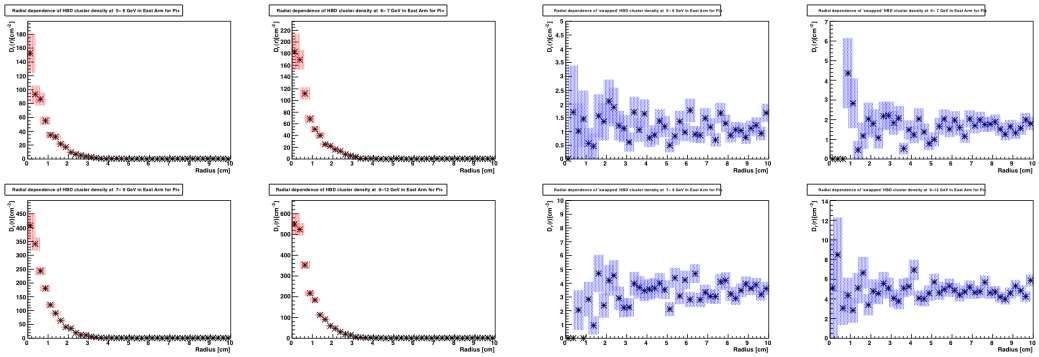

(a) π^+ clusters in west arm (Left) and associated 'swapped clusters' (Right)

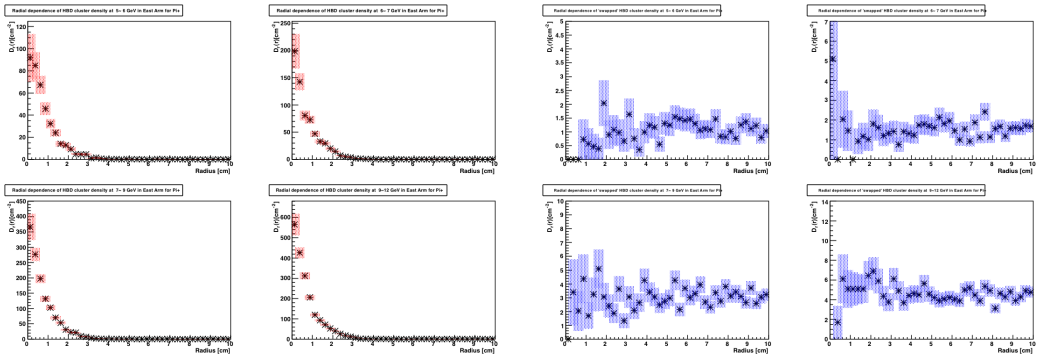

(b) π^+ clusters in east arm (Left) and associated 'swapped clusters' (Right)

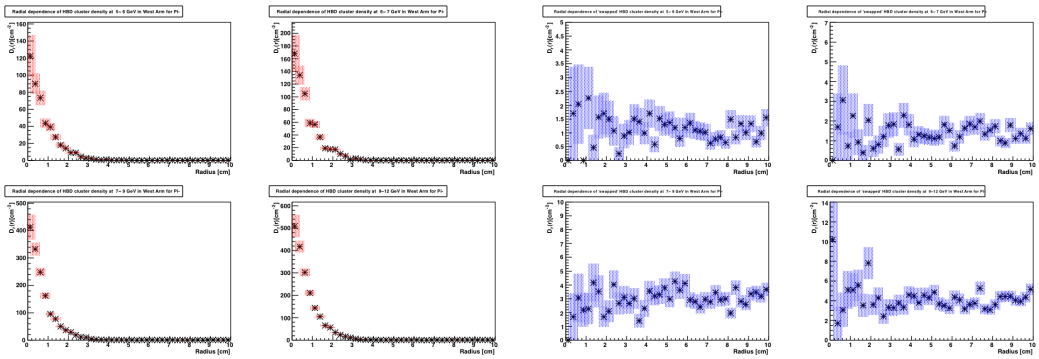

(c) π^- clusters in west arm (Left) and associated 'swapped clusters' (Right)

Figure 4.14: Maximum Triplet Method - continued on the next page with description.

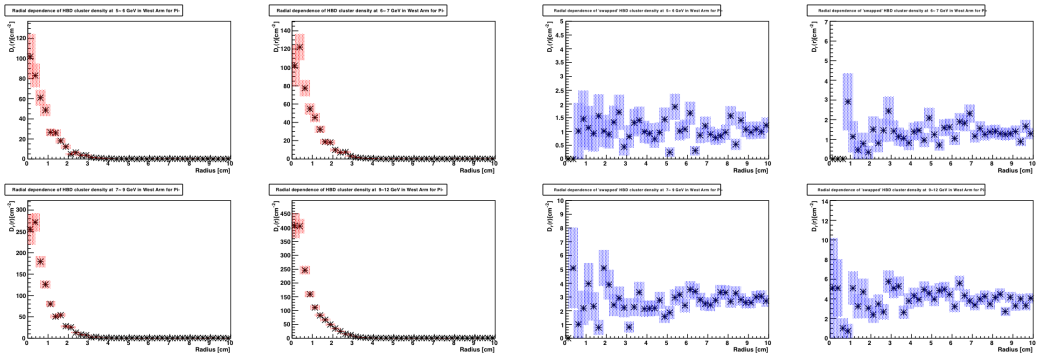

(d) π^- clusters in east arm (Left) and associated 'swapped clusters' (Right)

Figure 4.14: Maximum Triplet Method - The radial dependence of cluster densities. Repeating in a set of 2 by 2 panels are for charged pions with 5.0 $< p_T <$ 6.0 (top left), 6.0 $< p_T <$ 7.0 (top right), 7.0 $< p_T <$ 9.0 (bottom left) and 9.0 $< p_T <$ 12.0 (bottom right) GeV/c. X-axis: the radial distance from the track projection point ranging from 0 to 10 cm, Y-axis: cluster density $D_r(r)$ cm^{-2}

cluster charge is most likely from either a $\pi^{\pm}$ or a scintillation photon or (in very small fraction of time) ionization electrons from charged particles, rather than from the combination thereof.

The mean charge of background cluster barely increases with searching radius (Fig. 4.15), although the probability of background triplets ending up within the searching radius of candidate clusters does increase. Since most triplets can be spatially resolved as one can see in the example event display in Fig. 4.4, the triplets associated with $\pi^{\pm}$ candidates are distinguishable from the ones associated with background as long as the charge distribution of the two are quantitatively different.

This is actually the case as one can see in Fig. 4.16(b). There is a prominent two peak structure in the HBD cluster distribution plotted for Run 9 data. One peak at low charge is attributed mostly to scintillation photons and ionization electrons and the major peak at higher charge is from $\pi^{\pm}$ clusters. Since we have this distinctive two peak structure, removing background becomes a matter of determining the minimum cluster charge cut that allows us to maintain as high an efficiency as possible. This will involve understanding the probabilistic description of HBD charge distribution and fitting. This will be discussed in great detail in the next section.

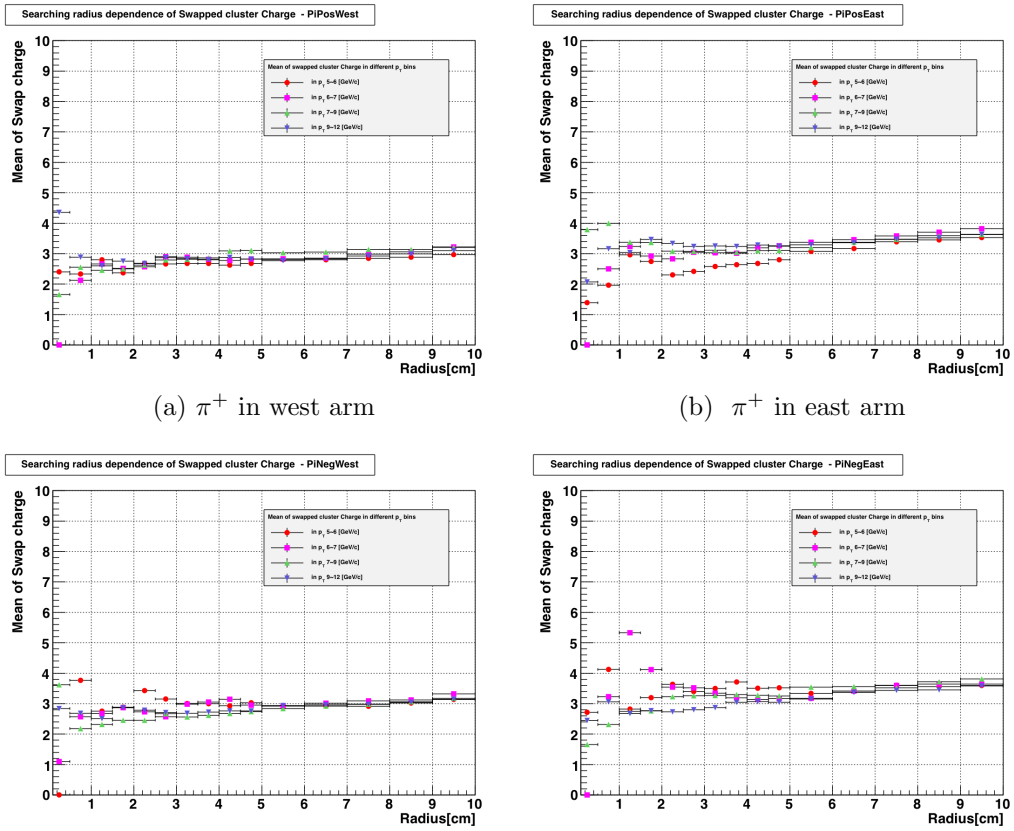

(a) π^+ in west arm

(b) π^+ in east arm

(c) π^- in west arm

(d) π^- in east arm

Figure 4.15: Maximum Triplet Method - The searching radius dependence of the mean charge of 'swapped clusters'. These swapped clusters are associated with charged pions with $5.0 < p_T < 6.0$ (red), $6.0 < p_T < 7.0$ (magenta), $7.0 < p_T < 9.0$ (green) and $9.0 < p_T < 12.0$ (blue) GeV/c.

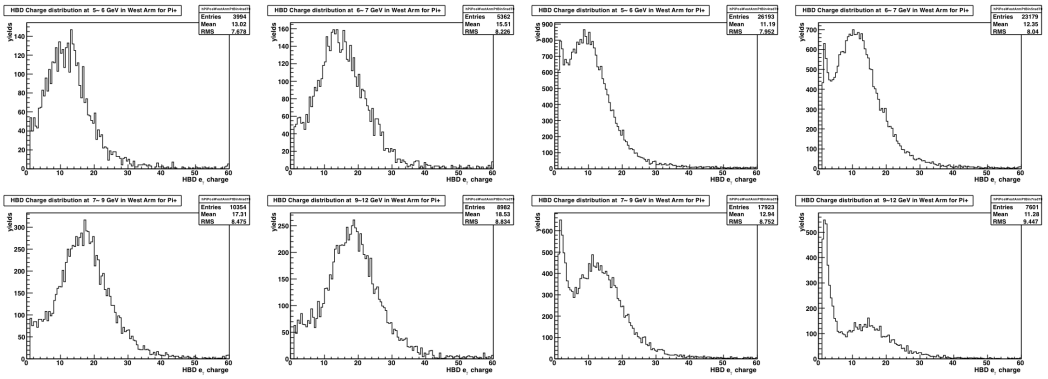

(a) Monte Carlo (b) Data

Figure 4.16: Maximum Triplet Method - The HBD cluster charge distribution from Monte Carlo and data. (2009)

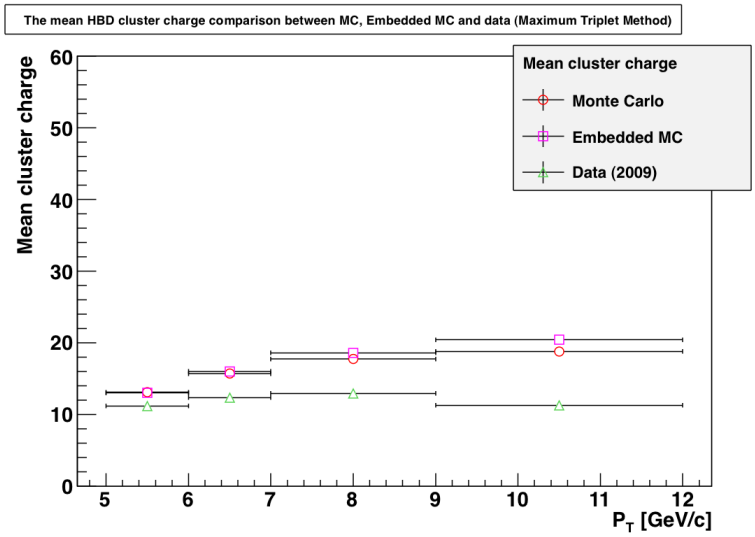

Figure 4.17: Maximum Triplet Method. The comparison of the p_T dependent mean HBD cluster charge for $\pi^{\pm}$ candidates.

Lastly, in Fig. 4.17, the mean cluster charge is compared between the three cases with the searching radius of 7.0 cm as previously used for the merged triplets method. The mean charge for embedded MC is much closer to the one for Monte Carlo, and data shows much lower mean charge than the other two cases. It indicates that the charge from background components, which were merged into the one for $\pi^{\pm}$ candidate clusters in the merged triplets method, are well separated.

4.5 HBD charge distributions : theory and data

As mentioned several times in earlier sections, the HBD cluster charge distribution will be described from first principles in this section. To begin, a theoretical model for the HBD photo-electron charge distribution that is based on probabilistic principles will be discussed. The cluster charge distribution from Run 9 data will be parametrized according to this model and the fitting results will be analyzed in detail.

As discussed previously, HBD is a Cerenkov detector and what we see as signal is originally "**Cerenkov light**", i.e., photons which at the cathode convert into photo-electrons or so called "**primary electrons**", which in turn multiplies in the Gas Electron Multiplier (GEM). What we see is at the end is the charge of these "**multiplied electrons**".

The photons or primary electrons follow simply the Poisson probability distribution given in Eq. 4.1. The argument λ in this function represents the number of photons created from Cerenkov radiation or equivalently the number of primary electrons. The other argument k corresponds to the mean or expectation value of the number of photons or primary electrons. The Poisson probability distribution is a discrete function.

$$P_{\text{Poisson}}(\lambda, k) = \frac{\lambda^k}{k!} e^{-\lambda} \tag{4.1}$$

The primary electrons go through avalanche process and multiply in the triple GEM stack. The end signal collected at the readout is known to follow

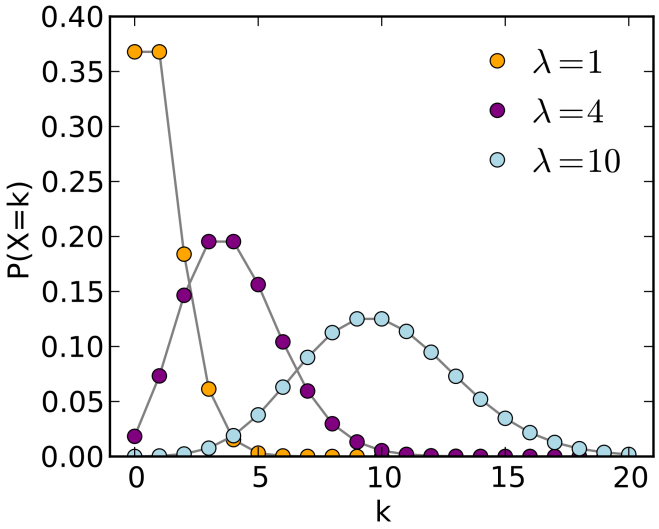

Figure 4.18: Examples of the Poisson probability distribution function with several different values of λ.

the Polya function and the distribution of the signal can be parameterized as in Eq. 4.2 where q is the number of electrons in avalanche and $\bar{q}$ is the mean number of electrons. θ is a normalization factor and is associated with the gain [53].

$$P_{\text{Polya}}(q, \bar{q}, \theta) \quad = \quad (\frac{1+\theta}{\bar{q}}) \cdot e^{-\frac{(1+\theta)q}{\bar{q}}} \tag{4.2}$$

This distribution is interesting for various reasons. One of the things that this function can be applied to is the scintillation photon signal. These photons are known to leave charges in one HBD pad, which is distinctive enough to be used for gain calibration. Gain is determined by taking the inverse slope of the ADC count distribution in log scale and dividing it by the mean number of photo-electrons per pad. In $p+p$ collisions, the mean number of photo-electrons per pad is 1, rendering the determination of gain rather straightforward. The dominant contribution to the ADC charge for scintillation lights is from a single primary electron and the distribution written in Eq. 4.3 for these electrons makes the gain calibration procedure clear.

$$P_{\text{single } e_\gamma}(q, G) \;=\; G \cdot e^{-G \cdot q} \tag{4.3}$$

What composes the background is the sum of these scintillation lights and ionization electrons created in the gas, however, the latter is largely suppressed in reverse bias mode. In swapped clusters, we see the mean of charge ∼3. It is slightly bigger than what is expected, but still is reasonable considering the fact that there are also residual components of ionization electrons on top of scintillation lights.

More importantly, the signal component from Cerenkov lights is described by a bit complicated variant of the Polya function, so called the 'folded' Polya distribution. This function takes into account all possible number of primary electrons that go through multiplication process. Combining all the cases based on the probabilistic principles, analytic form of the folded Polya probability distribution can be obtained as given by Eq. 4.5. Examples with a few different mean number of primary electrons are displayed in Fig. 4.19.

$$P_{\text{folded Polya}}(q, \lambda) \;=\; \frac{1}{N} \cdot \sum_k P_{Poisson}(\lambda, k)\ {}_{q-1}C_{k-1} \cdot e^{-q}, \tag{4.4}$$

where

λ : the mean number of primary electrons

k : the number of primary electrons

q : the calibrated HBD charge

N_λ : the normalization.$\left(\int dq\, P_{\text{folded Polya}}(q, \lambda) = 1\right)$

Now we are ready to analyze the HBD cluster distribution from data. The two components in the distribution will be parameterized with two independent functions. The Cerenkov photon part that is associated with the $\pi^\pm$ tracks can be parametrized as in the first term in Eq. 4.5. Similarly the second term in Eq. 4.5 describes the background component. Parameters [1] and [4] are scale factors and [2] and [5] are the mean number of primary electrons. [3] is introduced on account of the amount of charge lost by limiting the number of pads in a cluster to 3, and [0] is for additional gain correction.

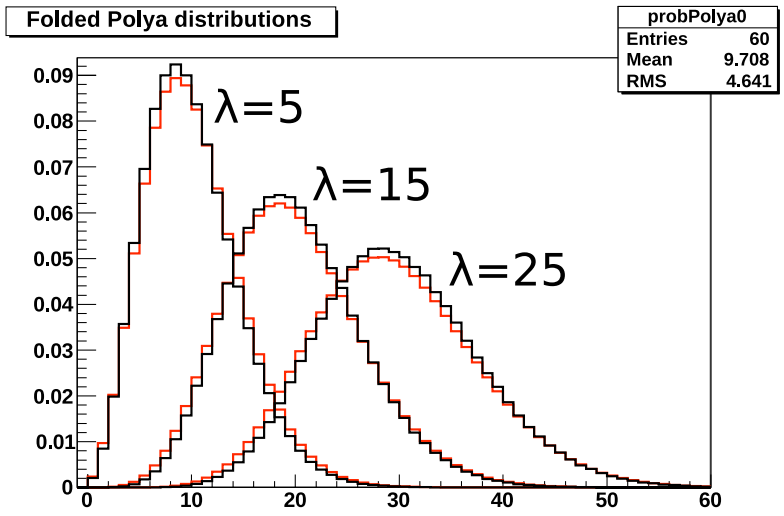

Figure 4.19: The 'folded' Polya probability distribution function. Black: random generator, Red: analytic function.

Fitting results and interpretations will be discussed in the next section.

$$
\begin{aligned}
f_{\text{cluster charge}}(q) &= f_{\text{Cerenkov}} + f_{\text{background}} \qquad (4.5)\\
&= [1]\cdot N_{[2]}\cdot P_{\text{folded Polya}}(\frac{q+[3]}{[0]},[2]) + [4]\cdot N_{[5]}\cdot P_{\text{folded Polya}}(\frac{q}{[0]},[5])
\end{aligned}
$$

4.6 Efficiencies and background estimation

In this section, we will discuss what one can learn from the fitting results of the HBD charge distribution when compared with the ones from simulation. Before presenting the final results of fitting, a couple things will be addressed.

First of all, preliminary fitting and a χ^2 test showed that the gain correction parameter[4] does not have much impact on the fit results. Secondly, the

[4]This parameter had been introduced in order to see whether the variation of gain with time is significant enough to need for second order corrections, and secondly to take into account any discrepancies between different arms.

parameters assigned for the mean number of primary electrons are integers as they correspond to the arguments in the Poisson probability distribution. For that reason, once these parameters are determined through preliminary fitting, they are going to be fixed later on for simplicity. After all, we are left with only two parameters to fit with great care. The fit results are shown in Fig. 4.20.

What should be immediately looked at is the mean number of primary electrons for 4 different p_T bins. The mean number of primary electrons fitted from data are 13, 16, 19 and 21 for 4 p_T bins in an increasing order. From the Cerenkov radiation intensity plot, one can estimate the relative number of primary electrons between different p_T bins. The estimates for 4 p_T bins, 0.00050∼0.00070, ∼0.00080, 0.00090∼0.00095 and 0.00105 are indeed consistent with the fitting results modulo proportionality constant.

Less straightforward though critical subject to discuss is the efficiencies that involve HBD. There are two kinds of efficiencies concerning HBD, first of which is the clustering efficiency of $\pi^{\pm}$ that was studied using the embedded MC tracks and briefly discussed in the previous section (See Fig. 4.13). To give a bit more detail, identical sets of PID cuts[5] except for the cuts that use HBD were used for 'embedded MC' and 'real data' in this study, putting the two on an equal footing and rendering comparisons straightforward. A clustering efficiency is defined as the ratio of yields between the tracks passing HBD matching cuts with positive cluster charge and the tracks passing only PID cuts other than the HBD related ones. This efficiency will be noted as $\epsilon^{\mathrm{HBDq>0}}$ to distinguish from the second kind and the the matching cuts will be dropped in the notation as the cuts applied here are implicit in the searching radius. It turns out that one can get a very clean sample of $\pi^{\pm}$ in the triggered data with high EMCal energy threshold, making the comparison even simpler. The efficiencies obtained from triggered data are presented in Chapter 5.1.3 and they prove to be consistent with the results shown here.

While we were only concerned about achieving the highest clustering efficiency when studying with tracks in 'embedded MC' with maximum triplet method, there is another competing factor that comes into play when studying 'real data'. The complication originates from the fact that there are misidentified $\pi^{\pm}$ tracks in 'real data' unlike in 'embedded MC' where tracks consist of 100% $\pi^{\pm}$. Misidentified $\pi^{\pm}$ tracks appear in the background

[5] $n1 > 0$, $|z_{\mathrm{vtx}}^{\mathrm{BBC}}| < 30$, track quality = 63 or 31, |zed| < 70, e/p < 0.9, $prob < 0.2$ and 3σ matching cuts for PC3 and EMCal .

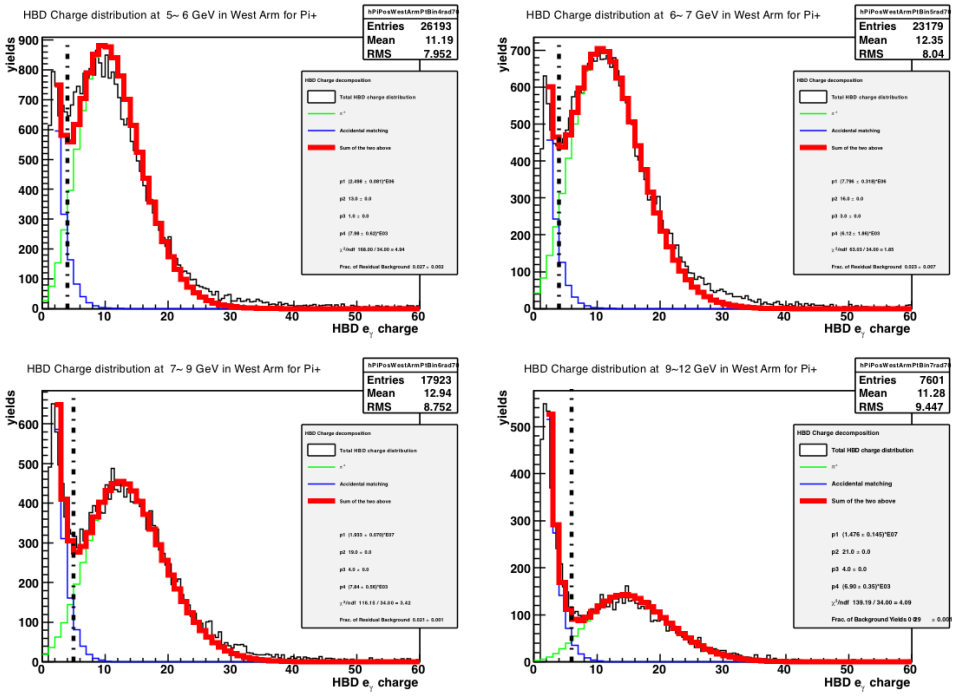

(a) π^+ in west arm

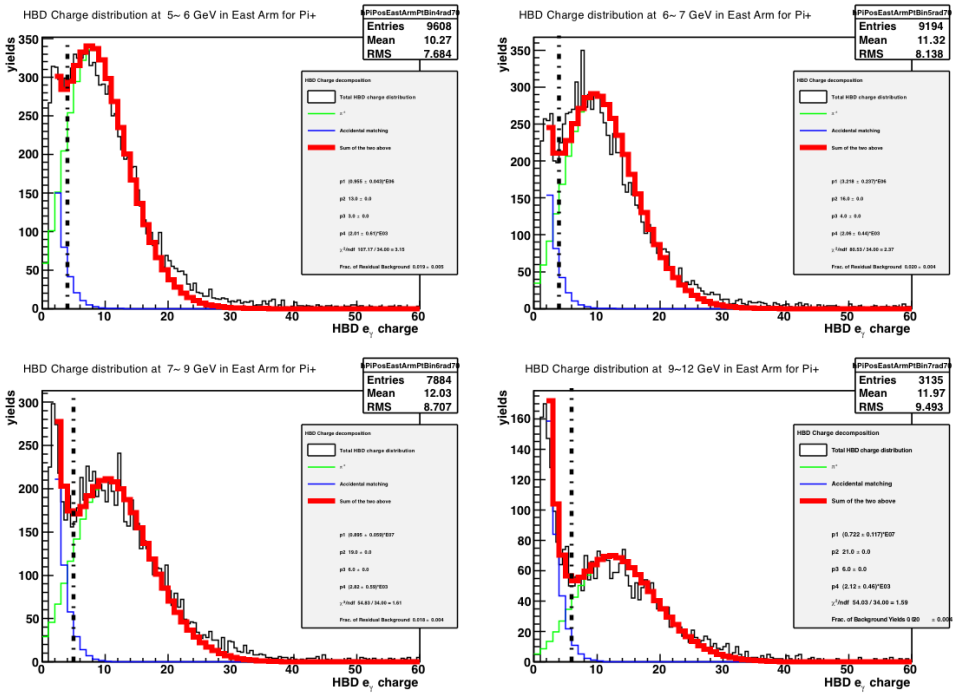

(b) π^+ in east arm

Figure 4.20: The fit results of HBD cluster charge distribution - continued on the next page with description.

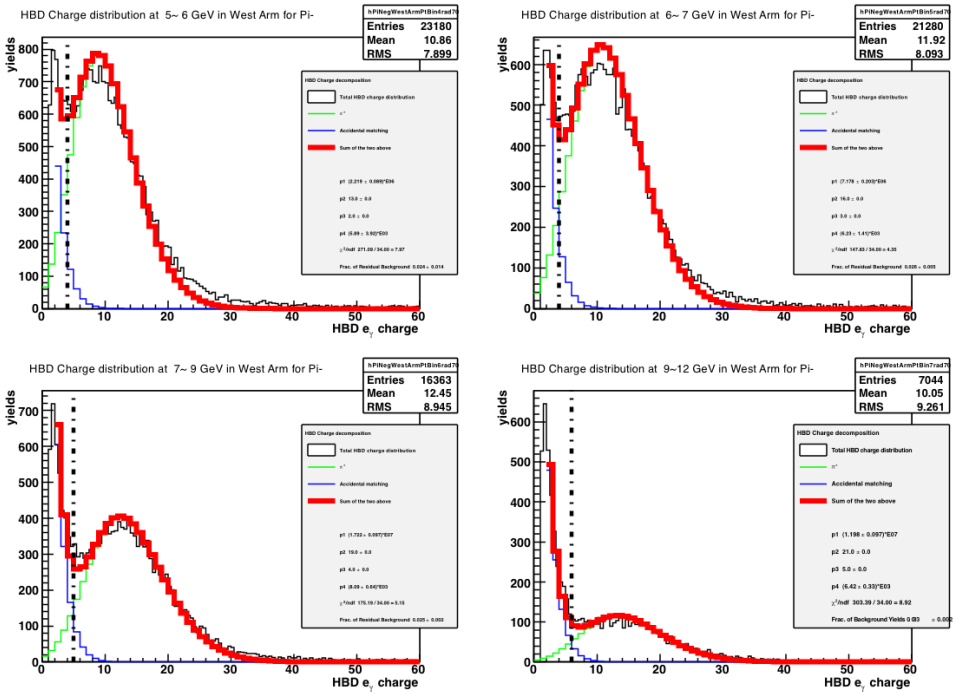

(c) π^- in west arm

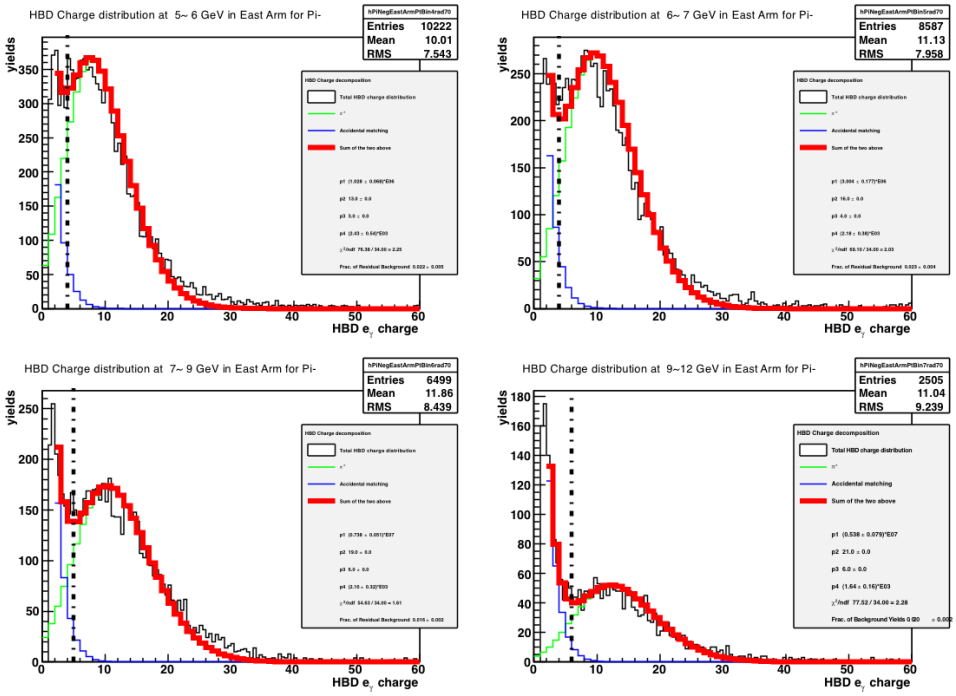

(d) π^- in east arm

Figure 4.20: The fit results of HBD cluster charge distribution. In blue (green) is the contribution from background ($\pi^{\pm}$ candidate clusters) and the sum of the two is shown in red.

cluster charge distribution, a peak at low cluster charge. In this picture, an optimal searching radius is found by taking into account not only the clustering efficiency factor but also the relative weights of background and $\pi^{\pm}$ components in the cluster charge distribution. In other words, we do not want to have too large a searching radius for high a clustering efficiency, risking too large a background component in the cluster charge distribution. When the weight of background component is too high, the two components will have a very wide overlap in the distribution. As such, the searching radius has been chosen to be 7.0 cm so that the two components in the cluster charge distribution are reasonably separable (See Fig. 4.20) while keeping high clustering efficiencies.

By choosing a searching radius, the maximum of the second efficiency has been also determined. This efficiency is called the HBD cluster charge cut efficiency, denoted by $\epsilon^{\mathrm{HBDq\,cut}}$ and defined as the ratio of yields between the tracks with cluster charge higher than the minimum charge cut and tracks with positive cluster charge. What determines this efficiency is where the minimum charge cut is set at, below which the tracks are rejected as background. The best cut is then expected to leave the least degree of residual background level while minimally compromising the $\epsilon^{\mathrm{HBDq\,cut}}$.

Best minimum charge cut varies from one p_T bin to another depending on their mean cluster charge and $\pi^{\pm}$/background . At lower p_T, the background component contribution is smaller, but the mean cluster charge is also smaller. At higher p_T, the situation is reversed. It means the minimum charge cut has to increase with p_T in order to have comparable $\epsilon^{\mathrm{HBDq\ \ cut}}$ between p_T bins.

$\epsilon^{\mathrm{HBDq\ cut}}$ for each p_T bin calculated from $\pi^{\pm}$ tracks generated with Monte Carlo is shown as a function of minimum cluster charge cut in Fig. 4.21. As in the case of $\epsilon^{\mathrm{HBDq>0}}$, we can measure $\epsilon^{\mathrm{HBDq\ cut}}$ using triggered data and the results are shown in Chapter 5.1.3. The two are mostly in good agreement within $\sim$2%. The final cluster charge cut efficiencies that are used to determine optimal charge cuts are the ones calculated from real triggered data. Final charge cuts are 4, 4, 5 and 6 for 5$\sim$6, 6$\sim$7, 7$\sim$9 and 9$\sim$12 GeV/c p_T bins, respectively, as shown in Fig. 4.20 in dashed vertical lines. Corresponding charge cut efficiencies are 0.924, 0.941, 0.927 and 0.902.

At last, residual background level with all optimized variables and cuts are shown in the legend of each graph in Fig. 4.20. These estimates are conservative upper limit for a reason that follows. The areal ratio between the charge

$>$ HBDq$_{\rm min}$ and the charge$>$0 calculated from the fit result, i.e., the Cerenkov light component of the distribution (shown in green in Fig. 4.20), is overestimated with respect to values from real data, mostly sitting above $\sim$ 0.95. This means that there are more $\pi^{\pm}$ clusters below the HBD cluster charge cut than what fit results say. This minor ambiguity is a genuine artifact of the clustering algorithm where we pick the highest firing triplets. And this does not introduce complications in any way other than overestimating background level since we can measure the correct efficiency from real data. The overall background level is < 0.03 in the entire p_T range.

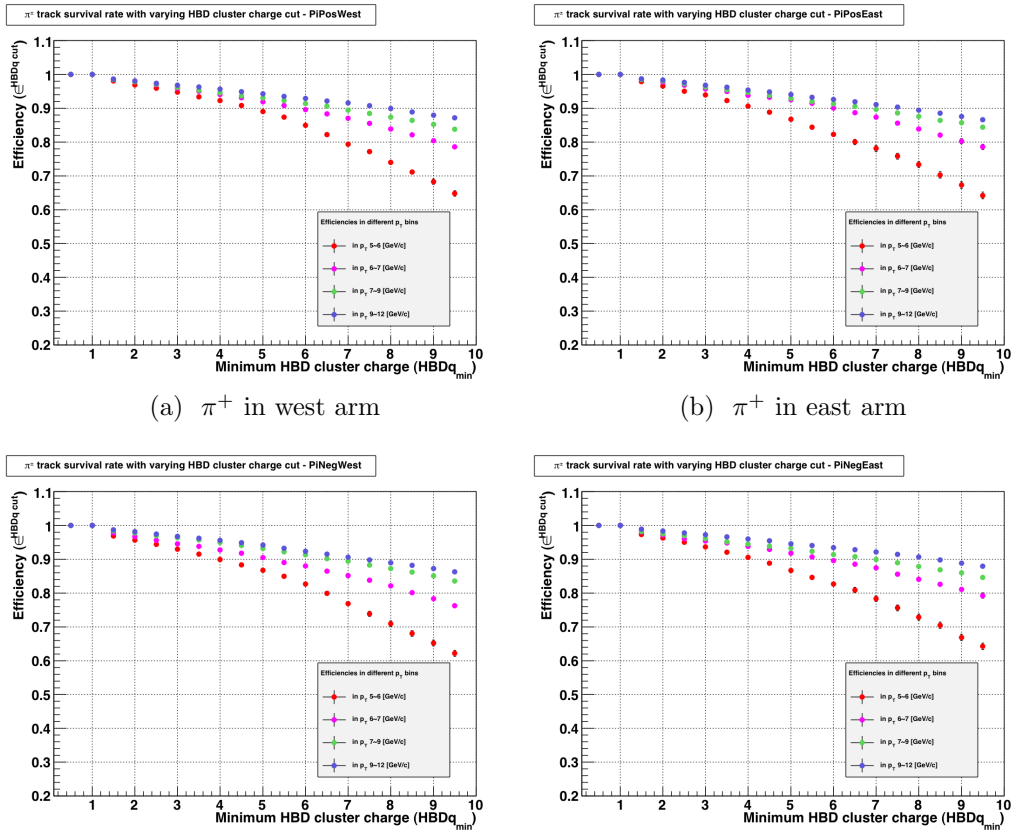

(a) π^+ in west arm (b) π^+ in east arm

(c) π^- in west arm (d) π^- in east arm

Figure 4.21: The $\pi^{\pm}$ survival rate as a function of minimum cluster charge cut. Calculated from MC simulated tracks.

Chapter 5

Measurement of Differential Cross sections

5.1 Correction Factors for Cross Section Measurements

In order to measure the cross section, there is a list of ingredients that need to be prepared. To begin, we need the number of $\pi^{\pm}$ events reconstructed from the good quality runs, denoted as $N^{\pi^{\pm}}$. In addition, a number of correction factors will need to be taken into account. This is the main subject of this section.

The correction factors can be broken into 4 groups by and large. First of all, the luminosity seen at PHENIX is only a fraction of machine luminosity which is delivered by CAD. This fraction is referred to as 'BBC efficiency' as BBC is the absolute luminosity counter at PHENIX. And the BBC efficiency (ϵ_{BBC}) has to be determined via vernier scan. Next, detectors are normally biased because they only cover a certain kinematic range and tend to 'see' more events of one type than others. Since this analysis cares about charged pions that triggered BBC and ERT 4x4c, corresponding trigger bias or efficiencies ($\epsilon_{\mathrm{bias}}^{\mathrm{trigger}}$) will be measured and incorporated into the cross section. These two correction factors are for calibrating the number of events seen, whereas the next one cares about the probability of tracks in these events being successfully reconstructed. The track-by-track reconstruction efficiencies (ϵ_{reco}) for all detectors used are going to be discussed in later sections. At last, geometrical acceptance correction take care of the detector acceptance and dead area in the detectors. Eq. 5.1 summarize all the correction factors needed.

$$E\frac{d^3\sigma}{dp^3} \approx \frac{N^{\pi^\pm}/(\hat{L}/\epsilon_{\rm BBC})}{p_T\Delta p_T \cdot \epsilon_{\rm bias}^{\rm trigger}\epsilon_{\rm reco}\cdot(2\pi\Delta\eta\epsilon_{\rm geo})} \tag{5.1}$$

5.1.1 The BBC Efficiency

As mentioned earlier, the BBC efficiency calibrates the luminosity at PHENIX and it is done by vernier scan analysis. The subject is fully discussed and documented, for example, in Ref. [54].

To get an idea of how vernier scan analysis is done, remember that there are two kinds of luminosity often referred to; machine luminosity and effective luminosity. The machine luminosity is expressed in the following form.

$$L_{\rm machine} \equiv \sum_{i=\text{bunch crossing}}^{n} [\frac{N^i_{\rm blue}\cdot N^i_{\rm yellow}\cdot f}{A}],$$

where $A = 2\pi\,\sigma_x\sigma_y$.

The numerator in the square bracket is proportional to the intensity of beam particles generated and it is measured using data recorded in the DC Current Transformer (DCCT) or the Wall Current Monitor (WCM). The number of particles in each bunch is not measured independently, instead the average number of particles per bunch across all the bunches in each ring is measured. That is, what is measured is $n\cdot < N_A >< N_B >$. The beam revolution frequency is measured to be 87 kH.

To determine the transverse dimensions of the diamond-shaped collision cross section, the Beam Position Monitor (BPM) is used to scan the horizontal and vertical dimensions and measure the widths of the beam overlap, σ_x and σ_y.

The effective luminosity that takes into account the z vertex range of BBC is then used along with the maximum rate $R_{\rm max}$ to define the BBC cross section as shown in Eq. 5.2.

$$\sigma_{\rm BBC} = \frac{R_{\rm max}}{L_{\rm effective}}, \qquad L_{\rm effective} \equiv L_{\rm machine}\cdot\epsilon_{\rm zvtx} \tag{5.2}$$

The result of the BBC cross section measurements for $\sqrt{s} = 200$ GeV at PHENIX is 23.0 mb ($\pm$9.7%). Finally, the BBC efficiency is determined by comparing the BBC cross section at PHENIX to the world data 42.2 mb.

5.1.2 The BBC Bias and ERT Bias (Efficiency)

BBC bias

BBC bias accounts for the bias in luminosity created from requiring an event be triggered by BBC, which sits in the very forward region. Events with ERT-triggered charged pions with high p_T, which are also part of jets, occur as a result of hard scattering of constituent partons in the protons, and most particles created from this hard interaction end up in the central arm region at mid rapidity. When this happens, fragments from the broken up protons will also go into BBC and trigger them. There are, however, other types of events in these ERT-triggered events such as the ones from elastic or diffractive scattering that do not trigger BBC. In other words, BBC can be blind-sighted with regards to these events. A cartoon in Fig. 5.1 illustrates what it exactly corrects for. The ratio between the fourth and third bars corresponds to the BBC bias. In short, the BBC bias scales back the luminosity that was overestimated by the BBC efficiency correction due to its blindness to certain types of events.

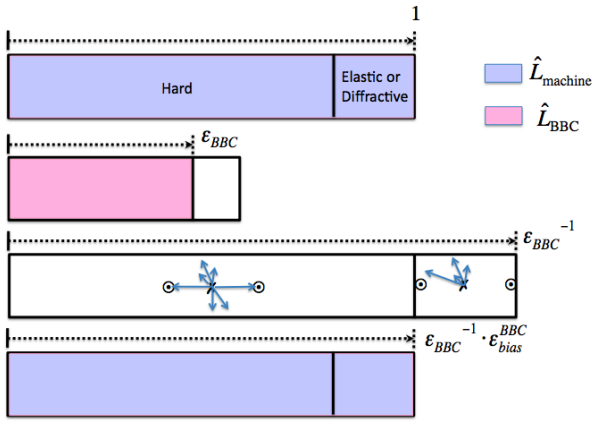

Figure 5.1: The illustration of concept of the BBC bias correction; The two dots in the box represent the BBC detectors and the arrows indicate particles created from the collision.

The BBC bias has been measured to be 0.795±0.02 at the beam energy of 200 GeV via neutral pions seen in the central arm. This measurement can be also done with charged pions at high p_T. What matters in measuring the BBC bias of interested events is that one should have a clean sample of particles that originate from hard scattering regardless of what particle species they are. Also, the ERT-triggered data, which is used for this measurement, have

to contain events triggered solely by ERT (without BBC) as well as the ones by ERT in coincidence with BBC.

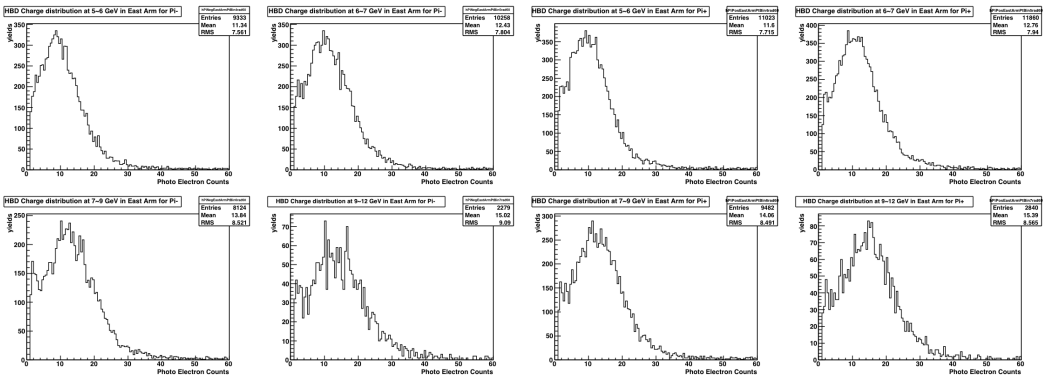

(a) Negative charge (b) Positive charge

Figure 5.2: The HBD charge distribution of $\pi^{\pm}$ with ERT 4x4a trigger without the requirement of BBC trigger.

The challenge is to get a pure sample of charged pions without using BBC trigger information. Fortunately, there is a trigger setting that meets all these conditions - ERT4x4a. Fig. 5.2 assures us that this data will allow us to have clean charged pion sample without BBC. With some extra caution with the PC3 detector so as to avoid requiring a BBC trigger unintentionally, the BBC bias for high p_T charged pions is measured to be 0.80±0.02.

ERT bias (efficiency)

The ERT bias is a bias in the sense that it is a correction factor for the number of events as opposed to the particle yields. It is also an efficiency in the sense that it does not so much care about the physical bias that could be introduced by kinematics or hardness/softness of the process as it does about how efficient the trigger is. In other words, the reason for failure in seeing a high p_T $\pi^{\pm}$ event in EMCal is the inefficiency of the ERT trigger. Comparing it with other bias, say with the BBC bias, the events that EMCal saw and BBC did not 'ARE' our concern, whereas the events that BBC saw and did not have any particle created in the EMCal acceptance are 'NOT' when considering the ERT efficiency.

Measuring the ERT trigger efficiency for high p_T charged pions had been unsuccessful at PHENIX. The main reason is because of the lack of

estimation/control over the background. The HBD detecor placed directly outside the beam pipe in 2009 allowed, for the first time, us to control the background at sub percent level and to measure the ERT bias directly from data.

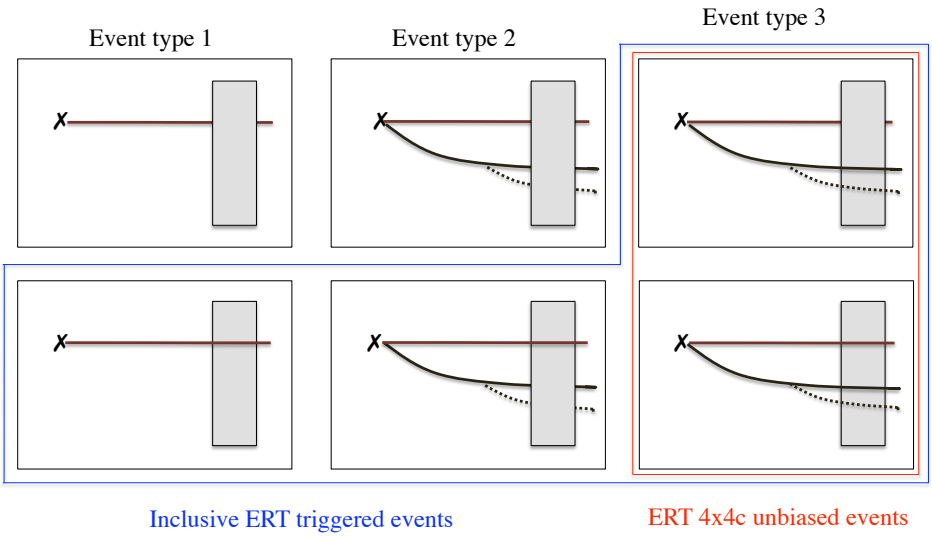

Figure 5.3: The event structure of minimum bias events. In each box, the upper solid line represents identified $\pi^{\pm}$ by HBD. A hidden (fully shown) line beneath (on top of) a gray rectangle indicates the failure (success) of triggering ERT 4x4c. The lines in the lower branch represent either $\pi^{\pm}$ identified by HBD (solid lines) or any EMCal clusters (dashed lines). This lower blob accounts for all possible combinations of positive number of lines rather than just two lines. Charged pions not shown in either type of lines are created out of the detector acceptance or with energy deposit below the threshold.

Normally, ERT trigger efficiency is measured from minimum bias data that only require an event be triggered by the BBC trigger. At high p_T, which this analysis is interested in, there is not enough statistics to be able to analyze the trigger efficiency. For this reason, we apply a method that enables us to collect an unbiased (against ERT 4x4c) $\pi^{\pm}$ sample out of biased (ERT4x4c) data.

The key to this method is to comprehend the event structure. As shown in Fig. 5.3, there are 3 types of events with different kinematic structure in minimum bias data. Each column represents one event type. The separation in rows indicates if a charged pion fired the ERT trigger. See the caption

for detailed description of the symbols. While, in principle, we can look into any pair of event types in a single column, only one column (boxed in red) is a viable option for the ERT efficiency study. So let us focus on the last column. An event that fits the description of the upper panel in Fig. 5.4 will be called an "HBD-type" event and the lower panel an "(HBD+ERT)-type" event. The naming is based on the $\pi^{\pm}$ identification method indicated in solid lines in upper part of each box. These identified pions will be called "primary $\pi^{\pm}$'s". As explained above, $\pi^{\pm}$'s in these events are unbiased against 4x4c. Also, "associated tracks (clusters)" are represented in a solid or dashed line in the lower part of a rectangle. The efficiency is then be defined as $\frac{N^{\pi^{\pm}}_{\text{HBD-type}}}{N^{\pi^{\pm}}_{\text{HBD-type}} + N^{\pi^{\pm}}_{\text{(HBD+ERT)-type}}}$, where $N^{\pi^{\pm}}_{\text{HBD-type}}$ ($N^{\pi^{\pm}}_{\text{(HBD+ERT)-type}}$) is the number of events of HBD-type ((HBD+ERT)-type).

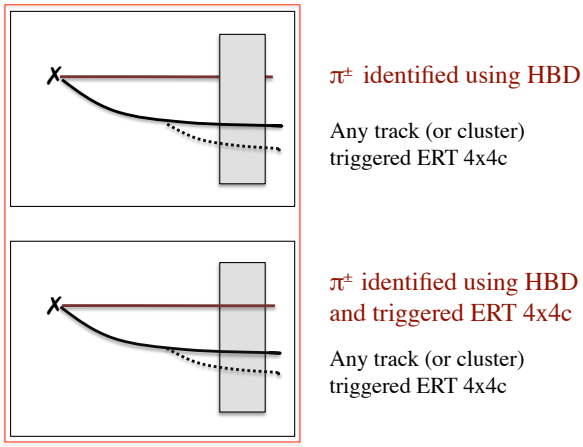

Figure 5.4: Two types in 'ERT 4x4c unbiased' $\pi^{\pm}$ events.

Now that we know how to measure the trigger efficiency, let us look into those two types of events in real data. All events have to meet the requirement that the primary and associated particles be separated enough so that there is no correlation between them. The reason being, there could be a so-called 'ringing effect' where a cluster that did not trigger ERT 4x4c appears to have triggered as it was in tight neighborhood of a cluster that actually triggered ERT 4x4c. When this happens, two clusters will appear to be coming from overlapping towers. Then one cannot tell which one of the two clusters actually triggered ERT 4x4c, and this event cannot be classified into any type of events due to this ambiguity. While the chances of a pion sharing a super module with other particles are not so high due to the low multiplicity environment in $p+p$ collision, this type of event legitimately fits

into the (HBD+ERT)-type when there is no separation requirement.

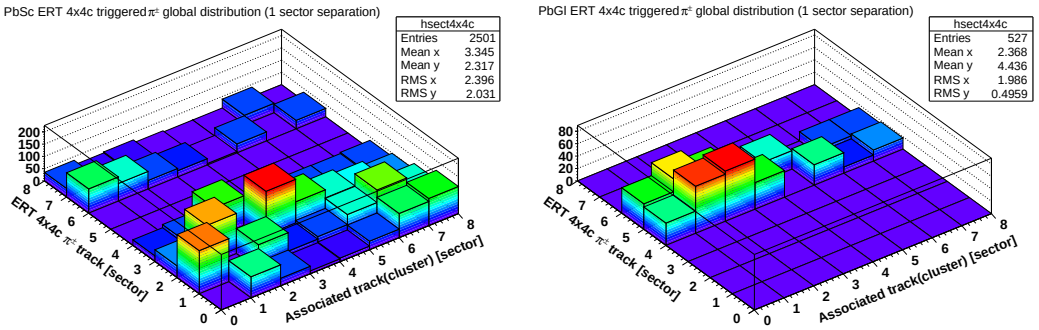

(a) PbSc with $\geq$ 1 SM separation between primary and associated particles

(b) PbGl with $\geq$ 1 SM separation between primary and associated particles

Figure 5.5: The global distribution of primary $\pi^{\pm}$ and associated tracks (clusters)

Having that in mind, it is worthwhile to map out the location of primary and associated particles and see how they are globally distributed. The location coordinates of each event is represented by a pair of the EMCal sector numbers of primary and associated particles, i.e., (p,a), where p is the sector on which a primary $\pi^{\pm}$ triggered ERT 4x4c or have a track projection depending on the event type. Requiring $\geq$ 1 SM separation, the distribution shows as in Fig. 5.5. Most events sit on either of the two diagonal lines depending on whether the primary and associated particles are in the same jet or in the opposite side of back-to-back jets. Note that the PbSC and PbGl detectors are treated independently. With further separation requirement, one will see additional empty lines adjacent to the diagonal lines mentioned above.

In the next step, one can plot the EMCal energy (emce) spectra for $\pi^{\pm}$ in the (HBD+ERT)-type events as well as for inclusive events[1]. Fig. 5.6 shows the emce spectra for $\geq$ 1 sector separation, $\geq$ 2 sector separation and the opposite arm cases. A peak is shown in the inclusive $\pi^{\pm}$ spectra at 0.3 GeV with which missing ionization particles (MIPs) are supposed to mostly deposit energy in PbSc.

[1]i.e., the union of the HBD-type and (HBD+ERT)-type events

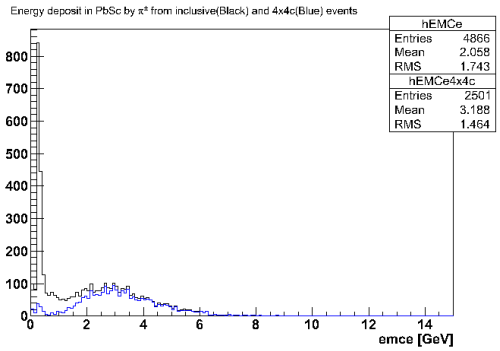

(a) $\geq$1 sector separation between primary and associated particles

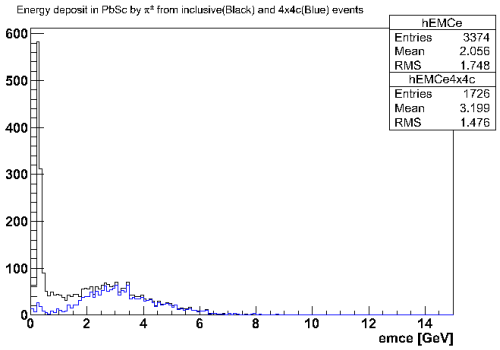

(b) $\geq$2 sector separation between primary and associated particles

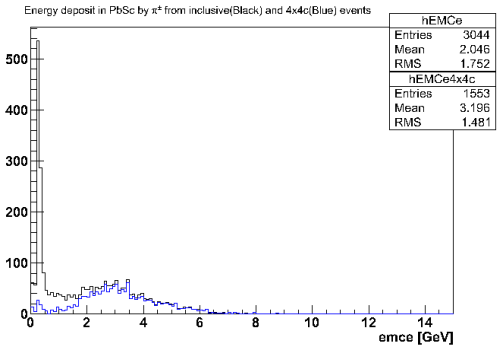

(c) primary and associated particles in opposite arms

Figure 5.6: The emce spectra for 4x4c and inclusive $\pi^{\pm}$ with various separation requirements in PbSc.

Using the emce spectra of $\pi^{\pm}$ in 4x4c and inclusive events, one can calculate the trigger efficiency at a given emce by taking a ratio between the number of 4x4c and inclusive events. Results are shown in Fig. 5.7 for three different separation conditions. Each trigger efficiency turn-on curve is fit to a Fermi function with 3 parameters associated with the threshold, the saturated efficiency and the turn-on slope. There is no indication of inconsistency between the different levels of separation requirement.

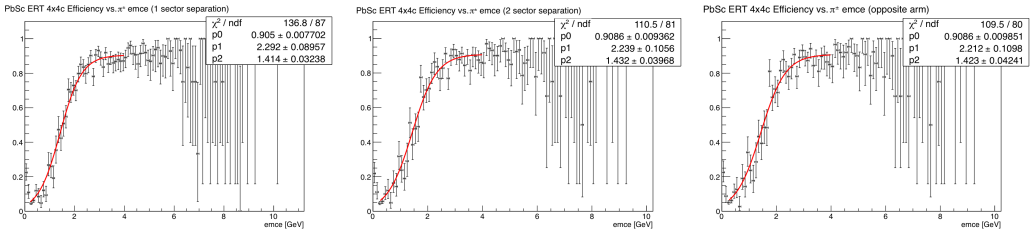

(a) ≥1 sector separation (b) ≥2 sector separation (c) oppsite arm

Figure 5.7: The trigger efficiencies for 4x4c $\pi^{\pm}$ in the p_T range of 5∼12 GeV/c with various separation requirements in PbSc.

The same procedure is done for PbGl. (Fig. 5.8) The effective threshold appears higher than the one for PbSc. One can also see that the random benefit effect is common for both PbSc and PbGl. The systematic effect study regarding this issue will be presented in a later section where various systematic uncertainty sources are examined. The overall trigger efficiency for $\pi^{\pm}$ in the p_T range of 5∼12 GeV/c is ∼29%, much lower than ∼51% for PbSc. The low ERT efficiency and the smaller acceptance explain why we see much smaller statistics in PbGl in comparison with PbSc, and we will only consider PbSc from here on.

Note that so far we have dealt with $\pi^{\pm}$'s in the p_T range of 5∼12 GeV/c altogether. The reason for that is because there is no one-to-one correspondence between the p_T and the emce of $\pi^{\pm}$'s[2]. For this analysis of cross section measurements, the efficiency at each p_T bin is calculated independently, not at a localized emce range but over the entire range of emce. Fig. 5.9 shows the p_T dependence of the normalized emce spectra for $\pi^{\pm}$'s inclusive events as well as (HBD+ERT)-type events.

[2]Charged pions do not deposit their entire energy through hadronic shower in the detector. This is in contrast to other particles such as photons and electrons, which shower and deposit almost all their energy in the detector.

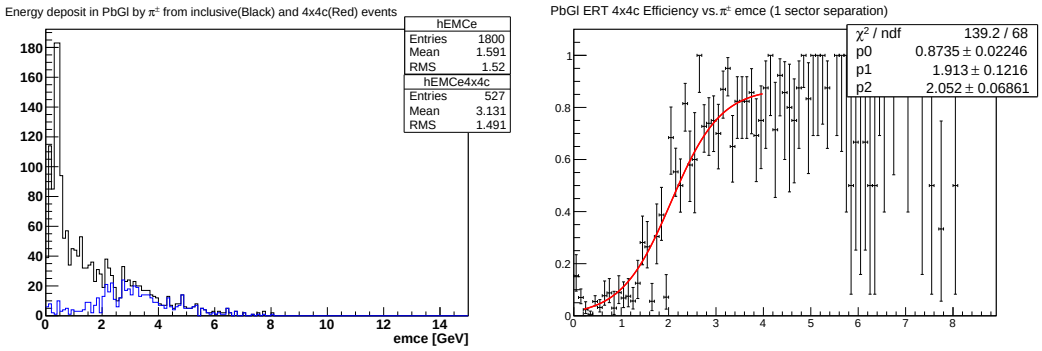

(a) $\geq$1 sector separation between primary and associated particles

(b) same separation as in emce spectra

Figure 5.8: The emce spectra and trigger efficiencies for 4x4c and inclusive $\pi^{\pm}$ in the p_T range of 5$\sim$12 GeV/c in PbGl.

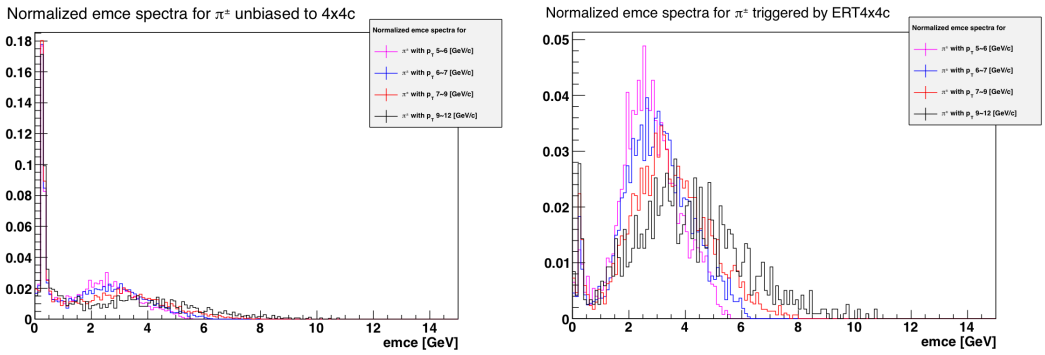

(a) Inclusive $\pi^{\pm}$

(b) 4x4c triggered $\pi^{\pm}$

Figure 5.9: The normalized emce spectra for four different p_T bins in PbSc.

Comparing the two spectra plots in Fig. 5.9, the difference in spectral shape of inclusive $\pi^{\pm}$ obviously resulted from the different emce spectra of triggered $\pi^{\pm}$. The higher the p_T of $\pi^{\pm}$, the higher the mean of the emce and the broader the spectra is. Despite the striking difference in the spectral shape, the ERT efficiency does not vary much with p_T when the emce threshold is very low less than 0.3 GeV. See Fig. 5.10.

The final trigger efficiency used in this analysis will be shown when the final emce threshold is determined in Sec. 5.2.

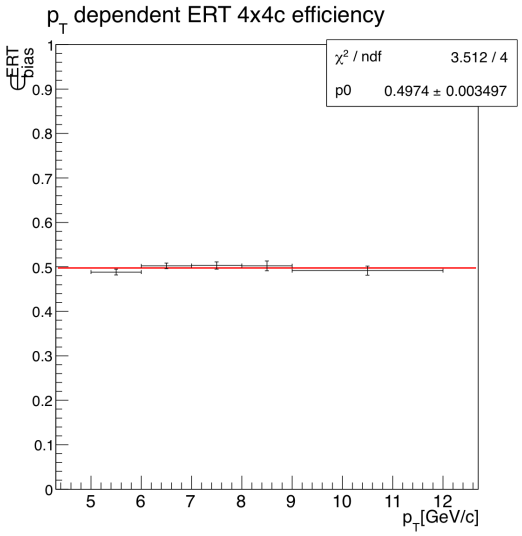

Figure 5.10: The p_T dependence of ERT 4x4c trigger efficiency when the emce threshold is set at 0.2 GeV in PbSc.

5.1.3 The Track Reconstruction Efficiencies and the Geometrical Acceptance Correction

Conventionally at PHENIX, track reconstruction efficiencies and geometrical acceptance corrections are estimated by using Monte Carlo simulation. In this analysis, we will try to get minimal assistance possible from simulation studies for reasons that follow. At first, incorporating time dependence of reconstruction efficiencies into the simulation is tricky because there is normally one or two representative runs that analyzers can use for each detector. Although that representative run is chosen and the dead area map is constructed with great care, there is limitation in reflecting all minor details of reality into simulations - it is not 'measurements' from 'data'.

The fact that this analysis is concerned only about single tracks as opposed to paired tracks and that we have strong control over the background led the author to come up with a scheme that works in this analysis. The basic idea is to factorize the geometrical acceptance correction ($\epsilon_{\rm geo}$) and the track reconstruction efficiencies ($\epsilon_{\rm reco}$). The former has a spatial component and the latter has a temporal component. And the idea comes from the realization that the two components are independent.

In this scheme, each correction factor is calculated based on certain as-

sumptions. Assume a perfect ϵ_{reco} in order to calculate the ϵ_{geo}. And detector efficiencies are assumed to be not time-correlated when calculating ϵ_{reco}. Starting with considerations of an ideal case will help understand how to go about calculating the ϵ_{geo} and ϵ_{reco}.

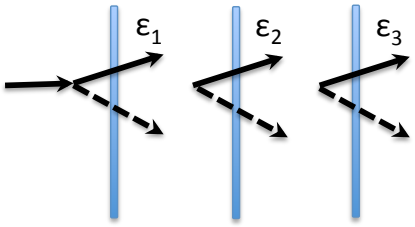

(a) 3 ideal detectors with efficiencies ϵ_1, ϵ_2 and ϵ_3; Tracks pass through detectors from left to right. A solid line indicates a hit recorded on a detector and a dashed line no hit.

0	0	0	$(1\text{-}\epsilon_1)$	$(1\text{-}\epsilon_2)$	$(1\text{-}\epsilon_3)$	=	C_{000}
0	0	1	$(1\text{-}\epsilon_1)$	$(1\text{-}\epsilon_2)$	ϵ_3	=	C_{001}
0	1	0	$(1\text{-}\epsilon_1)$	ϵ_2	$(1\text{-}\epsilon_3)$	=	C_{010}
1	0	0	ϵ_1	$(1\text{-}\epsilon_2)$	$(1\text{-}\epsilon_3)$	=	C_{100}
0	1	1	$(1\text{-}\epsilon_1)$	ϵ_2	ϵ_3	=	C_{011}
1	0	1	ϵ_1	$(1\text{-}\epsilon_2)$	ϵ_3	=	C_{101}
1	1	0	ϵ_1	ϵ_2	$(1\text{-}\epsilon_3)$	=	C_{110}
1	1	1	ϵ_1	ϵ_2	ϵ_3	=	C_{110}

(b) 8 cases and their probability of happening; On left, 1 indicates a hit on detector and 0 no hit. Columns correspond to detector 1, 2 and 3 from left to right. On right, each row shows the probability of corresponding case.

Figure 5.11: An ideal case of 3 detectors and their probabilistic behavior.

Imagine 3 detectors that are immaculate on the entire area and that perform in conformity with probabilistic principles. Fig. 5.11(a) depicts what happens when charged tracks go through detectors. On each detector, only a fraction of tracks will leave hits and the rest will pass through undetected. All detectors work independently of one another so they do not know what happened in other detectors. In other words, the conditional probability of, say, detector 2 having a hit on the condition that detector 1 has a hit is simply the probability of detector 2 having a hit by itself; $P(2|1) = \frac{P(2\cap 1)}{P(1)} = \frac{P(2)\cdot P(1)}{P(1)} = P(2)$. Therefore, the probability of any one of 8 cases occurring is computed by taking a simple product of all the independent probabilities corresponding to the case.

The efficiencies ϵ_1, ϵ_2 and ϵ_3 that are being discussed here are true efficiencies which are assumed to be unknown. In this case, there is a way to estimate the efficiencies from a set of tracks that left at least one hit on any one of 3 detectors. Each row in Fig. 5.12(a) shows the hit information on an individual track in an example sample of real data. Boxed in green are the tracks that recorded a hit in at least one of the detectors. There are a total of n tracks. A subset of t tracks boxed in red are the ones that left a hit in all detectors and successfully reconstructed. The variable that is proposed to estimate the

true efficiency of a detector is defined by the ratio of the number of tracks that are fully reconstructed and the ones that left a hit in all detectors other than the one of interest. As shown in Fig. 5.12(b), it indeed is a good estimator for the true efficiency of a detector. One should note that the overall efficiency in the estimator is based on the frequentist probability so it works best when the efficiency is reasonably far from 100% or 0%, which is the case in this analysis.

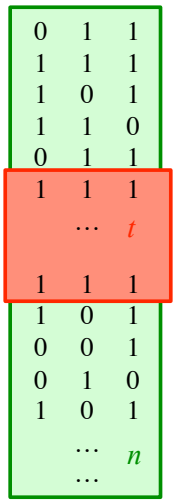

$$\frac{1}{e_1} = \frac{t + n \cdot C_{011}}{t}$$

$$= 1 + \frac{n}{t} \cdot C_{011}$$

$$= 1 + C_{111}^{-1} \cdot C_{011}$$

$$= 1 + \frac{1 - < \varepsilon_1 >}{< \varepsilon_1 >} = \frac{1}{< \varepsilon_1 >}$$

(a) An example of tracks recorded in real data. See the text for details.

(b) True efficiency and its estimator

Figure 5.12: An ideal case of 3 detectors and their probabilistic behavior

Taking an explicit example of how the numbers work, let us think of 3 detectors with known efficiencies of 98%, 97% and 95% for ϵ_1, ϵ_2 and ϵ_3, respectively. Then 10000 tracks are thrown into the detectors. According to the definition of the efficiency estimator, say for detector 3, one will be measuring e_3 shown in Eq. 5.3.

$$\begin{aligned} e_3 &= \frac{10000 \times 0.98 \times 0.97 \times 0.95}{10000 \times 0.98 \times 0.97 \times 0.95 + 10000 \times 0.98 \times 0.97 \times 0.05} \\ &= 0.95 \end{aligned} \tag{5.3}$$

In reality, detectors are not perfect and there are dead areas and time dependence to a certain level. In order for this scheme to work for this analysis, some preparatory work is needed. First of all, dead areas have to be masked. If inefficient areas are not masked out, tracks do now follow the probability

More complex and realistic example (one of the worst cases):
3168 tracks thrown within detector acceptance. At the end, 1121 tracks survived all PID cuts.
Estimated total efficiency is .354 ± .009.

2891	tracks had PC1 found (recorded in CNT)†,		pc1 efficiency is	.912 ± .005,
22	tracks failed to pass |bbcz|<30,		bbcz efficiency is	.980±.002,
95	tracks " have DC UV uniquely found,	dc quality	"	.921±.003,
130	tracks " pass PC3 found & 3σ matching,	pc3	"	.896±.004,
10	tracks " pass EMCal 3σ matching,	emcal matching	"	.991±.001,
762	tracks " pass EMCal shower shape,	emcal shower shape	"	.595±.005,
169	tracks " pass RICH n1>0 and disp<8,	rich n1>0 & disp>8	"	.868±.004,

Estimated total efficiency is .377 ± .004.

† In real data, PC1 efficiency is incorporated into geometrical acceptance correction.

Figure 5.13: More realistic example of efficiency calculation with the developed method (bottom). The result can be compared to what one obtains with traditional method (top). In most cases the results are consistent within statistical uncertainties. The example shown here is one of the worst cases which still are reasonable.

distribution as the geometry of detectors cause complications. When this happens, the two correction factors that we have assumed were independent will not be any longer independent.

Next, one needs to look to see if there is any significant change in the detector efficiency and break up the data into smaller groups accordingly. If, even after this procedure, there is larger fluctuation in the detector efficiency than the statistical fluctuation, how much there is has to be estimated and the systematic uncertainty has to be assigned towards it. This is a good point to put an emphasis on the fact that the scheme will not work for pair analysis cases as this scheme requires one be able to identify particles on an event-by-event basis. This conclusion does not change even when rigorous background estimation can be done in these analyses.

One major advantage of this method is it can also be applied to tracks simulated by Monte Carlo method. It not only provides a tool to test the integrity of the method, but it also tells us where exactly the issue is whenever wee see a discrepancy between the data and the simulation. Following in Fig. 5.13 is a realistic and more complex example to demonstrate how to calculate efficiencies using this method. As part of an integrity check of the method, the result is compared with the one by conventional method.

Out of all $\pi^{\pm}$ tracks generated, 3168 tracks were thrown into the central arm detector acceptance, left hits in PC1 and interacted with 5 detectors that were used for actual $\pi^{\pm}$ analysis. The reason PC1 is particularly mentioned here is that CNT[3] files only hold tracks that have PC1 found. In simulation, it is possible to estimate the efficiency of PC1 found as shown in the first row of the second block in Fig. 5.13. In data, we will incorporate this efficiency into the geometrical acceptance correction as they both are obtained from simulation. Also, the HBD detector is left out for simplicity, but it does not matter for current discussion as the tracks are already identified $\pi^{\pm}$ without any help from HBD and the calculation works in the same manner as other detectors.

The results of track reconstruction efficiency measurements for various detectors will follow next. An example will also be shown to demonstrate how to diagnose and localize problems by comparing data and simulation when we come to the Drift Chamber efficiency.

The Track Reconstruction Efficiencies

The method described previously can be applied in a few steps. We will adopt a bottom-up approach so as to save troubles that can come later in hindsight. There are roughly four steps to follow.

- Know what kind of efficiencies to measure based on the cuts used for the detector of interest.
- Look into the hit distribution in each detector to mask dead areas.
- Perform data QAs using efficiencies defined for each detector.
- Perform consistency check to make sure there is no unknown systematic sources of uncertainties.
- Get combined results.

Beginning with HBD, recall that there are two kinds of cuts or efficiencies involving HBD . A clustering efficiency $\epsilon^{\mathrm{HBDq>0}}$ that is associated with having positive HBD charge is the first kind, and there is also a mini-

[3]One type of data file that holds CeNTral arm track information at PHENIX.

mum charge cut efficiency $\epsilon^{\text{HBDq cut}}$ that is associated with having charge greater than the minimum charge cut. The latter is defined in such a way that having positive charge is already assumed, leaving it completely deconvoluted from the clustering efficiency. This will simplify the procedures for the charge cut efficiency, and so $\epsilon^{\text{HBDq cut}}$ will be dealt with briefly at the end. Most of the discussion will be dedicated to the clustering efficiency.

Moving onto the second step, Fig. 5.14 shows the cluster distribution on each sector. Clusters are either associated charged tracks or scintillation background. The conspicuous honey comb pattern is an artifact of the clustering algorithm where we merge the pad charge in 2 or 3 adjacent pads and take the center of gravity as the location of a cluster in most cases. Comparing it with Fig. 5.15 will help us construct a dead area map. If there is certain areas or pads where there are projected tracks and no associated clusters, then those areas have to be masked. The edge area is expected to be not fully efficient so strips surrounding edges also have to be excluded. For now, conservatively 3.0 cm from the end into the active area is considered dead and the final width will be determined later with more care. The dead map for HBD with tentative edge strip width is shown in Fig. 5.16.

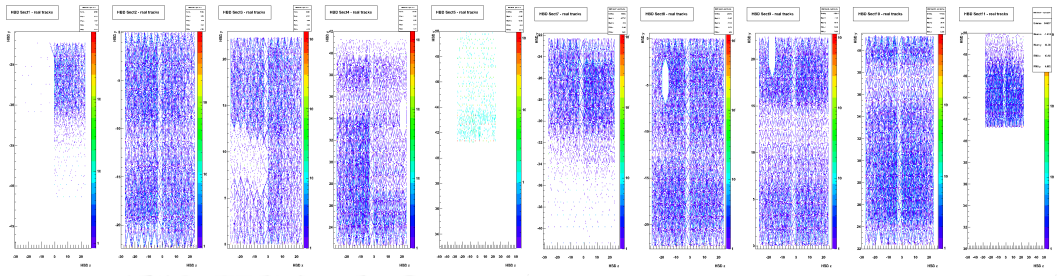

(a) East arm (b) West arm

Figure 5.14: The cluster distribution on HBD.

Now we can perform QA with the efficiency $\epsilon^{\text{HBDq}>0}$. HBD is one of the most crucial detectors for identifying $\pi^{\pm}$, however, it cannot be used when its efficiency is being studied. As such, one has to apply very tight cuts for other detectors so that the background in the $\pi^{\pm}$ sample does not results in a false efficiency. It was shown in the previous section (on the BBC bias) that ERT 4x4a data provides a fairly clean sample of $\pi^{\pm}$ even without using HBD. So we use this dataset for efficiency studies. Plot the efficiency fill by fill and fit it to a constant. There will be some outliers that need to be dropped.

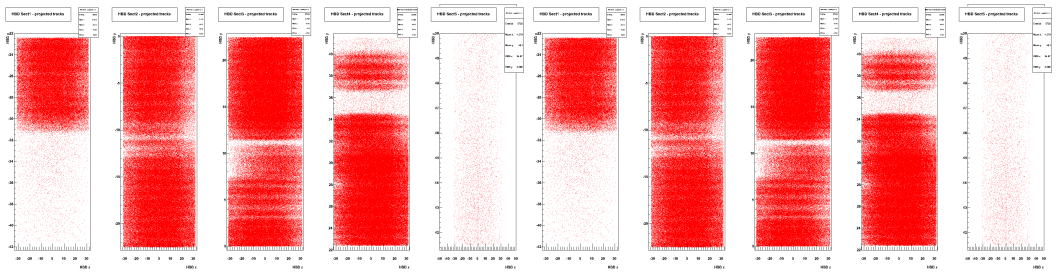

(a) East arm (b) West arm

Figure 5.15: The track projection on HBD.

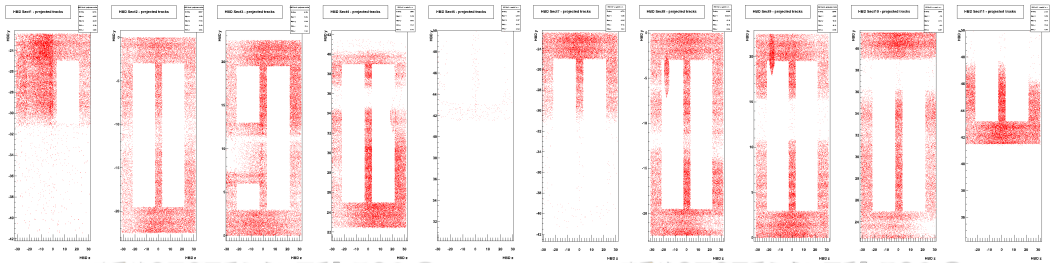

(a) East arm (b) West arm

Figure 5.16: The dead map (fiducial map) for HBD.

As can be seen Fig. 5.17(a), sectors in west arm appear to have stable and high efficiencies whereas ones in east arm show unstable and relatively low efficiencies. Looking into sector-by-sector efficiencies shown in Fig. 5.17(b), HBD sector 4 seems to have issues, so further investigation has to be done into HBD sector 4.

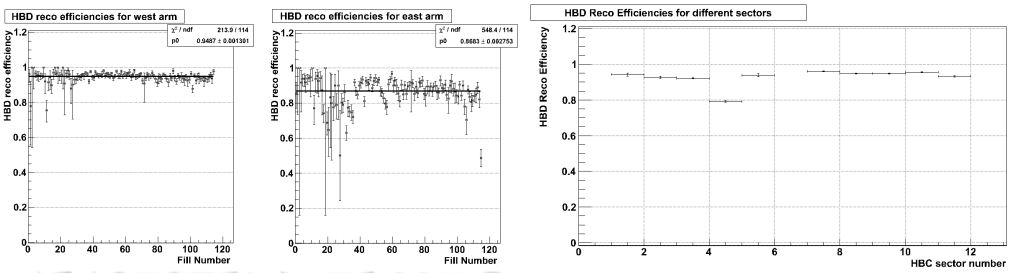

(a) fill by fill (b) sector by sector

Figure 5.17: The charge efficiency $\epsilon^{\mathrm{HBDq>0}}$ for HBD.

One way of examining the issue that we are facing is to see the HBD

charge distribution sector by sector. Indeed HBD sector 4 shows abnormal charge distribution in Fig. 5.18. To see it from a different perspective, the charge distribution is plotted by EMCal sector as well (Fig. 5.19) and the issue is not solely on HBD sector 4 but on the combination of HBD sector 4 ∗and∗ and EMCal sector 6. It indicates that the problem may not be with a sector on HBD itself but something unrelated to the performance of HBD.

What the HBD charge distribution for HBD sector4 and EMCal sector 6

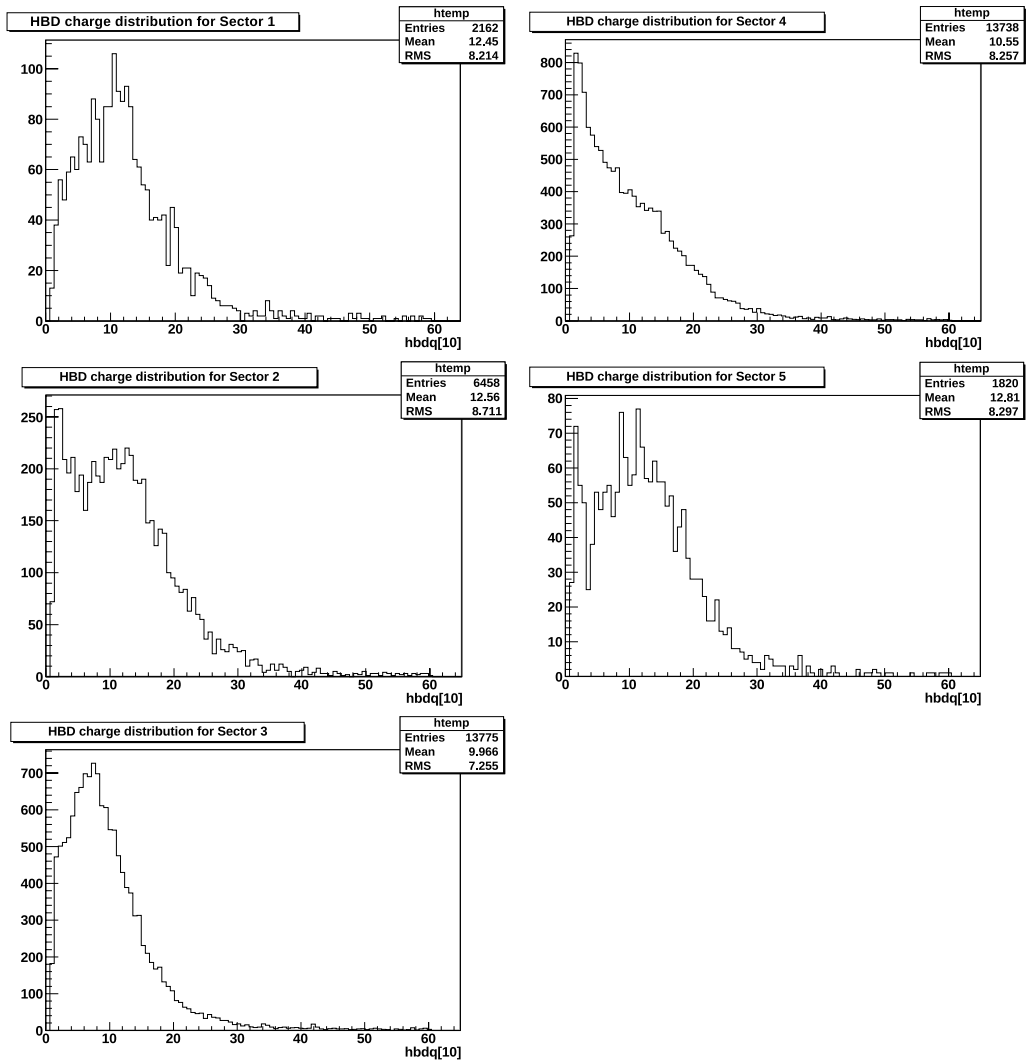

(a) East arm

Figure 5.18: The sector-by-sector HBD charge distribution - continued on the next page with description. HBD sector 4 is hown on top right.

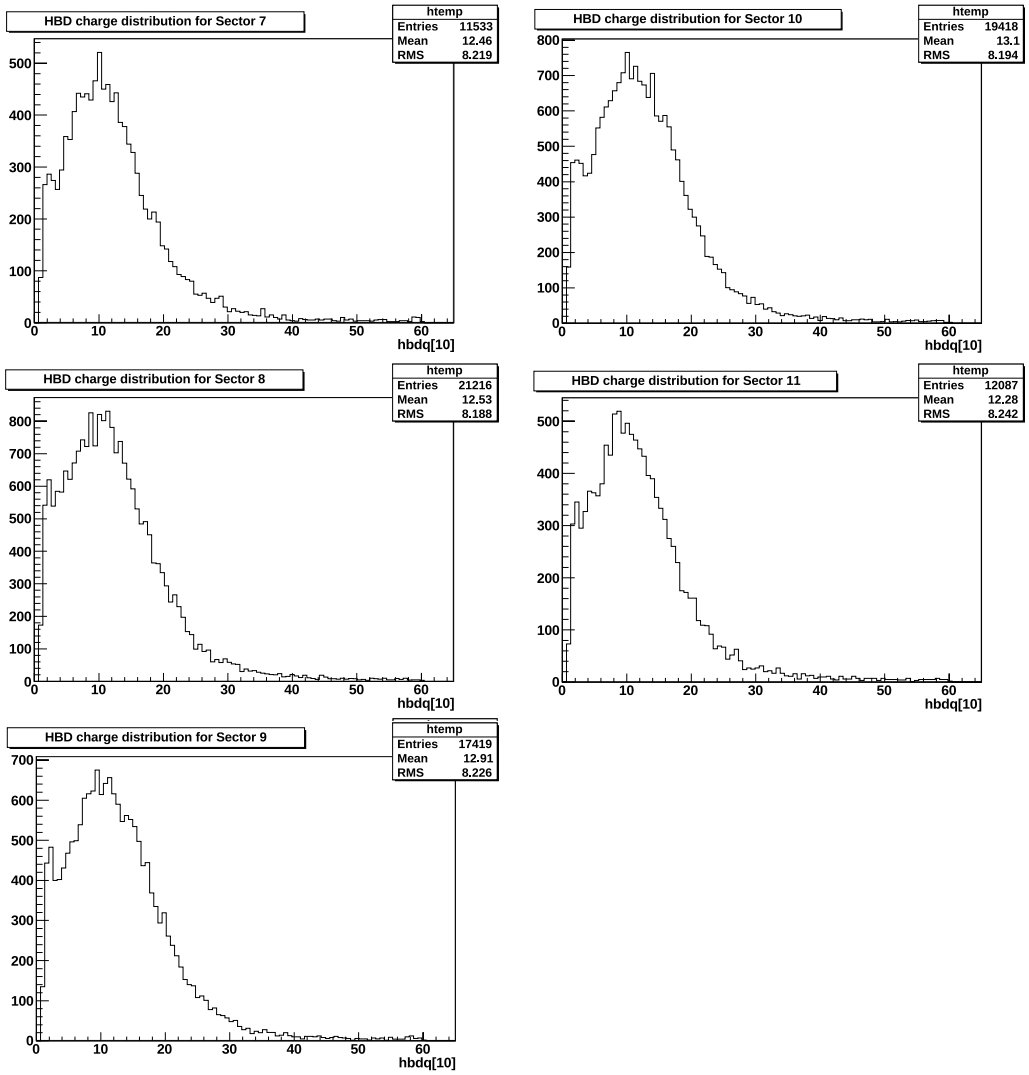

(b) West arm

Figure 5.18: The sector-by-sector HBD charge distribution.

is hinting us is there are excessive number of localized conversion electrons that accidentally became associated with scintillation light background clusters. Since conversion electrons normally have low p_T and get severely bent under the magnetic field, often faking high p_T, if the claim is true, there should be many tracks hit swapped arms between HBD and EMCal. This is actually confirmed as can be seen in Table 5.1. Tracks in each HBD sector are decomposed into two EMCal sectors and in each EMCal sector the ratio of the number of $\pi^{\pm}$ candidate tracks identified by HBD (with cluster-track match-

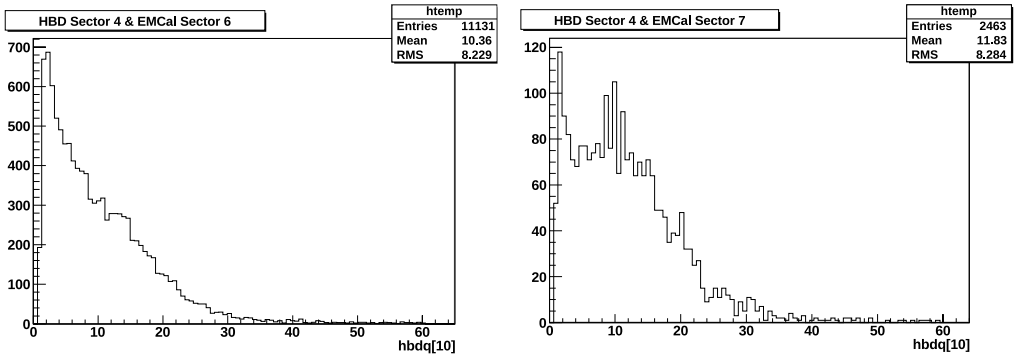

Figure 5.19: The HBD charge distribution for HBD sector 4 is broken into two distributions by EMCal sectors, 6 and 7.

ing) in addition to ERT4x4a (with super module-track matching) and the ones by only ERT4x4a. In HBD sector 4, there are disproportionately many tracks that hit swapped arms between HBD and EMCal (figures in red). There is an explanation for that, and it is the fact that there is a strut and cables, which act as a photon converter, placed asymmetrically only in the east side of HBD.

HBD sector	EMCal Arm	Number of tracks with (HBD+ERT4x4a) / ERT4x4a
1	West	14/19
1	East	877/901
3	West	32/41
3	East	6176/6275
4	West	55/1742
4	East	6357/8907

Table 5.1: The composition of $\pi^{\pm}$ candidate tracks on three HBD sectors in east arm.

Now that we localized the problem, the solution is rather simple. Mask the affected area 'HBD sector 4' for the efficiency calculation and extrapolate it to the unaffected area HBD 'sector 4 & EMCal sector 7'. Tracks in 'HBD sector 4 & EMCal sector 6' are eliminated as they are predominantly conversion electrons. The HBD efficiency $\epsilon^{\mathrm{HBDq>0}}$ by EMCal sector before and after excluding HBD sector 4 and tracks with swapped arms are compared in Fig. 5.20.

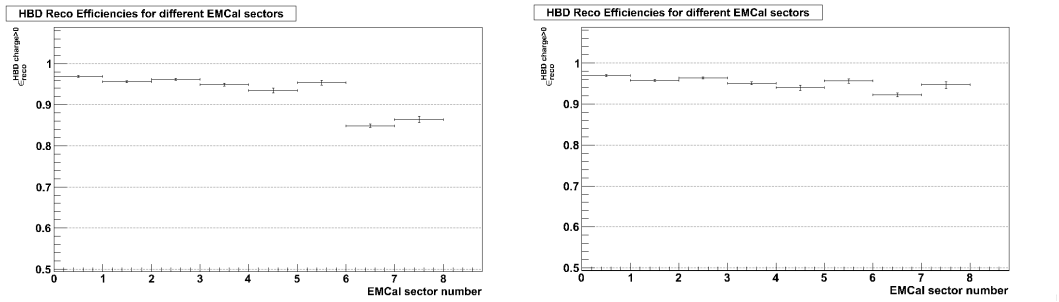

(a) before excluding HBD sector 4 (b) after excluding HBD sector 4

Figure 5.20: The HBD efficiency $\epsilon^{\mathrm{HBDq>0}}$ by EMCal sector (a) before and (b) after the exclusion of HBD sector 4.

Efficiencies shown in Fig. 5.17 are updated after this modification and shown in Fig. 5.21. The final efficiency $\epsilon^{\mathrm{HBDq>0}}$ for all sectors combined accounts for the cluster-track matching efficiency as well. The efficiency with its statistical uncertainty is 0.943±0.009 and proper systematic uncertainties will be assigned later.

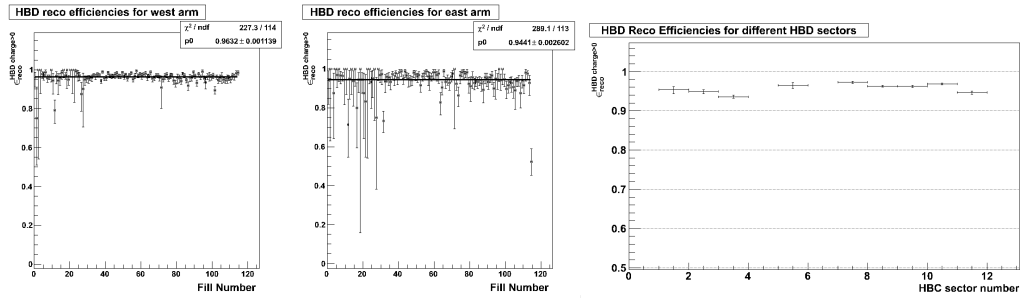

(a) fill by fill (b) sector by sector

Figure 5.21: The charge efficiency $\epsilon^{\mathrm{HBDq>0}}$ for HBD after excluding HBD sector 4 and tracks with swapped arms.

The HBD charge cut efficiency $\epsilon^{\mathrm{HBDq\ cut}}$ depends on the shape of the HBD charge distribution. From dedicated studies with HBD, we know that the optimal minimum charge cut for p_T bin 5∼6, 6∼7, 7∼9, and 9∼12 GeV/c are 4, 4, 5 and 6 respectively. Since $\pi^{\pm}$ tracks are also rejected if they have HBD charge less than the minimum charge cuts, corrections have to be calculated accordingly. These correction factors are best extracted from a clean sample of $\pi^{\pm}$ tracks from data. The efficiencies calculated from these distributions

are 0.924±0.002, 0.941±0.002, 0.923±0.002 and 0.902±0.002 for 4 p_T bins in an increasing order and whether there are any systematic uncertainty sources will be examined later.

The next detector that will be discussed is DC. One main point that an analyzer has to be extremely mindful about is that tracks that do not have track projection on the detector of interest should be disregarded for an efficiency analysis as those without projections are out of the geometrical acceptance and their corrections have to be taken into account when dealing with the geometrical acceptance corrections. DC, however, does not have any variable assigned for track projections in CNT files. Instead, there is a variable called 'track quality' that involves DC as well as PC1. In this case, one needs to take additional step and adopt an approach of factorizing the two components of the variable to calculate the efficiencies for each component separately. As for DC, knowing that the PC1 detector is immediately next to DC, one can use 'having a hit on PC1' as a proxy for having a projection on DC. To be more specific, tracks with uniquely found PC1 hits have to be looked into in order to calculate the DC part of the track quality efficiency $\epsilon_{\text{reco}}^{\text{DC quality}}$ that is defined as the efficiency of having 'unique X1 and X2 hits' and 'UV found or unique'. In terms of track quality values, $\epsilon_{\text{reco}}^{\text{DC quality}}$ is written as the ratio of the number of tracks with 'track quality = 63' and 'track quality > 48'. One may have concerns about the fact that valid values of quality variable do not include 'X1 ∗and∗ X2 not found'. These concerns can be eased by realizing the probability of $\pi^{\pm}$ tracks having both not found is the square of the one having only one not found. Since the probability of tracks having one of them not found is less than 0.1, the chances are negligible that $\pi^{\pm}$ tracks have both not found. A remaining component involves the efficiency of PC1 found. This efficiency cannot be calculated from data and will be incorporated into the geometrical acceptance correction for the reason explained at the beginning of this section.

The dead map is constructed based on the hit distribution of DC that is shown in Fig. 5.22. Clear edges are shown along ϕ = constant lines, while the boundaries where θ_0 = constant are relatively broader. The θ_0 boundaries are in general weaker because θ_0 is not a direct measure of z coordinate of the DC and is smeared by the z vertex distribution. Partially alive ϕ strips are due to broken wires, so those areas are also masked. The sector-by-sector efficiencies calculated according to the definition given above are presented in Fig. 5.25(a). It appears that some sectors are not as efficient as other sectors so those sectors (Group 0) need to be treated separately from the rest (Group

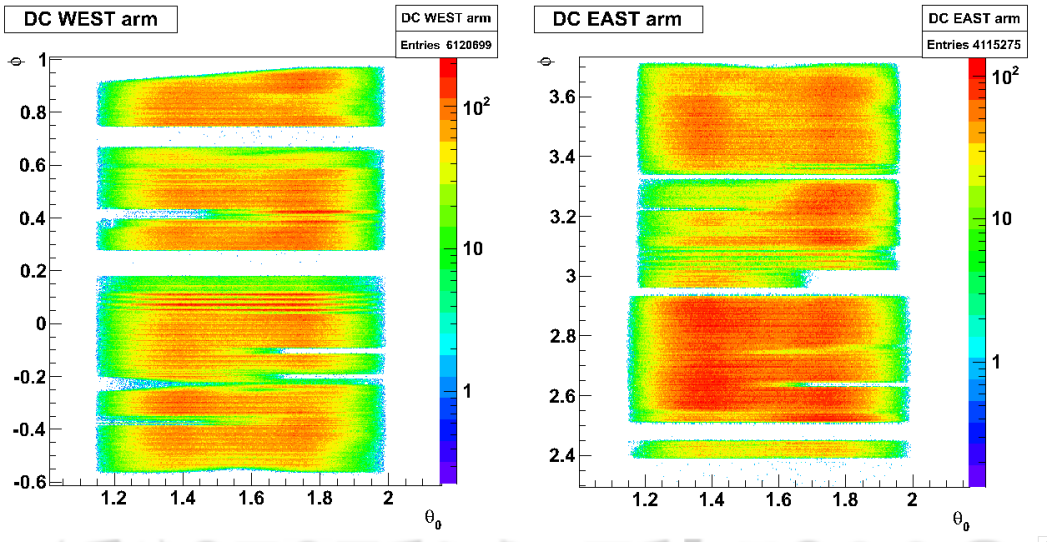

Figure 5.22: The DC hit distribution.

1). As a result, we have two independent groups, and the fill-by-fill efficiencies for each group are shown in Fig. 5.25(b).

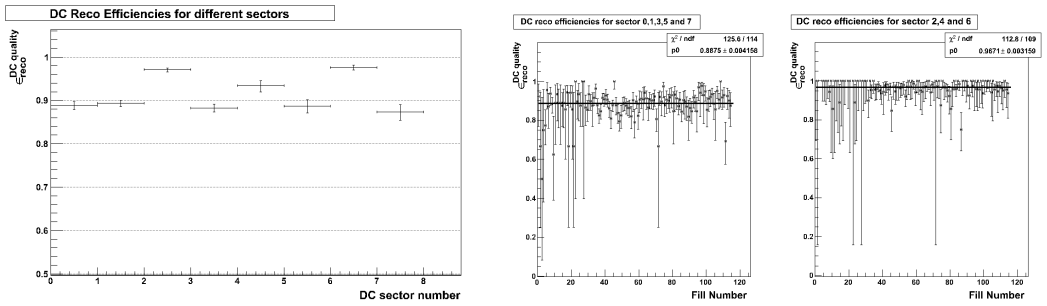

(a) fill by fill (b) sector by sector

Figure 5.23: The DC track quality efficiency $\epsilon_{\text{reco}}^{\text{DC quality}}$.

The final efficiencies for this analysis are calculated for 4 groups in total, two DC groups for PbSc and two for PbGl to take into account the strong sector dependence of the $\epsilon_{\text{reco}}^{\text{DC quality}}$. The results are 0.865±0.003 and 0.970±0.002 for G0 and G1, respectively, for PbSc and 0.895±0.012 and 0.946±0.008 for PbGl.

These results will be compared with the ones from simulation as stated in the previous section. There are actually visible discrepancies in the sector-by-sector efficiency (circled in red in Fig. 5.24), leaving it a good example to

demonstrate how a method applicable to data as well as simulation can be used as a diagnostic tool for analysis.

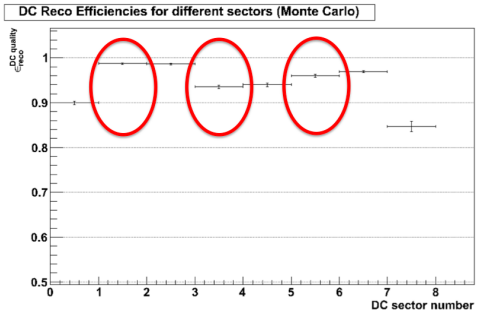

Figure 5.24: The sector-by-sector DC quality efficiency $\epsilon_{\text{reco}}^{\text{DC quality}}$ from simulation.

To see what causes the discrepancy between the data and simulation, we compare the hit distribution of tracks with 'track quality = 63'. There are indeed discernible differences in the distribution on the sections that showed significantly different efficiencies.

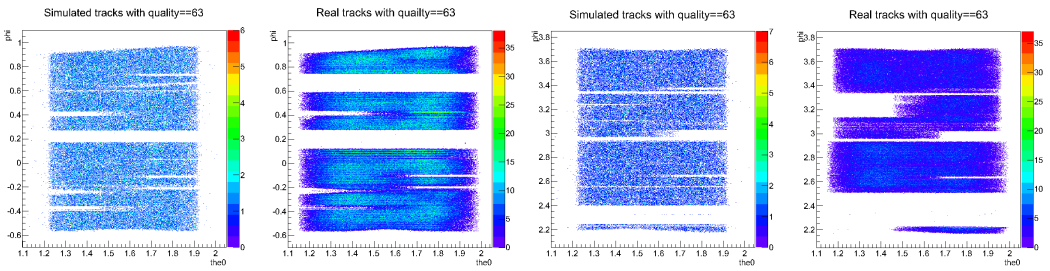

(a) West arm (b) East arm

Figure 5.25: The comparison of DC quality efficiency $\epsilon_{\text{reco}}^{\text{DC quality}}$ between the data and simulation.

Let us move on to the discussion of another detector PC3. Following the usual procedure, the hit distribution is shown in Fig. 5.26. While there are no sectors with significantly lower efficiencies, there are a lot of small patches of dead area. The acceptance of PC3 is time dependent like most other detectors. The PC3 efficiency $\epsilon_{\text{reco}}^{\text{PC3 matching}}$ is calculated by taking the ratio of the number of tracks with 'within 3σ matching' and 'projection on PC3'. Results are shown in Fig. 5.27. Unlike other detectors, the PC3 efficiency

shows time dependence, which is taken into account by breaking data into five groups. When calculating the efficiencies for 4 different groups, only one group G0 PbSc will be allowed to have varying efficiencies and the rest will have a uniform efficiency for each group. Results are: 0.866±0.001, 0.838±0.002, 0.784±0.005, 0.814±0.006, 0.826±0.006 for G0 PbSc, 0.822±.002 for G1 PbSc and 0.857±0.002 for PbGl.

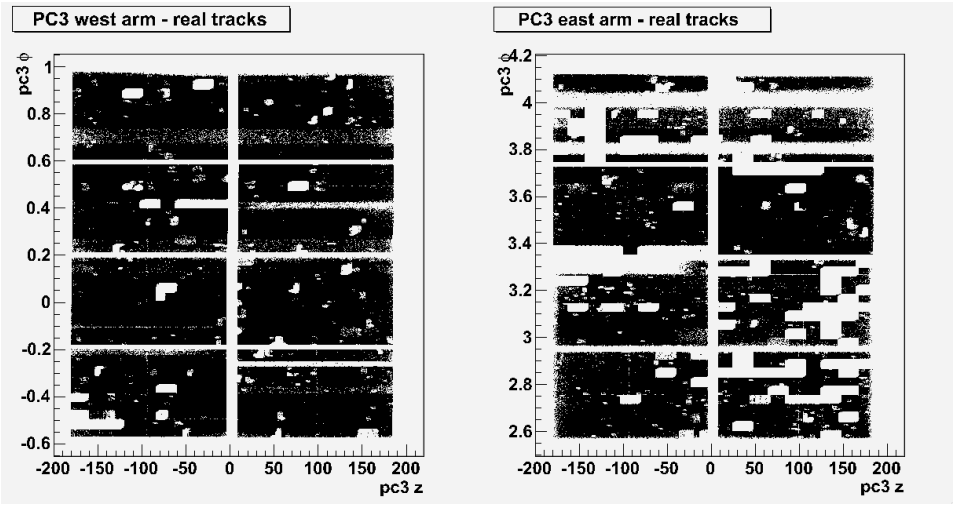

Figure 5.26: The PC3 hit distribution.

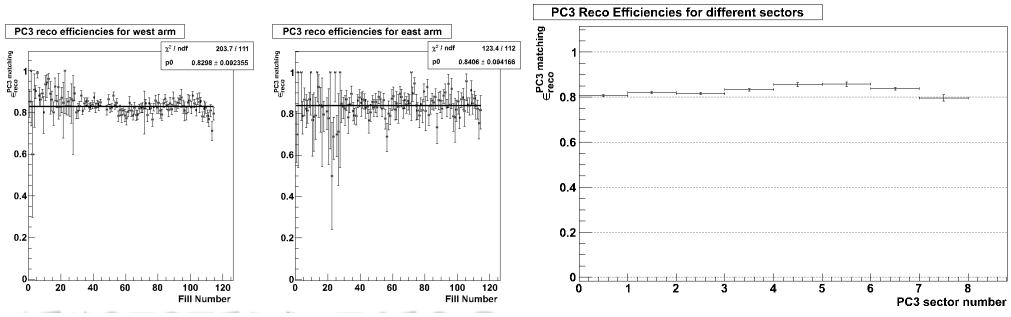

(a) fill by fill (b) sector by sector

Figure 5.27: The PC3 matching efficiency $\epsilon_{\text{reco}}^{\text{PC3 matching}}$.

The EMCal detector is the next to discuss. Track matching efficiency is already included in the trigger efficiency. There is no efficiency left for EMCal as we will drop the shower shape cut $prob < 0.2$ for this analysis. Previous analysis without HBD required tracks pass the shower shape cut because

it got rid of a large fraction of conversion electrons in the $\pi^{\pm}$ candidate sample. In current analysis, however, gains in statistics when dropping this cut are much larger than background rejections since HBD eliminates most conversion electron tracks. The hit distribution shown in Fig. 5.28 was also looked into in order to mask dead areas for trigger efficiency analysis.

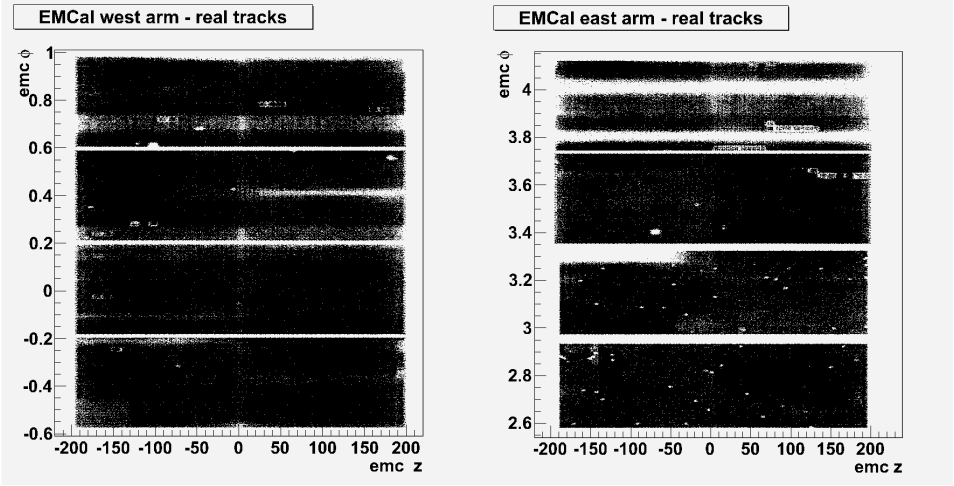

Figure 5.28: The EMCal hit distribution.

The last one we will discuss about is the RICH detector. Since RICH is a Cerenkov detector and the threshold momentum for $\pi^{\pm}$ is about 4.7 GeV/c, it is expected that the efficiency at low p_T is much lower than high p_T. When looking into the hit distribution, there does not seem to be any inactive area on the detector (Fig. 5.29). Although the p_T dependent efficiency will be more carefully measured later when we discuss the systematic uncertainties, we only consider four efficiencies for four p_T bins for the moment. They are calculated based on the definition given as the number of tracks with '$n_1 > 0$' and 'within the RICH acceptance'. In previous cases, we had to be certain that no tracks with their projection on the detector are counted in the analysis as they return wrong efficiencies. In the case of RICH, track projections are recorded only when there is a hit on RICH. That means we cannot use projections for making sure the tracks are in the geometrical acceptance. Alternatively, we require tracks be in active region on RICH by using acceptance variables of other detectors. The fill-by-fill results are shown in Fig. 5.30. The sector-by-sector efficiencies are not shown as they are meaningless due to their strong p_T dependence.

This completes the efficiency analysis for all detectors involved and we will

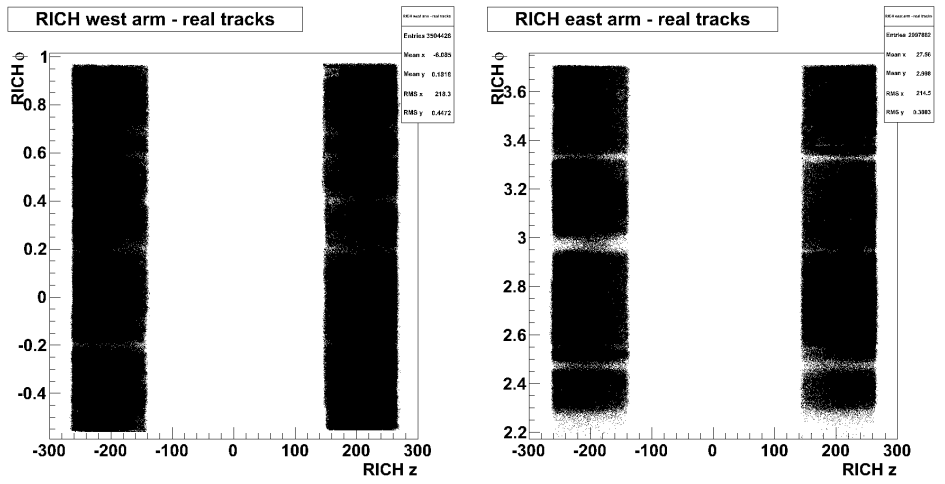

Figure 5.29: The RICH hit distribution.

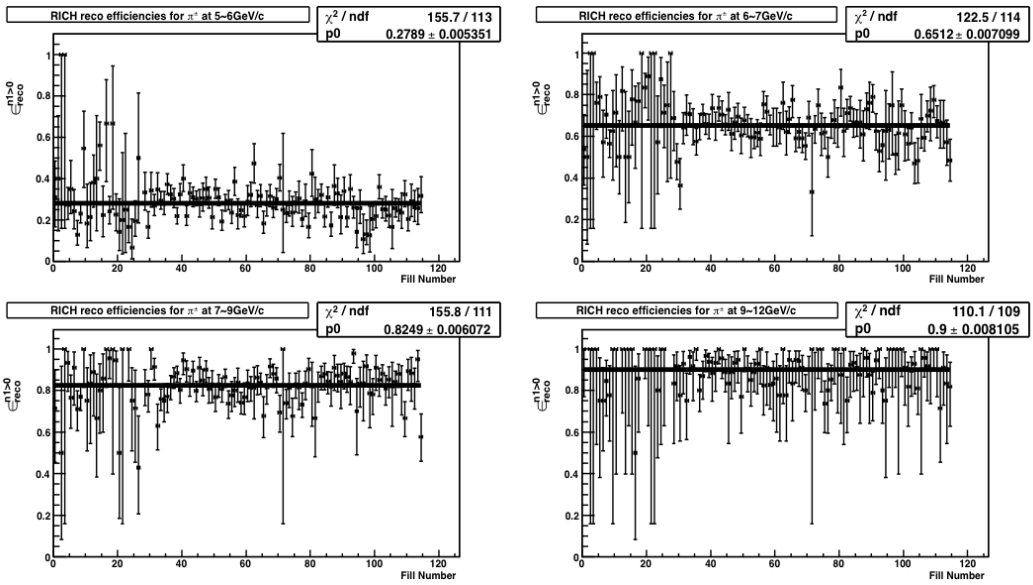

Figure 5.30: The RICH $n_1 > 0$ efficiency $\epsilon_{\text{reco}}^{n_1>0}$.

move onto the discussion of geometrical acceptance corrections in the following section.

The Geometrical Acceptance Correction

As stated in Sec. 5.1.3, we are working in a scheme where geometrical acceptance is factored out from reconstruction efficiency corrections. Dead

areas have been masked out in order for the assumptions to be compatible with the analysis, and data have been broken into smaller groups to reduce systematic uncertainties. Geometrical acceptance corrections $\epsilon_{\rm geo}$ are worked out carefully for each subgroup that is based on geometrical (time dependent) variation, charge and p_T bins, so there are 2 (PbSc/PbGl) $\times$ 2 (DC group G0/G1) ($\times$ 5 (time dependent acceptance for G0)) $\times$ 2 (charge) $\times$ 4 (p_T bin) correction factors.

There are parameters for two dimensions that we need to get corrections for; one is θ and the other is ϕ. In high energy collisions, pseudo rapidity η is a proxy for rapidity y, a Lorentz invariant. Since η can be written in terms of θ, η correction is equivalent to θ correction. And from the fact that the $|\eta|$ range of PHENIX is < 0.35, one can determine the correction factor $\Delta\eta$ to be 1.0/0.7 in order to have an η bin of unit size. The rest of $\epsilon_{\rm geo}$ contains acceptance in ϕ direction in most part and some additional corrections in θ direction through fiducial cuts.

Another aspect that is critical in this part of analysis is determination of the optimal HBD edge width. The reason this is a critical factor is that the geometrical acceptance is severely subject to the edge width of HBD in contrast to other detectors that are quite distant ($>\sim$2 m) from the beam pipes. An edge width is defined as the width of strips that mask boundary regions of the detector on account of inefficiency. The level of inefficiency depends on the clustering mechanism. In this analysis, a cluster is defined by three pads of the highest amount of charge within a radius of 7.0 cm from the projected track position. The length of the side of a hexagon pad is 1.55 cm. Hence the edge strip has to be at least greater than 1.55 cm in principle. The nominal zero of the HBD boundary is set based on the physical boundary of active area (see Fig. 5.14) to avoid any complications that might come from imperfectness in the alignment of subsections. Additional adjustment is made in order to take into account the fact that cluster distribution is not uniform across the surface of the detector. It is periodic as the cluster position is determined by taking the center of gravity of the collected charge and consequently end up along the borderline or at the center of pads. The final widths for group G0 and G1 are 1.0 and 1.5 cm respectively. Systematic uncertainties associated with making this choice will be discussed later in Sec. 5.2.

5.2 Systematic Uncertainties

In this section, we go over all potential sources of systematic uncertainties and assign proper uncertainties when necessary. To this end, we first need to categorize systematic uncertainties into several types based on the characteristics of sources of uncertainties[4]. There are basically 3 types :

- Type A : point-to-point uncertainty, uncorrelated between p_T bins.

- Type B : p_T correlated, all points move in the same direction but not by the same factor.

- Type C : all points move by the same factor independent of p_T.

A source of systematic uncertainty that potentially falls into type A is the choice of HBD charge cut that determines $\epsilon_{\rm reco}^{\rm HBDq\ cut}$. The RICH n_1 >0 efficiency is categorized into the source of type B uncertainty. Determination of all the other efficiencies and biases including the BBC trigger bias, the ERT efficiency, the DC quality efficiency, the PC3 matching efficiency and the HBD edge width are sources of type C systematic uncertainty. One should note that the DC track quality and PC3 matching efficiencies and the HBD edge width are in theory sources of p_T correlated systematic uncertainty due to the p_T dependent nature of momentum resolution. The correlation, however, becomes irrelevant since the p_T correlation gets swamped by other factors that determine systematic uncertainties such as time dependence or geometrical effects.

Starting with type A, let us consider the HBD charge cut efficiency. This efficiency was calculated using ERT 4x4a data with a benefit of overwhelmingly large signal-to-background ratio. The question one has to ask is whether this small sample of data reflects the entire data without introducing bias. One way to check is to see if the cross section changes significantly when the cut is changed.

First look at $\epsilon_{\rm reco}^{\rm HBDq\ cut}$ with a reference cut. Choose the cut that will be used for final result as a reference cut. Then look how the efficiency changes when the cut is varied. This will be a general approach for other sources as well. The cross section is recalculated with a new cut to compare against the one calculated with a reference cut. Take the ratio between the two and see if

[4]Sources of systematic uncertainties are found in considering PID cuts. To summarize the final cuts used for this analysis: $n_1 > 0$, $|z_{\rm vtx}^{\rm BBC}| < 30$, track quality = 63 or 31, $|zed| <$ 70, e/p < 0.9, emce > 0.2, p_T, 3σ matching cuts for PC3 and EMCal and HBD charge cuts.

they are consistent within the statistical uncertainty. Repeat this with several different cuts.

Fig. 5.31 shows how the efficiency changes with varying HBD charge cut. The p_T dependence reflects the shape difference in HBD charge distribution. The relative cross section at various cuts are with respect to the reference shown in Fig. 5.32. The results prove that the cross section is consistent at the new cuts examined within statistical uncertainties.

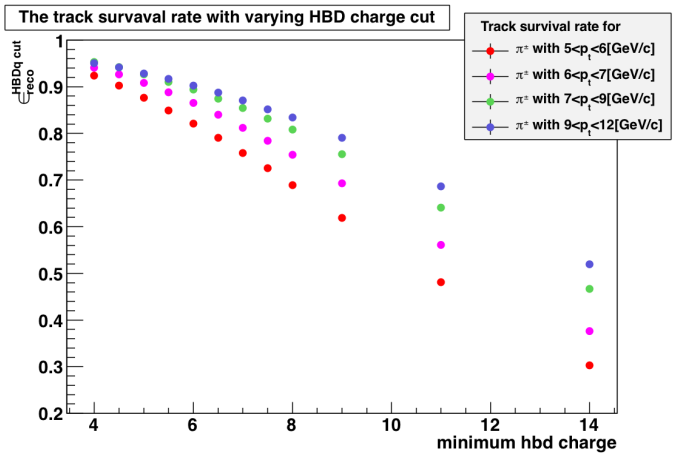

Figure 5.31: The HBD charge cut efficiency $\epsilon^{\text{HBDq cut}}_{\text{reco}}$ for 4 p_T bins.

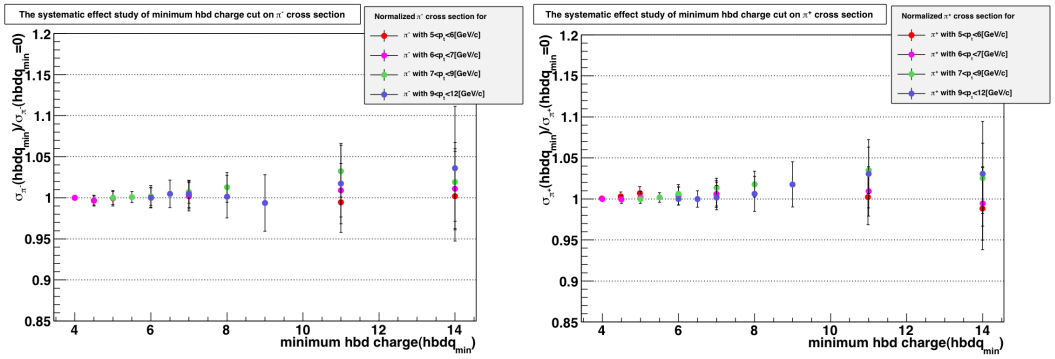

(a) Negative charge (b) Positive charge

Figure 5.32: The systematic effect study of the HBD charge cut.

Determination of the RICH $n_1 > 0$ efficiency needs to done with extra care. In Sec. 5.1.3, we measured the efficiencies for four p_T bins independently. This can still lead us to false results. Taking an example of the lowest p_T bin,

combining tracks with p_T range of 5 to 6 to get one efficiency value for this bin can overestimate the efficiency. The RICH threshold for $\pi^{\pm}$ being very close to 5 GeV/c, there will be much smaller pion yields in the lower half of p_T range than in the higher half. This will give more weight on the higher p_T and consequently overestimate the efficiency. A correct approach to measure the efficiency is that one should get an efficiency curve with fine enough p_T bins to be able to see a clear turn on. The turn on curve will then be fit to a Fermi function with two fit parameters that describe the rise of the efficiency; p_0 (height) and p_1 (threshold). The efficiency at p_T close to the threshold is now averaged with proper weight into each p_T bin. One can judge how reasonable measured efficiencies are by looking at the raw yield scaled by the inverse of measured efficiencies. See Fig. 5.33.

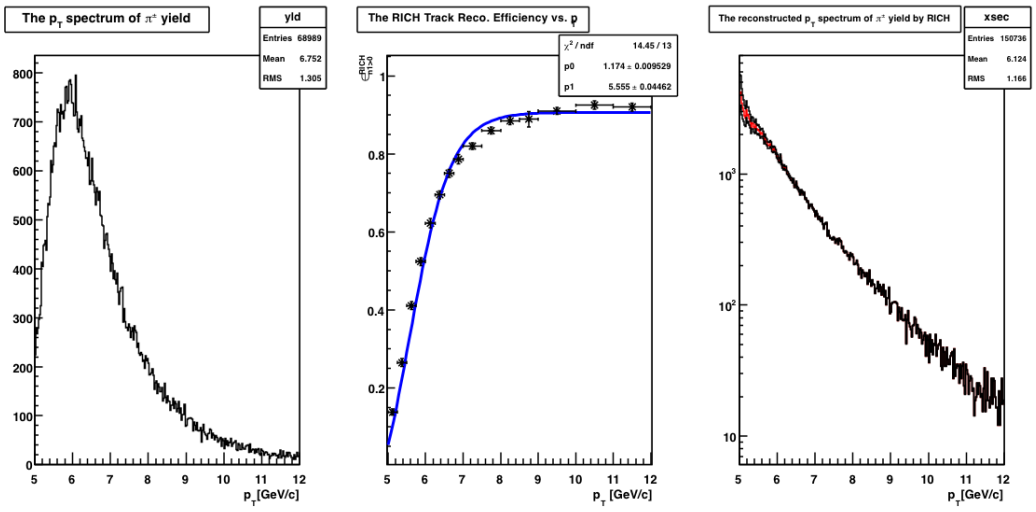

Figure 5.33: The raw yield (left), RICH efficiency (middle) and reconstructed yield by RICH (right).

The two lines in the reconstructed yield plot represent the upper/lower limit corresponding to the uncertainties on the fit parameters. It is now clear that the systematic uncertainty caused in determining the RICH efficiency is p_T correlated. The wider becomes the p_T bin size, the smaller the systematic uncertainty becomes. The results for four p_T bins and for continuous p_T are shown in Fig. 5.34.

Next we estimate systematic uncertainties coming from measuring detector efficiencies that vary with time. The $\epsilon_{\text{reco}}^{\text{DC quality}}$ has been measured with five divided groups based on time dependence of its efficiency. There can still be remaining systematic uncertainties from this, though it is reduced. How we

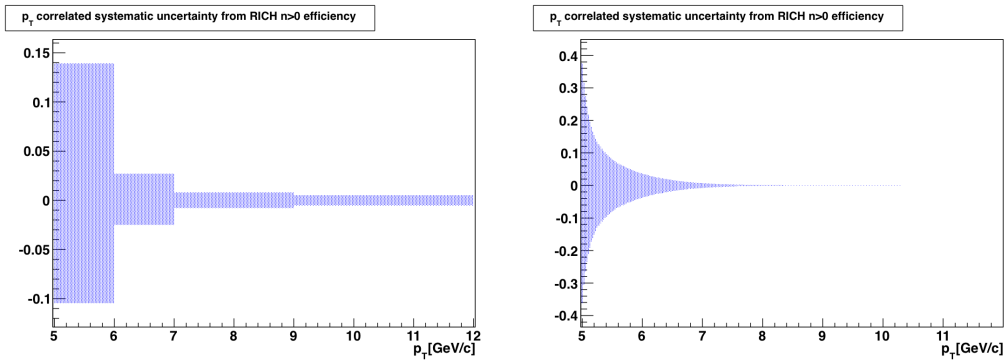

(a) Discrete (b) Continuous

Figure 5.34: The systematic uncertainties from the RICH $n_1 > 0$ efficiency vs. p_T.

estimate systematic uncertainties is as follows. First normalized efficiencies by an average efficiency of each run group and plot them altogether for the entire run groups. Then project the normalized efficiencies onto a 1 dimensional histogram and get the width of the Gaussian fit. One can go through the same procedure for the PC3 detector. Results are shown in Fig. 5.35 and Fig. 5.36. Estimated uncertainties for DC group 0 (DC group 1) for the DC track quality efficiency and the PC3 matching efficiency are 3.87 (1.77) % and 4.41 (4.58) %, respectively. The $\epsilon_{\text{reco}}^{\text{DC quality}}$ distribution for DC group 1 is non Gaussian because the efficiency is close to 100%. Final systematic uncertainties assigned to these efficiencies are the weighted average of the two. Results are 2.82% and 4.50% for $\epsilon_{\text{reco}}^{\text{DC quality}}$ and $\epsilon_{\text{reco}}^{\text{PC3 matching}}$, respectively.

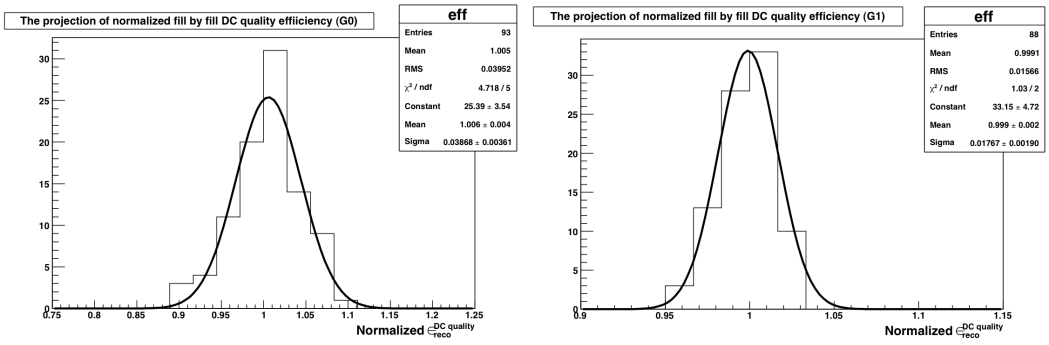

(a) DC group 0. (b) DC group 1

Figure 5.35: The distribution of normalized fill-by-fill $\epsilon_{\text{reco}}^{\text{DC quality}}$ and its fit to a Gaussian function.

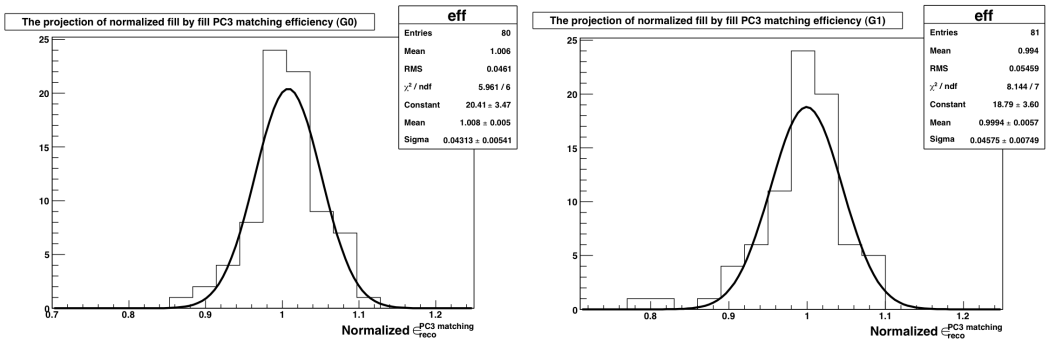

(a) DC group 0 (b) DC group 1

Figure 5.36: The distribution of normalized fill-by-fill $\epsilon_{\text{reco}}^{\text{PC3}}$ and its fit to a Gaussian function.

The same can be done for HBD clustering efficiency $\epsilon_{\text{reco}}^{\text{HBDq>0}}$. The distribution is shown in Fig. 5.37 and the systematic uncertainty assigned is 1.6%.

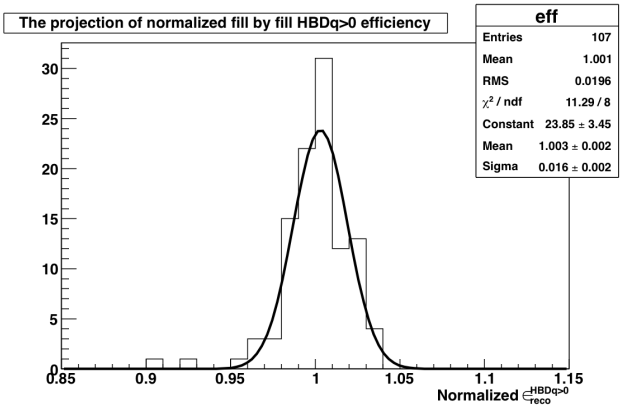

Figure 5.37: The distribution of normalized fill-by-fill $\epsilon_{reco}^{HBDq>0}$ and its fit to Gaussian.

The last source of type C systematic uncertainty is from determination of boundaries in the HBD. Previously the edge strip width was set to 3. cm conservarively on account of inefficiency at the end area of the sector. Here we are going to determine appropriate edge strip width by studying the pattern of the cross section changing with varing strip width. Recollecting how the position of clusters is determined in Section 5.1.3, one can anticipate that the cross section should vary periodically. Clusters are along the lines forming hexagons and as such the cross section will be higher when the boundary sits immediately outside of the lines and lower when just before the lines. This

pattern is displayed in Fig.5.38. Lines in red are the results of fitting to a sine function with common phase and frequency. Optimal edge strip witdh for DC group 0 (1) is determined to be 1.0 (1.5). The systematic uncertainties from this effect is assigned to be as large as half the amplitude of the sine function, 2%.

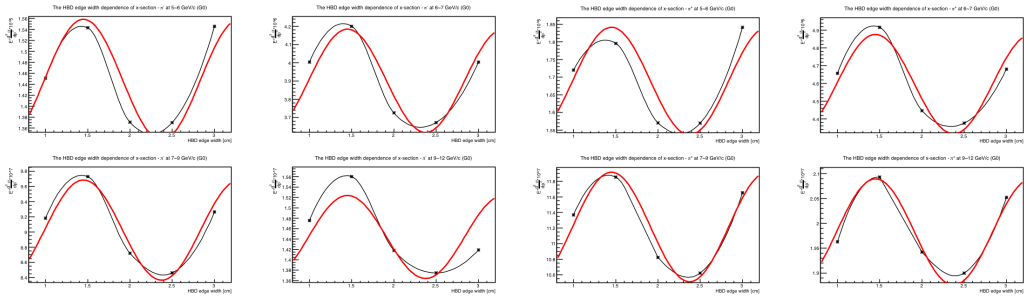

(a) DC group 0 for π^- (b) DC group 0 for π^+

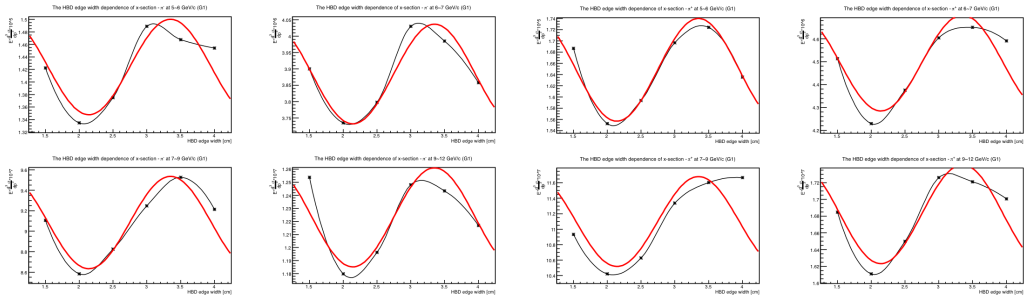

(c) DC group 1 for π^- (d) DC group 1 for π^+

Figure 5.38: The variation of the cross section with the edge strip width.

Measurement of the ERT efficiency that is potentially a source of type C systematic uncertainties was extensively discussed in Sec. 5.1.2. Determining final values for the minimum EMCal energy has been postponed until now as it requires systematic effect studies due to random benefit effect caused by accidental track matching of clusters.

One should understand that this random matching is acceptable to some degree in this analysis. The clusters of $\pi^{\pm}$ candidate tracks are not necessarily isolated from others unlike photons that necessarily have to pass isolation cuts for particle identification. In efficiency studies, we required separation between $\pi^{\pm}$ and associated clusters in order to avoid ambiguity. This does not forbid pion from being triggered by a third particle. Since we allow pions to be triggered accidentally by unrelated clusters, the ERT bias also has to be

measured in a manner that allows for this effect.

Furthermore, the probability of a pion being triggered by a third cluster is very low due to low multiplicity environment. This is confirmed by the fact that the trigger efficiency measured by $\pi^{\pm}$ is comparable particularly at above 2.0 GeV to the one measured by π^0 photons with the same trigger type and threshold. In that high energy region, whether or not one requires an isolation cut does not affect the trigger efficiency since both γ's and $\pi^{\pm}$'s are at high p_T and with lower multiplicity.

At intermediate energy region between 0.2 and 2.0 GeV, the nature of $\pi^{\pm}$ cluster is very different from the one for γ. First of all, how the efficiency is calculated is different for the two. The energy of photons is nearly same as the cluster energy, whereas the energy of $\pi^{\pm}$ does not have any direct relation with the cluster energy. At all p_T for this analysis the energy spectra of $\pi^{\pm}$ show a MIPs peak at 0.3 GeV and a broad tail even though the momenta of particles are much higher. And the trigger efficiency for each p_T bin is calculated by integrating the area below the energy spectra of inclusive and the (HBD+ERT) type events. This is very different from the photon case where the trigger efficiency of each p_T bin is calculated directly at the corresponding energy region. Also, the photons in this case are actually less hard photons with low p_T.

Another distinction is that $\pi^{\pm}$'s are not identified by cluster energy so much as their events are triggered by it, whereas photon identification requires it be isolated from other soft particles. Random benefit effects in photons are removed by applying isolation cuts and this is not the case for $\pi^{\pm}$. So the difference in trigger efficiency in this intermediate energy region is attributed to whether isolation cut is applied or not.

For the differences explained above, justification of the method can be done by a self-consistency check. The idea is similar to the method used so far. First vary the emce cut and get a new cross section with the new cut. Take a ratio of this to the one at the reference emce cut. Here we take the reference at 0.2 GeV, which is also used for the analysis. Having a reference at this energy is appropriate as statistical uncertainties at higher energy become larger. It also means that the systematic effects will be more transparent at lower energy. Trigger efficiencies with varying minimum emce cuts are displayed in Fig. 5.39 and the cross section ratio is presented in Fig. 5.40.

At most minimum emce values examined, cross sections are consistent within statistical uncertainties. Although there is slightly greater than 1 σ difference at the lowest energy less than 0.2 GeV, the difference is still less than 1% and it is explained by the outliers in the efficiency plot. Also,

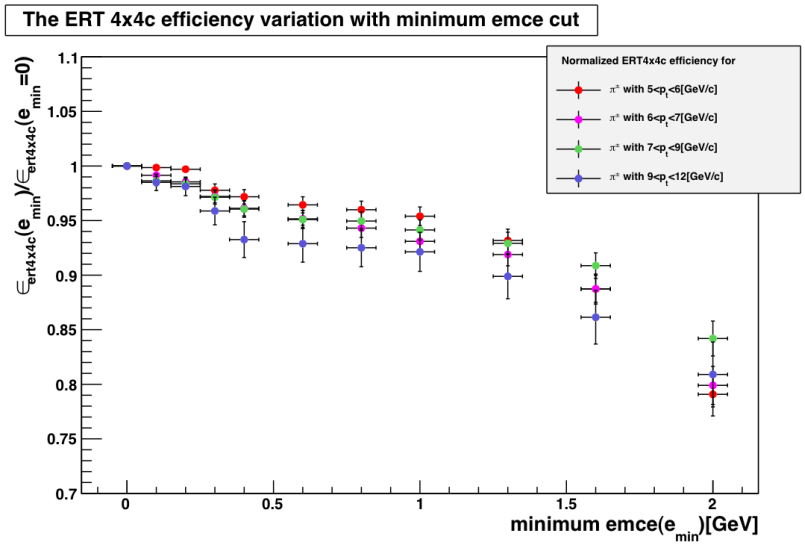

Figure 5.39: The ERT 4x4c trigger efficiency with varying minimum emce cuts.

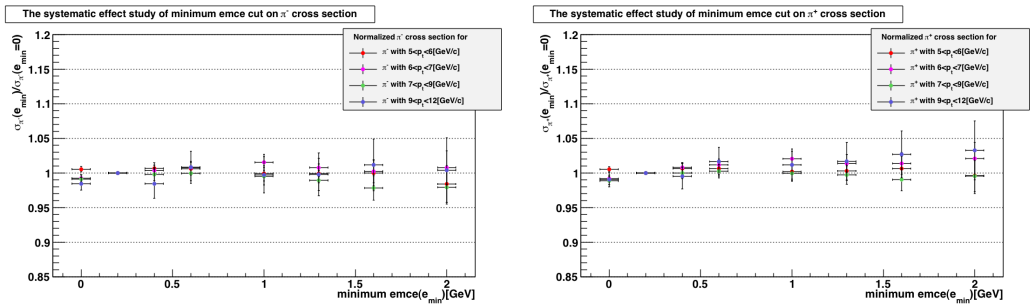

(a) π^-. (b) π^+

Figure 5.40: The study of systematic uncertainties from the ERT 4x4c trigger efficiency.

charged pion events at this low energy is not so critical to the cross section measurements given the way an efficiency is measured for each p_T bin and the fact that there is not much statistics that contribute at this energy. So we can conclude that the ERT 4x4c trigger efficiency measurement is self-consistent within statistical uncertainties as long as the minimum cut of 0.2 GeV is applied. The ERT efficiencies determined accordingly are 0.488, 0.502, 0.503 and 0.492 for respective p_T bins.

After this study, p_T binning has been extended and optimized. The new

p_T bins are 5∼6, 6∼7, 7∼8, 8∼9, 9∼11 and 11∼13 GeV/c. Reconstruction efficiencies affected by this are the HBD charge cut efficiency and the RICH efficiency. The minimum HBD charge for the new 6 p_T bins are 4, 4, 5, 5, 6 and 9 and corresponding efficiencies measure to be 0.922, 0.939, 0.923, 0.938, 0.908 and 0.821 with negligible statistical uncertainties.

A complete list of systematic uncertainties assigned is summarized in Table 5.2.

Table 5.2: Systematic uncertainties.(in %)

p_T [GeV/c]	$\epsilon^{\rm reco}_{\rm DC}$	$\epsilon^{\rm reco}_{\rm HBD}$	$\epsilon^{\rm reco}_{\rm PC3}$	$\epsilon^{\rm reco}_{\rm RICH}$	$\epsilon_{\rm geo.\ acc.}$
5 ∼6	2.8	1.6	4.5	12.1	2.0
6∼7	2.8	1.6	4.5	2.6	2.0
7∼8	2.8	1.6	4.5	0.9	2.0
8∼9	2.8	1.6	4.5	0.6	2.0
9∼11	2.8	1.6	4.5	0.5	2.0
11∼13	2.8	1.6	4.5	0.5	2.0

Chapter 6

Measurement of Double Longitudinal asymmetries

As discussed in Sec. 1.3, double longitudinal asymmetry A_{LL} of single inclusive production in proton-proton collisions is an observable through which one can extract information on polarized gluon distribution. This section will first discuss how we experimentally determine these asymmetries whose theoretical definition was given in Eq. 1.14. A number of statistical analyses that shed lights on potential systematic uncertainty sources will follow after that. The background asymmetries despite its small effect will be quantified at last.

6.1 Estimator

In order to determine an unbiased and efficient estimator for the stated asymmetry, a maximum likelihood method is adopted as often is the case for most experimental observables. Following is a few important pieces of information relevant to this method.

Asymmetries are calculated on a fill-by-fill basis for various reasons, one of which is the fact that we can make reliable polarization measurements of beam and target particles in this duration of time. Another important reason is because a fill is a period of beam collision time during which the detector performance is safely assumed even and stable. This is indeed one essential assumption that has been made in order to simplify the estimator for A_{LL}.

Asymmetry calculation involves counting number of events and so the probability distribution is Poissonian. From the known relation Eq. 6.1 for the expected number of pions produced from incoming protons with a certain combination of spin states,

$$
\begin{aligned}
E[N_\alpha^{\pi^{+(-)}}] &= c_0 \cdot d\sigma_\alpha(p+p \to \pi^{+(-)} + X) \cdot N_\alpha^{\mathrm{BBC}} \\
&\equiv d\bar{\sigma}_\alpha \cdot N_\alpha^{\mathrm{BBC}}
\end{aligned}
$$

$$
\begin{aligned}
\alpha = \{s_B, s_Y\} &: \text{ the spin states of blue and yellow beam} \\
N_\alpha^{\pi^{+(-)}} &: \text{the number of } \pi^{\pm}\text{events from a spin state } \alpha \\
N_\alpha^{\mathrm{BBC}} &: \text{the number of BBC counts} \\
c_0 &: \text{all spin state independent correction factors combined.}
\end{aligned} \tag{6.1}
$$

the maximum likelihood function is defined as given in Eq. 6.2. The superscript $+(-)$ in $\pi^{+(-)}$ will be suppressed from here on since it is obvious that pions with different charge have to be treated separately.

$$
\begin{aligned}
L(\bar{\sigma}, \epsilon) &= \log \prod_{\alpha=++,+-} f_{\mathrm{Poisson}}(N_\alpha^\pi, \bar{\sigma}(1 + P_B^{s_B} P_Y^{s_Y} \cdot \epsilon) N_\alpha^{BBC}) \\
&\text{where } f_{\mathrm{Poisson}}(k, \lambda) = \frac{\lambda^k}{k!} e^{-\lambda}
\end{aligned} \tag{6.2}
$$

In the function in Eq. 6.2, the second argument is nothing but the expectation value of N_α^π expressed in terms of two independent parameters newly introduced: $\bar{\sigma} = \frac{d\bar{\sigma}_{++} + d\bar{\sigma}_{+-}}{2}$ and $\epsilon = \frac{d\bar{\sigma}_{++} - d\bar{\sigma}_{+-}}{d\bar{\sigma}_{++} + d\bar{\sigma}_{+-}}$. The first parameter is the spin averaged differential cross section with all correction factors absorbed. In order for this to have a physical meaning, efficiencies over each fill have to be stable, which is a reasonably good assumption. The second parameter is the observable that we are interested in. Applying the maximum likelihood conditions $\frac{dL}{d\bar{\sigma}} = 0$ and $\frac{dL}{d\epsilon} = 0$ and using the relations $P_B^+ = -P_B^- = P_B$ and $P_Y^+ = -P_Y^- = P_Y$, the resulting experimental estimator and uncertainty are obtained through equations given in Eq. 6.3 and Eq. 6.4.

$$
A_{LL} = \frac{1}{P_B \cdot P_Y} \frac{N^{\uparrow\uparrow} - R \cdot N^{\uparrow\downarrow}}{N^{\uparrow\uparrow} - R \cdot N^{\uparrow\downarrow}}, \qquad R \equiv \frac{L^{\uparrow\uparrow}}{L^{\uparrow\downarrow}} \tag{6.3}
$$

$$\delta A_{LL} = \frac{1}{P_B \cdot P_Y} \frac{2 \cdot R \cdot N^{\uparrow\uparrow} \cdot N^{\uparrow\downarrow}}{(N^{\uparrow\uparrow} + R \cdot N^{\uparrow\downarrow})^2} \cdot \sqrt{\frac{1}{N^{\uparrow\uparrow}} + \frac{1}{N^{\uparrow\downarrow}}} \tag{6.4}$$

Following are discussions on various spin dependent systematic effect studies. Shuffled asymmetries and their χ^2 distributions, devised to detect potential systematic effects, are statistical tools that exploit the analytical form of the observable. Other physical asymmetries such as single spin asymmetries are also used for a cross check. Hypothesis tests for single sample and two-sample cases are employed as well for more quantitative analysis.

6.2 Systematic effects study

6.2.1 Bunch shuffling - χ^2 test

The first approach uses knowledge about the χ^2 distribution. Clarifying some properties and definitions is in order so as to avoid any misuse of statistical methods. The χ^2 distribution is defined as

the probability distribution function of $U = \sum_{j=1}^{m} Z_j^2$,

where $Z_1, Z_2, ...Z_m$ are independent **standard normal** random variables and m is called the degree of freedom.

In our case, $U = \sum_{j=1}^{m} (\frac{x_j - \bar{x}}{\sigma_j})^2$; here $\bar{x}$ is the asymmetry to be determined by minimizing χ^2 in fitting x_j's to a constant or equivalently by taking the weighted average of x_j's. Variable x_j represents the asymmetry calculated for the j'th fill, and there is a total of m fills. σ_j is the standard deviation of x_j. The degrees of freedom is m-1 as there is one parameter $\bar{x}$ to be determined. Since we are 'testing' properties of the random variables used in this analysis, we do not assume our Z_j's in the U variable meet the independence nor normal condition.

From its definition, one will realize that the χ^2 distribution can be used to test how "normal" the random variables (terms in the parenthesis) are. Although this could potentially be a very practical test on the asymmetry itself as the average of normal variables is also a normal variable, there are some level of subtleties worth revisiting later. A normal random variable can have a nonnormal distribution when there are unknown systematic effects involved in measurements, and we will see distortions in the χ^2 distribution

if those effects dominate the uncertainties. One should also beware of the fact that the test will not work so well in low statistics environment as the variables will hold the Poissonian distribution rather than the normal probability distribution even in the lack of prominent systematic sources. Fills without any charged pions in any one type of spin combination should also not be included since they are not physical. By the same token, fills with nonpositive count in any one of four spin combinations are excluded in this analysis.

To see if there is any correlation between the double asymmetries of different fills, which is the original goal of the test, let us consider a method called 'bunch shuffling'. In this method, we reassign a random spin polarization to each of all bunches in a fill. Do this procedure for all the fills simultaneously and then repeat it a large number of times. Abundant fill-by-fill fake asymmetries will be created as a result. Fitting these fill-by-fill asymmetries to a constant provides us with useful information although the average asymmetry value from each fit does not hold any physical meaning.

If the fake double asymmetries calculated with random spin combinations are truly independent, the variable U would follow the χ^2 (Gamma) probability distribution, which is given by Eq. 6.5, with the degrees of freedom m-1. The conclusion should be applied to physical asymmetries as well since the physical double asymmetries are merely one special case of a more general type. That is, one can test the independence of physical asymmetries by looking at the U distribution created from bunch shuffling[1]. Any significant deviation from the normal χ^2 distribution indicates the potential existence of correlation between the physical asymmetries for different fills.

We start the asymmetry calculation with a requirement of $N_\alpha > 2$ for each α state. The distributions of fake double asymmetries calculated under this condition are shown in Fig. 6.1 and Fig. 6.2. The distributions are indeed Gaussian with the mean sitting around zero as expected and the sigma of Gaussian is comparable to the statistical uncertainty of physical double asymmetries. The U distributions are shown in Fig. 6.3 and Fig. 6.4 with their expected χ^2 distributions in solid line. One can immediately notice the slight deviation from Gamma distribution in the highest p_T bin.

[1]The U distribution can be obtained by taking χ^2's resulted from fitting the fake (bunch-shuffled) asymmetries.

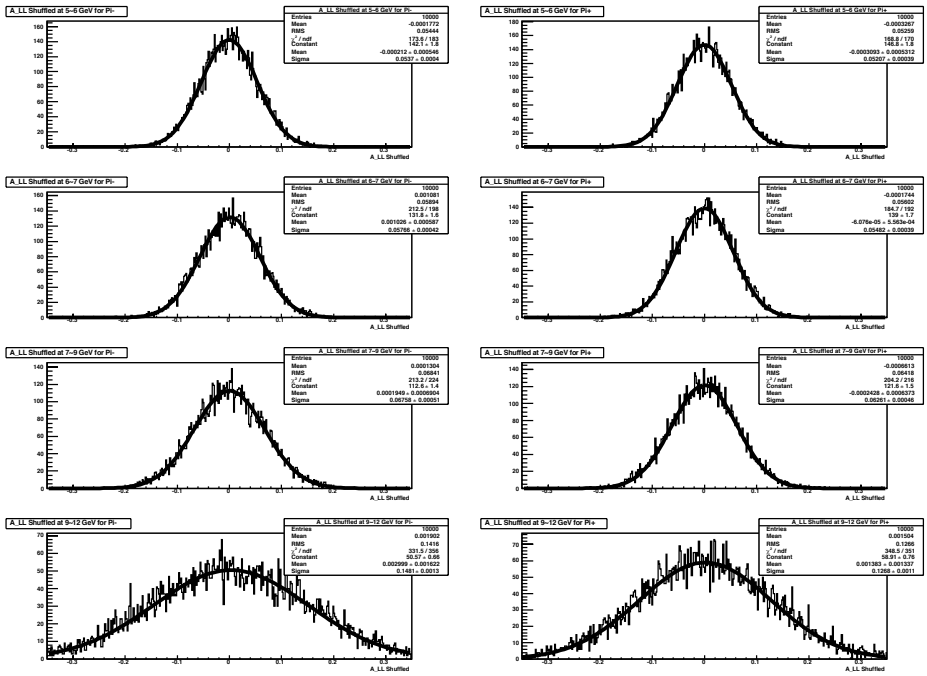

(a) Pattern 1. Left: π^-, Right:π^+

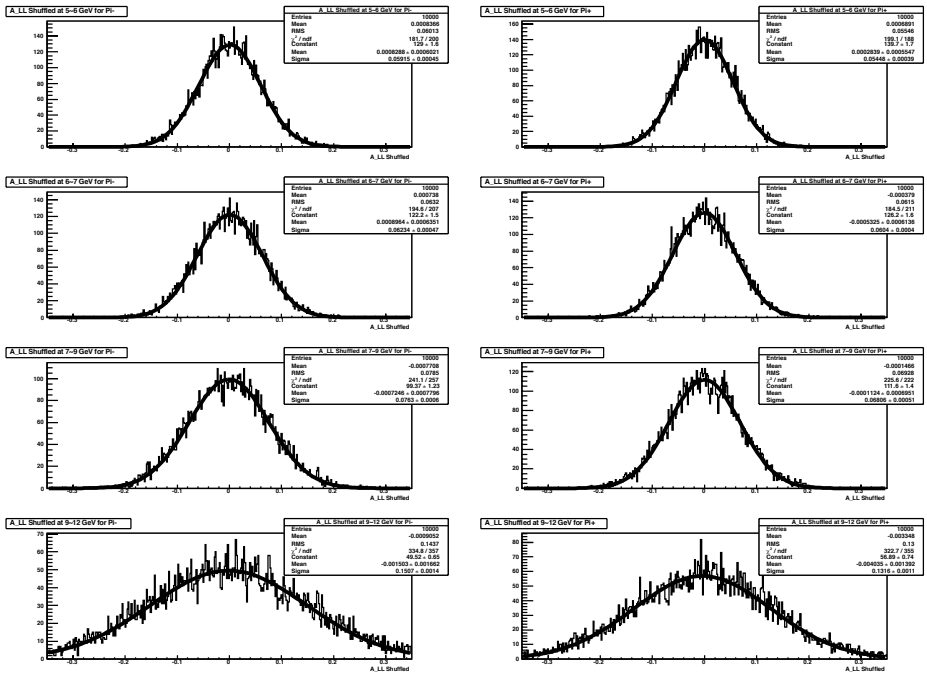

(b) Pattern 2. Left: π^-, Right:π^+

Figure 6.1: Fake double helicity asymmetries - continued on the next page with description.

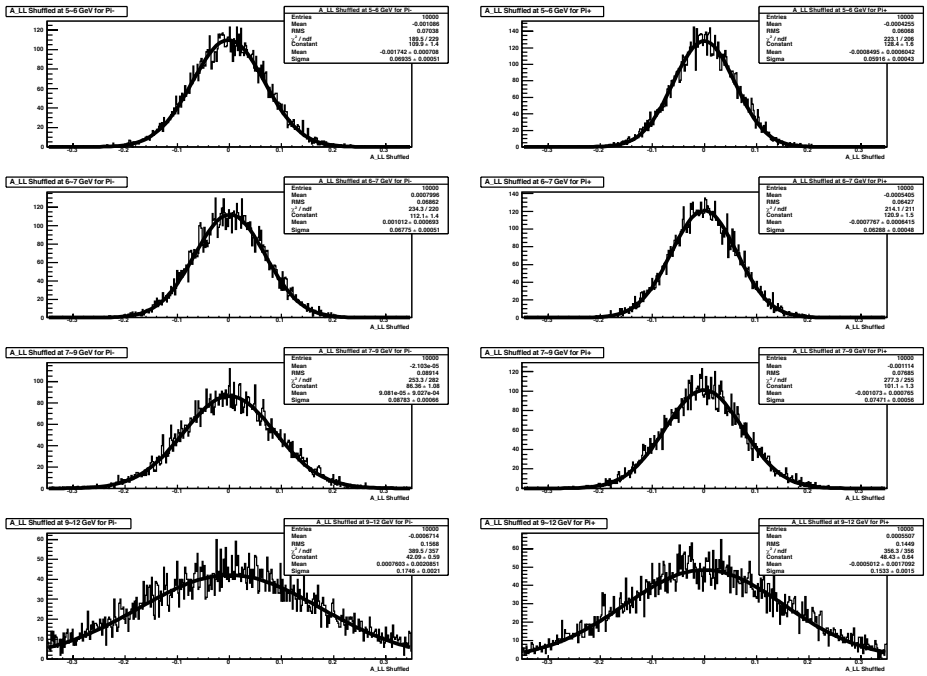

(c) Pattern 3. Left: π^-, Right:π^+

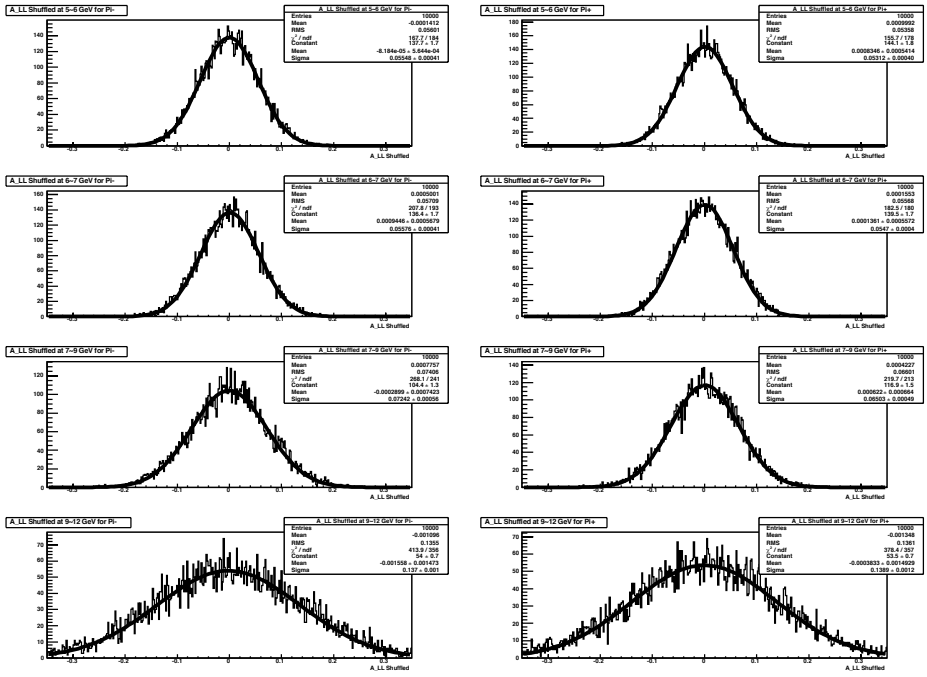

(d) Pattern 4. Left: π^-, Right:π^+

Figure 6.1: Fake double helicity asymmetries from bunch shuffling for even crossing.

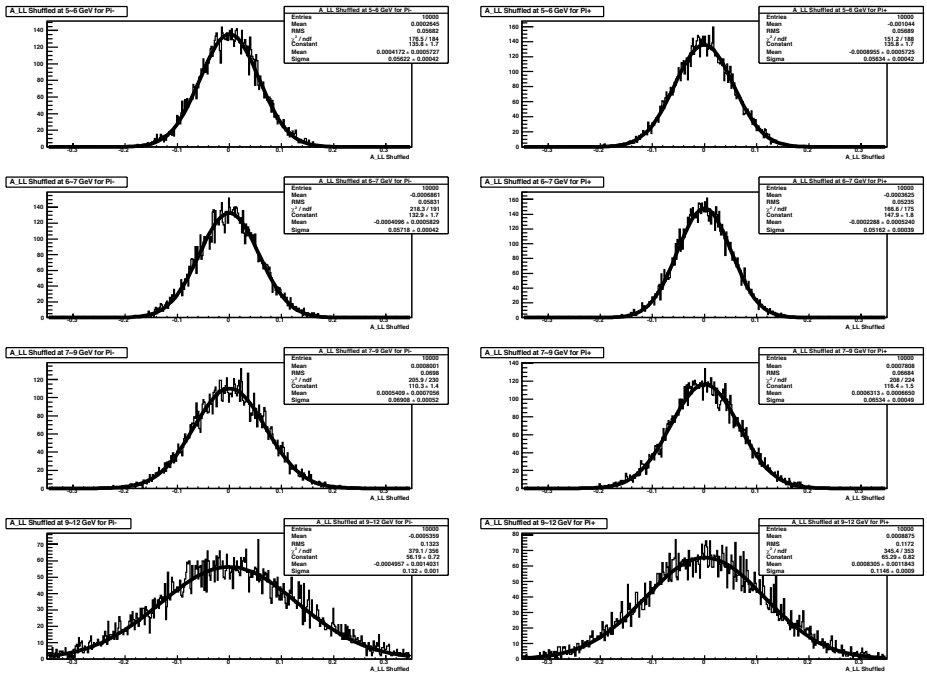

(a) Pattern 1. Left: π^-, Right:π^+

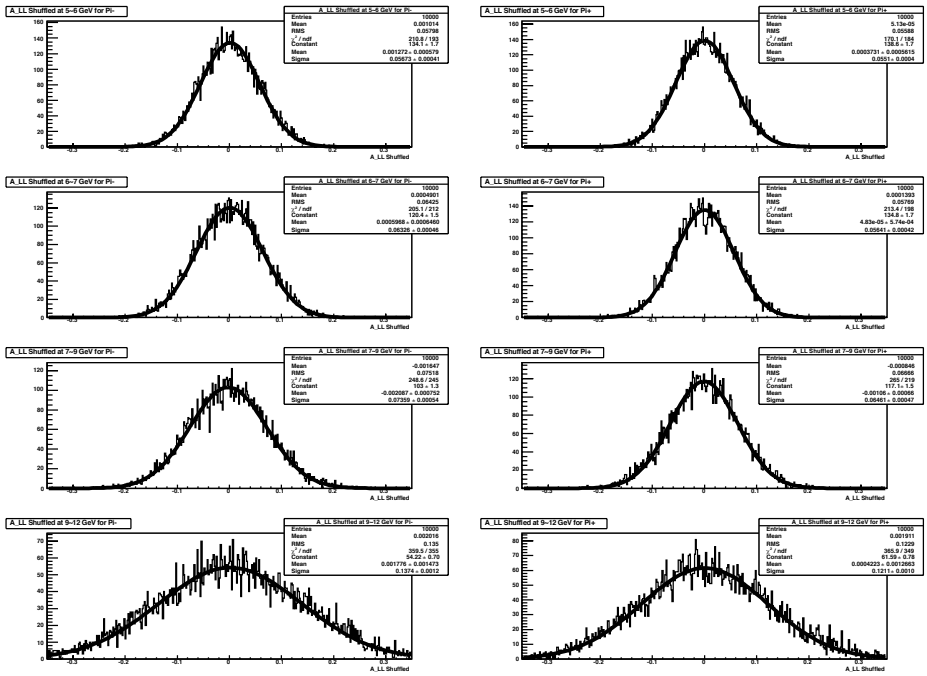

(b) Pattern 2. Left: π^-, Right:π^+

Figure 6.2: Fake double helicity asymmetries - continued on the next page with description.

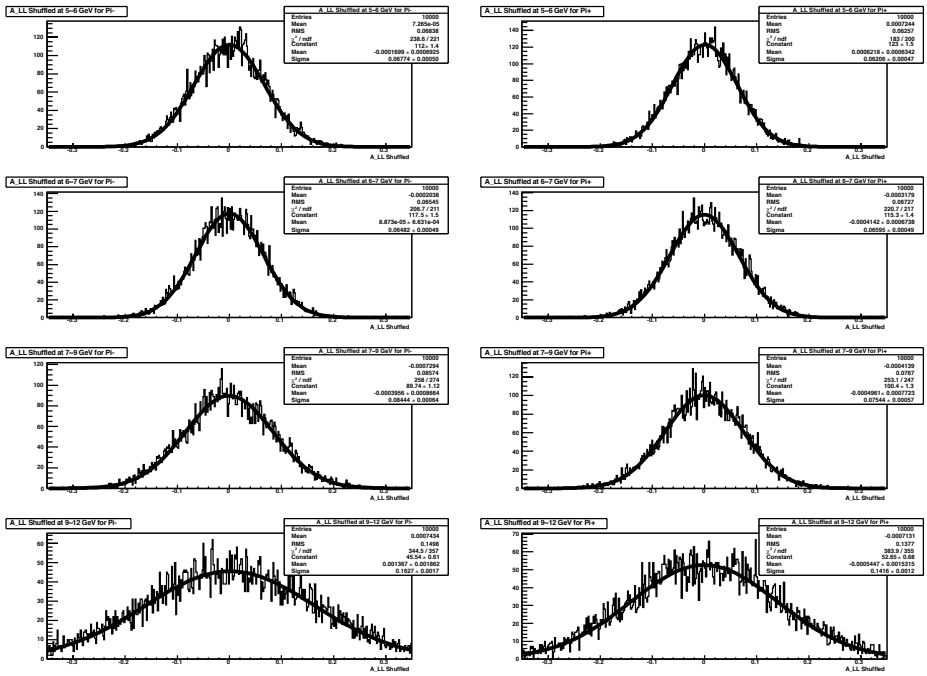

(c) Pattern 3. Left: π^-, Right:π^+

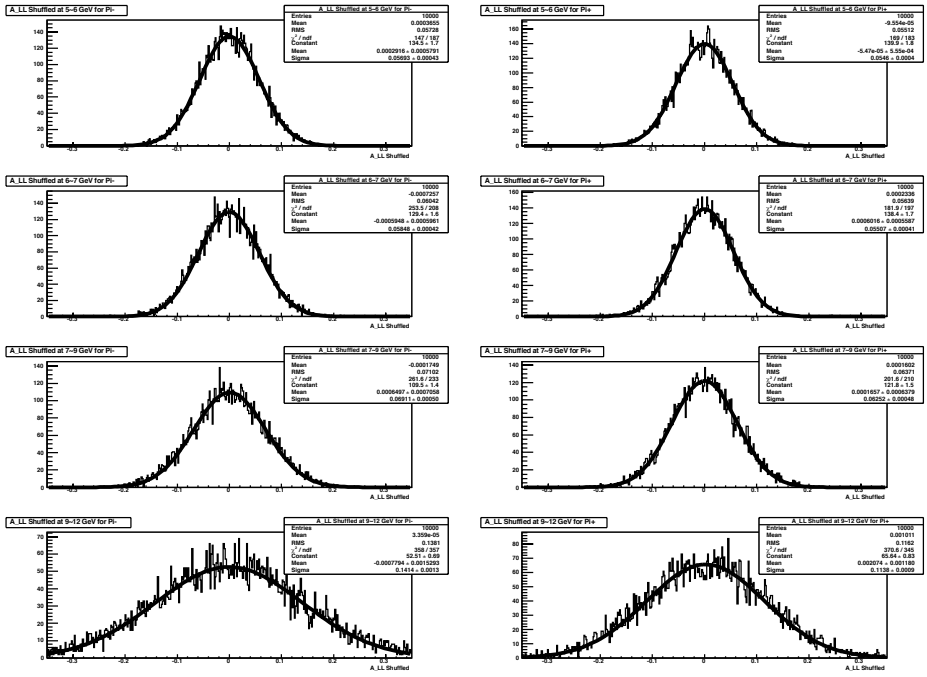

(d) Pattern 4. Left: π^-, Right:π^+

Figure 6.2: Fake double helicity asymmetries from bunch shuffling for odd crossing.

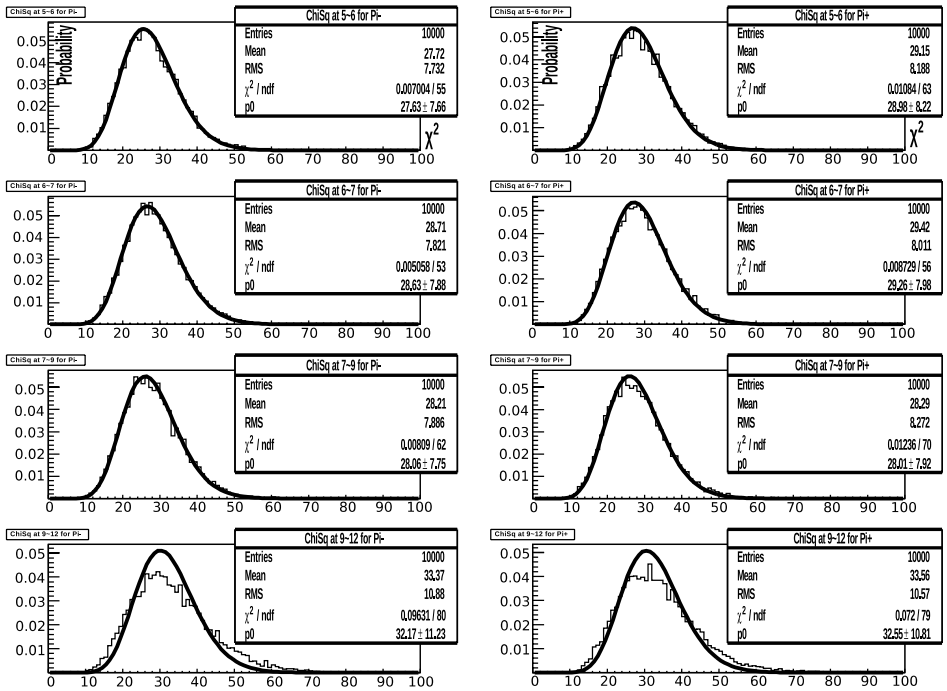

(a) Pattern 1. Left: π^-, Right:π^+

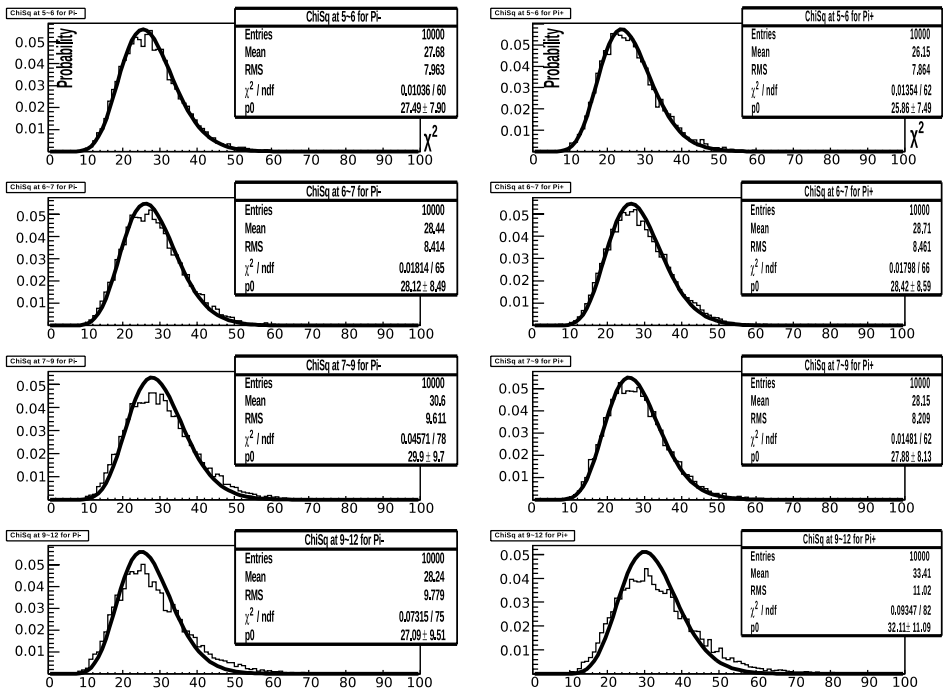

(b) Pattern 2. Left: π^-, Right:π^+

Figure 6.3: U distributions - continued on the next page with description.

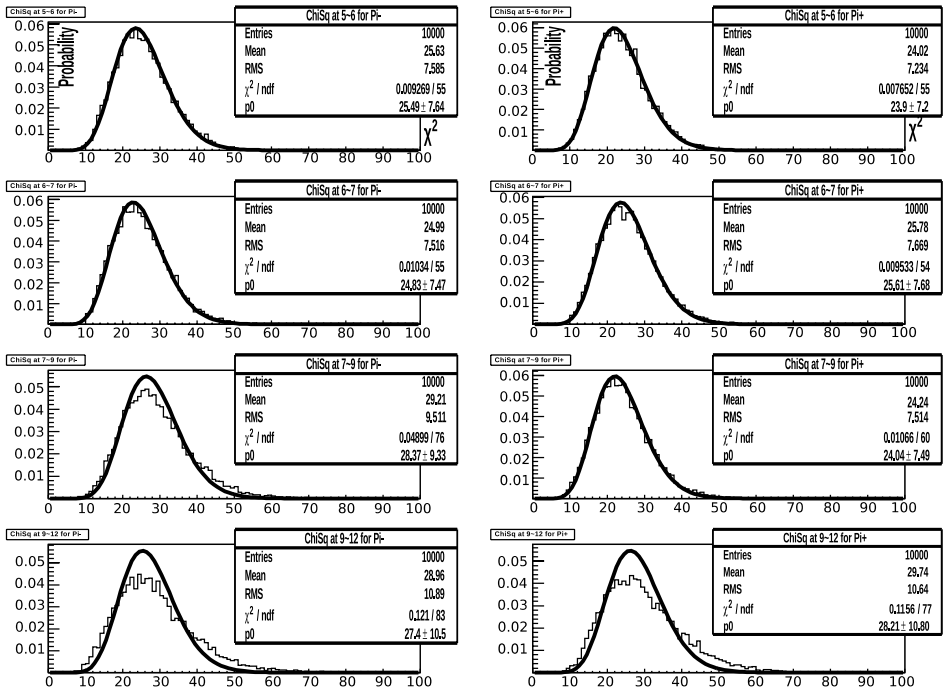

(c) Pattern 3. Left: π^-, Right:π^+

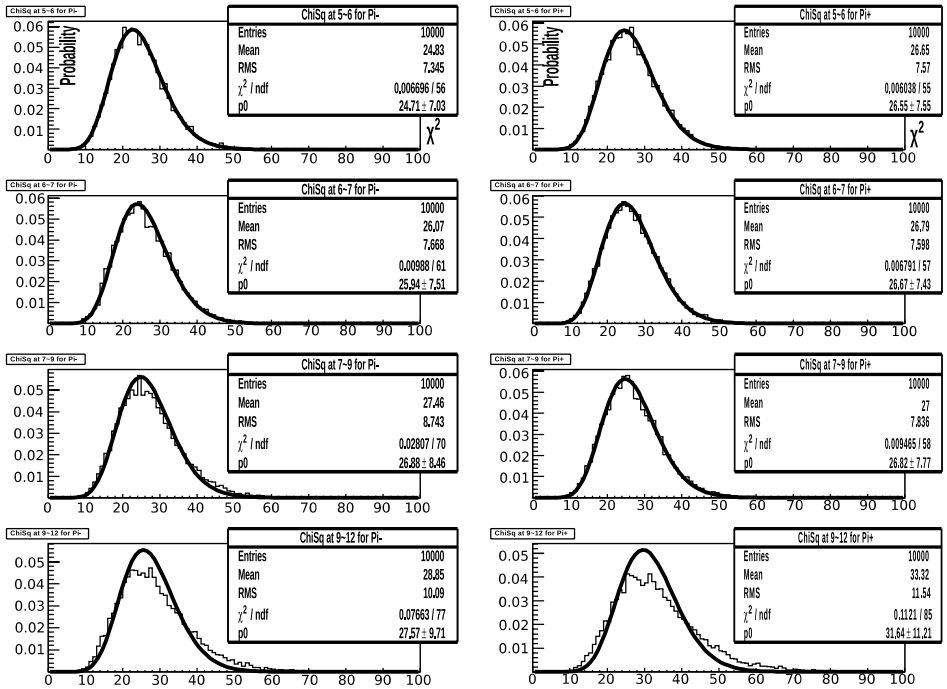

(d) Pattern 4. Left: π^-, Right:π^+

Figure 6.3: U distributions created from bunch shuffling for even crossing.

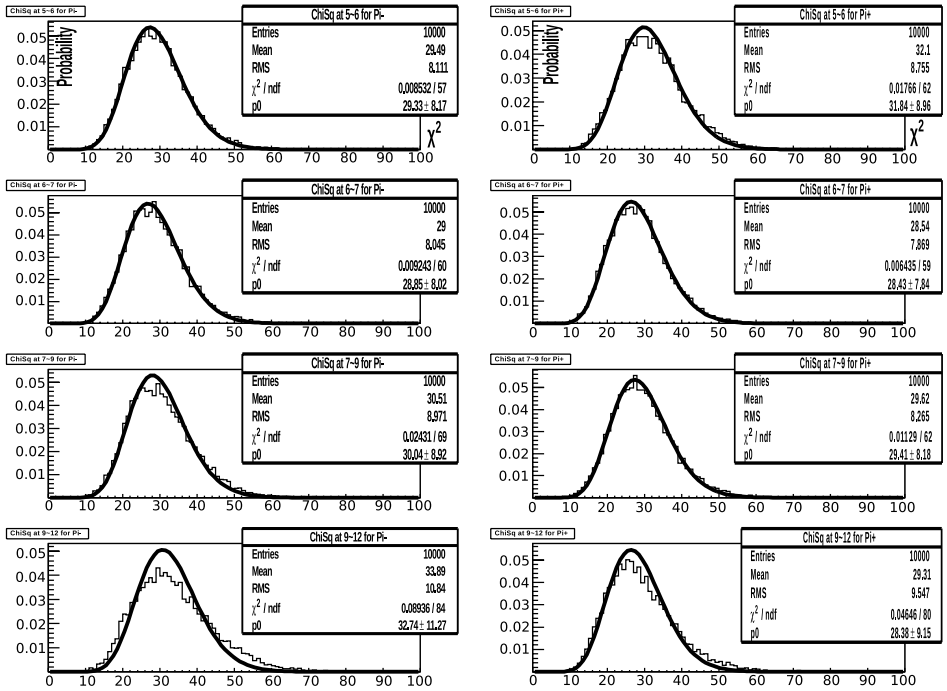

(a) Pattern 1. Left: π^-, Right:π^+

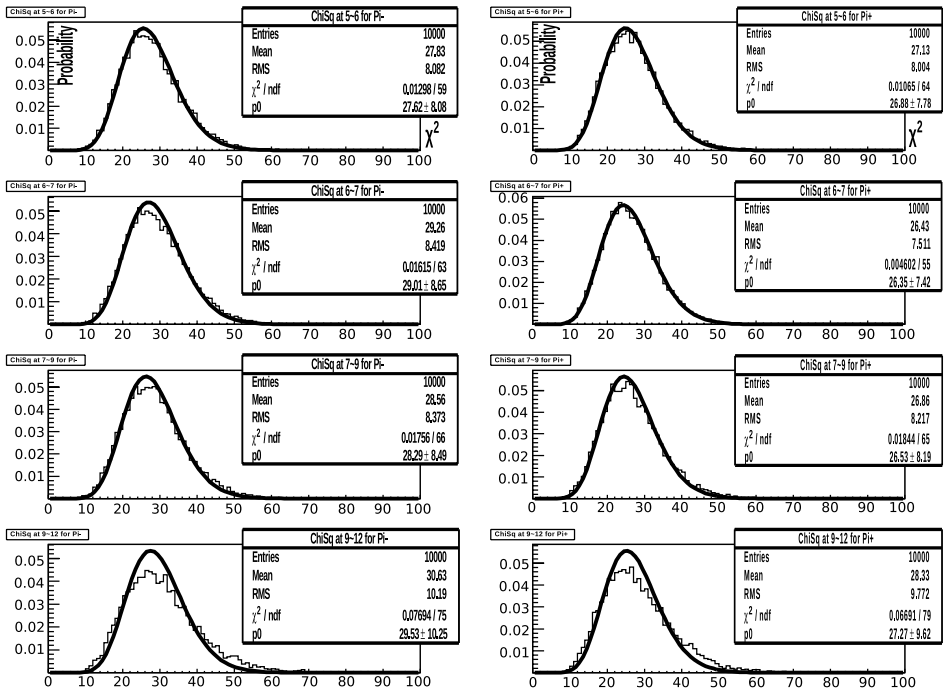

(b) Pattern 2. Left: π^-, Right:π^+

Figure 6.4: U distributions - continued on the next page with description.

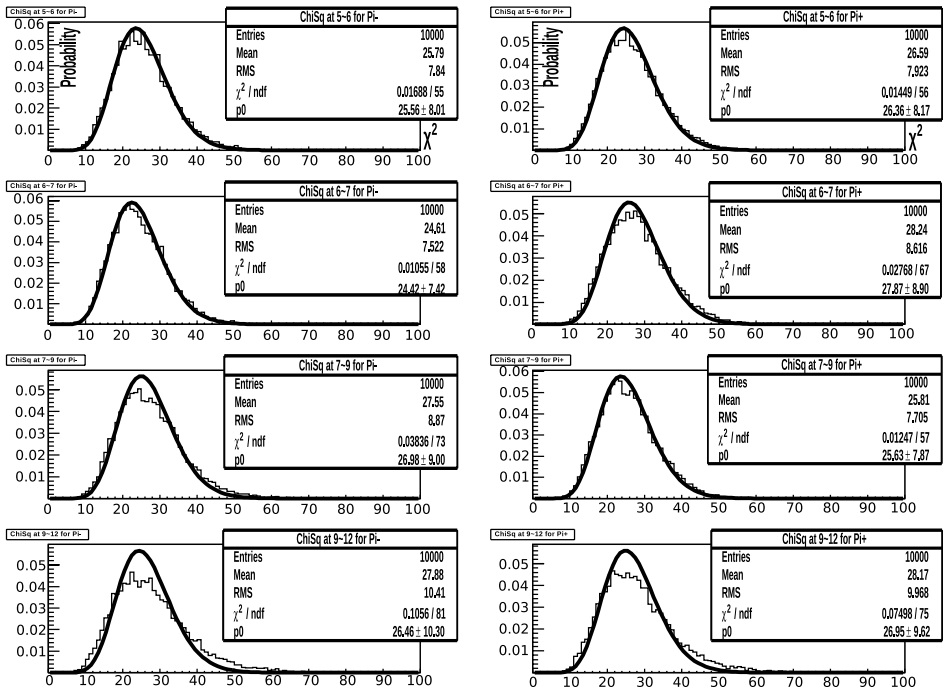

(c) Pattern 3. Left: π^-, Right:π^+

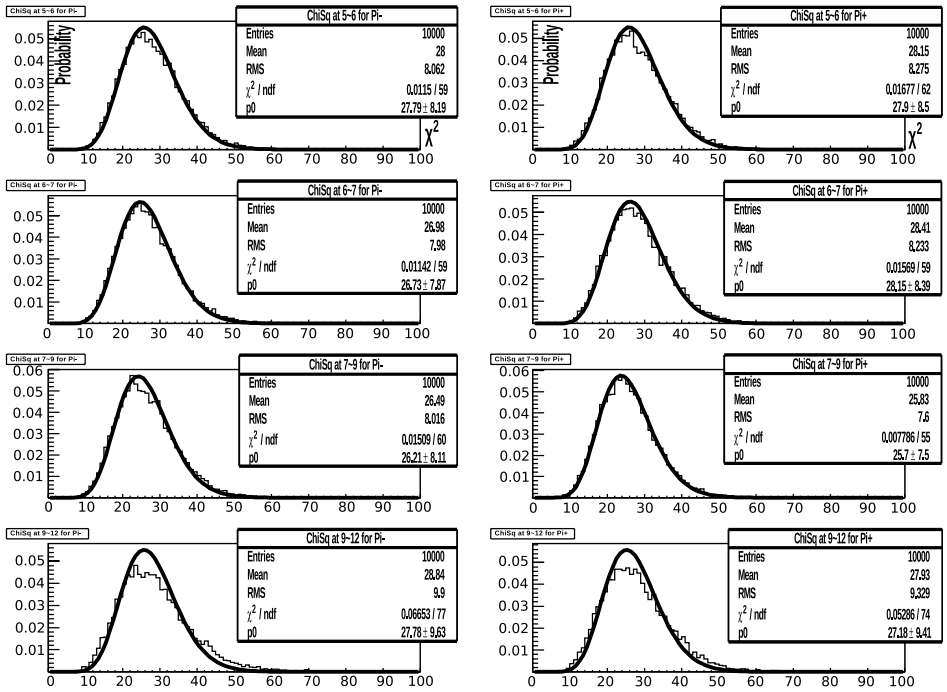

(d) Pattern 4. Left: π^-, Right:π^+

Figure 6.4: U distributions created from bunch shuffling for odd crossing.

$$f_U(u) \;=\; \frac{1}{2^{m/2}\;\Gamma(\frac{m}{2})}\;u^{(m/2)-1}\;e^{-u/2},\;\; u \geq 0 \quad : \text{ The } \chi^2 \text{ distribution} \tag{6.5}$$

Since we know that statistics runs out at the highest p_T, we can attempt to collect more statistics and see if this distortion purely comes from Poissonian probability distribution. There are two ways to collect more statistics: by combining either patterns or even/odd crossings. Results for both cases are shown in Fig. 6.5. Combining patterns does not seem to mitigate this effect, while combining crossings turns out to improve the shape of distributions. The reason for this is because combining patterns is equivalent to adding more fills, whereas combing crossings adds more statistics to N_α in each fill. What the U distribution cares about is the probability distribution for each N_α in individual fills rather than the one for the entire fills. Results from requiring $N_\alpha > 10$ in Fig. 6.5(c) confirms this claim.

On the other hand, it is noteworthy that the fake asymmetries are always normal regardless of the kind of probability distribution. This can be attributed to the theorem called the "Central limit theorem". It states that

Let W_1,W_2, ... be an infinite sequence of independent random variables, each with the same distribution. Suppose that the mean μ and the variance σ^2 of $f_W(w)$ are both finite. For any numbers a and b, then
$\lim_{n\to\infty} P(a \leq \frac{W_1+W_2\cdots+W_n-n\mu}{\sqrt{n}\sigma} \leq b) = \frac{1}{\sqrt{2\pi}}\int_a^b e^{-\frac{z^2}{2}}dz$.

Since the asymmetries we get by minimizing the χ^2 is the weighted average of the asymmetries for individual fills as we saw earlier, this theorem is applicable to our asymmetries. There is also enough number of fills to reach the large n limit. This is why we always see a normal distribution in the fake asymmetries.

From this section's analysis, we can safely conclude that the asymmetries follow anticipated statistical probability distributions and there is no systematic uncertainty found larger than the statistical one.

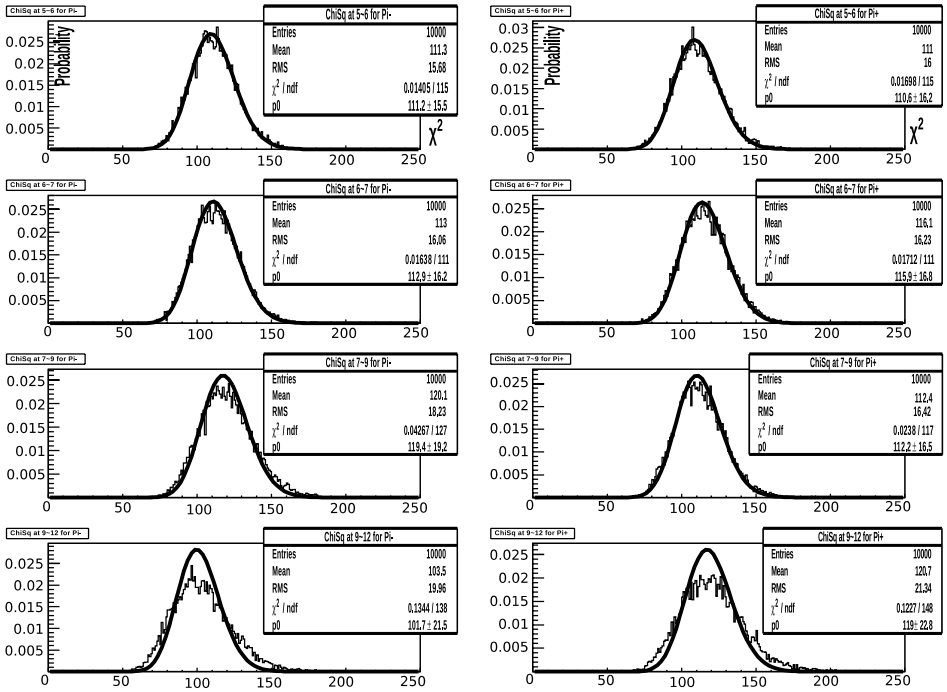

(a) Even crossings, Patterns combined. Left: π^-, Right:π^+

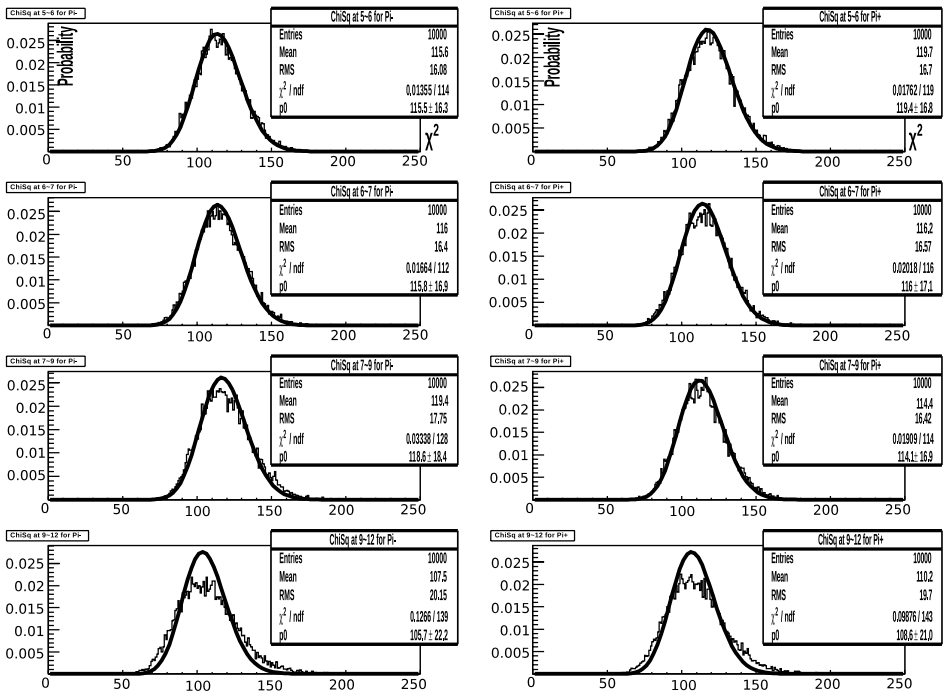

(b) Odd crossings, Patterns combined. Left: π^-, Right:π^+

Figure 6.5: U distributions - continued on the next page with description.

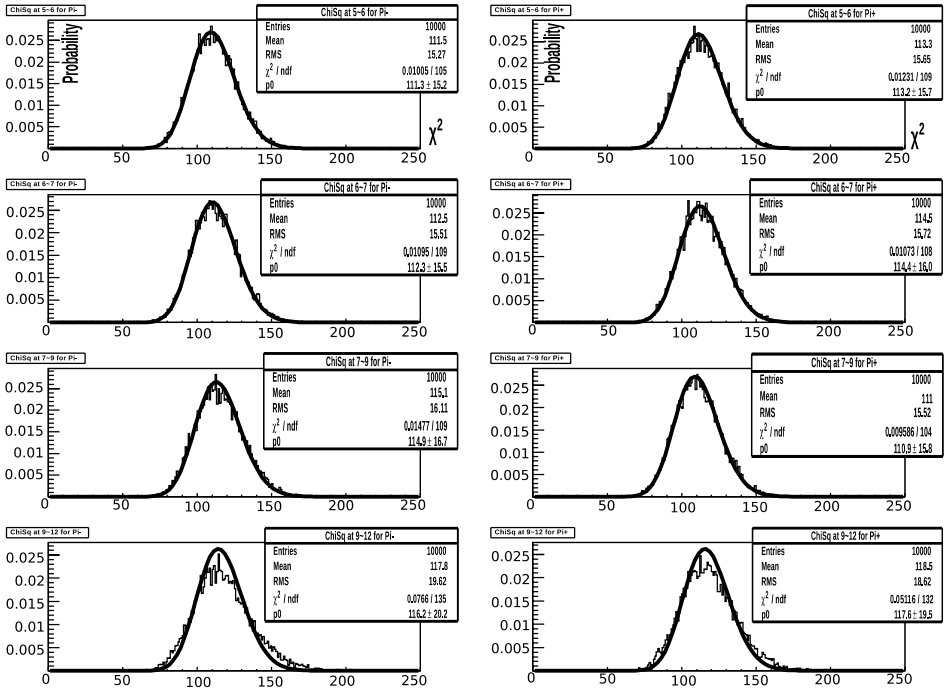

(c) Crossings and Patterns combined. Left: π^-, Right:π^+

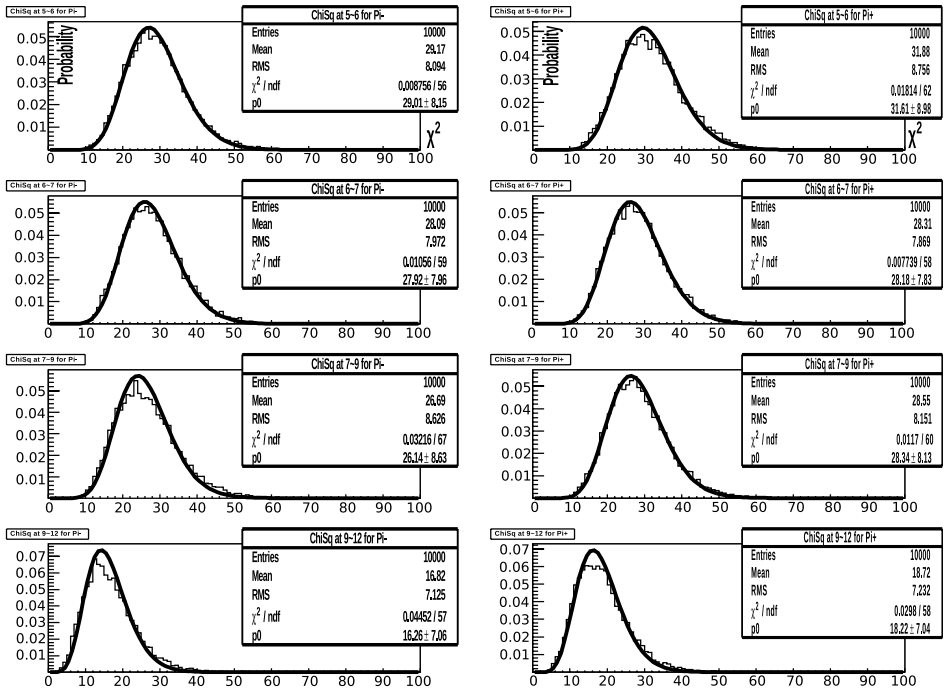

(d) Odd crossing Pattern 1 $N_\alpha > 10$. Left: π^-, Right:π^+

Figure 6.5: U distributions created from bunch shuffling for combined statistics.

6.2.2 Single spin asymmetries - test of parity conservation

The method described in the previous section made sure that the double asymmetries conform normal distribution and each measurement for a fill is independent of one another, but did not tell us much about bunch-to-bunch correlation which can directly affect the result of physical double asymmetries. To be able to judge how meaningful the measured asymmetries are, one needs something more than averaging fake asymmetries which ignore the asymmetry values themselves. A suitable candidate is the single spin asymmetry as this variable is orthogonal to (or independent of) the double longitudinal asymmetry.

Single longitudinal spin asymmetry A_L, can be determined for each side of yellow and blue beam. In a fashion similar to double longitudinal asymmetry, it is defined as the ratio of the difference and the sum of the opposite helicity cross section as given by Eq. 6.6.

$$A_L^{\uparrow 0} = \frac{\sigma^{\uparrow\uparrow} + \sigma^{\uparrow\downarrow} - \sigma^{\downarrow\uparrow} - \sigma^{\downarrow\downarrow}}{\sigma^{\uparrow\uparrow} + \sigma^{\uparrow\downarrow} + \sigma^{\downarrow\uparrow} + \sigma^{\downarrow\downarrow}} \tag{6.6}$$

$$A_L^{\uparrow 0} = \frac{1}{P}\frac{N^{\uparrow\uparrow}/L^{\uparrow\uparrow} + N^{\uparrow\downarrow}/L^{\uparrow\downarrow} - N^{\downarrow\uparrow}/L^{\downarrow\uparrow} - N^{\downarrow\downarrow}/L^{\downarrow\downarrow}}{N^{\uparrow\uparrow}/L^{\uparrow\uparrow} + N^{\uparrow\downarrow}/L^{\uparrow\downarrow} + N^{\downarrow\uparrow}/L^{\downarrow\uparrow} + N^{\downarrow\downarrow}/L^{\downarrow\downarrow}} \tag{6.7}$$

$$\begin{aligned}
\delta A_L^{\uparrow 0} &= \delta\left(\frac{1}{P}\frac{N^{\uparrow\uparrow}/L^{\uparrow\uparrow} + N^{\uparrow\downarrow}/L^{\uparrow\downarrow} - N^{\downarrow\uparrow}/L^{\downarrow\uparrow} - N^{\downarrow\downarrow}/L^{\downarrow\downarrow}}{N^{\uparrow\uparrow}/L^{\uparrow\uparrow} + N^{\uparrow\downarrow}/L^{\uparrow\downarrow} + N^{\downarrow\uparrow}/L^{\downarrow\uparrow} + N^{\downarrow\downarrow}/L^{\downarrow\downarrow}}\right) \\
&\simeq \frac{1}{P}\delta\left(\frac{R-1}{R+1}\right), \qquad \text{where } R \equiv \frac{N^{\uparrow\uparrow}/L^{\uparrow\uparrow} + N^{\uparrow\downarrow}/L^{\uparrow\downarrow}}{N^{\downarrow\uparrow}/L^{\downarrow\uparrow} + N^{\downarrow\downarrow}/L^{\downarrow\downarrow}} \\
&= \frac{2}{P}\frac{\delta(R)}{(R+1)^2} \\
&= \frac{2}{P}\frac{R}{(1+R)^2}\sqrt{(N^{\uparrow\uparrow} + N^{\uparrow\downarrow}(\frac{L^{\uparrow\uparrow}}{L^{\uparrow\downarrow}})^2 + N^{\downarrow\uparrow} + N^{\downarrow\downarrow}(\frac{L^{\downarrow\uparrow}}{L^{\downarrow\downarrow}})^2)}
\end{aligned} \tag{6.8}$$

It is trivial to check that double asymmetries are independent of single asymmetries: set $a \cdot A_{LL} + b \cdot A_L$ equal to 0 and prove that $a = b = 0$. Unlike the double asymmetries, the first (or second) pair of terms in the numerator in the definition of A_L cannot be added up as the two are not guaranteed to be the same by conservation law. The estimator of A_L and its uncertainties are worked out in a manner similar to double asymmetries, and the results are

given in Eq. 6.7 and Eq. 6.9.

With these correct definitions, we expect the single longitudinal asymmetries to be consistently zero due to parity conservation. In reality, unknown spin dependent systematic effects in experiment can cause nonzero single spin asymmetries. The first order effects such as detector efficiency or beam intensity variation in a fill are reduced by bunch-to-bunch spin flipping technique. The residual second order effects are expected to cancel out by rotating four different spin patterns from fill to fill. The studies with four spin patterns is postponed until the next section as it deserved a dedicated section of discussion. The efficiency difference between two separate ERT circuit boards is among the known sources of potential spin dependent effects. For this reason, asymmetries are calculated for even and odd crossings separately at first and then averaged over with weights later. The results are shown in Fig. 6.6 and Fig. 6.7.

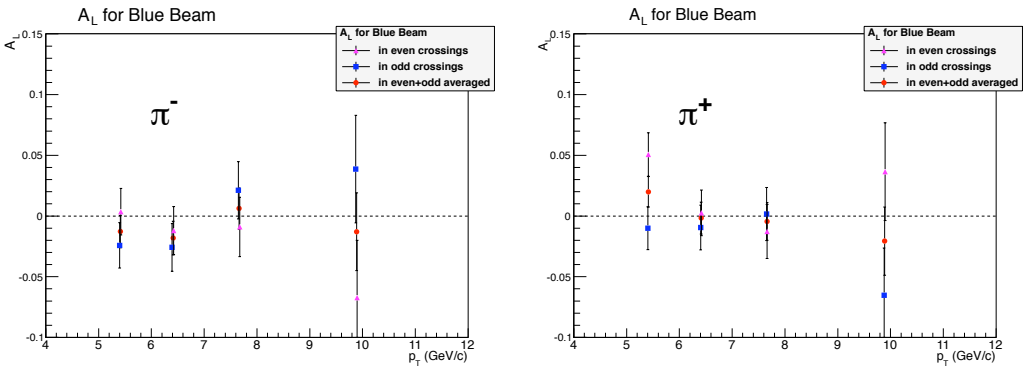

(a) even/odd/averaged-over crossings for π^- (b) even/odd/averaged crossings for π^+

Figure 6.6: A_L versus p_T for Blue Beam

In order to draw a conclusion regarding whether the asymmetries measured here are statistically consistent with zero, one should perform a z-test. The implication of this test results will be discussed in detail in the next section and only results will be presented in this section. The null hypothesis is $H_0 : A_L^{\text{Blue (Yellow)}} = 0$. Fig. 6.8 shows the z-ratio calculated for even/odd crossings $+/-$ charges and their projected distribution for each beam separately.

The test results allow us to conclude that the single longitudinal asymmetries are consistently zero as expected at the significance level of α= 0.10

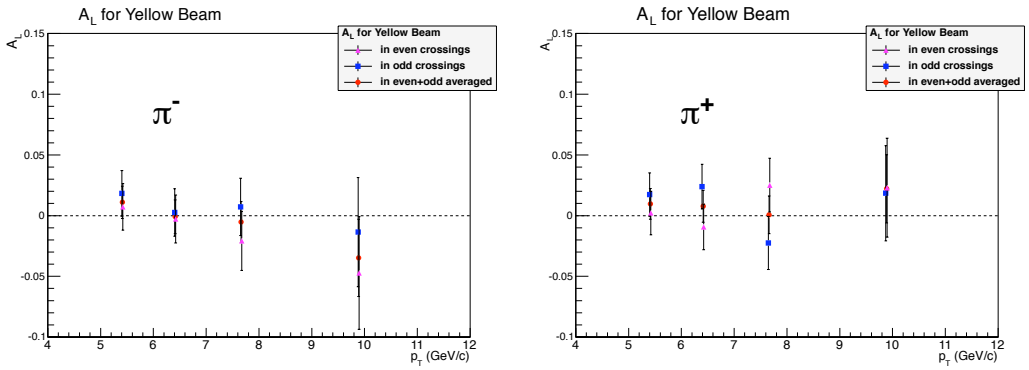

(a) even/odd/averaged-over crossings for π^- (b) even/odd/averaged crossings for π^+

Figure 6.7: A_L versus p_T for Yellow Beam

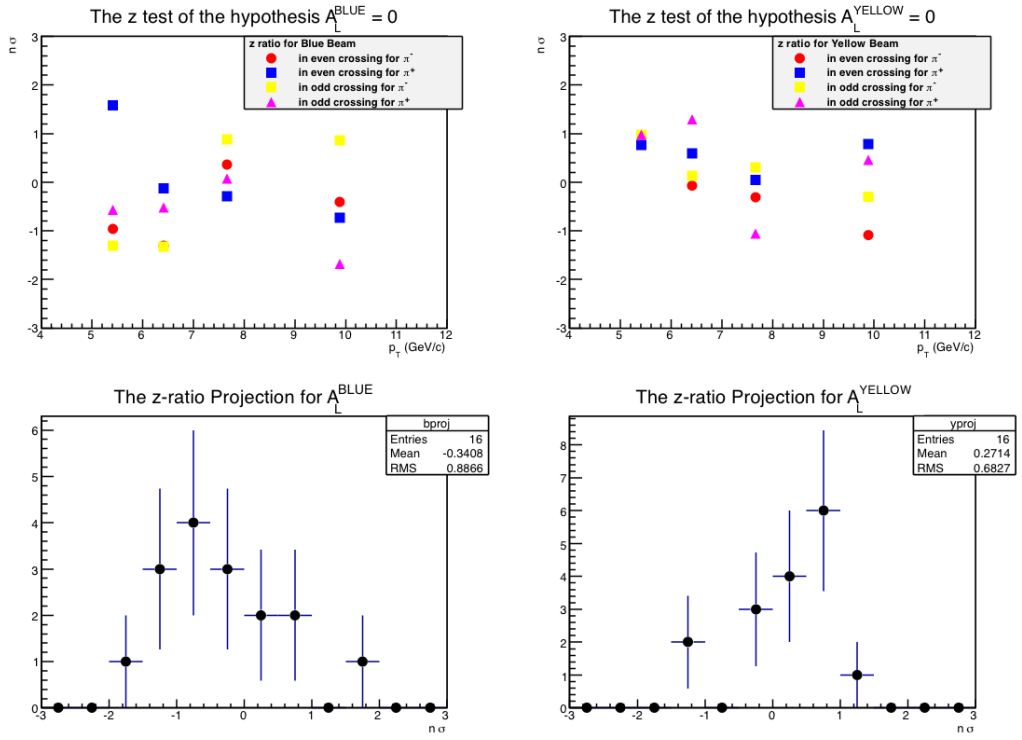

Figure 6.8: The z-test on the null hypothesis $H_0 : A_L^{\mathrm{B\,(Y)}} = 0$.

(two-sided). This completes the examination of all four independent observables that can be formed in terms of 4 helicity cross section - A_{LL}, A_L^{Blue}, A_L^{Yellow} and $1 = \frac{\sigma^{++}+\sigma^{+-}}{\sigma^{++}+\sigma^{+-}}$. Note that the common denominator of all four is

proportional to the spin averaged cross section. As we have seen in Chapter 5 one needs to do much more careful analysis in this case as there are various efficiencies that have to be considered. This is not the case in asymmetry measurements as all efficiencies in denominator and numerator are canceled against each other. On the other hand, the effects of remaining transverse component on A_{LL} in longitudinal running is estimated to be very small by measurement of A_{TT} [55].

6.2.3 Double helicity asymmetries with 4 different spin patterns - two sample z test

What is left to examine is the direct comparisons of double asymmetries between different spin patterns. Four spin patterns are defined as below :

	(BLUE)	(YELLOW)
Pattern 1	$+-+--+-+$	$++--++--$
Pattern 2	$-+-++-+-$	$++--++--$
Pattern 3	$+-+--+-+$	$--++--++$
Pattern 4	$-+-++-+-$	$--++--++$

The comparison will enable us to say conclusively that the measured double asymmetries follow statistical model and any significant inconsistency between independent measurements will be ruled out.

The nature of the problem we are facing here involves a sampling distribution that models the behavior of ***functions*** based on sets of n random variables rather than the ***individual*** measurements. There are several sampling distributions that are widely used such as normal distribution, student-t distribution, χ^2 distribution and F distribution. These distributions are utilized to reject/accept a null hypothesis of our interest as we saw in the previous section. For that reason, it is the next step to discuss what test functions are available and what distribution the test function will follow in particular cases, and eventually to determine what is appropriate in this case.

Common test functions are z-statistic or t-statistic, defined by $\frac{\bar{X}-\mu}{\sigma/\sqrt{N}}$ and $\frac{\bar{X}-\mu}{S/\sqrt{N}}$, respectively. Normally only one of the two can be used in a case, and which one can be used depends on whether the variance of random variable is known or not. Let's consider the case of **normal** random variable X. If the variation is known, the sampling distribution is simply the standard normal distribution, whereas, if unknown, the sampling distribution becomes the

student-t distribution of which discovery is credited to Willian Sealy Gosset. Thus knowing whether one knows the variance is critical as to what distribution has to be considered as a model.

If the variance is unknown, an estimator S is used instead of true σ as they become very close to each other when the sample is large, i.e., N is large. The two are distinguishable when N is small. The central peak of the t distribution is lower and fatter, and the tail is thicker. It is worth noting that the t ratio is a special case of more general form where the function is a ratio of a normal distribution to a square root of the χ^2 distribution function that is described by student-t distribution.

The question we are facing now is whether the variance is known in the asymmetry analyses. To answer this question, one should recall that counting yields is a Poisson process and the variance for that process is known to be the mean of the distribution. The asymmetries in bunch shuffling case showed the distributions followed Gaussian with good $\chi^2/d.o.f.$, indicating that the uncertainties calculated by propagating the Poissonian uncertainties on the yields of bunches are correct. So in this analysis simple z-test is appropriate to make comparisons between the asymmetries obtained from different spin

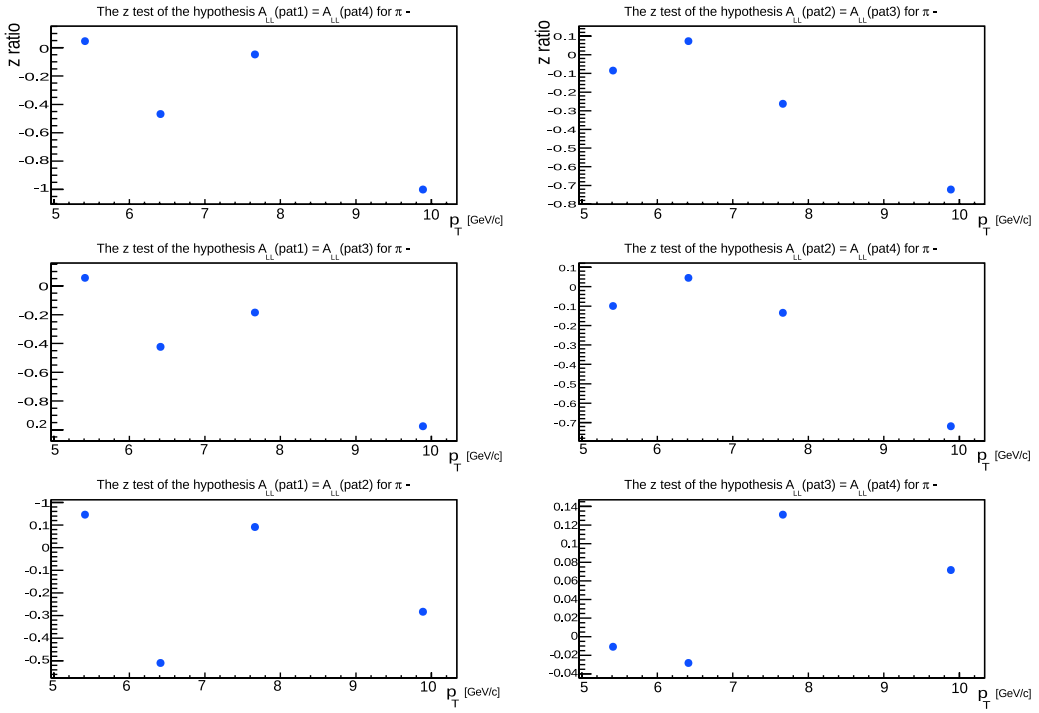

(a) z ratio for π^-

Figure 6.9: χ^2 distributions - continued on the next page with description.

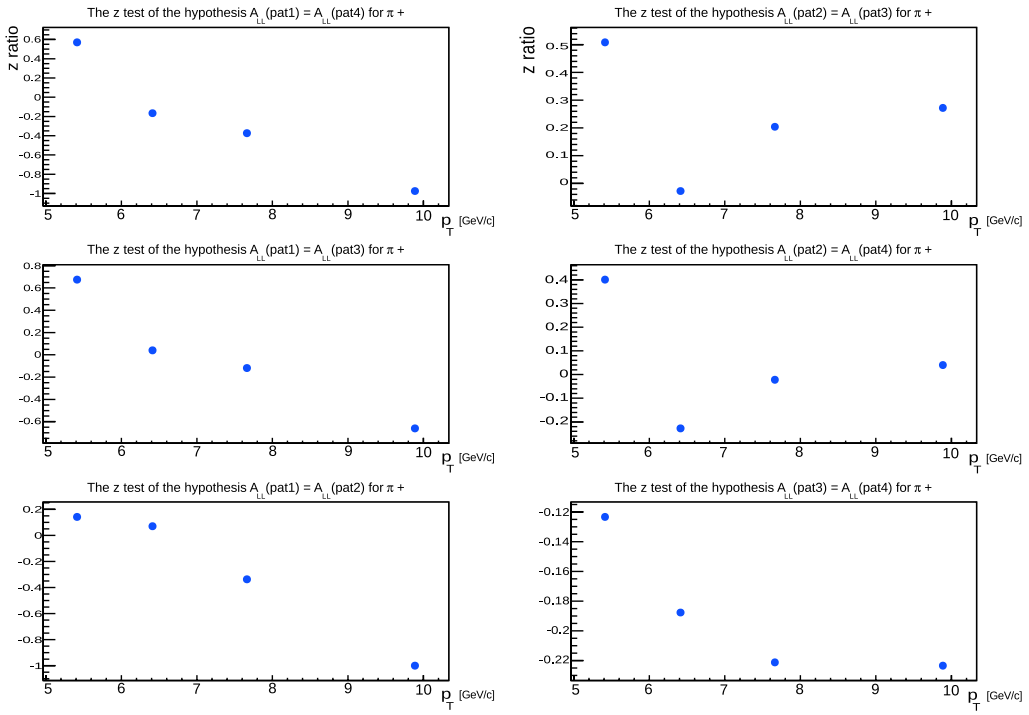

(b) z ratio for π^+

Figure 6.9: z ratio of the of the null hypothesis $\mu_i = \mu_j (i, j$: spin patterns) vs. p_T

patterns. The null hypothesis in this case is that the mean of asymmetries from a pair of different spin patterns is the same with one another. As shown in Fig. 6.9, most $\|z\|$ values are less than 1.0 and the P-value for a two sided alternative $\|z\|$ >1.0 is 0.317. This leads us to conclude that the hypothesis passed the two sample z-test at the significance level of up to 0.317. Adopting a popular rejection rule in experiments, at the significance level of $\alpha = 0.10$, the hypothesis of equal mean asymmetries between patterns remains valid.

6.3 Background A_{LL}

We previously saw the fraction of residual background is less than 3%. Along the way, we further optimized the PID cuts by reinstating the 'emce' cuts and dropping *prob* cut[2]. The cut 'emce > 0.2' which is just enough

[2]Final PID cuts for A_{LL} measurements are: $n_1 > 0$, $|z_{\rm vtx}^{\rm BBC}| < 30$, track quality = 63 or 31, $|zed| < 70$, e/p < 0.9, emce > 0.3 + 0.15 p_T, p_T, 3σ matching cuts for PC3 and EMCal and HBD charge cuts.

to eliminate ambiguities in ERT bias at low emce was used for cross section measurements after study. The p_T dependent emce cut 'emce $> 0.3 + 0.15\ p_T$' was used in charged pion analysis at PHENIX in old days towards the effect of eliminating photo-conversion background. It was dropped initially for this analysis as HBD cuts alone were sufficient to have the same effect. Later it was reinstated to minimize the mixed trigger effect at low emce, keeping the conventional form.

Background has been re-estimated with final set of cuts by fitting the HBD charge distribution. Residual background fractions in p_T bins 5∼6, 6∼7, 7∼9 and 9∼12 GeV/c are 1.7%, 1.6%, 1.2% and 1.3% respectively. The HBD charge distribution for each p_T bin is shown in Fig. 6.10.

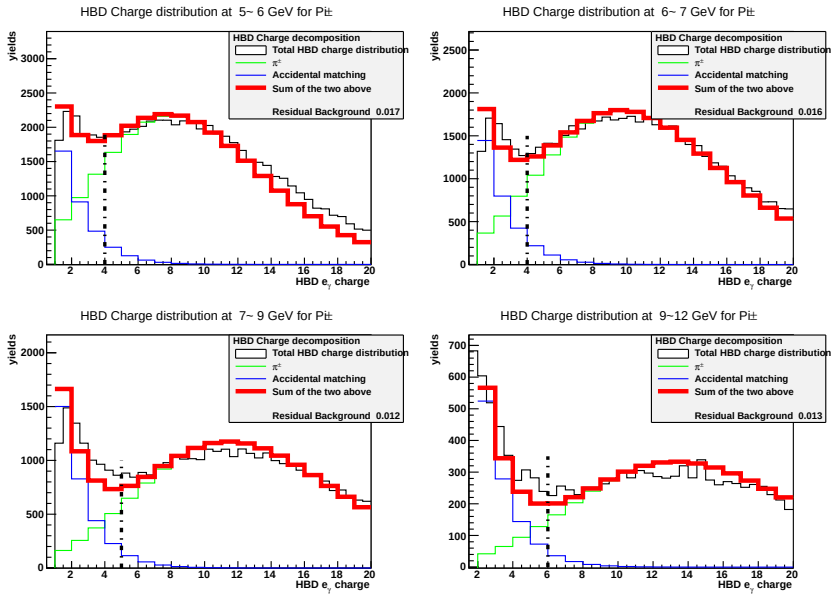

Figure 6.10: The HBD charge distribution for tracks passing final PID cuts used for A_{LL} measurements.

Although the residual background fraction is nonsizable, its effect on A_{LL} has been quantified by studying the distribution of the variable 'swapped HBD cluster charge'. This variable, which was introduced in Chapter 4 to study background, allows us to collect pure background sample. For this particular goal of measuring background A_{LL}, charge-separated tracks with 'swapped cluster charge' greater than 1 and less than 20 were considered. The result for background A_{LL} measurements is shown in Fig. 6.11. The average of measured background A_{LL} is 0.0071±0.0046.

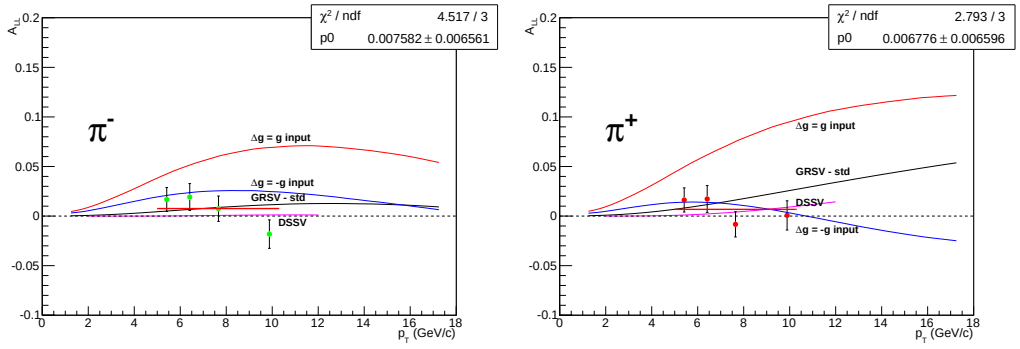

(a) Negative tracks (b) Positive tracks

Figure 6.11: Background A_L for charged tracks

Chapter 7

Results and Discussions

This section presents the result of measurements described in previous sections. Implications of the result of each measurement will be analyzed within the pQCD framework. Ideas will be proposed towards getting around some of the challenges that have been identified in interpreting the results. Finally, the limitation and the extent of the measurements' impact on constraining the first moment of polarized gluon distribution function will be discussed.

7.1 Invariant differential cross sections

The p_T and rapidity differential cross section was measured in order to validate current pQCD frame work and the sets of PDFs and FFs adopted for this analysis. The prediction provided by Marco Stratmann[1] used CTEQ 6.5 unpolarized PDFs and DSS FFs and pQCD calculations at NLO. The measurements are overlaid with the prediction for negative and positive charged pions separately in Fig. 7.1 and Fig. 7.2. The overall agreement is within the uncertainties coming from a theory scale. Here, the theory scale, which is set at p_T, is essentially the factorization scale of PDFs (μ_F) and FFs ($\mu_F^{'}$) and at the same time it is also the renormalization scale (μ_R). While there is no rule or symmetry that requires the three scales be the same with one another, they are chosen to be all equal to one another for practical reasons. Stable theoretical predictions were made for the unpolarized neutral pion cross section with this condition, and good agreement was seen between the measurements and prediction. The uncertainty propagated from the randomness of this choice is estimated by varying the scale by a factor of 2 and $\frac{1}{2}$ and displayed in dashed lines. At the bottom panel of the figure, a quantitative comparison between the measurement and the pQCD prediction, the ratio of

[1] private communication

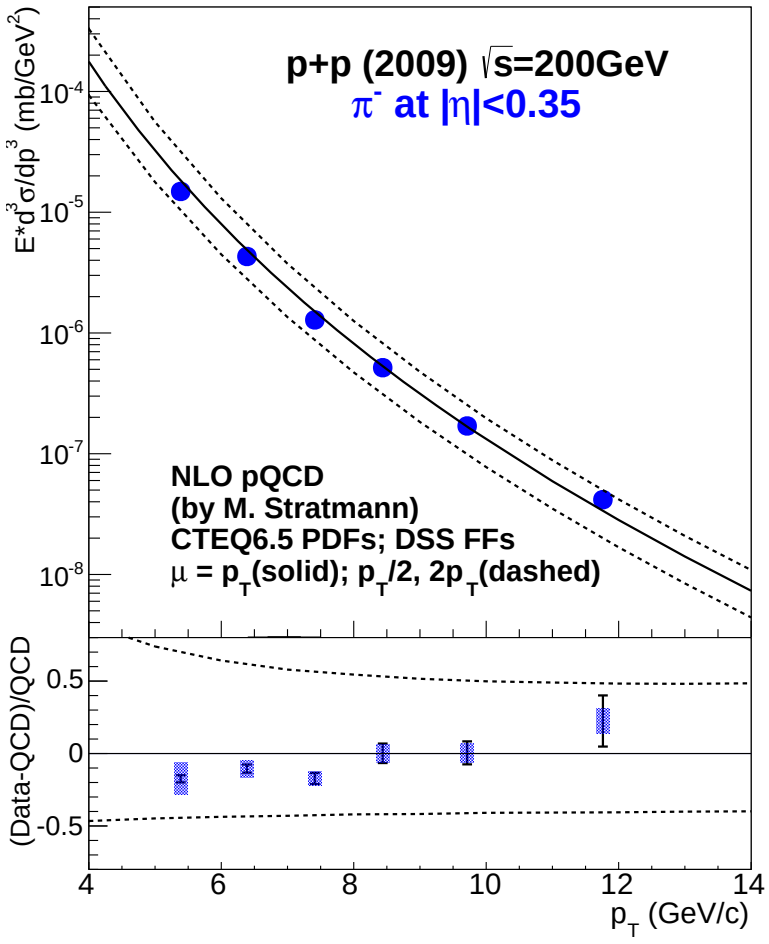

Figure 7.1: Invariant differential cross sections of high p_T π^- production.

(measurement-theory) to theory, is also shown along with the uncertainties from the theory scale. Statistical uncertainties are presented in a black bar and systematic uncertainties of type B-C are shown in a colored box.

Note that the differential cross section for pions of both charge trends up at higher p_T. Although they are still within the theory scale uncertainty, it is indicative of not-well-constrained parameters. We will come back to this issue shortly.

The measurements are also compared in Fig. 7.3(a) with recent STAR measurements on the invariant yield of charge pions [56]. The invariant yield is defined in a manner analogous to invariant cross section as $E\frac{d(N/N_{\rm evt})}{d^3p} = \frac{dN}{d\phi dy p_T dp_T}$. To make comparisons, it was converted into invariant cross section via the re-

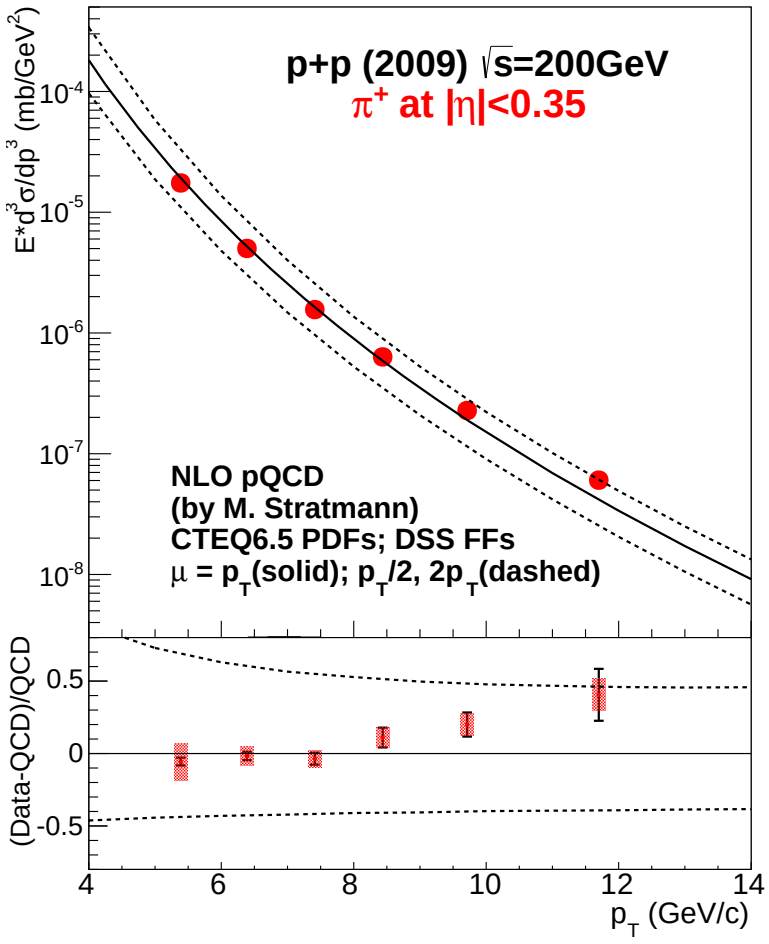

Figure 7.2: Invariant differential cross sections of high p_T π^+ production.

lation, $\sigma = (\frac{N}{N_{\rm evt}}) \times \sigma_{\rm pp\ inelastic}$, where N is the particle production yield, $N_{\rm evt}$ is the number of events and $\sigma_{\rm pp\ inelastic}$ is the production cross section for $p+p$ inelastic (total-elastic) collision processes. These variables can also be written in terms of raw measured quantities and correction factors: $N = N_{\rm raw}\ \frac{1}{\epsilon_{\rm reco}\cdot\epsilon_{\rm acc}}$, $N_{\rm evt} = \frac{N_{\rm BBC}}{\epsilon_{\rm BBC}\epsilon_{\rm bias}}$. For PHENIX, $\sigma_{\rm pp\ inelastic}$ can be written by $\frac{\sigma_{\rm BBC}}{\epsilon_{\rm BBC}}$ as the PHENIX BBC triggers collect inelastic $p+p$ collision events as mentioned in Sec. 5.1.2, whereas the STAR BBC collects Non-single-diffractive (NSD) events with $\sigma_{\rm BBC} = 26.1$ mb and the corresponding efficiency of 87%. Despite the difference, the fact that single diffractive interactions predominantly contribute at low p_T justifies multiplying the invariant yield by a constant factor

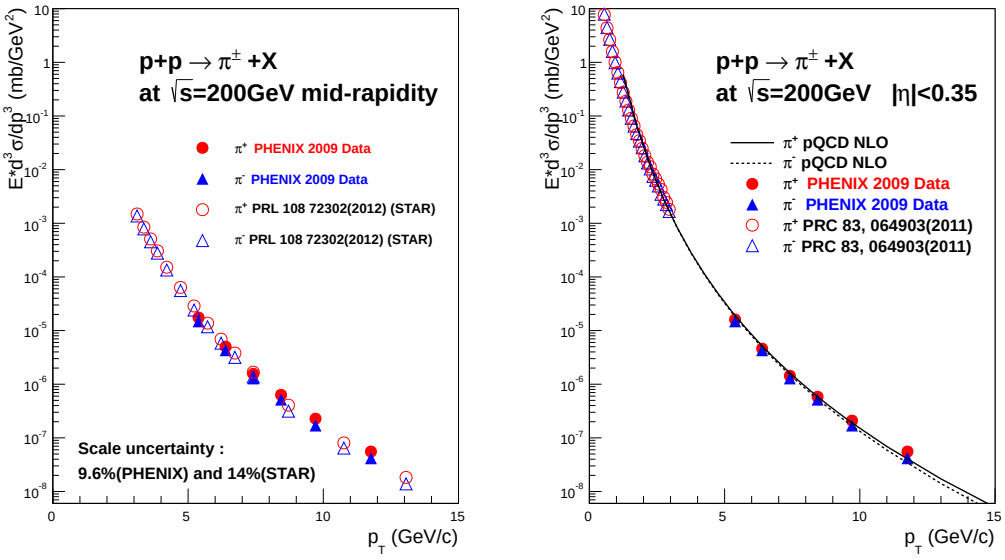

(a) Comparison of charged pion invariant cross section measurements with STAR results.

(b) PHENIX measurements of charged pion production cross section at low and high p_T

Figure 7.3: Invariant cross section measurements of $\pi^{\pm}$ at PHENIX and STAR.

for conversion.

In Fig. 7.3(b), the lower p_T results of PHENIX measurements [57] are shown together with high p_T measurements for completeness. The overlay of pQCD prediction aids to see the continuity of the two independent measurements by PHENIX.

By taking the ratio of the production cross sections for different charges, one can extract more information on fragmentation functions alone. This is possible because all the other components going into the cross section are common for π^+ and π^-. Although this ratio does not directly translate into the ratio of the fragmentation functions for different charges due to complicated convolution involved in the calculation of cross section, it does tell us to some extent whether we can trust the unpolarized FFs that have been used to make predictions for polarized cross sections. The result displayed in Fig. 7.4 shows that the prediction overshoots the measurements throughout the p_T of charged pions measured in this analysis. This result is consistent with the recent STAR results [56]. There can be several explanations for the discrepancy between the measurements and predictions. One plausible cause is that existing data sets

provide poor precision in constraining charge-separated FFs for charged pions. The data sets from e^+e^- annihilation processes have been primarily imposing constraints on hadron fragmentation functions. These data sets do not provide information on charge separation of hadron fragmentation functions as the decay rate of hadrons with one charge is the same as the one with the opposite charge. This can be easily understood by looking at Eq. 1.19 in Sec. 1.4.1. The single hadrons production cross section from e^+e^- at a fixed Q^2 has a term that is proportional to the sum of bare fragmentation functions with opposite charges. In the case of charged pions, the fragmentation function part for π^+ becomes $D_u^{\pi^+} + D_{\bar{u}}^{\pi^+}$. Applying charge conjugation symmetry, this is equal to $D_{\bar{u}}^{\pi^-} + D_u^{\pi^-}$. Finally, the valence contents of π^- and the isospin-symmetric sea assumption lead us to arrive at the equality of the former and $D_d^{\pi^-} + D_{\bar{d}}^{\pi^-}$. At low p_T where charged pion production is dominated by $g - g$ scattering, the ratio of π^- to π^+ cross section is close to 1 as can be seen in Fig. 7.4. At higher p_T where $q - g$ scattering dominates charged pion production, this symmetry is broken due to the valence structure of the proton. Anything that has u quark component is enhanced against the ones with d quark component. This explains why the ratio of π^- to π^+ cross section becomes smaller with p_T. Furthermore, it becomes clear that precise measurements of this ratio plays a crucial role in constraining the charge separation of hadron fragmentation functions.

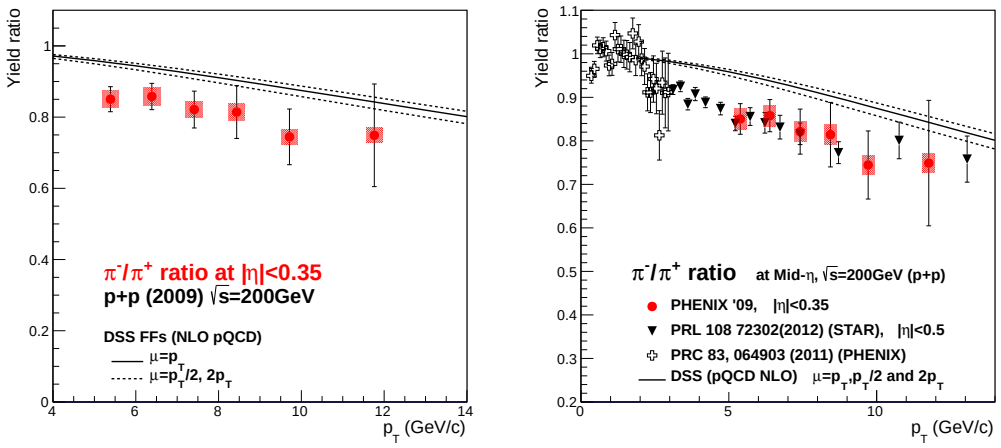

(a) PHENIX 2009 data.

(b) Comparison with other results.

Figure 7.4: The yield ratio of π^- to π^+.

The above scenario is quite plausible as it is well known that currently unpolarized PDFs are determined with great precision and no errors in the NLO

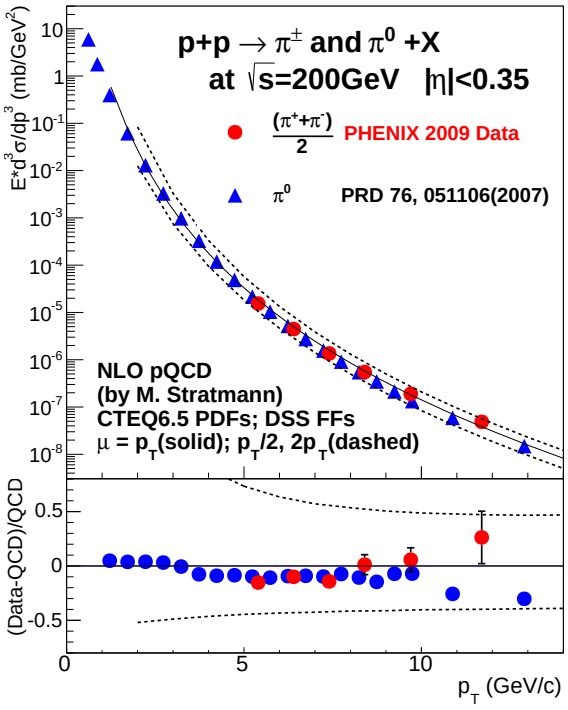

Figure 7.5: Invariant differential cross sections of π^0 and averaged π^+ and π^- productions.

calculation of hard scattering cross section nor evolution of parameters have been reported so far. For this reason measurements of the ratio discuss here are need to constrain the charge separation of hadron fragmentation functions in addition to semi-inclusive DIS processes that have similar effects in global analysis.

The charge averaged cross section is, on the other hand, in good agreement with the prediction. Based on isospin symmetry, the average of the charged pion cross section is expected to be equal to the one of neutral pions. Comparison between the average cross section of charged pions and the neutral pion cross section in Fig. 7.5 indeed shows that isospin symmetry is conserved in the pion production.

The results discussed in this section limit the extent to which current knowledge on distribution functions that describe long distance interaction is applied to make meaningful predictions and draw reasonable interpretation on polarized gluon distribution in terms of asymmetry measurements. In the following section, the results on asymmetry measurements will be presented, followed

by a proposal for an alternative observable that carefully takes into account the stated limitation.

7.2 Double longitudinal asymmtries

This section presents the results of double longitudinal asymmetry measurements. Events analyzed are the ones triggered by high p_T charged pions unless stated otherwise. Asymmetries for four different spin patterns are combined by taking the weighted average. It is appropriate not to combine the raw counts or it will wash out true asymmetries by mixing up events with different correction factors such as detector efficiencies, trigger efficiencies and relative luminosity.

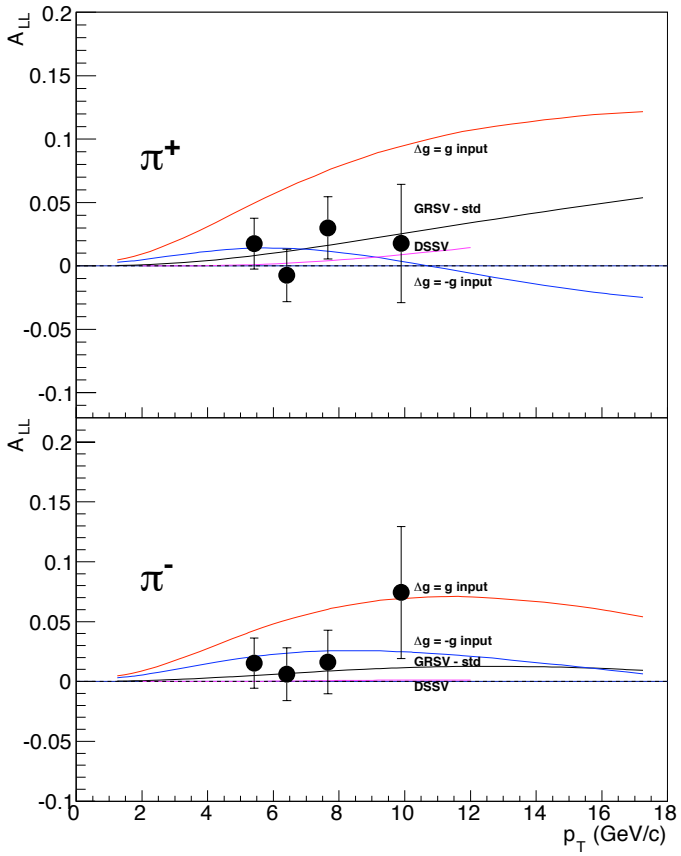

Figure 7.6: A_{LL} results from Run 9 data analysis with HBD.

Table 7.1: A_{LL} results with uncertainties.

p_T[GeV/c]	$A_{LL}^{\pi^-}$	$\delta A_{LL}^{\pi^-}$ (stat.)	$A_{LL}^{\pi^+}$	$\delta A_{LL}^{\pi^+}$ (stat.)
5.4	0.0153	0.0210	0.0176	0.0200
6.4	0.0061	0.0220	-0.0074	0.0206
7.7	0.0161	0.0266	0.0299	0.0245
9.9	0.0743	0 .0551	0.0177	0.0466

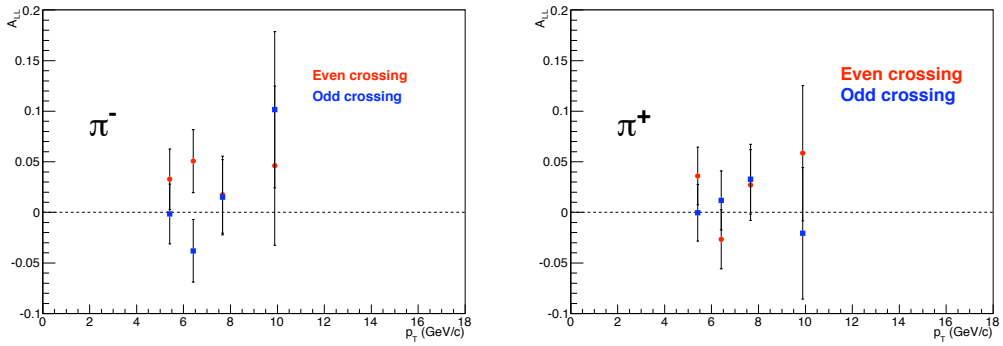

(a) even/odd crossings for π^- (b) even/odd crossings for π^+

Figure 7.7: A_{LL} versus p_T for even and odd crossings.

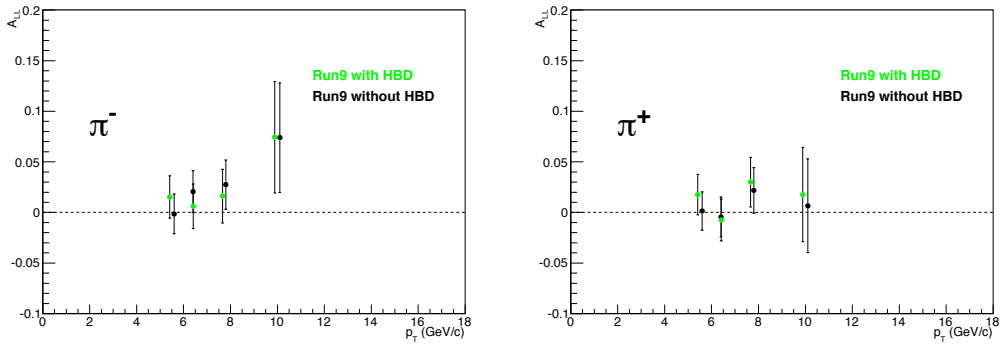

(a) π^- (b) π^+

Figure 7.8: Comparison between Run 9 results with and without HBD.

Fig. 7.7 shows the A_{LL} asymmetries for even/odd crossings and Fig. 7.6 shows the weighted average of even/odd crossings as final results. Asymmetry

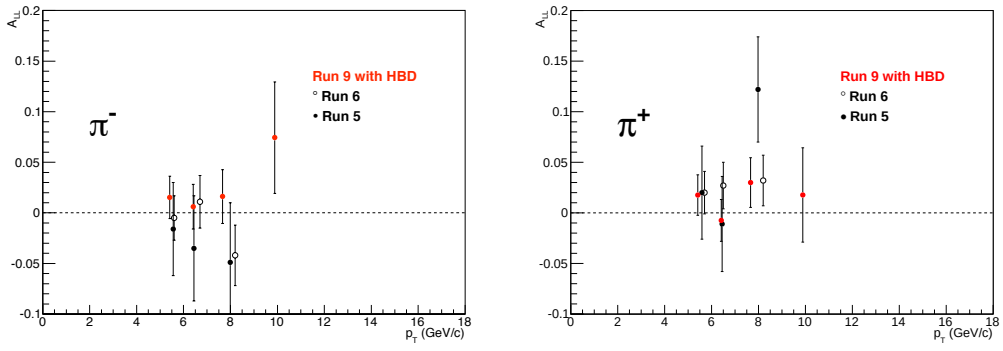

(a) π^- (b) π^+

Figure 7.9: Comparison between Run 5, Run 6 and Run 9 results with HBD.

values with uncertainties are summarized in Table 7.1. Comparison of run 9 results between without and with using HBD is presented in Fig. 7.8. Comparison with the old results (Run 5 and 6) is displayed in Fig. 7.9.

On another note, there are also events where high p_T charged pions are produced but do not trigger an event themselves. These events are mostly triggered by other particles in the same event such as photons and electrons. High p_T charged pions in these events should not be treated equally without careful examination as the ones that triggered the event. The reason for this is because they can potentially break the required single inclusiveness of the measurement, introducing bias in the momentum fraction z (the argument of fragmentation function) distribution. Inclusive measurements must not discriminate against any one of three event types shown in Fig. 5.3. Analyzing only the three types of events shown at the bottom does not break the inclusiveness as triggering on charged pions does not favor any one type over others, whereas inclusion of the events being discussed here, shown in top right panel of Fig. 5.3, potentially does. Under certain assumptions, incorporating this kind of events could be reduced to a matter of properly applying efficiency corrections. The assumption is that the contribution of type 1 events is negligible relative to the other types. This is a legitimate assumption when charged pion production is dominated by back-to-back jet events rather than multi-jet events. When type 1 events are ignored, the breakup between type 2 and type 3 events becomes the result of detector efficiency. Although one can easily justify the claim that charged pion production in multi-jet events is only a small fraction compared to the ones in di-jet events based on the considerations of the order of interaction strength $O(\alpha_s)$, how small is not quantified

at the moment. Nonetheless, results from including all types of events in ERT data that include high p_T charged pions are shown in Table 7.2 and Fig. 7.10. For the purpose of constraining gluon helicity distribution, we will stick with the results obtained from events triggered by high p_T charged pions.

Table 7.2: A_{LL} results of charged π mesons collected by mixed trigger (Run 9).

p_T[GeV/c]	$A_{LL}^{\pi^-}$	$\delta A_{LL}^{\pi^-}$ (stat.)	$A_{LL}^{\pi^+}$	$\delta A_{LL}^{\pi^+}$ (stat.)
5.4	0.0066	0.0142	0.0236	0.0137
6.4	0.0251	0.0150	0.0114	0.0142
7.7	0.0228	0.0178	0.0318	0.0163
9.9	0.0249	0.0316	0.0263	0.0284

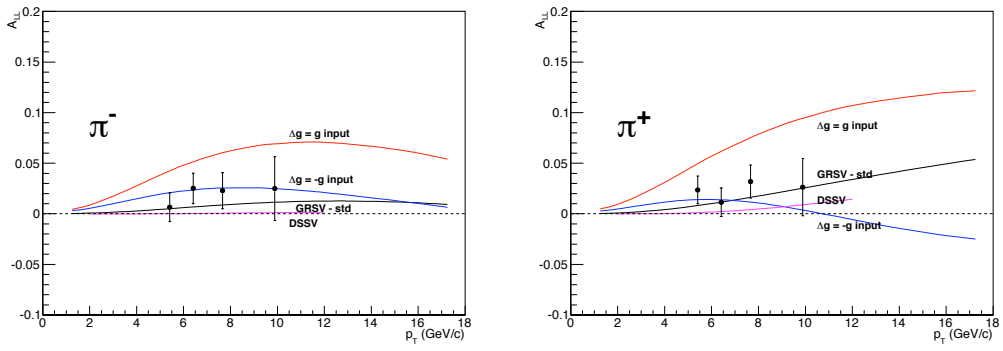

(a) π^- (b) π^+

Figure 7.10: A_{LL} results of charged π mesons collected by mixed trigger.

Turning to the subject of extracting information on the polarized gluon distribution, one has to first take the limitation of current theoretical framework into considerations. From measuring the ratio of the charged pion production cross section for different charges, we know that the pion cross section for individual charge is not well described by current set of fragmentation functions. This implies that the A_{LL} asymmetries of charge separated pions, predicted in the same framework, will not lead us to consistent interpretation regarding polarized gluon distribution. Fortunately, isospin symmetry among π mesons provides us with a means to get around this issue. In the previous section, we saw the average of the charged

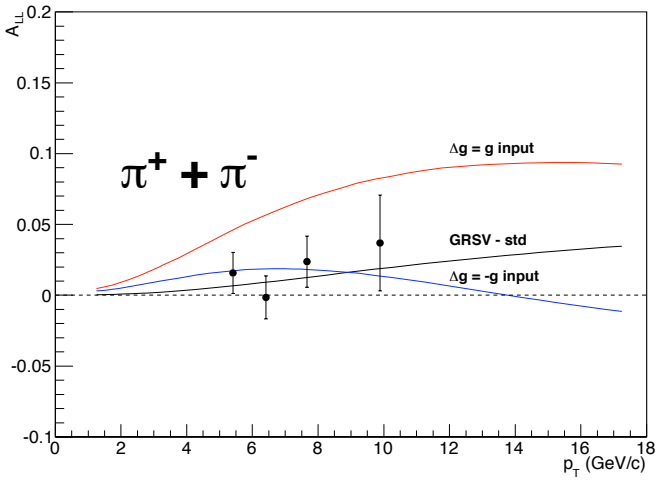

Figure 7.11: A_{LL} results for charge summed charged π mesons

pions cross sections was equivalent to the neutral pion cross section. Likewise, the double helicity asymmetry for the charge-summed charged pion asymmetry $A_{LL}^{\pi^+ + \pi^-}$ is equivalent to the one for neutral π's. Results of the charge-summed asymmetry are tabulated in Table 7.3 and plotted in Fig. 7.11.

Table 7.3: A_{LL} results for charge summed charged π mesons.

p_T[GeV/c]	$A_{LL}^{\pi^- + \pi^+}$	$\delta A_{LL}^{\pi^- + \pi^+}$ (stat.)
5.4	0.0157	0.0145
6.4	-0.0015	0.0150
7.7	0.0237	0.0180
9.9	0.0369	0.0338

Based on the discussions so far, there are two approaches towards interpreting the asymmetry results to address the sign of Δg. The ordering of A_{LL} among three π meson species visualizes the sign of Δg as discussed in Sec. 1.3. This first approach is not a full global analysis and offers only limited information on the sign of Δg). It requires sufficient statistical power to be able to determine the ordering with reasonable confidence level. This approach is not expected to be efficient at lower p_T where π meson production is dominated by $g - g$ scatterings: the same reason why even global analysis, the second approach, cannot help at this p_T range.

With full global analysis at higher p_T where $q-g$ scattering dominates π meson production, each species has its own constraining power in terms of the sign of Δg. In the p_T range of this analysis, $q-g$ scattering is the dominant π meson production mechanism and abundant neutral pion statistics begins to die out. In such circumstances, collecting more statistics from charge neutralized $\pi^{\pm}$ will greatly improve the constraining power with sign information. Currently, the charge-summed asymmetry of charged pion from this analysis provides comparable statistics as neutral pions. When a dedicated charged pion trigger is developed, it is expected to have much stronger impact on constraining Δg. While the initial reason we computed the A_{LL} asymmetries for charge-summed charged pions instead of separating pions with different charges was the limitation in interpretation due to poorly constrained charge-separated $\pi^{\pm}$ fragmentation functions, it turns out the new asymmetry will also strengthen the constraining power by overcoming large uncertainties on FFs. Furthermore, direct comparison between charge summed pion asymmetry $A_{LL}^{\pi^+ + \pi^-}$ and published result of neutral pion asymmetry $A_{LL}^{\pi^0}$ shown in Fig. 7.12(b) serves as a great cross check. In the next section, the result of global analysis incorporating the asymmetry results discussed in this section will be presented.

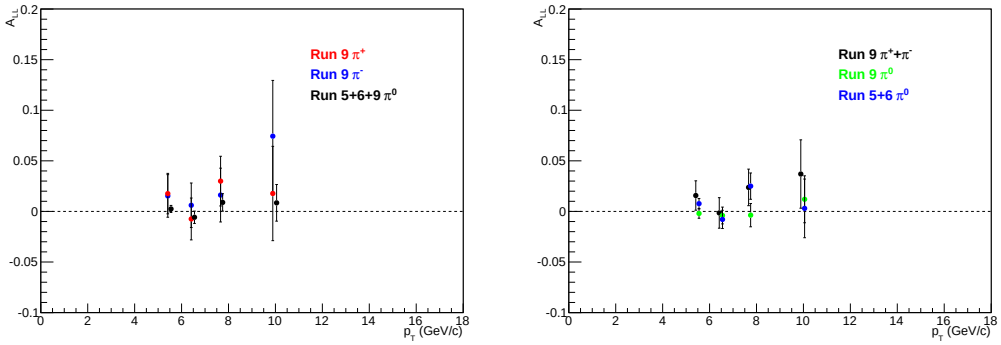

(a) π^+, π^- and π^0 (b) π^0 and $(\pi^+ + \pi^-)/2$

Figure 7.12: Comparisons of A_{LL} results between π meson species.

Finally, the kinematic range for high p_T charged π production via $p+p$ collisions at $\sqrt{s} = 200$ GeV has been simulated using PYTHIA and shown in Fig. 7.13. High Q^2 implied in high p_T pions produced in the collisions guarantees the factorization of the hard partonic scatterings and the soft hadronization processes in perturbative QCD is valid. Accessed Bjorken x ranges from $\sim$0.005 to $\sim$0.02. This information will be critical in constraining ΔG as will

become clear in next section when we discuss the global analysis that incorporates charged pion results.

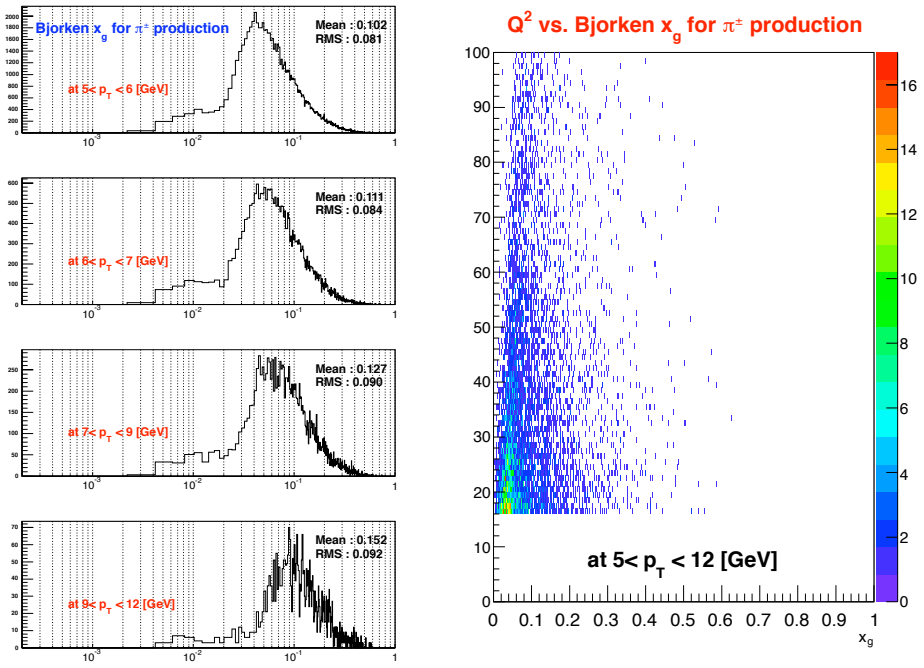

(a) Bjorken x_g (b) Q^2 vs. x_g

Figure 7.13: Accessible kinematic range in high p_T charged π production.

7.3 Impact on ΔG

7.3.1 Global Analysis

As discussed in the introduction, one needs to perform the "global analysis" in order to see the impact of the high p_T charged pion measurements on constraining ΔG. In this analysis, we will simultaneously fit all existing polarized data used in Ref. [32] together with charged pion measurements in order to constrain polarized PDFs. We will adopt the Lagrange multiplier method, which was also used for incorporating neural pion results [32], for χ^2 minimization and estimation of uncertainties on ΔG. A brief review on Lagrange multiplier method and a few comments regarding charged pion results will follow.

The basic idea behind the Lagrange multiplier method is to add a Lagrange multiplier term to χ^2 function and minimize the sum so that we can constrain ΔG at the same time as we minimize the original χ^2. The advantage of this method is that one can easily estimate the uncertainty on ΔG. The auxiliary function Φ newly defined in order to minimize χ^2 with M constraints is written as

$$\Phi(\alpha_1, ...\alpha_N, \lambda_1, ...\lambda_M) = \chi^2(\alpha_1, ...\alpha_N) + \sum_i^M \lambda_i \cdot (g_i(\alpha_1, ...\alpha_N) - c_i), \quad (7.1)$$

where $g_i - c_i$ is the i^{th} term that we want to constrain to zero and λ_i is the Lagrange multiplier associated with the i^{th} constraint. Depending on what we would like to constrain, g_i can be a (truncated) first moment of Δg or one of other polarized PDFs.

At the extremum point $\boldsymbol{\alpha}^* = (\alpha_1^*, ..., \alpha_N^*)$ where χ^2 is minimum, $(N + M)$ sets of equations below are satisfied.

$$\begin{aligned} \frac{d\Phi}{d\alpha_n} &= 0 \ (n = 1, ..., N) \\ \frac{d\Phi}{d\lambda_m} &= 0 \ (m = 1, ..., M) \end{aligned} \quad (7.2)$$

The solution to the first N set of equations can be written, in vector notation including N-dimensional gradient $\boldsymbol{\nabla}$, as $\boldsymbol{\nabla}\chi^2(\boldsymbol{\alpha}^*) + \sum_{i=1}^M \lambda_i \boldsymbol{\nabla} g_i(\boldsymbol{\alpha}^*) = 0$. Geometrically speaking, the direction of steepest ascent (or the gradient) of χ^2 is perpendicular to g_i's at the extremum. The M sets of equations on the second line return the constraints $g_i(\alpha_1, ...\alpha_N) = c_i$ $(i = 1, ..., M)$.

The values of the multipliers at solution points have significance as is often the case. Mathematically, a multiplier λ_i is the value of the partial derivative of Φ with respect to the constraint g_i. So it is the rate at which we could increase the Φ if we were to raise the target of that constraint (from zero). At the solution point $\boldsymbol{\alpha}^*$, however, $\Phi(\boldsymbol{\alpha}^*, \lambda) = \chi^2(\boldsymbol{\alpha}^*)$. Therefore, the rate of increase of the Φ with respect to that constraint is also the rate of increase of the maximally constrained value of χ^2 with respect to that constraint. An intuitive textbook example is the object allowed to only move on the designated two-dimensional surface. In this case, Lagrange multipliers become the frictional force when the auxiliary function that contains Hamiltonian is at extremum. The exact meaning of Lagrange multiplier in global analysis will become clear when we analyze for a specific case.

Following discussions in the previous section, we will use the charge-neutral

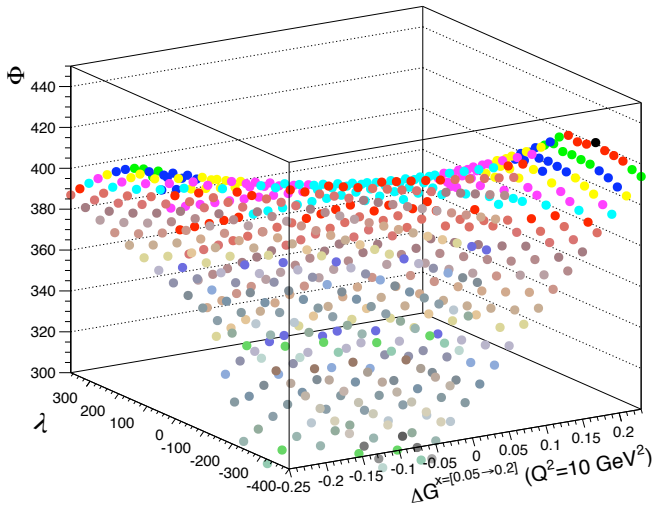

Figure 7.14: Φ vs. λ vs. $\Delta G^{0.050\to0.200}$

(summed) A_{LL} results to avoid issues with the fragmentation functions and in favor of larger statistics. Taking into account the Bjorken x range that high p_T charged pions cover, we constrain the truncated first moment of gluon helicity distribution $\Delta G^{0.050\to0.200}$ to a constant. At each value that $\Delta G^{0.050\to0.200}$ is constrained to, an extremum point is searched and the Lagrange multiplier associated with that point is found. Fig. 7.14 shows the Φ distribution as a function of λ and $\Delta G^{0.050\to0.200}$. Extremum points are easily found and it is not surprising to see that the Lagrange multiplier equals zero at the minimum χ^2. Consequent χ^2 versus $\Delta G^{0.050\to0.200}$ is displayed in Fig. 7.15. In this figure, the new result is compared with the original DSSV result [32].

Inclusion of new high p_T charged pion results shifts the truncated ΔG to a slightly higher value with a comparable uncertainty.

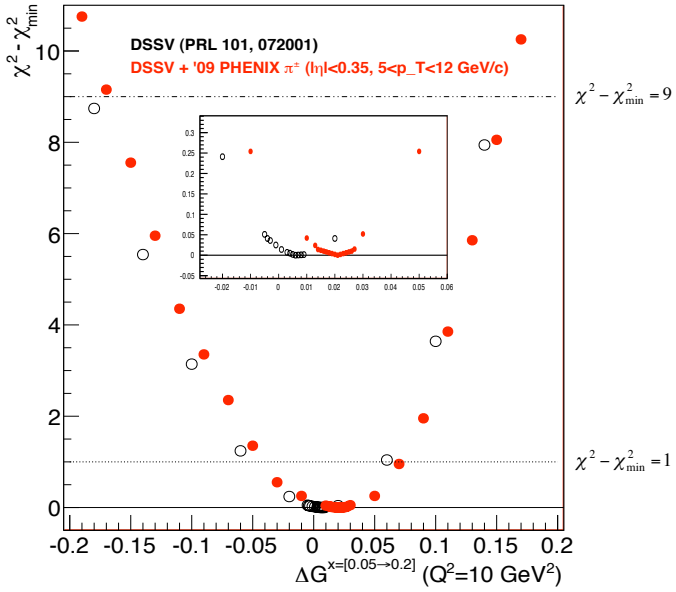

Figure 7.15: χ^2 distribution vs. constrained value of $\Delta G^{0.050\rightarrow0.200}$

Chapter 8

Conclusion and Outlook

We have seen from the measurements of $\pi^{\pm}$ cross section that using the current set of charged pion FFs can mislead us to incorrect interpretation on ΔG and how we still can extract information on ΔG from the alternative A_{LL} measurements. This alternative observable will be the only way of incorporating $\pi^{\pm}$ measurements into the global analysis until we will be able to put strong constraints on the charge separation of $\pi^{\pm}$ fragmentation functions. Determining the sign of ΔG based on the ordering of A_{LL}'s among different pion species is still valid as the facts behind this argument remain valid, though we should not expect to extract the correct size of ΔG. When we eventually have accumulated sufficient statistics and have constrained well the charge-separated FFs for $\pi^{\pm}$, the charge-separated and charge-summed charged pions A_{LL}'s and neutral pion A_{LL} will become truly independent cross checks in constraining ΔG. Recent addition of jet and neutral pion measurements have indeed already started gaining strong enough constraining power to be able to indicate sizable ΔG [58].

Currently, PHENIX is working on measuring π^0's at forward region in order to access smaller x_{BJ}. Double inclusive measurements such as forward-central or central-central π^0 correlation have been performed to access narrower x_{BJ} range. Also, major efforts are being put into open heavy flavor measurements with Vertex detector installed since 2012 [59]. Vertex detector is expected to allow for the separation between b and c decays, enabling us to reach very small x_{BJ} region.

Constraining flavor separate sea-quark polarization via maximally parity-violating W boson production is also an ongoing program at RHIC. Since the first measurement of single helicity asymmetry A_L using decay-electron at mid-rapidity in 2009, more datasets from 2011 and 2012 running with Vertex

detector are being analyzed. The angular[1] dependence of the single helicity asymmetry in decay-lepton production provides sensitivity to a polarized PDF of particular sea-quark depending on the rapidity of decay-leptons. Thanks to the forward muon trigger upgrade [60], the A_L measurement through decay-muon at forward-rapidity is also ongoing. When completed, it is expected to put further constraints on $\Delta\bar{u}$ and $\Delta\bar{d}$ which have been mainly constrained by semi-DIS measurements at COMPASS and HERMES [61]. In the future, Drell-Yan measurements at RHIC [62] will also independently give insights into sea-quark polarization. And SIDIS measurements at Jefferson Lab after the 12 GeV upgrade [64] will continue to address current interests such as the behavior of $\frac{\Delta d}{d}$ at high x.

In the coming years at COMPAS-II [65] and later after 12 GeV upgrade at Jefferson Lab, the Generalized Parton Distribution functions (GDP) measurements through Deeply Virtual Compton Scattering (DVCS) will give the first insights into the orbital angular momentum contribution, completely unknown component in the proton angular momentum sum rule. The orbital angular momentum components from quark or gluon have never been measured at experiment for a long time due to lack of gauge invariant observable. Jis decomposition of nucleon spin into gauge invariant terms suggested potential ways of measuring these, although gluon contribution cannot be further broken up into spin and orbital angular momentum terms. This will not be an issue as one can define the gluon orbital angular momentum as the difference between the total gluon angular momentum and the gluon spin in a similar manner to the quark and anti-quark contributions. In this formalism, he introduces a concept called off-forward parton distribution, now known as GPD, to generalize regular PDFs and elastic form factors. The original name comes from the fact that the new observables can be measured from deeply virtual Compton scattering (DVCS). As distinct from inclusive or semi-inclusive DIS, DVCS is an exclusive process where a real photon is detected in the final state along with a recoiled proton. Thus there are more variables describing the GPDs than ordinary PDFs, such as the skewness variable ξ and the four momentum transfer between initial and final state nucleons t. In the forward limit $\xi \to 0$, some GPDs regain the probabilistic interpretation with additional information on the transverse dimension. Various experimental observables such as the sum and difference between differential cross sections with opposite muon beam charge and polarization will allow to probe separately real and imaginary part of the complex DVCS amplitude, which is expressed in terms of GPDs. When azimuthal dependence is integrated, nucleon tomography is feasible as well.

[1] scattering angle θ in center of mass frame.

In relatively far future, Electron Ion Collider (EIC) [66] at RHIC will for the first time see collisions between polarized electrons and polarized ions that will extend the existing measurements to higher center of mass energies and higher Q^2.

Appendix A

QCD Lagrangian density

QCD is formally defined as a field theory by its Lagrangian density shown in Eq. A.1.

$$\begin{aligned} L_{eff}^{QCD} &= L_{inv} + L_{gauge} + L_{ghost}. \\ L_{inv} &= \sum_f \bar{\psi}_f (\imath \not{D} - m_f)\psi_f - \frac{1}{4}(F_{\mu\nu}^a)^2, \\ L_{gauge} &= \frac{\xi}{2}(\partial^\mu A_\mu^a)^2, \\ L_{ghost} &= \bar{c}^a(-\partial^\mu D_\mu^{ac})c^c, \end{aligned} \tag{A.1}$$

where $D_\mu^{ij} \equiv \partial_\mu \delta^{ij} + igA_\mu^a (T_a^{(F)})^{ij}$ is the covariant derivative and $F_{\mu\nu}^a \equiv \partial_\mu A_\nu^a$ $-\partial^a A_\nu - gC^{abc} A_{\mu,b} A_{\nu,c}$ is the gluon field strength. $N_c \times N_c$ matrices $(T_a^{(F)})^{ij}$'s are the Lie generators of SU(N_c) and N_c is the number of color. Greek letters denote Lorentz indices and alphabet letters are assigned for color indices.

The first term in gauge invariant term is attributed to the spin $\frac{1}{2}$ Dirac (anti-)fermions and their interaction with the gauge bosons (gluons), while the second term accounts for the self-interacting gluons. Each term gives rise to Feynman rules for propagation of (anti-)quark or gluon fields and their relevant interactions when properly quantized.

As in the case of Quantum Electro Dynamics (QED), in order to quantize the theory one has to add a gauge fixing term. The reason for this can be best understood in functional integral quantization method. It becomes obvious in this method that one has to avoid redundantly integrating over a continuous infinity of physically equivalent field configurations in the functional integral in order to correctly define gauge invariant correlation functions $< \Omega | T(O) | \Omega >$, where $T(O)$ is a time ordered gauge invariant field operator and Ω is a vacumm

state. A procedure to do this is called Fedeev-Popov formalism [6] and what it does is that it constrains the direction of gauge field by inserting the identity $1 = \int D\alpha\delta(G(A^\alpha))det(\frac{\delta G(A^\alpha)}{\delta\alpha})$ that enforces $G(A) = \partial^\mu A^a_\mu - \omega^a = 0$. Integrating over all configurations of scalar field $w^a(x)$ in the gauge fixing term then leaves us with a functional integral that counts physical field configuration only once and a normalization factor. This effectively adds the gauge fixing term in the Lagrangian. While Fedev-Popov formalism to fix the gauge leaves an overall constant that is independent of the photon gauge field in QED, in QCD the determinent in the normalization factor depends on the choice of gauge. From the infinitesimal form of the gauge transformation rules for gluon fields shown in Eq.A.2, one can obtain $\frac{\delta G(A^\alpha)}{\delta\alpha} = \frac{1}{g}\partial^\mu D_\mu$.

$$(A^\alpha)^a_\mu = A^a_\mu + \frac{1}{g}\partial_\mu\alpha^a + f^{abc}A^b_\mu\alpha^c = A^a_\mu + \frac{1}{g}D_\mu\alpha^a \tag{A.2}$$

Introducing the anti-commuting fields c and $\bar{c}$ belonging to the adjoint representation, the determinant term can be expressed as a functional integral over these new fields: $det(\frac{1}{g}\partial^\mu D_\mu) = \int DcD\bar{c}\exp[i\int d^4x\bar{c}(-\partial^\mu D_\mu)c]$. (Anti-)ghost fields are not physical as they have the wrong relation between spin and statistics. Nevertheless this term is needed to calculate amplitudes using correct Feynman rules. Fermions do not bring further subtleties than in the case of QED.

The symmetries in QCD Lagrangian density tells us a lot about the nature of strong interaction. Firstly, there are two internal symmetries: color and flavor (isospin) symmetries. Fermions (anti-fermions) carry 3 colors and they are in the fundamental (conjugate) representation of SU(3). Gluons are carriers of color force and their local gauge invariance requires gluon fields be in the adjoint repsentation of SU(3) group. This means gluon fields behave as if they are generators under symmetry transformation. From the SU(3) Lie group algebra we then know that gluons can interact with one another. This is in drastic contrast with the non self-interacting photons, in QED, which are invariant under U(1) local gauge symmetry transformation. And this nature takes a major part in the so-called "asymtotic freedom" phenomenon which will is the main subject of Chapter 1.4.3.

Fermion fields are in the fundamental representation of SU(n) group where n is the number of flavors. This global symmetry is called "isospin symmetry" and accounts for symmetries in hadron particle species.

Appendix B

Inclusive DIS cross section

The cross section of inclusive process e^-(electron)-P(proton)$\rightarrow e^- + X$ is given here. Note that the initial spin of an electron nor a target is not averaged over so that we can study more general cases.

$$\sigma(e+P\rightarrow e+X) = \frac{1}{4P\cdot q}\int \frac{d^3p'_e}{2E'(2\pi)^2}\frac{e^4}{Q^4}L^{\mu\nu}W_{\mu\nu}(2\pi),$$

$$\text{where} \qquad L^{\mu\nu} = \sum_{s'}[\bar{u}(p'_e,s')\gamma^\mu u(p_e,s)]^\dagger[\bar{u}(p'_e,s')\gamma^\nu u(p_e,s)]$$

$$\text{and} \qquad W_{\mu\nu} = \frac{1}{2\pi}\sum_X\prod_{i=1}^{n_X}\int\frac{d^3p_i}{(2\pi)^3\,2dp_i}(2\pi)^4\,\delta(P+q-\sum_{i=1}^{n_X}p_i)$$
$$\cdot < PS|J^\dagger_\mu(0)|X >< X|J_\nu(0)|PS >$$
$$= \frac{1}{2\pi}\int d^4\xi\; e^{iq\cdot\xi} < PS|J^\dagger_\mu(\xi)J_\nu(0)|PS > . \qquad \text{(B.1)}$$

The hadronic tensor $W_{\mu\nu}$ is a second rank Lorentz tensor depending only on p^μ, q^μ and S^μ. And the reduction formula tells us that the hadronic tensor can be written in an form analogous to the lectonic tensor : $W_{\mu\nu}(q,P,S) = \bar{u}(P,S)F_{\mu\nu}u(P,S)$, where $F_{\mu\nu}$ is a 4x4 matrix constructed from q^μ, P^μ and γ^μ. Both leptonic and hadronic tensors can be broken into the unpolarized (or spin averaged) and the polarized components of initial lepton and target, repectively. The spin averaged part of the hadronic tensor $\frac{1}{2}(W_{\mu\nu}(P,q,S)+W_{\mu\nu}(P,q,-S))$ is independent of the initial target spin as the leptonic tensor is of the initial lepton spin according to explicit calculation. Lack of knowledge on the substructure of the nucleon is parameterized in the structure functions of general form. The most general form of hadronic tensor can be obtained by requiring various symmetries that the electromagnetic

interaction observes.[15] Both leptonic and hadronic tensors satisfy patity conservetion, time reversal invariance, hermiticity and gauge invariant (or electromagnetic current conservation). Especially, parity conservation implies the spin averaged (polarized) part of the tensor to be polar and symmetric (antisymmetric), time reversal invariance implies the spin averaged (polarized) part to be real (imaginary). Also, gauge invariance ensures the tensor to be conserved. Eq. B.2 summarizes what is explained above well.

$$
\begin{aligned}
L^{\mu\nu}(p_e, p'_e, s) &= L^{\mu\nu}_{(S)}(p_e, p'_e) + iL^{\mu\nu}_{(A)}(p_e, p'_e, s) \\
&= 2(p'^{\mu}_e \cdot p^{\nu}_e + p^{\mu}_e \cdot p'^{\nu}_e - g^{\mu\nu}(p_e \cdot p'_e - m^2_e)) + 2im_e\epsilon^{\mu\nu\rho\sigma}s_\rho(p_e - p'_e)_\sigma, \\
W_{\mu\nu}(q, P, S) &= W^{(S)}_{\mu\nu}(q, P) + iW^{(A)}_{\mu\nu}(q, P, S) \\
&= -W_1\left(g_{\mu\nu} - \frac{q_\mu q_\nu}{q^2}\right) + \frac{W_2}{M^2}\left(P_\mu - \frac{P\cdot q}{q^2}q_\mu\right)\left(P_\nu - \frac{P\cdot q}{q^2}q_\nu\right) \\
&\quad + i\,\epsilon_{\mu\nu\rho\sigma}\,q_\rho\left(MS^\rho\,G_1 + \frac{1}{M}\left[P\cdot qS^\sigma - S\cdot qP^\sigma\right]G_2\right),
\end{aligned}
$$

consequently

$$
L^{\mu\nu}W_{\mu\nu} = L^{\mu\nu}_{(S)}W^{(S)}_{\mu\nu} - L^{\mu\nu}_{(A)}W^{(A)}_{\mu\nu} \tag{B.2}
$$

On the other hand, the introduced structure functions W_1 and W_2 are not associated with any particular polarization of the virtual photon γ^*, and both the cross sections for polarized and unpolarized virtual photon are written as a linear combination of the two structure functions. As a result, the structure functions can be expressed as a linear combination of polarized and polarization summed γ^*-N cross sections. In the Bjorken limit where $Q^2 \to \infty$, $\nu \to \infty$, $x = \frac{Q^2}{\nu}$ fixed, these relations simplify as shown in Eq. B.3. Subscript Σ denotes that the polarization of γ^* is summed over while T does the 2 transverse polarization states are averaged. L indicates longitudinally polarized virtual photons.

$$
\begin{aligned}
2M\,W_1 &= \frac{Q^2}{8\pi^2\alpha_{EM}x}(\sigma_\Sigma(\gamma^*N) + \sigma_L(\gamma^*N)), \\
\frac{\nu W_2}{x} &= \frac{Q^2}{8\pi^2\alpha_{EM}x}(\sigma_\Sigma(\gamma^*N) + 3\sigma_L(\gamma^*N)), \\
\text{where} \quad 2\sigma_T(\gamma^*N) &= \sigma_\Sigma(\gamma^*N) + \sigma_L(\gamma^*N).
\end{aligned} \tag{B.3}
$$

Introducing dimensionless structure fuctions F_1 and F_2 shown in Eq. B.4 becomes handy at this point. Rearranging equations in B.3 and B.4 enables us to define the transverse, longitudinal as well as unpolarized γ^* structure

functions in terms of F_1 and F_2. The new functions can then be written directly in terms of relevant cross sections as given by Eq. B.5.

$$F_1 = M\,W_1 \qquad \text{and} \qquad F_2 = \nu\,W_2. \tag{B.4}$$

$$\begin{aligned} F_L &= \frac{F_2}{x} - 2F_1 = 2\,(\frac{Q^2}{8\pi^2\alpha_{EM}x})\,\sigma_L(\gamma^* N), \\ F_T &= 2F_1 = 2\,(\frac{Q^2}{8\pi^2\alpha_{EM}x})\,\sigma_T(\gamma^* N), \\ \text{and} \qquad F_\Sigma &= F_T - \frac{1}{2}F_L = (\frac{Q^2}{8\pi^2\alpha_{EM}x})\,\sigma_\Sigma(\gamma^* N). \end{aligned} \tag{B.5}$$

Appendix C

Renormalizations of Field Theory

There are 2 equivalent approaches towards renormalization; reparamatrization approach and counter term approach. Some of the key steps in both approaches will be summarized in this section.

C.1 Quantum ElectroDynamics (QED)

In the reparameterization approach, in QED for instance, one can compute the divergent diagrams using a regulator, to obtain an expression that depends on the bare mass(m_0), the bare coupling constant(e_0) and some UV cutoff Λ. The physical mass m, coupling constant e are also computed in terms of infinite bare quantities e_0, m_0 and Λ upto the order of interest. Getting a finte expression for an amplitude in which infinite bare parameters are eliminated in favor of finite physical quantities is called the "Renormalization". In order to get a finite S-matrix amplitude in terms of physical quantities, one needs to additionally compute field strength renormalization constants Zs that bridge bare quantities to physical quantities. Fig. C.1 shows relevant QED 1 loop diagrams. In short, the electron field strength remormalization from electron self-energy gives rise to an electron field strength renormalization constant and a shift in mass from the bare mass to the physical mass. What is interesting is that this renormalization constant cancels the infinity coming from the vertex correction by Ward identity. Photon field strength renormalization, on the other hand, causes the bare coupling constant e_0 to be rescaled to physical coupling constant e.

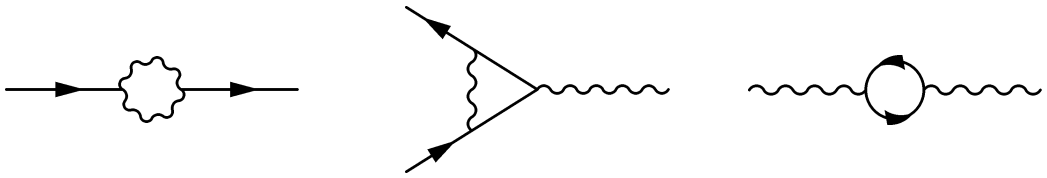

Figure C.1: 3 UV divergent QED diagrams at 1 loop level

Renormalization can be done more systematically once we understand the structure of UV divergences. To this end, the superficial degree of divergence defined as D $\equiv$ (power of k in numerator)-(power of k in denominator) is introduced to serve as a naive criteria to predict the existence of UV divergences since momenta in the denominator as in propagators aid convergence of the momentum integrals. It works well in most cases, including QED, as long as next to leading order loops and accompanying complications involving overlapping divergences are ignored. In the case of QED, D is equal to 4-N_γ-2N_e. Thinking in terms of amputated 1-particle-irreducible(1PI) diagrams will make it simpler to enumerate all of the divergent QED diagrams. Amputated diagrams do not have external legs and 1PI diagrams cannot be disconnected by cutting any one of internal lines by definition. The reasons for considering these diagrams are firstly the external legs do not cause divergence and secendly any divergent diagrams can be expressed as products of IPI diagrams. From this considerations, one can find 3 'primitively' divergent amplitudes in QED; the electron self energy, the photon self energy and the vertex correction. These are exactly the ones computed in reparameterization approach at order α. Although 2 of them have superficial degrees of freedom D>0, all 3 are only logarithmically divergent. Linear divergence($\sim \Lambda$) is restricted in electron self-energy diagram by chiral symmetry that requires the mass shift be proportional to m. Higher order divergence in photon self-energy gets canceled by Ward identity.

In counter term approach, understanding the structure of divergences discussed above will prove convenient in treating the divergences effectively especially at one loop level. The procedure is summarized in the following. First absorb the field-strength renormalizations into the Lagrangian by rescaling the fields: $\psi = Z_2^{\frac{1}{2}}\psi_r$ for electron fields from electron propagators $\frac{iZ_2}{\not{p}-m}+\cdots$ and $A^\mu = Z_3^{\frac{1}{2}}A_r^\mu$ for photon fields from photon propaga-

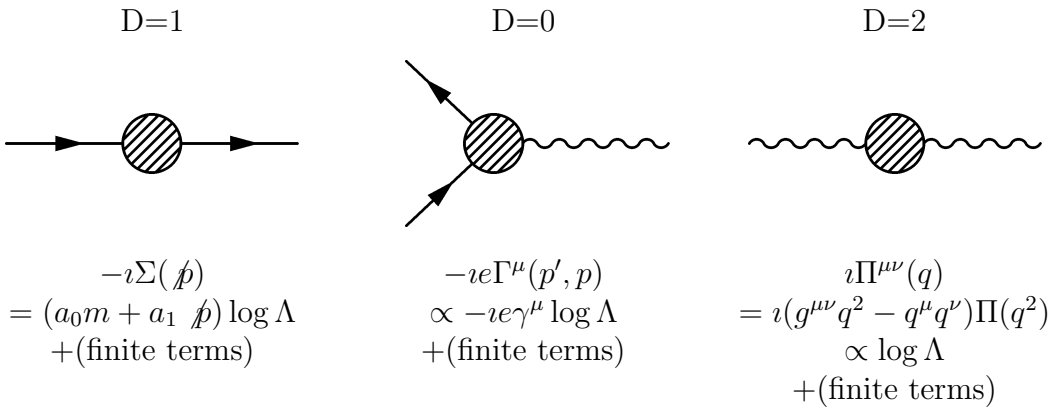

Figure C.2: 3 primitively divergent QED diagrams

tors $\frac{-iZ_3 g_{\mu\nu}}{q^2} + \cdots$. The Lagrangian can be written by the second line of Eq.C.1.

$$\begin{aligned} L &= -\frac{1}{4}(F^{\mu\nu})^2 + \bar{\psi}(i\not\partial - m_0)\psi - e_0\bar{\psi}\gamma^\mu\psi A_\mu \\ &= -\frac{1}{4}Z_3(F_r^{\mu\nu})^2 + Z_2\bar{\psi}_r(i\not\partial - m_0)\psi_r - e_0 Z_2 Z_3^{\frac{1}{2}}\bar{\psi}_r\gamma^\mu\psi_r A_r^\mu \\ &= -\frac{1}{4}(F_r^{\mu\nu})^2 + \bar{\psi}_r(i\not\partial - m)\psi_r - e\bar{\psi}_r\gamma^\mu\psi_r A_r^\mu \\ &\quad -\frac{1}{4}\delta_3(F_r^{\mu\nu})^2 + \bar{\psi}_r(i\delta_2\not\partial - \delta_m)\psi_r - e\delta_1\bar{\psi}_r\gamma^\mu\psi_r A_r^\mu \end{aligned} \tag{C.1}$$

Splitting each term of Lagrangian into two pieces, separating the infinite and unobservable shift into counterterms follows. The result is shown in the third line of Eq.C.1, where $\delta_2 = Z_2 - 1, \delta_3 = Z_3 - 1, \delta_m = Z_2 m_0 - m$ and $\delta_1 = Z_1 - 1 = (e_0/e)Z_2 Z_3^{\frac{1}{2}} - 1$. Consequently, corresponding counterterms to be added in the calculation are $\imath(\not p\delta_2 - \delta_m)$, $-\imath e\gamma^\mu\delta_1$ and $-\imath(g^{\mu\nu}q^2 - q^\mu q^\nu)\delta_3$ for electron self-energy, vertex correction and photon self-energy, repectively. Next step is to specify the renormalization conditions which "define" the physical masses and coupling constants and keep the field-strength renormalizations equal to 1. As indicated before, there are 4 infinite parameters that need to be absorbed or canceled in the final expression, so there must be 4 renormalization conditions, in on-shell renormalization conditions for instance:

$\Sigma(\not p = m) = 0$ for fixing the electeon mass at m,

$\frac{d}{d\not{p}}\Sigma(\not{p})|_{\not{p}=m} = 0$ to have the residue of the electron propagater at 1,

$\Pi(q^2 = 0) = 0$ to have the residue of the photon propagator at 1,

$-\imath e\Gamma^\mu(p' - p = 0) = -\imath e\gamma^\mu$ for fixing the the electron charge at e.

The last step is to compute diagrams and get the counterterms that maintain the renormalization conditions. In this step, dimensional regularization scheme is prefered for the sake of consistency, since gauge invariance (or Ward identity) is preserved in this scheme.

QED is a renormalizable theory in the sense that there are only finite number of amplitudes that superficially diverge, however, these ultraviolate divergences occur at all orders in perturbation theory. And the counterterm approach makes the renormalization process automatic at all orders. Another crucial information that can be extracted easily from counterterms is the behavior of running coupling constant. The bare Green's functions depend only on bare quantities like e_0, m_0 and momentum cutoff Λ. They do not have any reference to renormalization scale - the scale at which renormalization conditions are imposed - until the cutoff dependence is removed by rescaling the fields and eliminating bare parameters in favor of renormalized ones.

The two theories defined at two different renormalization scales M and M' are considered the same when they share the same bare Green's functions. In other words, renormalization scale is arbitrary. For this reason, one is allowed to introduce a genaral renormalization scale M and define QED with the set of four renormalization conditions rewritten at this scale. The renormalization conditions for propagators will be applied at $p^2 = -M^2$ and those for the vertex at a point where all three invariants are of order $-M^2$. Then the renormalized Green's functions in this theory will satisfy the Callan-Symanzik equation shown in Eq.C.2. There appreas one beta function associated with the electromagnetic coupling constant and a γ function for the photon and electron field each. These functions describe running of e and m with the changing renormalization scale as will be clear shortly.

$$[M\frac{\partial}{\partial M} + \beta(e)\frac{\partial}{\partial e} + n\gamma_2(e) + m\gamma_3(e)]G^{(n,m)}(\{x_i\}; M, e) = 0 \qquad \text{(C.2)}$$

The superscript n and m in the renormalized Green's function represent the number of electron and photon fields, respectively. β and γ functions de-

fined by $\beta \equiv \frac{M}{\delta M}\delta e$ and $\gamma_{2(3)} \equiv -\frac{M}{\delta M}\delta_{2(3)}$. These functions can be solved by calculating Green's functions. Especially at the lowest order, the renormalization scale dependence solely comes from the counterterms. This enables us to get the general solution for a theory with massless fermions and gauge bosons. From the generic structure of 2 point Green's functions (for instance, $G^{(2,0)}$ or $G^{(0,2)}$) of massless fields - the sum of a propagator, loop diagrams and counter terms - one can get the general form of the solution for γ functions, which is common for electron and photon as shown in the first line of Eq.C.3. Similarly, the β functions for a coupling constant g at the lowest order can be obtained from the generic form of the Green's function for n-point vertex. The Green's function for n-point vertex includes terms coming from vertex counterterm and external leg corrections that depend on the renormalization scale in addition to the 1PI loop diagrams. This results in the β function in the form shown in Eq.C.3.

$$\gamma_i = \frac{1}{2}M\frac{\partial}{\partial M}\delta_i \qquad \text{and}$$
$$\beta(g) = M\frac{\partial}{\partial M}(-\delta_g + \frac{1}{2}g\sum_i \delta_i)\ \text{, where}\ \ i \in \{i|\exists Z_i\}. \tag{C.3}$$

Inserting the evaluations of diagrams relevant in QED at renormalization scale $-M^2$ gives us the following results. $\gamma_2(e) = \frac{1}{2}M\frac{\partial}{\partial M}\delta_2 = \frac{e^2}{16\pi^2}, \gamma_3(e) = \frac{1}{2}M\frac{\partial}{\partial M}\delta_3 = \frac{e^2}{12\pi^2}$ and $\beta(e) = M\frac{\partial}{\partial M}(-\delta_1 + e\delta_2 + \frac{e}{2}\delta_3) = \frac{e^3}{12\pi^2}$. The β function is obtained from considerations of the Green's function for 3-point vertex. The first and the second term cancel out each other by gauge invariance and the final result only comes from photon field renormalization. Solving for β function gives us an explicit Q dependence of effective coupling constant α_{eff}.

C.2 Quantum ChromoDynamics (QCD)

QCD is also a renormalizable theory: divergences in QCD can be removed by a finite number of counter-terms. This procedure results in important byproducts, so-called renormalization equations, one of which is the beta function that describes the running of α_s. One should start from the general form of the renormalization equations given in Eq. C.3 in order to get the β function for QCD. The β function for QCD takes a similar form to the one for QED as shown in Eq. C.4, except that this time all three terms contribute.

$$\beta(g_s) = M\frac{\partial}{\partial M}(-\delta_1 + g_s\delta_2 + \frac{1}{2}g_s\delta_3). \tag{C.4}$$

Understanding the divergence structure requires enumerating all counter-terms needed for the renormalization of QCD. Analogously to QED, the QCD Lagrangian originally expressed in terms of bare quantities can be rewritten as a sum of the Lagrangian with bare fields replaced by renormalized fields (L_{ren}) and the counter-terms as shown in Eq. C.5. The gauge parameter ξ was chosen to be 1 for simplicity since the leading order β function does not depend on the gauge choice. There are eight counter-terms that depend on underlying five parameters. This indicates that there exist three relations among counter-terms and one needs to impose five renormalization conditions in order to renormalize QCD.

$$\begin{aligned}
L &= -\frac{1}{4}(\partial_\mu A^a_\nu - \partial_\nu A^a_\mu)^2 + \bar{\psi}(i\not{\partial} - m_0)\psi - \bar{c}^a\partial^2 c_a \\
&\quad + g_{s0}\bar{\psi}\gamma^\mu\psi A^a_\mu - g_{s0}f^{abc}(\partial_\mu A_{\nu,a})A^\mu_b A^\nu_c \\
&\quad - g^2_{s0}(f^{eab}A^\mu_a A^\nu_b)(f_{ecd}A^c_\mu A^d_\nu) - g_{s0}\bar{c}_a f^{abc}\partial^\mu A_{\mu,b}c_c \\
&= L_{ren} - \frac{1}{4}\delta_3(\partial_\mu A^a_\nu - \partial_\nu A^a_\mu)^2 + \bar{\psi}_r(i\delta_2\not{\partial} - \delta_m)\psi_r - \delta_2^c\bar{c}^a\partial^2 c^a \\
&\quad + g_s\delta_1 A^a_\mu\bar{\psi}_r\gamma^\mu\psi_r - g_s\delta_1^{3g}f^{abc}(\partial_\mu A_{\nu,a})A^\mu_b A^\nu_c \\
&\quad - g_s^2\delta^{4g}(f^{eab}A^\mu_a A^\nu_b)(f_{ecd}A^c_\mu A^d_\nu) - g_s\delta_1^c\bar{c}_a f^{abc}\partial^\mu A_{\mu,b}c_c
\end{aligned} \tag{C.5}$$

At one-loop level, the three equations can be written

$$\delta_1 - \delta_2 = \delta^{3g} - \delta_1 = \frac{1}{2}(\delta_1^{4g} - \delta_3) = \delta_1^c - \delta_2^c$$

and this is a result of gauge invariance[1].

In order to obtain the β function of QCD, one has to compute the three counter-tems. First of all, δ_2 can be identified with the coefficient of $\not{p}$ in the computation of fermion self-energy diagram, since this counter-term is proportional to $\not{p}$. Next, we consider the fermion-gluon interaction vertex diagram. There are two 1-loop diagrams of which divergence can be canceled by adding the counter-term δ_1. See Fig. C.3 and Fig. C.4 for corresponding diagrams. Finally, corrections to gluon field propagators have to be computed to get δ_3. There are more terms considered in QCD than in QED because of

[1] Although it is more complicated, this is very similar to QED where the first two counter-terms simply cancel out.

Electron self-energy $= i \not{p} \delta_2$

Figure C.3: A UV correction to a fermion propagator at 1 loop level and the counter-term in QCD.

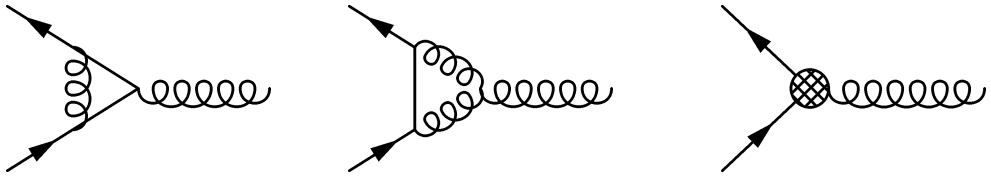

Vertex corrections $= i g_s t^a \gamma^\mu \delta_1$

Figure C.4: One-loop corrections to 3-point fermion-gluon vertex and their counter term in QCD.

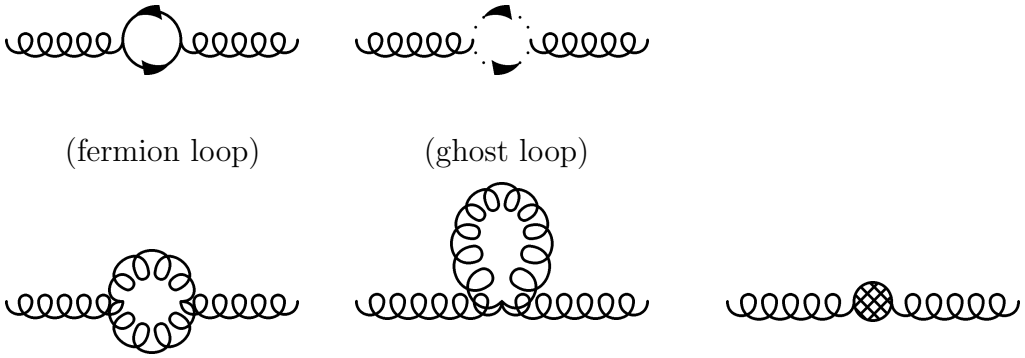

(fermion loop) (ghost loop)

(Pure gluonic) Gluon self-energy corrections $= -\mathrm{i}\,(k^2 g^{\mu\nu} - k^\mu k^\nu)\delta^{ab}\delta_3$

Figure C.5: One-loop corrections to gluon propagator their counter-term in QCD.

gluons being self-interacting gauge bosons and the ghost field contribution[2].

[2]Including ghost loop contributions ensures transverse (physical) Lorentz structure when

Relevant diagrams are presented in Fig. C.5.

all terms are summed.

Bibliography

[1] M. J. Alguard *et al.* (SLAC-Yale Collaboration, E80), Phys. Rev. Lett. **37**, 1261 (1976); G. Baum *et al.* (SLAC-Yale Collab.), Phys. Rev. Lett. **45**, 2000 (1980).

[2] G. Baum *et al.* (SLAC-Yale Collaboration, E130), Phys. Rev. Lett. **51** 1135, (1983).

[3] J. Ellis, R. L. Jaffe, Phys. Rev. D **9**, 1444 (1974); J. Ellis, R.L. Jaffe, Phys. Rev. D **10**, 1669(E) (1974); M. Gourdin, Nucl. Phys. **B38**, 418 (1972).

[4] J. Ashman *et al.* (European Muon Collaboration), Phys. Lett. B **206**, 364 (1988); J. Ashman *et al.* (European Muon Collab.), Nucl. Phys. **B328**, 1 (1989).

[5] D. Adams *et al.* (Spin Muon Collaboration), Phys. Lett. B **329**, 399 (1994); D. Adams *et al.* (SM Collab.), Phys. Lett. B **339**, 332(E) (1994).

[6] L.D. Faddeev and V.N. Popov, Phys. Lett. B **25**, 29 (1967).

[7] J. B. Kogut and D. E. Soper, Phys. Rev. D **1**, 2901 (1970).

[8] R. L. Jaffe and A. Manohar, Nucl. Phys. **B337**, 509 (1990).

[9] D. J. Gross and F. Wilczek, Phys. Rev. Lett. **30**, 1343 (1973); H.D. Politzer, Phys. Rev. Lett. **30**, 1346 (1973).

[10] J. C. Collins, D. E. Soper and G. Sterman, arXiv:hep-ph/0409313.

[11] J. Beringer *et al.* (Particle Data Group) Phys. Rev. D **86**, 010001 (2012).

[12] G. Abbiendi *et al.* Eur. Phys. J. C **19**, 587 (2001).

[13] http://pdg.lbl.gov/2009/reviews/rpp2009-rev-frag-functions.pdf

[14] G. Altarelli and G. Parisi. Nucl. Phys. **B126**, 298 (1977); Yu. L. Dokshitzer. Sov. Phys. JETP **46**, 641 (1977).

[15] E. Derman, Phys. Rev. D, **7** 2755 (1973).

[16] C. G. Callan and D. J. Gross, Phys. Rev. Lett. **22**, 156 (1969).

[17] A. Bodek *et al.* Phys. Rev. D **20**, 1471 (1979).

[18] http://pdg.lbl.gov/2009/reviews/rpp2009-rev-structure-functions.pdf

[19] M. Alekseev *et al* (COMPASS Collaboration), Phys. Lett. B **676**, 31 (2009).

[20] A. Airapetian *et al.* (HERMES Collaboration), Phys. Rev. Lett. **84**, 2584 (2000); P. Liebing *et al.* (HERMES Collaboration), AIP Conf. Proc. **915**, 331 (2007); E. S. Ageev *et al.* (COMPASS Collaboration), Phys. Lett. B **633**, 25 (2006); B. Adeva *et al.* (SMC Collaboration) Phys. Rev. D **70**, 012002 (2004).

[21] J. Babcock, E. Monsay, and D. Sivers, Phys. Rev. Lett. **40**, 1161 (1978); Phys. Rev. D **19**, 1483 (1979).

[22] B. Jager, A. Schafer, M. Stratmann, and W. Vogelsang,Phys. Rev. D **67**, 054005 (2003).

[23] Eur. Phys. J. C **63**, 189 (2009).

[24] V. Y. Alexakhin *et al.* [COMPASS Collaboration], Phys. Lett. B **660**, 458 (2008); P. L. Anthony *et al.* [E155 Collaboration], Phys. Lett. B **493**, 19 (2000); A. Airapetian *et al.* [HERMES Collaboration], Phys. Rev. D **75**, 012007 (2007); K. V. Dharmawardane *et al.* [CLAS Collaboration], Phys. Lett. B **641**, 11 (2006); X. Zheng *et al.* [Hall A Collaboration], Phys. Rev. Lett. **92**, 012004 (2004).

[25] B. Adeva *et al.* [Spin Muon Collaboration], Phys. Lett. B **420**, 180 (1998); A. Airapetian *et al.* [HERMES Collaboration], Phys. Rev. D **71**, 012003 (2005); M. Alekseev *et al.* [COMPASS Collaboration], Phys. Lett. B **660**, 458 (2008).

[26] A. Adare *et al.* (PHENIX Collaboration), Phys. Rev. Lett. **106**, 062001 (2011).

[27] A. Adare *et al.* (PHENIX Collaboration), Phys. Rev. Lett. **103**, 012003 (2009).

[28] M. Glueck, E. Reya, M. Stratmann and W. Vogelsang, Phys. Rev. D **63**, 094005 (2001).

[29] D. de Florian, G. Navarro, R. Sassot, Phys. Rev. D **71**, 094018 (2005).

[30] B.A. Kniehl, G. Kramer, B. Ptter, Nucl. Phys. **B582**, 514 (2000).

[31] D. de Florian, R. Sassot, M. Stratmann, Phys. Rev. D **75**, 094009 (2007).

[32] D. de Florian, R. Sassot, M. Stratmann, W. Vogelsang, Phys. Rev. Lett. **101**, 072001 (2009).

[33] I. Alekseev, C. All, M. Bai *et al.*, Nucl. Instrum. and Methods, **A499**, 392 (2003).

[34] A.N. Zelenski *et al.*, Optically-pumped polarized H^- ion sources for RHIC and HERA colliders, in Proceedings of PAC 1999, 1999, p. 106.

[35] H. Okada, Ph.D. thesis, Kyoto University, 2006.

[36] H. Okada *et al.* Phys. Lett. B **638**, 450 (2006).

[37] H. Huang *et al.*, Nucl. Phys. **A721**, 356 (2003).

[38] Y. Fukao *et al.*, Phys. Lett. B **650**, 325 (2007).

[39] C. Adler *et al.*, Nucl. Instrum. and Methods **A470**, 488 (2001)

[40] W. Anderson *et al.*, Nucl. Instrum. and Methods **A646**, 35 (2011).

[41] S.H. Aronson *et al.*, Nucl. Instrum. and Methods **A499**, 480 (2003).

[42] D. Ben-Tzvi and M.B. Sandler , " A Combinatorial Hough Transform ", Pattern Recognition Letters 11, 1990, pp 167-174

[43] K. Adcox *et al.*, Nucl. Instrum. and Methods **A499**, 489 (2003).

[44] H. Bethe and W. Heitler, in *Proceedings of the Royal Society of London, 1934*, Series A, Vol. 146, Issue 856, p. 83.

[45] L. Aphecetche *et al.*, Nucl. Instrum. and Methods **A499**, 521 (2003).

[46] M. Aizawa *et al.*, Nucl. Instrum. and Methods **A499**, 508 (2003).

[47] N.H. Buttimore, E. Gotsmann and E. Leader, Phys. Rev. D **18**, 694 (1978).

[48] J. Schwinger, Phys. Rev. **73**, 407 (1948).

[49] S. Eidelman *et al.*, Phys. Lett. B **592**, 1 (2004).

[50] K. Nakamura *et al.* (Particle Data Group), J. Phys. G: Nucl. Part. Phys. **37**, 075021 (2010).

[51] A. Adare *at al.* (PHENIX Collaboration), Phys. Rev. C **81**, 034911 (2010).

[52] A. Adare *et al.* (PHENIX Collaboration), Phys. Rev. Lett. **97**, 252002 (2006) .

[53] J. Va'vra *at al.*, Nucl. Instrum. and Methods **A324**, 113 (1993).

[54] S.Belikov *at el.*, PHENIX internal analysis note AN184 (2003).

[55] K. Boyle, Ph.D. thesis, Stony Brook University, 2008.

[56] G. Agakishiev *et al.* (STAR Collaboration), Phys. Rev. Lett. **108**, 072302 (2012).

[57] A. Adare *et al.*, Phys Rev. C **83**, 064903 (2011).

[58] RHIC SPIN "White paper" (2012).

[59] Atsushi Taketani, Nucl. Instrum. and Methods **A541**, 137 (2005).

[60] S. Adachi *at al.*, Nucl. Instrum. and Methods **A703**, 114 (2013).

[61] A. Airapetian *et al.* (HERMES Collaboration) Phys. Rev. D **71**, 012003 (2005); M.G. Alekseev *at el.* Phys. Lett. B **693**, 227 (2010).

[62] http://www.bnl.gov/npp/docs/pac0611/DY_pro_110516_final.2.pdf.

[63] http://www.fnal.gov/directorate/program_planning/June2012Public/P-1027_Pol-Drell-Yan-proposal.pdf.

[64] J. Dudek *at el.*, arXiv:1208.1244 [hep-ex].

[65] F. Gautheron *et al.* (COMPASS Collaboration), COMPASS II proposal, CERN-SPSC-2010-014, SPSC-P-340 (2010).

[66] A. Accardi *at el.*, arXiv 1212.1701 [hep-ex].